

## ABSTRACT

McCOY, BRAD CHRISTOPHER. Design and Implementation of a New Retrofit for Prestressed Concrete Bridge Elements Using Mechanically-Fastened Fiber-Reinforced Polymer. (Under the direction of Drs. Rudolf Seracino and Min Liu).

Currently, departments of transportation (DOTs) must post load restrictions or closures on bridges with deteriorated prestressed concrete superstructures that can no longer carry original design loads. These posted restrictions and closures result in detours that increase travel time and vehicle operating costs for detoured vehicles, impacting commerce, public transportation, and emergency services. Often, load restrictions and closures must remain in place for several years to allow for budgeting, design, and contracting cycles prior to scheduling and completion of permanent repairs or superstructure replacement which must occur to remove posted restrictions. A retrofit solution, which is capable of restoring prestress losses and strength reduction in mild to moderately deteriorated prestressed concrete bridge superstructures such that the useful service life of the bridge can be extended for 3 to 5 years allowing a more permanent solution to be planned and budgeted, would be useful. A practical retrofit alternative is one that that can be installed relatively rapidly by DOT maintenance personnel, can immediately restore traffic upon installation, can be easily inspected and maintained as necessary, and should not be more costly than user costs associated with load restrictions or closures. The thesis describes the results of an experimental program to examine the practical and technical feasibility of restoring prestress losses in deteriorated prestressed concrete C-channel beams using a mechanically-fastened fiber-reinforced polymer (MF-FRP) retrofit methodology. This study found that the developed MF-FRP retrofit methodology is capable of restoring the original bridge load rating and can be installed by a single DOT maintenance crew within 1 to 2 days, depending upon the length and level of deterioration of the candidate bridge. Small-scale testing to optimize the mechanical anchor pattern with respect to the capacity of the FRP material was examined and the number of fasteners required for a typical application was determined. A prestressing mechanism for the retrofit and connection design to attach the MF-FRP retrofit system was developed, including effects of the significant spatial restrictions found in the field. The methodology was optimized with respect to FRP efficiency and retrofit installation time. The MF-

FRP retrofit solution was tested on 6 full-scale prestressed concrete C-channel beams recently removed from service. The full-scale tests examined the behavior of the undamaged (control) and deteriorated beams with and without the MF-FRP retrofit. The results of the full-scale tests indicated that the MF-FRP retrofit solution presented in this study is capable of restoring the original load rating of prestressed concrete C-channel beams with mild to moderate prestress loss due to deterioration, and it is feasible for the MF-FRP retrofit to be rapidly installed on-site on a bridge and immediately restore traffic upon installation. Technical limitations and difficulties with field installation techniques used in the initial design resulted in significant changes in both the design and field-fabrication methods. Basic production rates for the initial and improved designs were determined, confirming that the field installation can be completed in as little as a single work day by a typical 4-worker DOT maintenance crew. Additionally, a limited qualitative cost comparison indicates that the proposed MF-FRP methodology is economically feasible with the break-even point between the initial installation and material cost to the DOT and the vehicle operating cost savings occurring between a few days and a few months, depending upon the traffic volume, detour length, and posted restriction level for a deteriorated bridge.

© Copyright 2019 by Brad Christopher McCoy

All Rights Reserved

Design and Implementation of a New Retrofit for Prestressed Concrete Bridge Elements Using  
Mechanically-Fastened Fiber-Reinforced Polymer

by  
Brad Christopher McCoy

A thesis submitted to the Graduate Faculty of  
North Carolina State University  
in partial fulfillment of the  
requirements for the degree of  
Doctor of Philosophy

Civil Engineering

Raleigh, North Carolina

2019

APPROVED BY:

---

Dr. Rudolf Seracino  
Co-Chair of Advisory Committee

---

Dr. Min Liu  
Co-Chair of Advisory Committee

---

Dr. Michael L. Leming

---

Dr. Gregory W. Lucier

**DEDICATION**

*To my wife, Stephanie, and our two boys, Gabriel and Michael, for their unending love and support throughout this project and in life; and to my parents, Ron and Mary Lu, for teaching me to never quit anything.*

## BIOGRAPHY

Lieutenant Colonel Brad McCoy is a native of Omaha, Nebraska. He enlisted in the U.S. Army in 1995 and later earned a B.S. in civil engineering from the U.S. Military Academy (USMA) at West Point, NY in 2001, after which he was commissioned a second lieutenant in the Corps of Engineers. His overseas assignments include Korea, Afghanistan and Iraq with stateside duty at Fort Irwin, CA; Fort Bragg, NC; West Point, NY; and Fort Riley, KS. His operational assignments include Platoon Leader, Company Commander, Battalion Operations Officer, Battalion Executive Officer, Brigade Executive Officer, and Brigade Rear-Detachment Commander. Brad's non-operational assignments include Aide-de-Camp to the Commanding General – National Training Center and Fort Irwin, Aide-de-Camp to the Commanding General – Civilian Police Assistance Training Team-Iraq, Assistant Professor in the Dept. of Civil and Mechanical Engineering at USMA, and multiple student assignments at Fort Sill, OK, Fort Leonard Wood, MO, and Fort Benning, GA. His combat deployments include a 14-month tour in Iraq (September 2004-October 2005) and a 15-month tour in Afghanistan (February 2007-April 2008).

His military awards and decorations include the Bronze Star Medal (2), Meritorious Service Medal (3), Army Commendation Medal (3), Joint Service Achievement Medal, Army Achievement Medal (4), National Defense Service Medal (2), Afghan Campaign Medal, Iraq Campaign Medal, Global War on Terrorism Service Medal, Good Conduct Medal, Korean Defense Service Medal, NATO-ISAF Service Medal, Outstanding Volunteer Service Medal, Humanitarian Service Medal, Joint Meritorious Unit Award, Valorous Unit Award, Meritorious Unit Citation, Combat Infantry Badge, Combat Action Badge, Expert Infantry Badge, Parachutist Badge, Pathfinder Badge, German Parachutist Badge, and Ranger Tab.

Brad holds a M.S. in civil engineering from North Carolina State University (NCSU) (2011). He entered the Ph.D. program at NCSU in August, 2016. Upon completion of the Ph.D. program, Brad will return to USMA as a senior faculty member. Brad holds a Professional Engineer license in the state of Missouri and is a credentialed Envision® Sustainability Professional.

He is married to the former Stephanie Wright of Manteca, California. They have two children, Gabriel (15 years), and Michael, (12 years).

## ACKNOWLEDGMENTS

This project was successful because of the collaborative efforts across multiple people and organizations which comprise the research team, all of whom are the recipients of my sincere gratitude. Most notably, I extend thanks to the guidance and collaboration of Dr. Rudolf Seracino, Dr. Gregory Lucier, Dr. Min Liu, and Dr. Michael Leming. I am incredibly grateful for your wisdom, support, and patience throughout my 33-month stay in the Ph.D. program. I offer thanks to Dr. Thomas Birkland for his service on my committee and professional insight. Additionally, I extend my gratitude to Mr. Zakariya Bourara for his teamwork and friendship as a graduate student working with me for the latter two years of the project, and to Ms. Juliet Swinea, Second Lieutenant Timothy Langerhans, Cadet Cade Fleaher, and Mr. Thomas Stirewalt for their support as undergraduate research assistants at various times during the project.

The North Carolina Department of Transportation (NCDOT) and the *I/UCRC Center for the Integration of Composites into Infrastructure* provided funding for the project. Additionally, Mr. William Briley of the NCDOT Division 5 Bridge Maintenance Division in Wake County, NC provided the six full-scale C-channel beams for proof-of-concept testing, and Mr. Brian Hanks, Mr. Gichuru Munchane, Mr. Dan Muller, and Mr. Tim Sherrill at the NCDOT Structures Maintenance Unit provided invaluable support throughout the project. Turnbuckle assemblies for the MF-FRP prestressing mechanism were provided by Cleveland City Forge.

I offer special thanks to Colonel Karl “Fred” Meyer, Colonel Brad Wambeke, and Colonel Joseph Hanus at the U. S. Military Academy for their incredible mentorship, support, and friendship; and to Mr. Jerry Atkinson, Mr. Johnathan McEntire, and Mr. Benjamin Smith at the Constructed Facilities Laboratory for countless hours of support during preparation and testing – thank you for your expertise and friendship.

I am eternally grateful to my family and friends who provided continuous love and support during long days and late nights throughout this endeavor.

## TABLE OF CONTENTS

LIST OF TABLES.....	vii
LIST OF FIGURES .....	x
LIST OF ACRONYMS .....	xiv
NOTATION.....	xvi
<b>Chapter 1: Introduction.....</b>	<b>1</b>
Background .....	1
Problem Statement and Primary Research Objective.....	6
Research Phases and Intermediate Research Objectives.....	8
Overview of Chapters and Appendices .....	10
<b>Chapter 2: Literature Review .....</b>	<b>12</b>
Fiber-Reinforced Polymer Strengthening Systems .....	12
In-place Concrete Strength.....	20
Concrete Splitting Behavior .....	23
Bridge Load Rating Considerations .....	25
Vehicle Operating Costs.....	29
Digital Image Correlation.....	30
<b>Chapter 3: Addressing Superstructure Load Rating Criteria for Deteriorated Prestressed Concrete Members Using a Proposed MF-FRP Retrofit .....</b>	<b>34</b>
Abstract .....	34
Introduction .....	35
Research Significance .....	38
AASHTO Rating Criteria.....	38
NC Bridge 380093 Case Study.....	41
Proposed Retrofit Solution .....	52
Conclusions and Recommendations.....	62
<b>Chapter 4: Anchor Bolt Patterns for Mechanically-Fastened FRP Plates.....</b>	<b>65</b>
Abstract .....	65
Introduction .....	66
Research Significance .....	66
Background .....	67
Methodology .....	71
Results and Discussion.....	81
Conclusions and Recommendations.....	96
<b>Chapter 5: Additional Mechanical Fastener Diameters .....</b>	<b>98</b>
Introduction .....	98
Methodology .....	98
Results and Discussion.....	99
Conclusions .....	106
<b>Chapter 6: Prestressed MF-FRP: An Experimental Study of a Rapid Retrofit Concept for Deteriorated Prestressed C-Channel Beams .....</b>	<b>107</b>
Abstract .....	107
Introduction .....	108
Research Significance .....	111

Experimental Program.....	112
MF-FRP Retrofit Design .....	116
Results and Discussion.....	126
Conclusions and Recommendations.....	136
<b>Chapter 7: Conclusions and Recommendations for Future Research .....</b>	<b>139</b>
Conclusions .....	139
Future Research.....	142
<b>References .....</b>	<b>145</b>
<b>APPENDICES.....</b>	<b>151</b>
Appendix A: Small-scale Test Matrix and Detailed Test Data .....	152
Appendix B: Bridge 380093 Supporting Calculations.....	165
Appendix C: MF-FRP 2.0 Design Calculations and Detail Drawings.....	174
Appendix D: Overview of MF-FRP Retrofit Field Installation Activities.....	189
Appendix E: ACI 214.4 Calculations and Concrete Core Data.....	191
Appendix F: Methodology and Example of Alternate Method for Determining In-Place Concrete Strength .....	193

## LIST OF TABLES

Table 1.1: North Carolina C-channel Bridge Restriction Summary.....	2
Table 1.2: Total C-channel Bridge Restrictions Impacting Public Service Vehicles.....	3
Table 2.1: Advantages and Disadvantages of Adhesively-Bonded and MF-FRP Systems.....	13
Table 2.2: MF-FRP Literature Summary.....	16
Table 3.1: Structural Material Properties and Strand Details.....	42
Table 3.2: C-Channel Design Section Properties Without Curb.....	46
Table 3.3: C-Channel Section Properties Including Curb.....	48
Table 3.4: Inventory Rating Summary.....	50
Table 3.5: Operating Rating Summary.....	52
Table 4.1: MF-FRP Literature Summary.....	70
Table 4.2: Initial Small-Scale Test Matrix.....	72
Table 4.3: Data Provided by Manufacturer.....	75
Table 4.4: Calculated Data and Sample Size for 90% CL.....	75
Table 4.5: Test Results Summary.....	81
Table 4.6: Mean Specimen Measurements.....	82
Table 4.7: Multi-factor ANOVA Results.....	85
Table 4.8: Single Factor ANOVA Results (DBL16, DBL18, DBL20, DBL22).....	91
Table 4.9: Single Factor ANOVA Results (DBL18, DBL20, DBL22).....	91
Table 4.10: Supplementary Test Matrix.....	95
Table 5.1: Additional Bolt Diameter Test Matrix.....	98
Table 5.2: Test Results Summary – 0.375 in. and 0.75 in. Diameter Bolts.....	99
Table 5.3: Average Maximum Displacement by Treatment Group.....	102
Table 6.1: North Carolina C-channel Bridge Restriction Summary.....	108
Table 6.2: Total C-channel Bridge Restrictions Impacting Public Service Vehicles.....	109
Table 6.3: C-channel Test Matrix.....	113

Table 6.4: C-channel Specified Material Properties.....	115
Table 6.5: C-channel Test Results Summary .....	126
Table 6.6: MF-FRP Retrofit Installation Times for a Single C-channel .....	131
Table 6.7: C-channel Concrete Core Data.....	136
Table A.1: Small-scale FRP Material Test Matrix.....	152
Table A.2: Small-scale FRP Material Test Results Summary.....	153
Table A.3: Detailed FR Material Test Result Data .....	154
Table B.1: Undamaged Inventory Load – 15% losses, $f_t \leq 6\sqrt{f'_c}$ (psi).....	165
Table B.2: Undamaged Inventory Load – 15% losses, $f_t \leq 0\sqrt{f'_c}$ (psi).....	166
Table B.3: Undamaged Inventory Load – 22% losses, $f_t \leq 6\sqrt{f'_c}$ (psi).....	166
Table B.4: Undamaged Inventory Load – 22% losses, $f_t \leq 0\sqrt{f'_c}$ (psi).....	167
Table B.5: Undamaged Ultimate Capacity.....	168
Table B.6: Damaged Inventory Load – 15% losses, $f_t \leq 6\sqrt{f'_c}$ (psi).....	169
Table B.7: Damaged Inventory Load – 15% losses, $f_t \leq 0\sqrt{f'_c}$ (psi).....	169
Table B.8: Damaged Inventory Load – 22% losses, $f_t \leq 6\sqrt{f'_c}$ (psi).....	170
Table B.9: Damaged Inventory Load – 22% losses, $f_t \leq 0\sqrt{f'_c}$ (psi).....	170
Table B.10: Damaged Ultimate Capacity .....	171
Table B.11: AASHTO Lump Sum Results .....	173
Table C.1: MF-FRP 2.0 Variables .....	176
Table C.2: MF-FRP Retrofit Material Properties.....	177
Table D.1: Installation Activity Summary List .....	190
Table E.1: ACI 214.4 Alternate Method Results .....	191
Table E.2: In-place Strength Adjustment Factors.....	191
Table E.3: Concrete Core Data .....	192

Table F.1: Example Compressive Strength Data.....	198
Table F.2: MA3 Results for Candidate $f'c = 3000$ psi; Threshold Coefficient = 1.34.....	200
Table F.3: MA3 Results for Candidate $f'c = 4000$ psi; Threshold Coefficient = 1.34.....	201
Table F.4: MA3 Results for Candidate $f'c = 5000$ psi; Threshold Coefficient = 1.34.....	202

## LIST OF FIGURES

Figure 1.1: Examples of repairable deterioration of prestressed concrete bridge beams .....	1
Figure 1.2: Types of strengthening with composite laminate materials.....	5
Figure 1.3: MF-FRP retrofit concept sketch .....	7
Figure 2.1: Types of fasteners in the current literature .....	15
Figure 2.2: Fastener bearing examples.....	17
Figure 2.3: AASHTO HS-15 and HS-20 loading.....	25
Figure 3.1: Example of repairable deterioration of prestressed concrete bridge beams.....	35
Figure 3.2: Exterior girder deterioration .....	36
Figure 3.3: Bridge 380093 exterior girder SLAB S1 with Prestressing Pattern A.....	43
Figure 3.4: Overview of Bridge No. 380093.....	43
Figure 3.5: Typical interior girders .....	44
Figure 3.6: Transverse post-tensioning .....	45
Figure 3.7: Bridge 380093 exterior girder (SLAB S1) at mid-span; neglecting monolithic curb.....	46
Figure 3.8: Types of strengthening with composite laminate materials.....	53
Figure 3.9: FRP plate schematic .....	55
Figure 3.10: Proposed MF-FRP retrofit applied to C-channel beam .....	56
Figure 3.11: Concrete cover patching prior to MF-FRP installation.....	58
Figure 3.12: Bridge 150035 hollow core slab cross-section .....	59
Figure 3.13: Example deterioration of hollow core slab .....	60
Figure 3.14: Proposed MF-FRP retrofit applied to a hollow core slab .....	60
Figure 3.15: AASHTO girder examples .....	62
Figure 4.1: FRP plate sample examined in this study .....	67
Figure 4.2: Types of fasteners used in previous studies.....	68
Figure 4.3: Fastener bearing due to 4.5 mm PAF .....	69
Figure 4.4: Example DIC strain field and specimen speckle pattern .....	76

Figure 4.5: Test treatment configurations and specimen identification .....	78
Figure 4.6: UTM setup (no-hole and open-holes) and failed specimen .....	79
Figure 4.7: Bolted connection test schematic.....	80
Figure 4.8: Shear strain map of disturbed regions and shear failure .....	86
Figure 4.9: Load-displacement curves for single-bolt tests with 38 mm edge distance.....	87
Figure 4.10: Single-bolt bearing failure modes with DIC inset showing shear strain.....	88
Figure 4.11: Box plots of multi-bolt peak load distributions .....	92
Figure 4.12: Mean multi-bolt load-displacement curves (DBL series).....	93
Figure 4.13: FRP failure modes .....	94
Figure 4.14: Variation of mean peak load and FRP failure modes .....	95
Figure 5.1: S-B-X-0.375 load-displacement curves.....	100
Figure 5.2: Failure mechanisms for DBL20-B and DBL20-B-0.375 treatment groups.....	101
Figure 5.3: 0.5 in. and 0.375 in. bolt diameter peak load distribution .....	102
Figure 5.4: Load-displacement behavior for DBL22-B and DBL22-B-0.375 treatment groups .....	104
Figure 5.5: Load-displacement behavior for DBL14-B-4-0.75 treatment group .....	105
Figure 6.1: Example C-channel deterioration .....	108
Figure 6.2: Damaged C-channel beam.....	112
Figure 6.3: FRP plate examined.....	113
Figure 6.4: C-channel cross section details.....	114
Figure 6.5: Test set-up.....	116
Figure 6.6: MF-FRP 1.0 design details .....	118
Figure 6.7: MF-FRP 1.0 connection photos.....	119
Figure 6.8: MF-FRP 2.0 design details .....	120
Figure 6.9: MF-FRP 2.0 connection photos.....	121
Figure 6.10: $\Delta L_{TOT}$ measurement marks for MF-FRP 2.0 at $P_{FRP} = 82.3$ kN (18.5 kips).....	125
Figure 6.11: Full-scale C-channel beam load-deflection results .....	127

Figure 6.12: FRP failure mode for MF-FRP 2.0 .....	129
Figure 6.13: Installation time comparison of MF-FRP 1.0 and MF-FRP 2.0 by time category .....	134
Figure A.1: Box plots of all multi-bolt peak load distributions .....	158
Figure A.2: Variation of mean peak load vs. bearing surface area for 0.5 in. and 0.375 in. bolts .....	158
Figure A.3: S-B-X load-displacement curves .....	159
Figure A.4: S-B-X-0.375 load-displacement curves .....	159
Figure A.5: DBL14-B load-displacement curves .....	160
Figure A.6: DBL16-B load-displacement curves .....	160
Figure A.7: DBL18-B load-displacement curves .....	161
Figure A.8: DBL18-B-0.375 load-displacement curves .....	161
Figure A.9: DBL20-B load-displacement curves .....	162
Figure A.10: DBL20-B-0.375 load-displacement curves .....	162
Figure A.11: DBL22-B load-displacement curves .....	163
Figure A.12: DBL22-B-0.375 load-displacement curves .....	163
Figure A.13: DBL14-B-4-0.75 load-displacement curves .....	164
Figure A.14: DBL14-B-6-0.75 load-displacement curves .....	164
Figure C.1: Fixed plate design detail .....	178
Figure C.2: FRP connector plate 1 design detail .....	179
Figure C.3: FRP connector plate 2 design detail .....	180
Figure C.4: FRP connector plate 2 with design weld detail .....	181
Figure C.5: Turnbuckle plate with design weld detail .....	182
Figure C.6: Fixed plate machinist as-built drawing .....	183
Figure C.7: Shoulder bolt (pin) machinist as-built drawing .....	184
Figure C.8: Fixed plate-pin as-built assembly detail .....	185
Figure C.9: FRP connector plate 1 machinist as-built drawing .....	186
Figure C.10: FRP connector plate 2 machinist as-built drawing .....	187

Figure C.11: Turnbuckle (TB) plate machinist as-built drawing.....	188
Figure F.1: Graphical MLE (MA3) Analysis, Example 1; Threshold Coefficient = 1.34.....	199

## LIST OF ACRONYMS

AASHTO .....	American Association of State Highway Transportation Officials
ACI.....	American Concrete Institute
AISC .....	American Institute of Steel Construction
ANOVA .....	Analysis of Variance
ASCE .....	American Society of Civil Engineers
ASD .....	Allowable Stress Design
ASR.....	Allowable Stress Rating
ASTM .....	American Society for Testing and Materials
BMS.....	Bridge Management System
C.....	Contributing Time
CICI .....	Center for Integration of Composites into Infrastructure
CIP .....	Cast-in-Place
CL .....	Confidence Limit
DBB .....	Design-Bid-Build
DHHS.....	Department of Health and Human Services
DIC.....	Digital Image Correlation
DOD.....	Department of Defense
DOT .....	Department of Transportation
EB .....	Externally-Bonded
EB-FRP .....	Externally-Bonded Fiber-Reinforced Polymer
FAMA.....	Fire Apparatus Manufacturers Association
FHWA.....	Federal Highway Administration
FRP .....	Fiber-Reinforced Polymer
HC .....	Hollow Core
I/UCRC .....	Industry-University Cooperative Research Centers

LFD.....	Load Factor Design
LFR.....	Load Factor Rating
LRFD.....	Load Resistance Factor Design
LRFR.....	Load Resistance Factor Rating
MF-FRP.....	Mechanically-Fastened Fiber-Reinforced Polymer
NW.....	Not Working Time
NCDOT.....	North Carolina Department of Transportation
NIOSH.....	National Institute for Occupational Safety and Health
NSF.....	National Science Foundation
OSHA.....	Occupational Safety and Health Administration
PAF.....	Powder Actuated Fastener
RF.....	Rating Factor
RWL.....	Recommended Weight Limit
SR.....	State Route
SV.....	Single Vehicle
TB.....	Turnbuckle
TTST.....	Tractor Trailer Semi Truck
USACE.....	U.S. Army Corps of Engineers
UTM.....	Universal Testing Machine
VOC.....	Vehicle Operating Cost
W.....	Working Time
WIM.....	Weigh-in-Motion

## NOTATION

$A_1$	= dead load factor
$A_2$	= live load factor
$A_b$	= bearing surface area
$A_{FRP}$	= cross-sectional area of FRP plate
$A_{ps}$	= cross-sectional area of prestressing steel
$b_a$	= effective width of concrete prism in mechanical fastener array
$C$	= factor for number and type of members (ACI 214.4) / capacity of bridge member (AASHTO)
$c$	= concrete cover to side of bolt
$CV$	= coefficient of variation
$D$	= dead load effect
$d_{bolt}$	= bolt diameter
$d_f$	= fastener diameter
$d_{strands}$	= centroid depth of prestressing strand layers
$dy$	= magnitude of out-of-plane movement
$\Delta f_{pR}$	= change in prestress due to relaxation
$\Delta f_{pR,transfer}$	= change in stress due to relaxation at time of transfer
$\Delta f_{pR,400k}$	= change in stress due to relaxation after 400,000 hours
$\Delta f_{pT}$	= total prestress loss due to elastic shortening, shrinkage, and creep
$\Delta L_p$	= change in length of the FRP plate due to applied prestress force
$\Delta L_{slip}$	= amount of elongation to account for bolt slip in FRP bolted connections
$\Delta L_{TOT}$	= total elongation required to achieve desired $P_{FRP}$
$e$	= eccentricity of prestressing strands
$E_c$	= concrete elastic modulus

$E_{FRP}$	= elastic modulus of the FRP plate
$\epsilon_{ce}$	= prestressing strand strain due to decompression of concrete
$\epsilon_{error}$	= strain error
$\epsilon_{FRP}$	= strain in the FRP plate
$\epsilon_{ps}$	= prestressing strand strain
$\epsilon_{xx}$	= transverse strain
$\epsilon_{yy}$	= longitudinal strain
$f_{allow}$	= allowable stress
$f_c$	= adjusted compressive strength of an individual concrete core
$f_{core}$	= compressive strength of individual concrete core
$f'_c$	= specified design concrete compressive strength
$\bar{f}_c$	= sample mean strength for a set of concrete cores
$(\bar{f}_c)_{CL}$	= lower-bound estimate of mean in-place concrete compressive strength
$f_{cb}$	= resistance of concrete to splitting stress
$f'_{c,eq}$	= equivalent in-place concrete compressive strength
$f_{ci}$	= in-place compressive strength of an individual concrete core
$f_{pe}$	= effective prestress after losses
$f_{pi}$	= initial prestress
$f'_{pi}$	= prestress immediately after transfer
$f_{ps}$	= prestress level in prestressing steel
$f_{pu}$	= ultimate strength of prestressing strand
$f_{py}$	= yield stress of HS prestressing strand
$f_t$	= concrete splitting strength
$f_{t,allow}$	= allowable concrete tensile strength

$f_y^*$	= prestressing steel yield stress
$F_{b,s}$	= force limit per bolt before initial softening
$F_{b,u}$	= maximum capacity per bolt
$F_d$	= adjustment factor for damage due to drilling during core extraction (ACI 214.4) / unfactored dead load stress (AASHTO)
$F_{dia}$	= adjustment factor for core diameter
$F_{l/d}$	= adjustment factor for core length-to-diameter ratio
$F_{mc}$	= adjustment factor for core moisture conditioning
$F_p$	= unfactored prestress force
$F_s$	= unfactored stress due to secondary prestress forces
$F_l$	= unfactored live load stress including impact
$H_0$	= null hypothesis
$H_a$	= alternate hypothesis
$L_g$	= gauge length over which $\Delta L_p$ is measured
$\phi M_n$	= nominal moment capacity of the section
$\phi R_n$	= nominal strength of the section
$\phi V_n$	= nominal shear strength of the section
$h_a$	= effective height of concrete prism in mechanical fastener array
$I$	= impact factor
$I_{xx}$	= weak axis moment of inertia
$I_{yy}$	= strong axis moment of inertia
$l_f$	= fastener length
$L$	= live load factor
$M_a$	= available moment capacity
$M_{curb}$	= moment due to curb weight

$M_{LL}$	= maximum allowable service live load moment
$M_{LL+I}$	= maximum allowable service live load moment including impact
$M_{LL,R}$	= maximum allowable rated live load moment for a given rating criteria
$M_n$	= ultimate nominal moment capacity
$M_{sw}$	= moment due to self-weight
$M_{WS}$	= moment due to dead load of wearing surface
$\hat{\mu}$	= estimator of population mean
$n$	= number of specimens/replicates in a sample set
$n_b$	= number of bolts
$\nu$	= Poisson's ratio
$T$	= critical value from student's- $t$ distribution
$P_e$	= effective prestress force
$P_{eff,400k}$	= effective prestress force at 400,000 hours after release
$P_{FRP}$	= prestress force in the FRP after post-tension is applied
$P_i$	= initial prestress force
$P_{min,one}$	= minimum splitting force for 1 fastener in a single line of fasteners
$P_{min,two}$	= minimum splitting force for 2 fasteners in 2 lines of fasteners
$P_{split}$	= splitting force for mechanical fastener in concrete with effective length greater than $1.8d_{bolt}$
$RF$	= rating factor for bridge live load capacity
$RT$	= bridge member rating tonnage
$s$	= sample standard deviation
$s_a$	= standard deviation of adjustment factors
$s_c$	= standard deviation of core strengths
$S_L$	= center-to-center longitudinal spacing of bolts for MF-FRP 2.0 fixed plate
$S_T$	= edge-to-edge transverse spacing of bolts for MF-FRP 2.0 fixed plate

$\hat{\sigma}$	= estimator of population standard deviation
$T_o$	= open-hole capacity of FRP plate
$T_p$	= tension force in FRP plate
$t_p$	= thickness of FRP plate
$W$	= weight of nominal vehicle
$\bar{x}$	= sample mean
$y$	= distance between camera focal point and test specimen
$y_{bottom}$	= distance from N.A. to bottom fiber
$y_{top}$	= distance from N.A. to top fiber
$Z$	= critical value from standard normal distribution

## CHAPTER 1: INTRODUCTION

### Background

Prestressed concrete elements of various shapes and forms are among the common bridge superstructure systems currently in service in North Carolina and across the United States. Many such bridges are in varying states of distress and require retrofit to extend their useful service life prior to complete superstructure replacement. Examples of deteriorated prestressed concrete beams include, but are not limited to: 1) C-channel girders such as that of Bridge No. 380093 (Figure 1.1a), located on Service Route No. 1156 across Owen Creek in Granville County, North Carolina, which was the subject of a 2014 study by the North Carolina Department of Transportation (NCDOT); and 2) cored slabs such as that of Bridge No. 150035 (Figure 1.1b), located on US Highway 70 across Ward Creek in Carteret County, North Carolina and the subject of a 2016 NCDOT study (Van Brunt et al., 2016).



(a) C-channel girder – Bridge No. 380093

(b) Cored slab – Bridge No. 150035

**Figure 1.1:** Examples of repairable deterioration of prestressed concrete bridge beams.

Of particular interest for this research are the 269 bridges in North Carolina with C-channel superstructures, of which 226 have load restrictions posted (or are closed) due to superstructure deterioration (NCDOT BMS, 2018). Deterioration of the prestressed concrete channel beams often results in prestress losses and requires both inventory and operating rating levels to be reduced (McCoy et al., 2019c). These bridge load restrictions are categorized by the American Association of State Highway and Transportation Officials (AASHTO) as: 1) single vehicle (SV); and 2) truck tractor semi-trailer (TTST)

(AASHTO, 2018). Table 1.1 provides a summary of the in-service C-channel bridges across North Carolina.

**Table 1.1:** North Carolina C-channel Bridge Restriction Summary.

	SV	TTST
Total Posted Restrictions	225	208
Percent Posted (%)	83.6	77.3
Average Restriction Value (kN / ton)	227 / 25.5	267 / 30.0
Median Restriction Value (kN / ton)	214 / 24	258 / 29
Minimum Restriction (kN / ton)	44.5 / 5	44.5 / 5
Maximum Restriction (kN / ton)	365 / 41	400 / 45
Total Closures	1	3
Average Detour (km / mi.)	12.6 / 7.8	12.1 / 7.5

The average detour length across the 226 restricted or closed bridges is 12.6 km and 12.1 km (7.8 mi. and 7.5 mi.) for SV and TTST, respectively. Detours due to bridge restrictions and closures increase vehicle operating costs (VOC) for industries that routinely use routes with restricted bridges, which can lead to substantial highway customer costs and increased travel time. While not the focus of this research, a previous study conducted by the North Carolina Department of Transportation (NCDOT) concluded that the average VOC for vehicles greater than 231 kN (26 tons) is \$1.61 per km (\$2.59 per mi.) and \$1.16 per km (\$1.86 per mi.) for vehicles less than 231 kN (26 tons) (Cavalline et al., 2015), meaning these detours are directly costing each vehicle owner approximately \$14-20 each way. Further, the study concluded the average detour speed is 64.5 km/h (40 mph) resulting in an 11.7-minute average detour time for SV and 11.3-minute average detour time for TTST.

The detours due to bridge load restrictions and closures not only impact industry, but public transportation and emergency services as well. Table 1.2 shows the number of C-channel bridges in North Carolina with restrictions that detour a typical Type C School Bus (151 kN / 16 ton), a typical pumper truck fire apparatus (187 kN / 21 ton), and a typical aerial ladder truck fire apparatus (338 kN / 38 ton) (FAMA, 2017). Bridge restrictions that detour fire trucks increase emergency response times in those areas and impact the safety of residents. Using an average emergency vehicle travel speed of 72.5 km/h (45 mph), the response times for pumper trucks and aerial ladder trucks are increased by approximate 9

and 12 minutes, respectively. These increases alone are more than double the U.S. national benchmark response time of 5 minutes (Ammons, 2001). It is important to note that North Carolina is one of 21 states in the U.S. that do not exempt emergency service vehicles from weight restrictions (FAMA, 2017). Therefore, it is reasonable to include bridge restriction detours in emergency service response times in North Carolina (and in all non-exempt states).

**Table 1.2:** Total C-channel Bridge Restrictions Impacting Public Service Vehicles.

	SV	TTST	Average Detour (km / mi.)
Type C School Bus	13	NA	24 / 15
Pumper Truck Fire Apparatus	68	NA	11 / 6.8
Aerial Ladder Truck Fire Apparatus	NA	177	14 / 8.7

The 226 C-channel bridge restrictions and closures across North Carolina increase travel time, vehicle operating costs (VOC), and emergency response capabilities, significantly impacting commerce and the lives of residents. Current solutions available to address bridge superstructure deterioration include immediate bridge replacement, temporary posted restrictions or closures until bridge replacement can be scheduled, and long-term restrictions or closures. In most cases in NC, the scheduling process for bridge replacement takes 3-5 years, including the time required for capital project funding and the design-bid-build or design-build project delivery cycles. Therefore, a retrofit solution is desired which can be installed rapidly, can be easily inspected and maintained, and would be capable of restoring prestress losses for a period of 3-5 years. Such a system would allow deteriorated C-channel beams to remain in service without posted load restrictions or closures while a permanent superstructure replacement is scheduled and completed.

The challenge is to develop retrofit techniques that are durable, easy to install, monitor and maintain, and that may be applied to the range of prestressed concrete beam types. Critically, state Departments of Transportation (DOT) must also be able to rate the proposed retrofit using approved American Association of State Highway and Transportation Officials (AASHTO) methods before it may be applied in the field.

AASHTO (2018) requires bridges be rated for two categories – operating and inventory rating. McCoy et al. (2019c) describes in detail the requirements and impacts for each rating criteria. Inventory rating criteria establish the maximum load level which can be applied to the bridge without damage for an indefinite period of time and an indefinite number of cycles. Inventory ratings are typically based on elastic stress limit states. Operating rating criteria establish a load level which can be applied safely to a bridge for an extended period of time, but may cause incremental damage with each loading. The operating rating is based on strength limit states and is typically a specified factor of the ultimate strength capacity. In most cases, the operating rating controls bridge capacity and load restrictions; however, to adequately remove posted load restrictions from deteriorated prestressed concrete bridge superstructures, both operating and inventory rating criteria must be addressed.

A feasible retrofit solution must restore prestress losses such that concrete stress limits at service load levels are within AASHTO (2018) allowable limits:

$$f_{t,allow} = 0.5\sqrt{f'_c} \text{ (MPa)} \quad (1.1a)$$

or

$$f_{t,allow} = 6\sqrt{f'_c} \text{ (psi)} \quad (1.1b)$$

where  $f_{t,allow}$  is the allowable concrete tensile stress, and  $f'_c$  is the concrete design compressive strength. Equation 1.1 is the controlling inventory rating criteria for prestressed C-channel beams (McCoy et al., 2019c). Many bridge owners, in accordance with AASHTO (2018) provisions, further reduce  $f_{t,allow}$  to  $0.25\sqrt{f'_c}$  MPa (or  $3\sqrt{f'_c}$  psi) or 0 depending upon environmental conditions. Therefore, to address the most conservative tensile stress limits, a desirable retrofit solution must be capable of limiting concrete tensile stress to zero at inventory rating levels, and must be capable of restoring the ultimate strength capacity such that the operating rating of a deteriorated C-channel beam is equal to or greater than the original operating rating.

Typical strengthening systems include those which attach composite laminate materials to the tension face of elements to provide additional capacity. The laminate materials are attached through external

adhesive bonding (Figure 1.2a), mechanical fasteners (Figure 1.2b), or a combination of both (hybrid) (Figure 1.2c). The schematics presented in Figure 1.2 represent a simply supported beam, in positive bending such that the composite material is attached to the tension face of the beam to provide additional tensile capacity to the strengthened element.

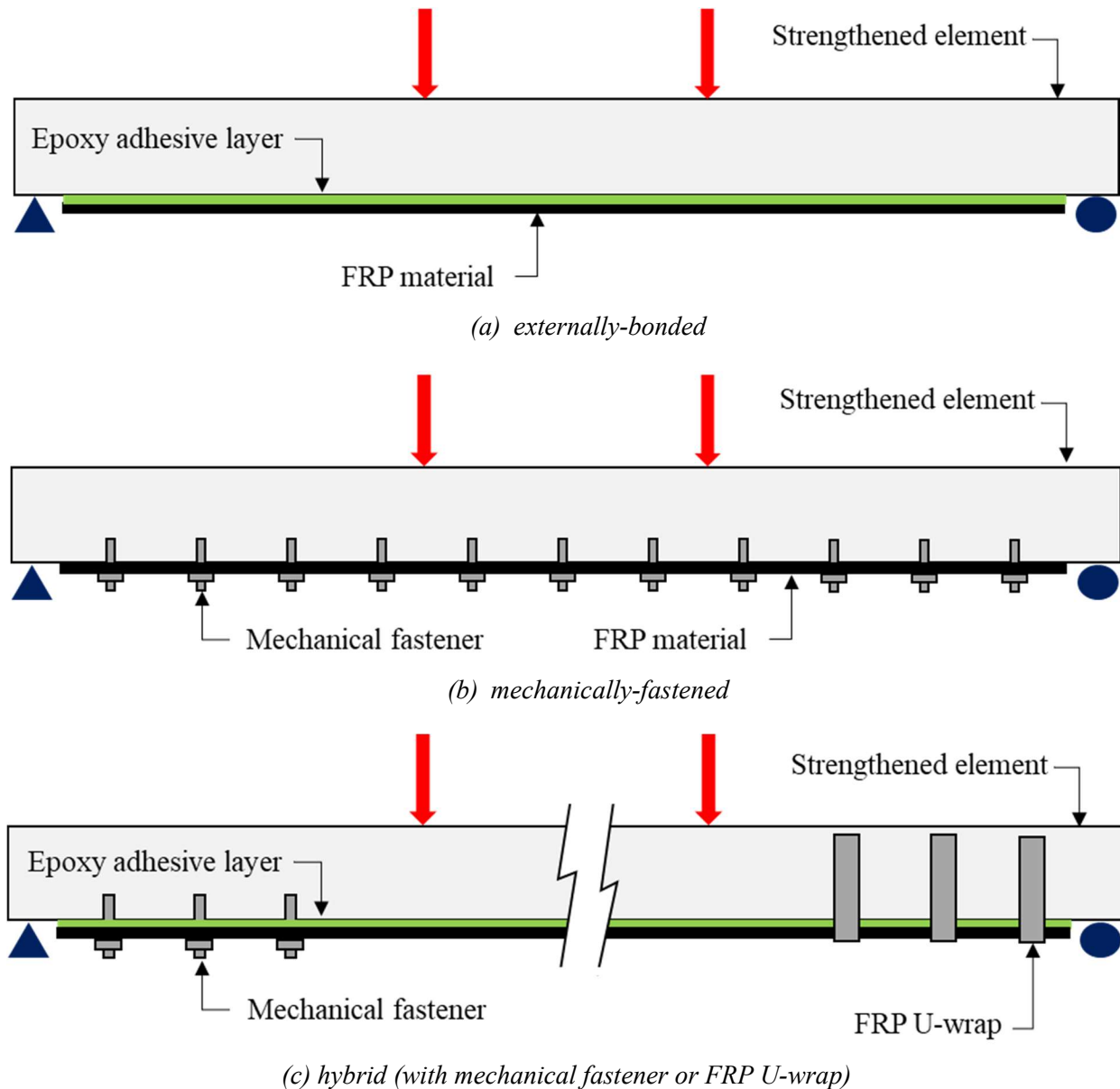


**Figure 1.2:** Types of strengthening with composite laminate materials.

Externally bonded and hybrid systems, while often effective methods of strengthening, present challenges which do not exist with mechanically fastened systems. The epoxy cure time to achieve the desired bond required creates extended installation time leading to longer bridge closure time, which

increases direct and indirect costs due to delays and extended travel time due to detours. Additionally, the quality of the adhesive bond is difficult to control and monitor during subsequent bridge inspections. Therefore, the retrofit technique developed in this research focuses on the use of mechanical fastening only to present a solution that is reasonably quick to install, is traffic ready upon installation, and the quality of the attachment can be easily inspected at time of installation and during subsequent bridge inspections throughout the life of the system. Further, the retrofit solution must have a mechanism for prestressing to restore prestress losses due to deterioration and bring concrete tensile stresses to within AASHTO (2018) allowable limits, an effect that is not conveniently achieved with externally bonded systems.

### **Problem Statement and Primary Research Objective**

Temporary strengthening and restoration of prestress losses is necessary to maintain sufficiently high operating and inventory ratings to keep deteriorated bridges functional while replacement is scheduled. In lieu of an acceptable retrofit solution, the bridge may need to be load posted or closed, often resulting in significant detours and disruption. The primary research objective of this project is the development of a methodology and experimental program that is fundamental to extending the useful life of existing infrastructure through rapid restoration of prestress losses in deteriorated prestressed concrete bridge superstructures. The product of the methodology is a mechanically-fastened fiber-reinforced polymer (MF-FRP) retrofit solution which can be applied to deteriorated prestressed concrete bridge superstructures and prestressed to a level such that prestress losses due to deterioration are restored. Restoration of the prestress losses must result in concrete tensile stresses that are within allowable AASHTO limits permitting the retrofitted bridge to remain open, without posted load restrictions, until member replacement, or complete bridge reconstruction can occur. A concept sketch of the retrofit solution applied to a C-channel beam is presented in Figure 1.3.

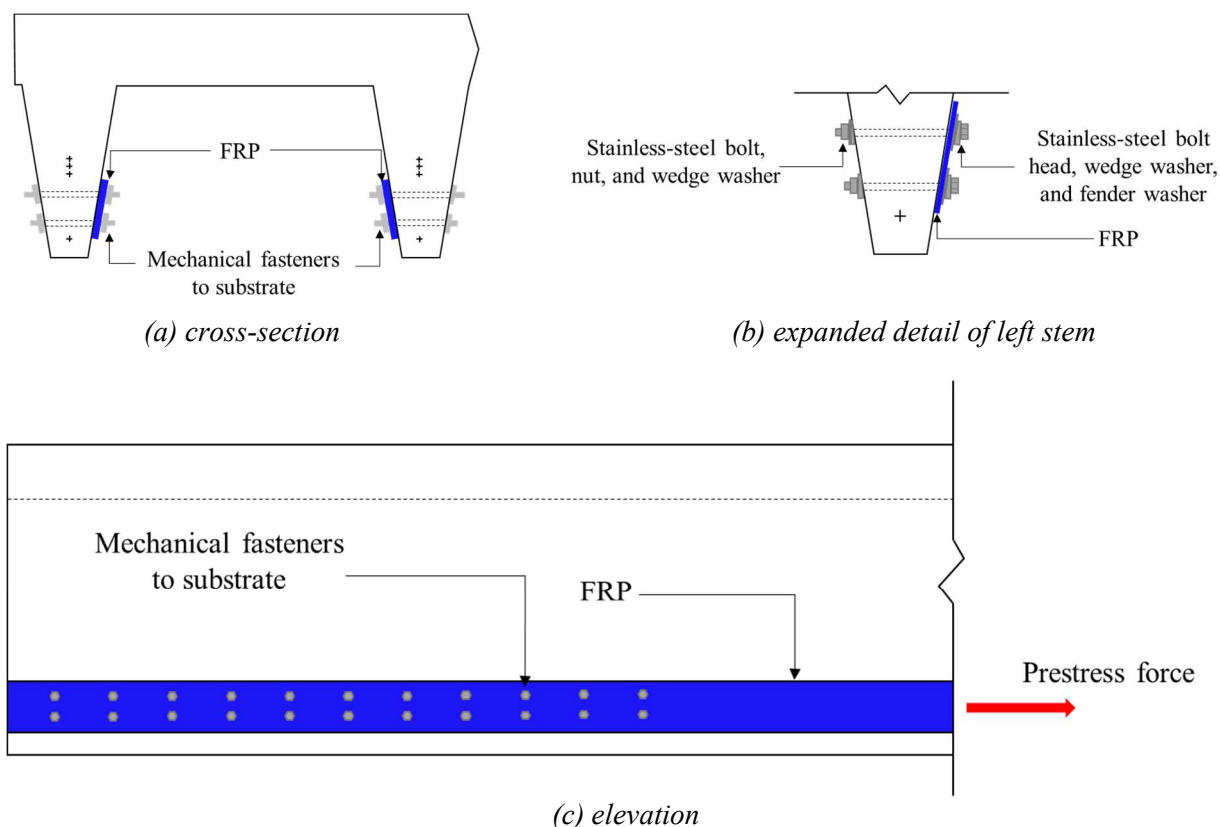


**Figure 1.3:** MF-FRP retrofit concept sketch.

### *Research Questions, Summary Tasks and Significance*

Three key research questions support the primary research objective and form the summary tasks:

- 1) What is necessary to restore prestress losses on deteriorated prestressed concrete superstructures such that the existing bridge can remain in place without posted restrictions or closures until permanent replacement can occur?
- 2) Can a commercially available FRP material develop the necessary tensile capacity through mechanical fasteners to restore prestress losses due to deterioration of concrete cover and corrosion of high-strength steel prestressing strands?
- 3) Can MF-FRP be designed for rapid installation on prestressed concrete elements and prestressed with a field-expedient prestressing mechanism with the use of common tools and without the need for special labor skills?

Key summary tasks of this project include 1) understanding of AASHTO inventory and operating rating requirements for prestressed concrete bridges, 2) development of an MF-FRP anchor system capable of developing the necessary prestress levels in the applied FRP plate to restore inventory and operating rating loads, 3) development of a field expedient prestressing mechanism which can be incorporated into the MF-FRP retrofit design, 4) complete design of an MF-FRP retrofit solution which can be installed with common tools and labor skill, and 5) full-scale testing for proof-of-concept of the developed prestressed MF-FRP methodology and installation time minimization.

While the MF-FRP retrofit solution and installation processes and procedures are of particular interest to the NCDOT, the methodology, experimental program, retrofit solution, and installation methods are of interest to departments of transportation across the country and in other nations where deteriorated prestressed concrete bridge superstructures are in need of restoration or replacement. The retrofit techniques developed during this project could also be of interest to a broader set of applications, to include those within the Department of Defense (DOD) in theaters of operations where rapid restoration or strengthening of bridges may be necessary for the success of military operations. The MF-FRP retrofit solution developed in this research is specific to prestressed C-channel beams; however, the methodology and experimental program can be extended to other beam cross-sections with mild to moderate prestress loss due to deterioration.

### **Research Phases and Intermediate Research Objectives**

The primary research objective is addressed through the following phases:

- 1) Small-scale material testing – The intermediate research objective of this phase is to gain a fundamental understanding of the FRP material behavior within the context of the primary research objective. The following tests are presented with sufficient number of replicates for each test treatment to provide statistical significance to the results. All tests are conducted using Digital Image Correlation measurement techniques to provide continuous strain mapping of the test specimens.

- a. No holes: Uniaxial tension testing of the FRP plate with no holes to inform the ultimate capacity, strain behavior, and failure mode of the plate. The shear strain behavior around each hole will inform the appropriate fastener spacing requirements to minimize the interaction of the disturbed region around each hole.
  - b. Open holes: Uniaxial tension testing of the FRP plate with open holes to inform the capacity, strain behavior, and failure mode with holes without bearing. Aligned and staggered hole patterns will be considered to determine the effects of each pattern on material behavior.
  - c. Single-bolt bearing: Uniaxial tension testing of the FRP plate in single bolt bearing to inform the localized bearing capacity and strain behavior. Single-bolt results inform the number of bolts considered in subsequent multi-bolt bearing tests.
  - d. Multi-bolt bearing: Uniaxial tension testing of the FRP plate in multi-bolt bearing in desired fastener patterns and numbers to inform the material behavior and examine the FRP strain development through the fastener pattern as load increases.
- 2) Design of prestressing mechanism and MF-FRP connection – The intermediate research objective of this phase is to provide a field-ready prestressing mechanism and MF-FRP connection that is capable of developing the necessary prestress force with common tools and no specialty labor skills. The development of the MF-FRP retrofit solution includes the design of the prestressing mechanism and connection of the FRP plate to the prestressing mechanism and the connection of the MF-FRP retrofit to the concrete substrate. Design of the prestressing mechanism and connection considers steel yielding due to tension and bearing, bolt shear, and concrete splitting and crushing due to bearing of the mechanical fasteners. The MF-FRP retrofit is designed with A572 Grade 50 steel and A325 Grade 8 bolts for the purposes of concept development in the lab; however, it is recommended that the MF-FRP retrofit connections and prestressing mechanism be constructed of A306 or A316 stainless steel to resist corrosion in the field.

- 3) Full-scale testing – The intermediate research objective of this phase is a proof-of-concept of the designed retrofit solution and optimization to enable rapid installation of the solution. This phase, while specific to a single bridge beam section type, provides a validation of the methodology and experimental program developed in this research. This phase consists of testing the MF-FRP retrofit concept on undamaged and damaged full-scale C-channel beams. Testing includes installation (anchorage and prestressing) and post-installation loading of the member. The time required to install the MF-FRP retrofit is also recorded and design adjustments recommended to reduce installation time and increase efficiency of the MF-FRP retrofit solution. Deflection controlled loading is applied statically through beam failure. Data collection during testing includes applied load, vertical deflection, FRP strain, concrete cracking pattern and failure mode. Digital Image Correlation is also used to record FRP strain development at the end-anchorage region of the MF-FRP retrofit.

### **Overview of Chapters and Appendices**

The research presented in this dissertation is organized into chapters by key topic. The organization of the thesis is as follows:

Chapter 2: Chapter 2 is a consolidated literature review by critical topic. Elements of Chapter 2 are repeated in subsequent chapters as necessary for a focused background presentation within each chapter, particularly for chapters that are stand-alone publications.

Chapter 3: Chapter 3 presents a case study which serves as the impetus for the proposal and development of a prestressed MF-FRP methodology to address deteriorated prestressed concrete elements. Chapter 3 is currently under peer review with the *ASCE Journal of Performance of Constructed Facilities*.

Chapter 4: Chapter 4 investigates the capacity of several mechanical fastener patterns using 0.5 in. diameter bolts. Statistical rigor is applied to provide results that are statistically significant at the 90% confidence limit or higher. Chapter 4 is accepted for publication in the *ASCE Journal of Composites for Construction*.

Chapter 5: Chapter 5 investigates the capacity of alternate bolt diameters building upon the results presented in Chapter 4. The results presented in Chapter 5 are programmed for submission to ASCE *Journal of Composites for Construction* upon completion of additional research to investigate creep effects and fatigue behavior of the MF-FRP fastener patterns.

Chapter 6: Chapter 6 draws upon the small-scale testing phase to develop an initial design solution to apply the prestressed MF-FRP methodology to deteriorated prestressed concrete C-channel beams. A subsequent design is developed increase efficiency of the MF-FRP system and minimize jobsite-level installation tasks and time. Chapter 6 is currently under peer review with the ASCE *Journal of Performance of Constructed Facilities*.

Chapter 7: Chapter 7 is a presentation of conclusions and recommendations for future research.

Appendix A: Appendix A presents detailed data and charts for mean peak load, mean peak stress, and load-displacement behavior for all small-scale material tests.

Appendix B: Appendix B presents supporting calculations for the case study bridge presented in Chapter 3. The calculations presented are a collaborative effort with the co-authors of the journal paper submitted to ASCE *Journal of Performance of Constructed Facilities*.

Appendix C: Appendix C presents a limit state summary, detailed design calculations, design drawings, and machinist as-built drawings for the MF-FRP 2.0 design.

Appendix D: Appendix D presents an overview of field-level installation activities for DOT maintenance personnel consideration.

Appendix E: Appendix E presents detailed data for the concrete cores taken from specimens MF-FRP-D1, MF-FRP-D2, and MF-FRP-U2. Additionally, relevant variable values for the ACI 214.4 (2010) Alternate Method results presented in Chapter 6 are also presented.

Appendix F: Appendix F presents the methodology and an example result for a method of obtaining reasonable values of in-place concrete strength using maximum likelihood estimation (MLE). The MLE methodology is an alternate method to the more common methods described in ACI 214.4 (2010), discussed in Chapters 2 and 6 of this thesis.

## **CHAPTER 2: LITERATURE REVIEW**

This chapter presents a summary of the literature review conducted for this research and the knowledge gaps and conclusions relevant to the research are identified. Each subsequent chapter is a separate journal publication, and, therefore, begins with an introduction and literature review / background section that is specific to the research presented in the respective chapter.

### **Fiber-Reinforced Polymer Strengthening Systems**

Compared to structural steel, FRP provides advantages in durability (Rahman et al., 1998) and material weight, which reduces overall cost of the system. The weight of the FRP plate presented in this thesis is significantly less than an A572 Grade 50 (50 ksi yield strength) structural steel plate of appropriate geometry to achieve the desired strengthening effects. A structural steel plate would need to have a cross sectional area of 1.2 in<sup>2</sup> to achieve the desired strengthening effects. The length of the plate examined in this study is approximately 275 in., resulting in a 90 lb., 23-ft.-long steel plate, compared to just 8 lb. for the same length of the FRP plate. Further, the FRP plate examined in this thesis can be rolled and carried by single worker, making the FRP much easier to transport to the job site and install. Therefore, because of the weight and installation advantages over a comparable steel plate, FRP is desired for the primary strengthening element for the retrofit developed in this thesis.

### ***Externally-bonded fiber reinforced polymer***

Externally-bonded FRP (EB-FRP) strengthening systems are among the common methods for strengthening concrete structures, to include bridge superstructures. The primary advantage to EB-FRP systems is the efficiency of the system (Oehlers and Seracino, 2004). The adhesive bond between the FRP material and concrete substrate allows full-interaction to develop, and therefore, efficiently transfers force to the bonded FRP to increase strength and stiffness. Additionally, FRP sheets can take many geometric forms, allowing for installation on a wide-range of cross-sections.

There are, however, a number of disadvantages to EB-FRP systems, as outlined by Oehlers and Seracino (2004): 1) the quality of the bond along the length of the applied FRP is often difficult to verify

in the field which causes quality assurance problems at time of installation, and subsequent inspections throughout the life of the installed system; 2) debonding occurs through intermediate crack (IC) debonding, critical diagonal crack (CDC) debonding, and plate end (PE) debonding; 3) brittle failure mechanisms for EB-FRP systems occur from mechanical debonding or environmental factors which cause chemical deterioration of the adhesive; 4) performance of the system depends largely upon the strength of the concrete cover in the strengthened element, which is typically the most degraded concrete in deteriorated concrete structures; and 5) installation requires time consuming and labor intensive preparation of the concrete surface, application of the adhesive, and adhesive curing, all of which delay use of the strengthened structure. A summary of advantages and disadvantages, with a focus on bridge strengthening applications, is presented in Table 2.1.

For the purposes of this research, the disadvantages of the EB-FRP systems prohibit the feasible consideration of the system as a rapid retrofit solution for deteriorated prestressed concrete superstructures.

**Table 2.1: Advantages and Disadvantages of Externally-bonded and MF-FRP Systems.**

	FRP Application Method	
	Externally-bonded	Mechanically-Fastened
Advantages	<ul style="list-style-type: none"> <li>- full-interaction offers efficient system</li> <li>- FRP sheet in-situ installation can take many geometric forms</li> </ul>	<ul style="list-style-type: none"> <li>- ductile failure</li> <li>- environmental impacts reduced with treated fasteners</li> <li>- installation in hours</li> <li>- installed with simple tools</li> <li>- no concrete surface preparation required</li> <li>- immediate loading after installation</li> </ul>
Disadvantages	<ul style="list-style-type: none"> <li>- surface preparation required</li> <li>- increased labor skill required</li> <li>- epoxy cure time</li> <li>- deterioration of epoxy in exposed environments</li> <li>- bond quality difficult to inspect</li> <li>- premature debonding in flexural elements (IC, CDC, PE)</li> <li>- brittle failure</li> <li>- requires sound concrete for complete bond</li> </ul>	<ul style="list-style-type: none"> <li>- partial interaction due to bolt slip</li> <li>- potential for concrete damage due to fastener installation</li> <li>- requires sound concrete for fastener bearing in anchor zones</li> </ul>

### ***Mechanically-fastened fiber-reinforced polymer***

Strengthening of reinforced concrete bridge decks and girders to increase the Federal Highway Administration (FHWA) load rating using MF-FRP was the subject of previous research projects (Bank et al., 2002; Lamanna et al., 2004a; Lamanna et al., 2004b; Borowicz et al., 2004; and Lamanna et al., 2001), which focus on various types of fasteners, and the interactions between the concrete and fasteners. Additional experimental projects for the Wisconsin DOT and Missouri DOT which examine the increased load rating and construction procedures required to strengthen reinforced concrete bridge decks using MF-FRP plates are presented by Bank (2004).

Compared to externally-bonded systems, MF-FRP offers several advantages: 1) failure modes are generally ductile in nature due to bolt bearing in the FRP material or concrete substrate which propagates progressively prior to complete failure of the system (Oehlers, 2001); 2) the mechanical fasteners can be treated to withstand environmental effects in marine environments and in situations where elevated temperatures are of concern (Oehlers, 2001); 3) installation of MF-FRP systems are quick – often completed within a matter of hours; 4) installation requires no special tools or labor skills, no concrete surface preparation; and 5) MF-FRP systems can be loaded immediately after installation (Sena-Cruz et al., 2012) (Table 2.1).

However, MF-FRP strengthening systems also present disadvantages compared to EB-FRP systems. Due to bolt-slip at each fastener, MF-FRP systems only develop partial interaction at the concrete-FRP interface which reduces the efficiency of the system (Oehlers, 2001). Additionally, depending upon the type of fastener, moderate to significant damage of the concrete substrate may occur during installation, weakening the interaction between the FRP material and concrete substrate (Oehlers, 2001) (Table 2.1).

Ebead and Saeed (2014) examined the behavior of reinforced concrete beams strengthened with externally bonded FRP, MF-FRP, and hybrid solutions that use both external bonding and mechanical fasteners. The research presented concludes that mechanically fastening the FRP to the strengthened member increases shear transfer across the interface between the FRP and reinforced concrete beam when compared to externally bonded solutions – a desirable effect for the prestressed MF-FRP application

examined during this project. Further, Elsayed et al. (2009) examined two types of mechanical fasteners and compared the performance to external bonding alone for FRP strengthening of concrete elements using SAFSTRIP®. The results of the study conclude a sufficient number and proper spacing of fasteners enables a higher load in MF-FRP plates compared to externally bonded FRP plates – 19.4 kips and 11.3 kips, respectively – with the failure modes resulting in FRP rupture in the mechanically fastened system with a sufficient number of fasteners, and debonding of the FRP from the strengthened element in the EB system.

Table 2.2 provides a summary of the available MF-FRP research with the size and type of fasteners used. While Table 2.2 does not include all available literature on MF-FRP studies, the studies listed represent the majority of available studies specific to MF-FRP systems using powder-actuated fasteners (PAF), wedge anchors, or screw anchors (Figure 2.1), and are all conducted using the commercially available SAFSTRIP® FRP plate material.

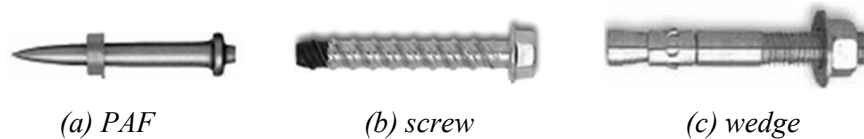


**Figure 2.1:** Types of fasteners in the current literature (adopted from Martinelli et al., 2014).

Results for each study were reported in various ways – percent increase from a control test, total applied load to a strengthened beam in four-point bending, and maximum applied load for pure tension tests – therefore, it is difficult to draw direct comparison across the studies presented in Table 2.2. However, many of the studies show similar results. Those examining powder-actuated fasteners as a means for attaching the FRP to the strengthened member concluded fastener pull-out is the primary failure mode in all cases (Borowicz, 2002; Lamanna et al., 2001; Elsayed et al. 2009). This pull-out failure is likely due to a combination of concrete damage during application of the PAF, smooth shank, and relatively short fastener length ( $l_f$ ) compared to many of the wedge and screw anchors examined.

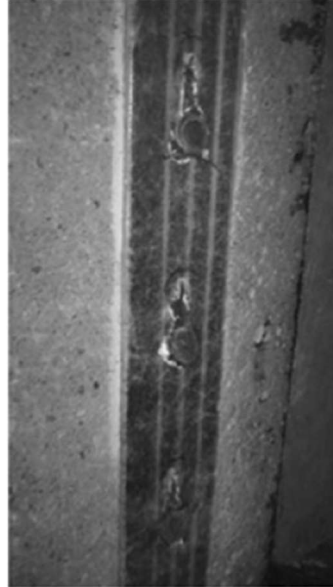
Studies that examine fastener arrays with relatively thin wedge and screw anchor systems, a fastener diameter ( $d_f$ ) less than 0.50 in., failed in bearing – a typical example is shown in Figure 2.2a – due to the small diameter of the anchors (Realfonzo et al., 2012; Ebead, 2011; Martinelli et al., 2014; Elsayed et al.,

2009). Martin and Lamanna (2008) used 0.50 in. diameter screw fasteners to attach a single FRP plate to a reinforced concrete beam and reported a 38.5% increase in strength with minimal bearing in the FRP at each fastener location (Figure 2.2b). A combined failure of bearing (ductile failure) and FRP rupture (brittle failure) is desired to create a ductile strengthening system as noted by Lee, Lopez and Bakis (2009). These findings indicate that an efficient anchorage which fully develops the capacity of the FRP plate with slight bearing at each fastener can be obtained with fastener diameters of 0.50 in. or greater.

**Table 2.2:** MF-FRP literature summary (adopted from Martinelli et al., 2014).

Source	Type	Fastener			Test Type
		$d_f$ (in) <sup>1</sup>	$l_f$ (in) <sup>1</sup>	# lines <sup>2</sup>	
Borowicz (2002)	PAF	0.175	1.85	2-a	4P Bending
Ebead (2011)	Screw	0.187	1.5	1-a / 2-a	
Ekenel et al. (2005)	Wedge	0.375	1.6	1-s	
	PAF	0.157	1.26	2-a	
	Wedge	0.315	2.17	1-s	
El-Maaddawy (2013)	Screw	0.315	2.17	1-s	
	PAF	0.157	1.26	1-a / 2-a	
			2.05	1-a / 2-a	
Galati et al. (2007)	Wedge	0.472	3.93	1-s / 2-a	
		0.157	0.866	2-a	
Lamanna (2002)	PAF	0.146	1.06	1-a	
		0.146	1.26	1-a	
Lamanna et al. (2001)	PAF	0.137	1.06	2-a	
		0.146	1.26	1-a	
Bank et al. (2002)	PAF	0.177	1.26	2-a	
Lamanna et al. (2004)	PAF	0.177	1.85	2-a	
Lee et al. (2007)	PAF	0.137	0.984	2-a	
		0.137	1.26	2-a	
Bank and Arora (2007)	PAF / Wedge	0.158 / 0.50	1.75 / 2.75	1-a	
Martin and Lamanna (2008)	Screw	0.50	2.0	1-a / 1-s	
Napolin et al. (2008)	Screw	0.375	1.75	1-s	
Dempsey and Scott (2006)	Screw	0.177	2.0	2-a	
Realfonzo et al. (2012)	Screw	0.236	1.77	1-a	
				2-s	
Elsayed, Ebead, and Neale (2009)	PAF	0.147	1.85	1-a	
	Screw	0.187	1.45	1-a / 2-a	

Notes:<sup>1</sup> value converted from SI units; <sup>2</sup>“a” denotes “aligned” lines; “s” denotes “staggered” lines; lines are in the longitudinal direction; <sup>3</sup>MF-FRP applied to timber elements. 1 in. = 25.4 mm.



(a) 0.15 in. PAF

(Elsayed, Ebead, and Neale, 2009)



(b) 0.50 in. screw

(Martin and Lamanna, 2008)

**Figure 2.2:** Fastener bearing examples.

The fastener patterns presented throughout the research are predominantly single or double aligned fastener rows. While five of the studies presented in Table 2.2 examine staggered fastener patterns, only Realfonzo et al. (2012) presents a staggered pattern with sufficient transverse spacing for consideration in this study. The remaining four staggered fastener patterns presented in the literature are of systems in which the fastener pattern extends along the length of the FRP plate, with the holes offset from the centerline only slightly (referred to in much of the literature as a single-row staggered pattern). Realfonzo et al. (2012) presents a two-row staggered pattern of four (4) total fasteners which fail in bearing in a similar manner to the two-row and single-row fastener patterns presented throughout the literature. Because the predominance of available research examines either single or two-row aligned fastener patterns, or patterns with only slight staggering, there is a knowledge gap with respect to the behavior of MF-FRP using staggered fastener patterns. This apparent gap in the current research indicates that a study to determine the effect and statistical significance of a two-row staggered fastener pattern on the ultimate anchorage capacity of MF-FRP systems could be useful in the development of the proposed retrofit system.

### ***Prestressed Fiber Reinforced Polymer***

Previous studies which examine the application of prestressed FRP sheets to strengthen reinforced concrete elements also exist. Triantafillou and Deskovic (1991) examined the short-term behavior of prestressed FRP fabric sheets adhesively bonded to reinforced concrete beams to determine the optimum combination of materials and geometry to achieve the desired performance. Diab et al. (2009) conducted experimental work to determine the long-term effectiveness of a prestressed FRP sheet anchorage system which relies on adhesive bonding only, and a hybrid system (similar to that of Ebead and Saeed, 2014) which uses both adhesive bonding and mechanical fastening to strengthen reinforced concrete beams. The level of prestressing in the Diab et al. (2009) study varied from 20% of ultimate stress ( $\sigma_u$ ) and 2.01 kips for the externally bonded system to 40% of  $\sigma_u$  and 11.6 kips for the hybrid system. The study concluded that for prestress levels less than 30%  $\sigma_u$ , debonding between the bonded FRP and concrete did not occur within 500 days, and the use of a hybrid anchor system enhanced the composite action of the FRP-concrete interface.

While prestressed MF-FRP systems are not present in the available literature, there is limited literature available describing a hybrid prestressed system which incorporates mechanical fasteners at the anchored ends and adhesive bonding along the entire length of, or along a partial length (gradient zone) of an attached unidirectional FRP laminate (Michels et al., 2014). The hybrid systems examined by Michels et al. are commercially available solutions and represent the current state of strengthening available for prestressed members using external, prestressed FRP laminates.

Studies suggest that hybrid systems provide the greatest stress transfer across the interfacial zone between FRP and concrete (Ebead and Saeed, 2014; Michels et al., 2014); however, installation time constraints, impacts on traffic, maintenance and inspection procedures, and the associated costs with each, support a proposed bridge retrofit solution which excludes any external bonding. Therefore, this research focuses on the on the development of a mechanical fastener system which can achieve the maximum capacity of the applied FRP plate, with holes, and without external bonding and the associated costs.

***MF-FRP knowledge gaps and conclusions***

1) MF-FRP systems offer a strengthening solution which can be installed rapidly, with little-to-no surface preparation requirements, and no special labor skills or tools.

2) The ultimate capacity of the FRP SAFSTRIP® material with multiple holes is not known. This open hole capacity is necessary to understand the full capability of the material with a sufficient number of fasteners to force rupture in the plate and avoid premature bearing failure. Small-scale material testing to examine the behavior of the FRP plate with and without holes is necessary to fully understand the capabilities of the plate in pure tension prior to introducing bearing as a potential failure mode.

3) Few studies examine the effects of a staggered fastener pattern on the ultimate capacity of the FRP plate; however, to truly optimize the anchor system, a staggered fastener pattern should be considered. A study during small-scale material testing to measure the effects of a staggered fastener pattern would be helpful in determining the most efficient anchorage for an MF-FRP system with end anchorages to develop a prestress force in the FRP plate.

4) The bearing behavior of the FRP plate with 0.50-in. diameter fasteners is not well documented within the literature; however, Martin and Lammana (2008) indicates that a 0.50 in. diameter fastener is likely necessary to fully develop the capacity of the FRP plate with holes prior to complete bearing failure between the fastener and FRP plate. Small-scale material testing to determine the bearing capacity of the FRP plate used in this project is necessary. Single-bolt bearing and multi-bolt bearing tests are likely needed to understanding the development of the full anchorage system capable of developing the necessary prestressing forces for the retrofit solution.

5) Concrete splitting in the strengthened member due to the concentrated force at each fastener location must be considered in determining the number and size of fasteners for the anchorage array of the proposed MF-FRP system. The use of existing models to determine the preliminary allowable force limits at each fastener with respect to concrete splitting is necessary. Full-scale testing which includes installation of the retrofit solution on a full-size C-channel beams and loading the member through failure

is necessary to confirm the validity of the system with respect concrete splitting during each phase of the test.

6) Hybrid MF-FRP and externally bonded solutions present positive strengthening results, but are outside the scope of this research due to the increased installation and curing time, and extended inspection and maintenance requirements for externally bonded systems. They are not investigated further as a feasible solution in this research.

### **In-place Concrete Strength**

The retrofit of an existing bridge superstructure with MF-FRP requires sound concrete at the location where the MF-FRP retrofit is anchored to the concrete substrate. Therefore, it is necessary to determine the equivalent in-place concrete strength of the candidate prestressed concrete C-channel using accepted evaluation methods. Further, in-place concrete strength should be considered for when conducting a structural analysis to determine the flexural capacity of the strengthened section.

ACI 214.4R10 (2010) describes two methods to calculate an equivalent in-place strength,  $f'_{c,eq}$ , based on cores taken from existing structures. Additionally, ACI 562 (2016) provides a simplification of the Alternate Method described in ACI 214.4, but is limited in scope. The ACI 214.4 Alternate Method is a statistically based estimation method and includes several experimentally determined factors. The results of the ACI 214.4 Alternate Method establish  $f'_{c,eq}$  as the lower 10<sup>th</sup> percentile (or 10% fractile) of the distribution of in-place strengths taken from cores,  $f_{ci}$ , which is consistent with the statistical relationship which defines distribution of in-place concrete strength with a given design strength,  $f'_c$ , that is mixed, placed, and cured following standard construction practices. The 10% fractile is somewhat conservative, as the actual fractiles presented by Bartlett and Macgregor (1996) are 13.5% for tall members, such as walls and columns, and as much as 23% for shallow members, such as beams and slabs. Characteristics of a normal distribution are used to determine an  $f'_{c,eq}$  below which no more than about 10% of  $f_{ci}$  would fall due to random variation alone.

According to Bartlett and MacGregor (1995), strengths from cores often overestimate the actual in-place strength variability due to core damage sustained during core drilling, variation in transportation of cores, storage, moisture conditioning, and testing. This can lead to a value of  $f'_{c,eq}$  that is unnecessarily low. Bartlett and MacGregor (1996) concludes that the variability of average in-place concrete strengths between structures (from one element to the next) controls the variability of the in-place strength. Therefore, adjustments to the core strengths based on geometry, moisture condition, and damage due to coring are necessary to convert core strengths into equivalent in-place strengths (ACI 214.4, R2016). Correction factors for the sources of the sample such as from one or multiple members, single or multiple batches of concrete, and whether from precast or cast-in-place (CIP) members are also provided. The values of  $f'_{c,eq}$  form a continuum of estimates of equivalent specified strengths, that is,  $f'_{c,eq}$  can take on any numerical value.

ACI 214.4 (2010) Alternate Method estimates  $f'_{c,eq}$  using Equations 2.1 through 2.6), by first determining a lower bound estimate of the in-place strength from core strength data (Equation 2.1), and then the 10<sup>th</sup> percentile of the in-place strength,  $f'_{c,eq}$ , is determined (Equation 2.6).

$$(\bar{f}_c)_{CL} = \bar{f}_c - \sqrt{\frac{(Ts_c)^2}{n} + (Zs_a)^2} \quad (2.1)$$

and

$$\bar{f}_c = \frac{1}{n} \sum_{i=1}^n f_c \quad (2.2)$$

and

$$f_c = F_{l/d} F_{dia} F_{mc} F_d f_{core} \quad (2.3)$$

and

$$s_c = \sqrt{\sum_{i=1}^n \frac{(f_c - \bar{f}_c)^2}{(n-1)}} \quad (2.4)$$

and

$$s_a = \bar{f}_c \sqrt{\sum CV^2} \quad (2.5)$$

and

$$f'_{c,eq} = C(\bar{f}_c)_{CL} \quad (2.6)$$

where  $f_c$  is the adjusted compressive strength of an individual core (psi),  $f_{core}$  is the compressive strength of an individual core (psi);  $F_{l/d}$ ,  $F_{dia}$ ,  $F_{mc}$ , and  $F_d$  are the adjustment factors for the length to diameter ratio ( $l/d$ ) of the core, the core diameter ( $dia$ ), the moisture content ( $mc$ ) of the core, and the damage ( $d$ ) to the core during extraction, respectively (from Table 8.1 in ACI 214.4);  $(\bar{f}_c)_{CL}$  is the lower-bound estimate of the mean in-place compressive strength (psi) at a given lower CL;  $\bar{f}_c$  is the sample mean in-place compressive strength of a set of cores (psi);  $T$  is a factor derived from the Student's  $t$ -distribution for  $n$  samples at some given CL, with  $n-1$  degrees of freedom,  $n$  is the number of cores in the sample set;  $s_c$  is the sample standard deviation of the in-place strengths;  $Z$  is the critical value from a standard normal distribution for a given CL (from Table 8.3 in ACI 214.4);  $s_a$  is the standard deviation of the strength correction factors;  $CV$  are the coefficients of variation for the applicable  $F$  adjustment factors  $l/d$ ,  $dia$ ,  $mc$ , and  $d$ ; and  $C$  is the factor accounting for distributions affected by number and type of members (from Table 8.5 in ACI 214.4), adjusted for a given CL. ACI 214.4 (2010) prescribes a  $C$  value of 0.88 for precast concrete elements, such as the prestressed concrete C-channels examined in this research, if the 10<sup>th</sup> percentile is the desired lower bound.

In summary, the ACI 214.4 Alternate Method provides a statistically appropriate method to convert individual core strengths,  $f_{core}$ , taken from existing structures to equivalent in-place strengths at a specific location,  $f_c$ , and the mean,  $\bar{f}_c$ , is estimated. The lower confidence limit of that estimate is determined, including the effects of both the standard deviation of the sample set and the variability of the strength adjustments. The lower-bound estimate of the mean is then determined for the desired fractile, typically the 10% fractile, to account for the sampling variability at a given CL (a 90% CL in the case of a 10% lower-bound fractile). The CL are important factors in arriving at a point estimate of the specified strength.

The confidence limits referenced in ACI 214.4 for the Tolerance Factor Method are 75% for “ordinary structures,” 90% for “important buildings,” and 95% for “critical components in nuclear power

plants” (Hindo and Bergstrom, 1985) and the CL alternates provided in Tables 8.3 and 8.4 (ACI 214.4, 2010), the  $Z$ - and  $T$ -factors, are 75%, 90%, and 95%. ACI 214.4 references the Bartlett and MacGregor (1995) suggestion that a 90% CL is “probably conservative” for general use with the Alternate Method because it is accepted that, in practice, the actual variability for tall and shallow elements is 13.5% and up to 23%, respectively. However, a 90% CL is used to construct Table 8.5 for the  $C$ -factor. Regardless of desired lower-bound percentiles, 10%, 13% or 23 %, consistent CL should be used to determine appropriate  $Z$ -,  $T$ -, and  $C$ -factors using the Alternate Method.

### ***In-place Concrete Strength Conclusions***

- 1) The ACI 214.4 Alternate Method is an accepted method for determining the equivalent in-place concrete strength for existing structures.
- 2) Equivalent in-place concrete strength is an appropriate value for use in calculations to determine available strength of concrete in a given structure, while providing for an appropriate level of strength variability throughout the structural element.
- 3) For C-channel beams, the MF-FRP retrofit is attached the stems of the C-channel. Drilling cores from C-channel stems is not feasible, and therefore, a method to calibrate  $f'_{c,eq}$  drilled from the C-channel flange with the concrete in the C-channel stem is necessary.

### **Concrete Splitting Behavior**

While much of the MF-FRP literature is focused on the type, size, spacing, and pattern of the fastener used in the system, it is also necessary to understand the effects on localized concrete splitting due to concentrated forces at each fastener and consider this behavior in the development of a prestressed MF-FRP system. The interaction between the MF-FRP fasteners and the strengthened concrete member is similar to that of composite steel and concrete beams where shear studs are used to transfer stress between the two elements of the composite member. Oehlers and Bradford (1995) provides a relationship for concrete splitting in composite beams, which can be applied to MF-FRP systems with a single line of fasteners:

$$P_{min,one} = 12.7b_a h_a f_{cb} \quad (2.7)$$

where  $P_{min,one}$  is the minimum splitting force,  $b_a$  is the effective width of the concrete prism on which the fasteners act – taken as the diameter of the fastener,  $h_a$  is the effective height on the concrete prism on which the fasteners act – taken as the lesser of the length of the fastener or 1.8 times the diameter of the fastener,  $d_{bolt}$ , and  $f_{cb}$  is the resistance of concrete to splitting stresses, typically taken as  $0.5\sqrt{f_c}$  (MPa) or  $6\sqrt{f_c}$  (psi).

For connections in which two lines of fasteners are used, the minimum splitting force becomes:

$$P_{min,two} = 7.5b_a h_a f_{cb} \quad (2.8)$$

where  $b_a$ ,  $h_a$ , and  $f_{cb}$  are the same as in Equation 2.7, except that  $b_a$  is taken as the transverse spacing between the inside edges of the fasteners when transverse spacing is no greater than  $3b_a$ . Oehlers and Bradford (1995) conclude that all connections with fasteners longer than  $1.8d_{bolt}$  are flexible connections, and, therefore, the  $h_{a,effective}$  should be limited to  $1.8d_{bolt}$ .

Oehlers (2001) presents a specific form of Equation 2.7, which assumes  $h_{a,effective}$  is equal to  $1.8d_{bolt}$ :

$$P_{split} \approx 7\pi c d_{bolt} f_t \left(1 - \frac{d_{bolt}}{2c}\right)^{-2} \quad (2.9)$$

where  $c$  is the concrete cover to the side of the bolt (edge cover),  $d_{bolt}$  is the diameter of the fastener, and  $f_t$  is the splitting tensile strength of the concrete in the strengthened member. The relationship in Equation 2.9 is specific to MF-FRP studies conducted by Oehlers (2001), and, therefore, will be the fundamental relationship in this research for determining the maximum force ( $P$ ) that can be transferred to the concrete member at each fastener location.

### ***Concrete splitting behavior conclusions***

1) The design guide presented by Oehlers (2001) (Equation 2.9) is sufficient for predicting the concrete splitting force at the bolt-concrete interface in MF-FRP systems.

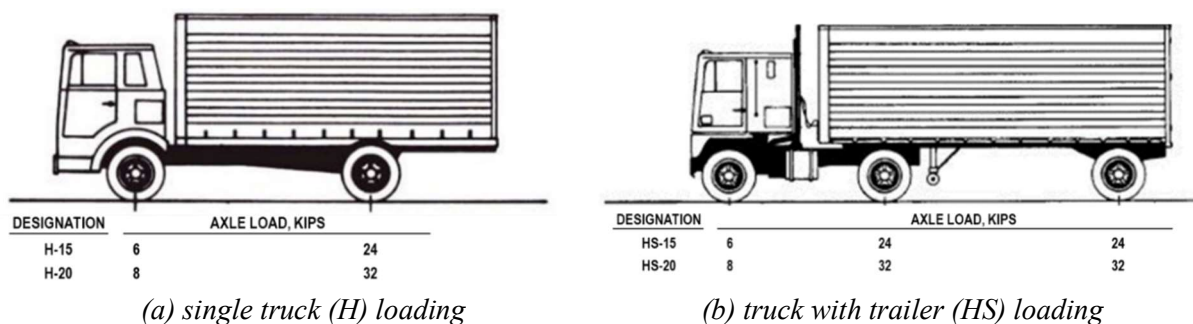
2) The maximum effective length of the bolt-concrete interface is  $1.8d_{bolt}$ .

## Bridge Load Rating Considerations

### *C-channel beam history and load rating*

North Carolina bridges with prestressed concrete C-channel beam superstructures are the primary candidates for the MF-FRP retrofit solution developed in this research. C-channel beams are currently the oldest prestressed concrete superstructures in the North Carolina state bridge inventory with the oldest bridges dating back to 1956 (NCDOT, 2018b). Channel beam superstructures, however, are not unique to North Carolina, and became widely used during World War II as a bridge superstructure that was economical and could be erected relatively quickly. In the mid-1960s, North Carolina adopted a standardized suite of channel beam designs which could accommodate span-lengths of 20-, 25-, and 30-ft. at operating loads up to 15 tons (NCDOT, 1966) – the AASHTO H-15 (Figure 2.3a) and HS-15 (Figure 2.3b) load rating (AASHTO, 2016)

The NCDOT standardized channel beam designs consisted of internal and exterior girder cross-sections, with 2 prestressing strand patterns (Pattern A and Pattern B). Pattern A is an 8-strand (4 per stem) pattern which uses grade 270 ksi 7-wire stress relieved prestressing strands, and Pattern B is a 10-strand (5 per stem) pattern which uses grade 250 ksi 7-wire stress relieved prestressing strands. The two patterns have similar capacity and behavior under loads, but are not permitted to be mixed within a single bridge (NCDOT, 1966). The 30-ft. channel beams examined in this research are Pattern A beams (discussed in detail in Chapter 3) and had an original operating rating of H-15 (NCDOT, 1966). The live load moment for a 30-ft. span with an H-15 or HS-15 load configuration (shown in Figure 2.3a) is 102.2 kip-ft (including impact factor) along a single vehicle wheel line (AASHTO, 2016).



(a) single truck (H) loading

(b) truck with trailer (HS) loading

**Figure 2.3:** AASHTO HS-15 and HS-20 loading (AASHTO, 2016).

### ***AASHTO Load Rating Criteria***

The American Association of State Highway and Transportation Officials (AASHTO) load rating criteria for bridges are separated into two categories, inventory and operating rating (AASHTO, 2016). Load ratings based on inventory rating criteria address routine traffic, and specifically apply stress limits such that the bridge may be safely used at the inventory limit, across multiple lanes, for an indefinite period of time without the risk of incremental damage due to traffic load effects. The inventory rating loads typically correspond to serviceability stress limits, but reflect the existing bridge condition as determined through routine bridge inspection processes. Load limits imposed by operating rating criteria specifically address non-routine traffic using strength limit states to establish the maximum live load permissible. The operating load limit typically allows a maximum live load which exceeds inventory rating stress limits, and thus incremental damage may occur at this load limit. This is acceptable as the operating rating limit is for non-routine, infrequent traffic loading. Typically, operating rating governs the maximum permissible live load for a bridge; however, increasing strength without reducing concrete tensile stress creates a situation in which the inventory rating controls posted load limits. The opposite could be true for a retrofit solution which only addresses inventory rating criteria. Therefore, a complete retrofit solution must address both the operating rating and inventory rating criteria to remove posted load limits and allow the bridge to remain open without restrictions.

Inventory and operating rating load limits for all bridges are calculated using the following general form of the AASHTO (2016) rating equation:

$$RF = \frac{C - A_1 D}{A_2 L(1 + I)} \quad (2.10)$$

and

$$RT = (RF)W \quad (2.11)$$

where  $RF$  is the rating factor for the live load capacity of the bridge,  $C$  is the capacity of the member,  $D$  is the dead load effect,  $L$  is the live load effect,  $I$  is the impact factor,  $A_1$  is the dead load factor (taken as 1.0 for allowable stress method analysis),  $A_2$  is the live load factor (taken as 1.0 for allowable stress method

analysis),  $RT$  is the bridge member rating tonnage, and  $W$  is the weight of the nominal vehicle used to determine  $L$ . AASHTO (2016) provides provisions for Allowable Stress Rating (ASR) or Load Resistance Factor Rating (LRFR), and Load Factor Rating (LFR) methods to be used for bridge rating analysis. These methods correspond with Allowable Stress Design, Load Resistance Factor Design, and Load Factor Design methods respectively. The bridge owner has discretion as to which method is used.

Using the LRFR method, specific forms of Equation 2.10 determine the inventory rating factor for five limiting conditions. Equations 2.12 through 2.16 show the specific forms for concrete tension, concrete compression, prestressing steel tension, and flexural and shear strength, respectively (AASHTO, 2016).

$$RF = \frac{6\sqrt{f'_c} - (F_d + F_p + F_s)}{F_l} \quad (2.12)$$

and

$$RF = \frac{0.6f'_c - (F_d + F_p + F_s)}{F_l} \quad (2.13)$$

and

$$RF = \frac{0.6f'_c - 0.5(F_d + F_p + F_s)}{F_l} \quad (2.14)$$

and

$$RF = \frac{0.8f_y^* - (F_d + F_p + F_s)}{F_l} \quad (2.15)$$

and

$$RF = \frac{\phi R_n - (1.3D + S)}{2.17L(1 + I)} \quad (2.16)$$

where  $f'_c$  is the concrete compressive strength (psi),  $6\sqrt{f'_c}$  is the allowable concrete tensile strength (psi) – can be reduced to  $3\sqrt{f'_c}$  or 0 in accordance with AASHTO (2016) specifications,  $F_d$  is the unfactored dead load stress (psi),  $F_p$  is the unfactored prestress force after all losses (psi),  $F_s$  is the unfactored stress due to secondary prestress forces (psi),  $F_l$  is the unfactored live load stress including impact (psi),  $f_y^*$  is the prestressing steel yield stress (psi),  $\phi R_n$  is the nominal strength of the section ( $\phi M_n$  or  $\phi V_n$ ) (in-lb. or

lb.),  $D$  is the unfactored dead load moment or shear (in-lb. or lb.),  $S$  is the unfactored prestress secondary moment or shear (in-lb. or lb.),  $L$  is the unfactored live load moment or shear (in-lb. or lb.), and  $I$  is the impact factor.

Operating rating criteria use specific forms of Equation 2.4 to evaluate the rating factor for flexural and shear strength, and prestressing steel tension (AASHTO, 2016). Equations 2.17 and 2.18 show the specific forms for flexural and shear strength, and prestressing steel tension, respectively.

$$RF = \phi R_n - \frac{(1.3D+S)}{1.3L(1+I)} \quad (2.17)$$

and

$$RF = \frac{0.9f_y^* - (F_d + F_p + F_s)}{F_t} \quad (2.18)$$

Equation 2.10 provides an evaluation of residual capacity of bridge elements after dead loads are applied for each of the evaluated limits. A rating factor of 1.0 or greater is necessary to avoid reduced load capacity for a given bridge member, and the overall load rating of the bridge is controlled by the member with the lowest rating.

The allowable stress capacity,  $C$ , must remain constant regardless of current bridge condition, while the dead load effects,  $D$ , of the element increase with prestress losses. Thus, the rating factor for the bridge element is reduced, and the bridge load rating,  $RT$ , is reduced. Therefore, for the rating factor of a deteriorated bridge element to be equal to the original rating factor, either the dead load effect for the evaluated condition must be reduced, or the live load effect must be reduced. While, the live load effect for deteriorated bridge elements with reduced capacity may be reduced to keep  $RF$  unchanged, a reduced live load effect also requires the nominal vehicle weight,  $W$ , to be reduced, and the overall member rating,  $RT$ , is reduced. Reducing live load effects, and thus imposing load limits which correspond to the appropriate nominal vehicle weight, is a common practice for DOTs to leave deteriorated bridges in service with restrictions.

State DOTs also have the option to repair deteriorated bridge elements to reduce dead load effects and restore the  $RF$  to the pre-deteriorated value, keeping the bridge open without restrictions. In prestressed

concrete bridge elements, the specific form of Equation 2.10 for the inventory rating criterion which places stress limits on concrete tension is of particular interest when considering candidate bridges that are deteriorated and experiencing loss of prestress effects due to corrosion.

NCDOT (2018), in accordance with AASHTO (2016), prescribes  $f_{t,allow}$  as 0 psi for prestressed concrete elements in areas which exhibit increased corrosion such as coastal regions; the regions in which a number of deteriorated candidate bridges are located. Therefore, a retrofit solution which restores the prestress losses such that the concrete tensile stress is less than or equal to 0 at service load levels considered in the inventory load rating is necessary for a deteriorated prestressed concrete bridge to remain in service without restrictions.

#### ***AASHTO load rating criteria conclusions***

1) The C-channel cross sections examined in this research have an undamaged load rating of H-15; therefore, the retrofitted beam must maintain an operating load rating of H-15 or greater.

2) Retrofit solutions and repair techniques must address both inventory and operating rating criteria to allow the bridge to remain open without posted restrictions or closures.

3) Retrofit systems which only provide increased strength are not sufficient to increase the inventory rating in deteriorated prestressed concrete bridge superstructures with significant prestress losses due to stress limits at the tension face of the cross-section.

#### **Vehicle Operating Costs**

The NCDOT conducted a study in 2014 (Cavalline et al., 2015) to validate the current Bridge Management System () model for determining vehicle operating costs (VOC). Data was collected from four different roadway types (interstate, federal highway, state highway, and state route) using eight Weigh-in-Motion (WIM) stations (2 per roadway type) from across the state. The WIM data provided number of vehicles and vehicle type for each station location. This data, coupled with user cost information was used to determine average VOC information. Cavelline et al. (2015) presents VOC for two categories, vehicles weighing between 3 and 26 tons, and vehicles weighing more than 26 tons. For

vehicles weighing between 3 and 26 tons, the average VOC is \$1.86 per mile, and for vehicles weighing more than 26 tons, the average VOC is \$2.59 per mile.

### ***VOC Conclusions***

The VOC information presented by Cavelline et al. (2015), when paired with NCDOT BMS detour information for each bridge, can be used to determine the cost-benefit of individual bridges with posted load restrictions or closures.

### **Digital Image Correlation**

#### ***Brief history and applications in civil engineering***

Digital Image Correlation is a strain measurement technique that is common within the structural engineering and material science communities. Peters and Ranson (1982) and Sutton et al. (1983) first introduce the methodology of comparing images to measure the strain or deformations which occur during testing. DIC techniques are used throughout this project to develop a continuous strain map over the entire specimen during testing. A detailed, technical description and discussion of DIC is provided by Xie and Kang (2015) and Hoult et al. (2013), but excluded here as it is not the subject of the research, but rather a tool used to enhance the results of the research.

DIC uses a series of photos taken of the material surface before (reference image) and during testing to measure the relative distance between speckles which are applied to the material surface before testing. A random speckle pattern is applied to the surface of the test specimen and calibrated to the camera resolution and field of view used during the test. This calibration ensures the accuracy of the DIC system, and is consistent with the calibration requirements discussed by Hoult et al. (2013) and Bomarito et al. (2017). An example DIC speckle pattern and strain map result is shown in Figure 4.4a in Chapter 4 of this thesis.

As computing power and speed increased in the early 2000s, DIC became an attractive and efficient measurement technique for the structural engineering and material science research industry. Borowicz and Bank (2013) used DIC to measure out-of-plane strain and displacement of FRP beams. Ramos et al.

(2015) proposes the use of DIC as a practical and reliable method for structural health monitoring over extended periods of time.

Huang et al. (2009) described the use of a DIC technique to determine the elastic modulus (Young's Modulus) of concrete cylinders and compared the DIC results to traditional methods using a foil strain gauge, a compressometer, and a mechanical strain gauge. In all cases, Huang et al. (2009) found that DIC results in a smaller standard deviation (less variability) and increased accuracy compared to the other methods in the study.

DIC is also useful to practicing engineers in the field to identify cracks in structural elements that are not visible to the naked eye (Yang et al., 2015). In a lab application, this same result can assist research engineers in mapping crack propagation in concrete to create a digitized "pen-stroke" map on a tested structural element. Hamrat et al. (2016) suggest that when DIC is used in this application it detects the initial formation of cracks in flexural elements with increased precision and can be used to measure the crack width at any point during crack formation.

The accuracy of DIC compared to conventional strain gauge measurements is a recurring topic throughout the literature with the common understanding that when the system is properly calibrated, the accuracy of strain measurements using DIC is equal to or greater than properly calibrated foil strain gauge measurements (Hoult et al., 2013; Ramos et al., 2015; and Bomarito et al., 2017). The benefits of DIC include the ability to visualize a continuous strain (longitudinal, transverse, and shear) field over the entire surface of a specimen rather than at discrete points where individual strain gauges are, and the ability to measure strain well beyond the point after typical strain gauges debond from the material surface. Further, the application of the speckle pattern required for DIC measurement is sufficiently quicker and less susceptible to introducing erroneous measurements than traditional strain gauge application.

The most common source of error in DIC measurement is the out-of-plane movement of the speckled surface due to specimen misalignment or change in specimen thickness during the test due to conservation of mass principles. This out-of-plane movement is not accounted for in a 2-Dimensional

DIC (2D DIC) system which uses just one camera to collect images during testing. Hoult et al. (2013) describes this error as:

$$\varepsilon_{error} = \frac{dy}{y} \quad (2.19)$$

where  $dy$  is the magnitude of the out-of-plane movement and  $y$  is the distance between the camera focal point and test specimen. This error can be minimized by increasing  $y$  sufficiently such that  $\varepsilon_{error}$  is within the accuracy of the DIC system used. For example, in the tension tests conducted during the small-scale testing phase of this project (discussed later in the report) very small out-of-plane movement is possible as the specimen becomes thinner during testing. The relationship between longitudinal strain ( $\varepsilon_{yy}$ ) and transverse strain ( $\varepsilon_{xx}$ ) is quantified using Poisson's ratio:

$$\nu = \frac{-\varepsilon_{xx}}{\varepsilon_{yy}} \quad (2.20)$$

where  $\nu$  is Poisson's ratio. At failure,  $\varepsilon_{yy}$  for the FRP plate used in this research is typically 0.015 in./in., and a typical value for  $\nu$  is 0.25; therefore,  $\varepsilon_{xx}$  is approximately 0.00375 in./in. The initial thickness of the specimen is 0.125 in., which presents a total thickness change of 0.0005 in. at failure. Using 0.0005 in. for  $dy$  and 160 in. for  $y$  (typical distance for the small-scale test set-up discussed later in this thesis) in Equation 2.29 gives an  $\varepsilon_{error}$  of  $3\mu\varepsilon$  due to out-of-plane movement, which for the purposes of this research is considered negligible. Adjusting the DIC measurements to account for this error is possible if the out-of-plane movement can be measured (as is the case with some 2D DIC systems which use laser measurement to record the distance between camera and material surface for each image). Three-Dimensional DIC (3D DIC) systems (two or more cameras to collect images from one test specimen) account for all specimen movement, regardless of movement plane, throughout the test, and therefore this source of error is not a factor when using 3D DIC.

***DIC conclusions:***

1) With proper application techniques and calibration, DIC is a reliable, accurate, and easily repeatable measurement technique for the purposes of this project which requires multiple specimens for each test to obtain statistically significant results. Material surfaces should be painted with a sufficiently

thin paint (almost a whitewash) to not create a strain difference between the tested material surface and the paint surface. Further, a speckle pattern suitable for the camera resolution and field of view should be selected to generate the continuous strain map during testing.

2) 2D DIC has a potential for error due to out-of-plane surface movement as the specimen thickness lessens during tensile elongation. Sufficient distance between the camera focal point and the test specimen surface should be used to minimize the effects of this error such that the error is less than that of system variability.

3) DIC provides increased precision over pen-stroke techniques for mapping crack propagation in various materials and in measuring crack widths during testing. Therefore, with an appropriate camera array, DIC could be used during full-scale testing to provide a digital version of the concrete crack propagation map at critical regions of the tested structural element.

**CHAPTER 3:  
ADDRESSING SUPERSTRUCTURE LOAD RATING CRITERIA FOR DETERIORATED  
PRESTRESSED CONCRETE MEMBERS USING A PROPOSED MF-FRP RETROFIT**

*(ASCE Journal of Performance of Constructed Facilities, under review)*

Brad C. McCoy, P.E., ENV SP: Ph.D. Candidate, North Carolina State University, Department of Civil, Construction, and Environmental Engineering, Corresponding Author: [bcmccoy@usma.edu](mailto:bcmccoy@usma.edu)

Hatem M. Seliem, Ph.D., P.E., PMP: Associate Professor, Faculty of Engineering,  
Helwan University, Egypt

Rudolf Seracino, Ph.D.: Professor, North Carolina State University, Department of Civil, Construction,  
and Environmental Engineering

Gregory W. Lucier, Ph.D.: Assistant Research Professor, North Carolina State University, Department of  
Civil, Construction, and Environmental Engineering

**Abstract**

This chapter presents a case study analysis of a deteriorated prestressed concrete C-channel beam which experienced corrosion due to fertilizer runoff in an agricultural region of North Carolina. The analysis is conducted using the American Association of State Highway and Transportation Officials (AASHTO) bridge load rating criteria for prestressed concrete bridges and concludes that repair techniques which strengthen deteriorated bridge elements without also restoring prestress losses due to deterioration are not sufficient to allow the bridge to remain open without posted limits or closures. Based on the evaluated load rating criteria for the case study bridge, a prestressed mechanically-fastened fiber-reinforced polymer (MF-FRP) retrofit solution is presented. The analysis shows that the proposed MF-FRP retrofit solution is capable of restoring prestress losses due to deterioration, and restoring the original inventory and operating ratings to allow the retrofitted bridge to remain open, without posted load limits or closures, until permanent superstructure replacement can be budgeted and scheduled. The study also concludes that the proposed MF-FRP retrofit can be applied to hollow core slab cross-sections which experience similar deterioration and prestress loss.

*Keywords: Inventory Load Rating, Operating Load Rating; Prestressed Concrete; Strengthening and repair; Fiber Reinforced Polymer; Prestressed Mechanically Fastened-FRP*

## Introduction

Prestressed concrete elements of various shapes and forms are among the common bridge superstructure systems currently in service in North Carolina and across the United States. Many such bridges are in varying states of distress and require retrofit to extend their useful service life prior to complete superstructure replacement. Examples of deteriorated prestressed concrete beams include, but are not limited to: 1) C-channel girders such as that of Bridge No. 380093 (Figure 3.1a), located on Service Route No. 1156 across Owen Creek in Granville County, North Carolina, which was the subject of a 2014 study by the North Carolina Department of Transportation (NCDOT); and 2) cored slabs such as that of Bridge No. 150035 (Figure 3.1b), located on US Highway 70 across Ward Creek in Carteret County, North Carolina and the subject of a 2016 NCDOT study (Van Brunt et al., 2016).

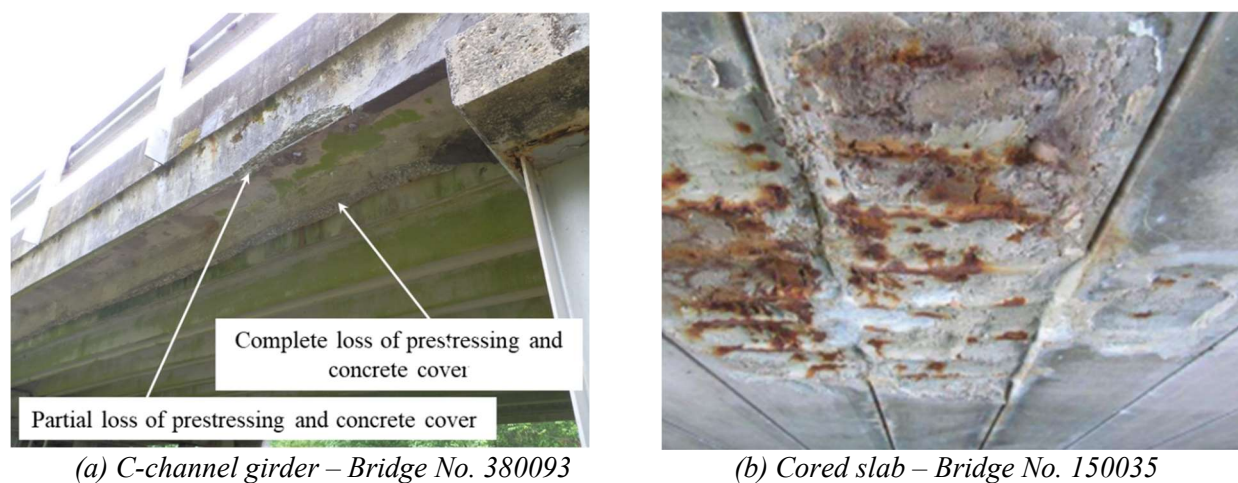


**Figure 3.1:** Examples of repairable deterioration of prestressed concrete bridge beams.

The NCDOT maintains hundreds of bridges in inventory having precast prestressed concrete C-channel girders tied together with grouted shear keys and transverse post-tensioning. In several cases, girders on these bridges showing signs of deterioration. Bridge No. 380093 in Figure 3.1a is an example of a bridge superstructure which exhibited significant signs of distress on some exterior girders, in the form of significant spalling of the concrete cover at several discrete locations. The interior girders appeared to be in reasonably sound condition. In extreme cases, exterior girders had areas where the concrete at the bottom of the stems was missing along significant portions of the span (Figure 3.2). The

lowermost prestressing strand in these areas was severely corroded, and in one case missing, resulting in a significant loss of prestressing along the length of the girder.



**Figure 3.2:** Exterior girder deterioration.

State Departments of Transportation (DOTs) face significant challenges in scheduling and budgeting bridge replacements or major repairs. Once a bridge is identified as deficient through routine inspection processes (AASHTO, 2013), a significant repair or replacement, which is not deemed an emergency, is most commonly procured through design-bid-build (DBB) project delivery due to state and federal legislative contracting requirements. For the purposes of this discussion, a significant repair is defined as a repair which cannot be performed by DOT maintenance crews, and therefore must be performed through contracted resources. Contracted resources are procured through DBB project delivery, which typically awards the project to the lowest qualified bid, and therefore, offers the lowest cost solution for the project. DBB is the most common project delivery method for government agencies due to the low cost compared to other project delivery methods which may have higher costs (Knutson et al. 2009). While DBB project delivery provides a low-cost option, DBB is often a time-intensive project delivery method, and it is not uncommon for DBB to last several years from identification of the project need

through project completion (Knutson et al. 2009). In addition to the DBB procurement time, capital improvement projects with budgetary requirements outside the annual maintenance budget often require several years for government appropriation of funds (Roper and Payant, 2014). Therefore, budgeting and project delivery requirements force state DOTs to impose posted load limits, detours, or closures on deteriorated bridges which are awaiting major repairs or replacement.

As with many of the deteriorating C-channel bridges in North Carolina, Bridge 380093 was scheduled for replacement within a few years of the 2014 study, but interim repairs were required to maintain a sufficiently high operating rating to prevent reducing the posted load limits or bridge closure. While the traffic count on this bridge was relatively low, closure of the bridge would have a significant impact on local traffic as the detour is over seven miles long. A rapid, efficient, and easy-to-install temporary repair method, which can be budgeted within annual maintenance budget requirements, was needed to keep Bridge 380093 and similar bridges across the state operational, without lowering posted load limits or closures, until replacements can be budgeted and scheduled.

Current repair techniques using fiber reinforced polymer (FRP) materials include externally bonded, mechanically fastened, and hybrid FRP systems, which are discussed more later in the chapter. These available FRP systems increase the flexural capacity of deteriorated elements, but generally do not address prestress losses in deteriorated prestressed concrete members. Increased flexural capacity of deteriorated elements is often necessary to maintain the bridge operating rating (AASHTO, 2016); however, inventory rating (AASHTO, 2016) requirements impose concrete stress limits which must be achieved through restoration of prestress effects. Therefore, repairs to deteriorated prestressed concrete elements must restore flexural strength and prestress losses due to deterioration to maintain both operating and inventory rating levels.

Other techniques to repair deteriorated cross-sections or increase capacity for members with new load demands exist. Systems that are attached or bonded to existing structural members include bonded concrete and reinforcement systems, bonded or mechanically fastened steel plates, and unbonded external-post-tensioned steel or carbon fiber prestressing strand systems. These systems are part of the

current state of practice. The performance of these systems, and the aforementioned FRP systems, is dependent upon the force transfer between the concrete substrate and strengthening system through adhesive bonding or mechanically fastened mechanisms (ACI 562, 2016). Therefore, retrofit systems which restore losses due to deterioration must be designed to properly transfer forces across the interface between the repair material and concrete substrate to ensure efficient use of the retrofit material and successful restoration of deteriorated capacity.

### **Research Significance**

This chapter presents a structural assessment of the deteriorated superstructure elements of NCDOT Bridge 380093 against which a retrofit concept is proposed for rapid repair of deteriorated prestressed C-channel superstructures. The concept presented uses mechanically fastened-fiber reinforced polymer (MF-FRP) plates applied to the deteriorated superstructure elements using a post-tensioned prestressing method to restore prestress losses and reduce concrete tension stress to within limits prescribed by AASHTO (2016) load rating requirements such that posted load limits may be removed. The proposed retrofit may be applied to deteriorated hollow core elements and other cross-sections as necessary. The following constraints are considered in the retrofit development:

- 1) bridge superstructure replacement through the DBB project delivery and capital budgeting cycles is scheduled within three to five years, so the proposed method can be considered a temporary repair and long-term environmental durability is likely not a controlling consideration,
- 2) bridges shall be repaired with minimal disruption to traffic and down-time; therefore, solutions involving removal and replacement of deteriorated girders are not considered, and
- 3) due to limited access constraints a simple repair method not requiring heavy or special equipment is desired.

### **AASHTO Rating Criteria**

A retrofit solution which enables candidate bridges to remain in service without posted load limits or closures must address AASHTO (2016) load rating requirements. Load rating criteria are separated into two categories, inventory rating and operating rating (AASHTO, 2016). Load ratings based on inventory

rating criteria address routine traffic, and specifically apply stress limits such that the bridge may be safely used at the inventory limit, across multiple lanes, for an indefinite period of time without the risk of incremental damage due to traffic load effects. The inventory rating loads typically correspond to serviceability stress limits, but reflect the existing bridge condition as determined through routine bridge inspection processes. Load limits imposed by operating rating criteria specifically address non-routine traffic using strength limit states to establish the maximum live load permissible. The operating load limit typically allows a maximum live load which exceeds inventory rating stress limits, and thus incremental damage may occur at this load limit. This is acceptable as the operating rating limit is for non-routine, infrequent traffic loading. Although it is commonly the operating rating criteria which is used to post load limits on bridges, a retrofit solution which only increases the operating rating can create a situation in which the inventory load rating controls posted load limits, and therefore restrictions would remain in place. The opposite could be true for a retrofit solution which only addresses inventory rating criteria. Therefore, a complete retrofit solution must address both the operating rating and inventory rating criteria to remove posted load limits and allow the bridge to remain open without restrictions.

Inventory and operating rating load limits for all bridges are calculated using the following general form of the AASHTO (2016) rating equation:

$$RF = \frac{C - A_1 D}{A_2 L (1 + I)} \quad (3.1)$$

and

$$RT = (RF)W \quad (3.2)$$

where  $RF$  is the rating factor for the live load capacity of the bridge,  $C$  is the capacity of the member,  $D$  the dead load effect,  $L$  is the live load effect,  $I$  is the impact factor,  $A_1$  is the dead load factor (taken as 1.0 for allowable stress method analysis),  $A_2$  is the live load factor (taken as 1.0 for allowable stress method analysis),  $RT$  is the bridge member rating tonnage, and  $W$  is the weight of the nominal vehicle used to determine  $L$ . AASHTO (2016) provides provisions for Allowable Stress Rating (ASR) or Load Resistance Factor Rating (LRFR), and Load Factor Rating (LFR) methods to be used for bridge rating

analysis. These methods correspond with Allowable Stress Design (ASD), Load Resistance Factor Design (LRFD), and Load Factor Design (LFD) methods respectively. The bridge owner has discretion as to which method is used. For the purposes of this study, and the development of a retrofit solution which addresses both inventory and rating criteria, LRFR will be used; however, the use of ASD or LFR would result in the same conclusions for the retrofit concept and impacts on inventory and operating rating analysis.

All three methods define  $C$  for the analyzed member as the allowable stress capacity as prescribed by AASHTO (2016) for the rating level desired. Inventory rating criteria determine  $C$  based on concrete or prestressing steel serviceability stress limits, or reduced strength for flexural and shear capacities; whereas, operating rating criteria allow for higher capacities of nominal strength and prestressing steel stress limits. Specific forms of Equation 3.1 are used to determine the inventory rating factor for five limiting conditions: concrete tension, concrete compression, prestressing steel tension, and flexural and shear strength (AASHTO, 2016). Operating rating criteria use specific forms of Equation 3.1 to evaluate the rating factor for flexural and shear strength, and prestressing steel tension (AASHTO, 2016). Equation 3.1 provides an evaluation of residual capacity of bridge elements after dead loads are applied for each of the evaluated limits. A rating factor of 1.0 or greater is necessary to avoid reduced load capacity for a given bridge member, and the overall load rating of the bridge is controlled by the member with the lowest rating.

The allowable stress capacity,  $C$ , must remain constant regardless of current bridge condition, while the dead load effects,  $D$ , of the element increase with prestress losses. Thus, the rating factor for the bridge element is reduced, and the bridge load rating,  $RT$ , is reduced. Therefore, for the rating factor of a deteriorated bridge element to be equal to the original rating factor, either the dead load effect for the evaluated condition must be reduced, or the live load effect must be reduced. While, the live load effect for deteriorated bridge elements with reduced capacity may be reduced to keep  $RF$  unchanged, a reduced live load effect also requires the nominal vehicle weight,  $W$ , to be reduced, and the overall member rating,  $RT$ , is reduced. Reducing live load effects, and thus imposing load limits which correspond to the

appropriate nominal vehicle weight, is a common practice for DOTs to leave deteriorated bridges in service with restrictions.

State DOTs also have the option to repair deteriorated bridge elements to reduce dead load effects and restore the  $RF$  to the pre-deteriorated value, keeping the bridge open without restrictions. In prestressed concrete bridge elements, the specific form of Equation 3.1 for the inventory rating criterion which places stress limits on concrete tension is of particular interest when considering candidate bridges that are deteriorated and experiencing loss of prestress effects due to corrosion. Under normal conditions, AASHTO (2016) specifies the allowable concrete tensile capacity as:

$$f_{t,allow} = 0.5\sqrt{f'_c} \quad (3.3)$$

where  $f'_c$  is the concrete design compressive strength (MPa). However, AASHTO (2016) provides a clause which allows for bridge owners to limit  $f_{t,allow}$  to  $0.25\sqrt{f'_c}$  (MPa) or  $0\sqrt{f'_c}$  depending upon varying conditions. NCDOT (2018), in accordance with AASHTO (2016), prescribes  $f_{t,allow}$  as 0 MPa for prestressed concrete elements in areas which exhibit increased corrosion such as coastal regions; the regions in which a large majority of deteriorated candidate bridges are located. Therefore, a retrofit solution which restores the prestress losses such that  $f_t$  is 0 MPa at service load levels considered in the inventory load rating is necessary for a deteriorated prestressed concrete bridge to remain in service without restrictions.

### **NC Bridge 380093 Case Study**

A case study of a deteriorated prestressed concrete bridge in rural North Carolina serves as the basis for development of a retrofit concept which is capable of restoring prestress loss and restoring flexural capacity such that the bridge may remain in service, without restrictions, until a permanent replacement can be budgeted, contracted, and construction completed within the time limits previously discussed.

#### ***Bridge Description***

NCDOT Bridge 380093 carries State Route 1156 (SR1156) across Owen Creek in Granville County, North Carolina. The total length of the bridge is 27.4 m and the width of the bridge deck is 7.8 m with a

clear roadway width of 7.3 m. The bridge deck is constructed of precast prestressed C-Channel girders supported on a prestressed bent cap. Three simply-supported 9.1 m spans form the 27.4 m long bridge. Three types of C-channel members were used for the interior and exterior girders. Exterior girders are denoted as SLAB S1 and interior girders are denoted as SLAB S2 or SLAB S3. The cross-section of the S2 and S3 interior girders are nearly identical, with only a difference in the shear key on one edge. However, the cross-section of the S1 exterior girders have a monolithic curb along the exterior.

Two prestressing patterns were permitted for use with 9.1 m girders. Pattern A (Figure 3.3) was used in the S1 girders, and is, therefore, the only pattern considered in this study. All engineering design information related to the bridge, including structural detailing and material properties (Table 3.1) were extracted from structural drawings provided by the NCDOT.

**Table 3.1:** Structural Material Properties and Strand Details (adapted from NCDOT, 1966).

Concrete	
Design Compressive Strength, $f'_c$ (MPa)	35.5
Compressive Strength at Transfer of Prestress Force, $f_{ci}$ (MPa)	27.6
High Strength (HS) Prestressing Strand	
Ultimate Strength, $f_{pu}$ (MPa)	1860
Diameter (mm)	11.1
Area (mm <sup>2</sup> )	75.3
Ultimate Prestressing Force, $P_u$ (kN)	138
Prestressing Pattern A (Figure 3.3) Details	
Number of Strands	8
Type of Strand	HS
Applied Prestressing Force, $P_i$ (kN)	96.5

### ***Bridge Condition***

Site visits of Bridge 380093 were conducted on May 3<sup>rd</sup>, 2013 and October 9<sup>th</sup>, 2013. An overview of the bridge is shown in Figure 3.4. At the time of the first visit, the bridge was closed to traffic; however, during the second visit, the bridge was re-opened with closures on the two shoulders, preventing wheel loads from bearing directly on the deteriorated exterior girders.

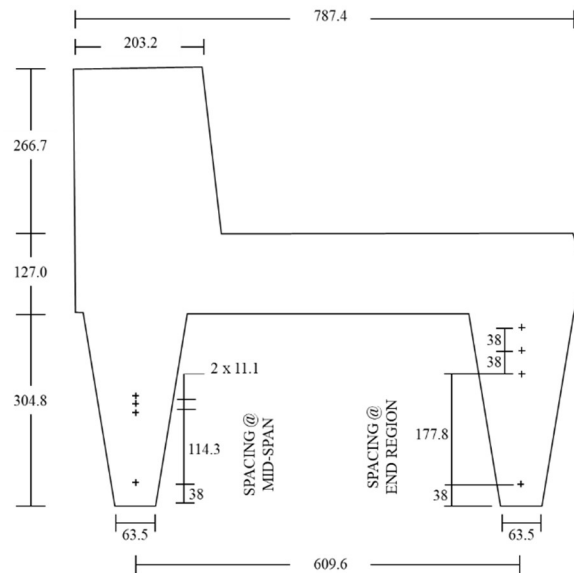


**Figure 3.3:** Bridge 380093 exterior girder SLAB S1 with Prestressing Pattern A. (adapted from NCDOT, 1966)

Note: All dimensions are in millimeters; “+” denotes single prestressing strand



**Figure 3.4:** Overview of Bridge No. 380093.

Visual inspection of the bridge revealed, in general, the exterior girders were deteriorated while the interior girders were not. Spalling and minor loss of concrete at discrete locations were exhibited in several areas on the exterior girders, as shown in Figure 3.1a and reported in previous bridge inspection reports. Two exterior girders exhibited severe loss of concrete with the lower portion of one stem missing entirely, as shown in Figure 3.2. In all areas where concrete was missing, the prestressing strands were

corroded. The two exterior girders missing concrete along the entire span were also missing the bottom prestressing strand over the full span length.

The poor condition of the exterior girders contrasts with the good visual condition of the interior girders. As shown in Figure 3.5, the interior girders did not exhibit any visible signs of deterioration, and subsequent analysis of the interior girders indicated no reduction in capacity. This difference in condition between exterior and interior girders is likely attributed to the gutters and drains at the edge of the roadway which allowed runoff from the roadway to flow down exterior stems of the exterior girders. Bridge 380093 is located in an agricultural region of North Carolina where the runoff contains elevated concentrations of fertilizer and other corrosive materials leading to increased deterioration of the exterior girders.



**Figure 3.5:** Typical interior girders.

The transverse prestressing strand grout ports were also visible and corroded, as shown in Figure 3.6. However, no longitudinal cracking in the wearing surface was observed, indicating that the transverse post-tensioning and shear keys remained effective and relative movement between adjacent girders was minimal.



**Figure 3.6:** Transverse post-tensioning.

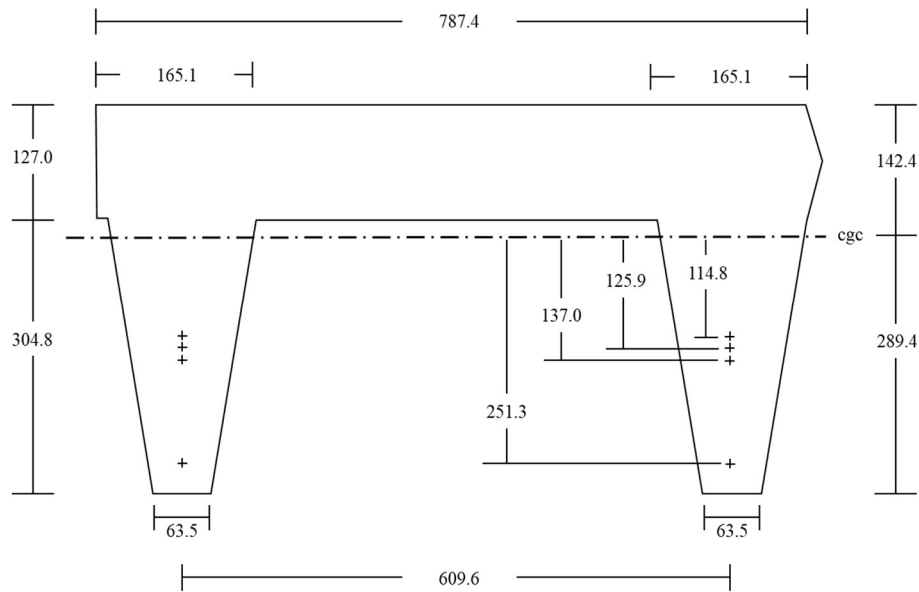
### *Flexural Strength Of Exterior Girders*

Design and as-built drawings were provided by the NCDOT to determine the theoretical strength of the exterior girders prior to damage. The flexural strength was evaluated at two limit states, service and ultimate.

Per the design documents, the monolithic curb on the exterior girders (Figure 3.3) was disregarded in the design of the cross-section. This overly conservative design approach does not account for a substantial area of concrete (approximately  $54.2 \times 10^3 \text{ mm}^2$ ) in the compression region of the girder. Including the area of the monolithic curb in the design of the girder increases the cross-sectional area of the compression region of the girder by 54%; however, the curb is not included in the NCDOT design specifications, and is therefore not included in the initial design calculations presented in this chapter. The cross-sectional dimensions and prestressing strand placement at mid-span for the design of the exterior girder, SLAB S1 (neglecting the curb), are shown in Figure 3.7 and the geometric properties are summarized in Table 3.2.

**Table 3.2:** C-Channel Design Section Properties Without Curb (adapted from NCDOT, 1966).

Gross Area (mm <sup>2</sup> )	170.7 x 10 <sup>3</sup>
Weak Axis Moment of Inertia, $I_{xx}$ (mm <sup>4</sup> )	2.181 x 10 <sup>9</sup>
Strong Axis Moment of Inertia, $I_{yy}$ (mm <sup>4</sup> )	11.90 x 10 <sup>9</sup>
Distance from cgc to top, $y_{top}$ (mm)	142.5
Distance from cgc to bottom, $y_{bottom}$ (mm)	289.3

**Figure 3.7:** Bridge 380093 exterior girder (SLAB S1) at mid-span; neglecting monolithic curb. (adapted from NCDOT, 1966)

Note: All dimensions are in millimeters; "+" denotes a single prestressing strand

### Service Limit State

The internal moment of SLAB S1 (Figure 3.7) under service load conditions can be calculated using AASHTO (2017) and Prestressed Concrete Institute (PCI, 2010) allowable stress limits at full service load after prestress losses:

$$f_{c,allow} = 0.6 f'_c \quad (3.4)$$

and

$$f_{t,allow} = 0.5 \sqrt{f'_c} \quad (3.5)$$

where  $f_{c,allow}$  is the allowable concrete compressive stress (MPa),  $f'_c$  is the concrete design compressive strength (MPa), and  $f_{t,allow}$  is the allowable concrete tensile stress (MPa). Total prestress losses were taken as 15%; therefore,

$$f_{pi} = 0.70 f_{pu} \quad (3.6)$$

and

$$f_{pe} = 0.85 f_{pi} \quad (3.7)$$

or

$$f_{pe} = 0.59 f_{pu} \quad (3.8)$$

where  $f_{pi}$  is the initial prestress level before losses (MPa),  $f_{pu}$  is the ultimate strength of the prestressing strand (MPa), and  $f_{pe}$  is the effective prestress after losses (MPa). The maximum applied service load moment,  $M_a$ , of the exterior girder is the minimum moment based on the compressive and tensile limits, and is calculated using the following:

$$f_{allow} \geq f_{pe} + \frac{\sum P_e e}{S} + \frac{M_{sw}}{S} + \frac{M_a}{S} \quad (3.9)$$

where  $f_{allow}$  is the allowable stress level,  $P_e$  is the effective prestress force for an individual strand,  $e$  is the eccentricity of the prestressing strands (mm),  $M_{sw}$  is the applied moment due to self-weight (N-mm), and  $S$  is the section modulus (mm<sup>3</sup>) for the region of the girder considered (top or bottom). Using Equation 3.9,  $M_{a,top}$  (compression controlled) is 319 kN-m, and  $M_{a,bottom}$  (tension controlled) is 112 kN-m. Therefore,  $M_a$  is 112 kN-m based on  $f_{t,allow}$  in Equation 3.5.

The superimposed dead load of the monolithic curb,  $M_{curb}$ , with an assumed concrete unit weight of 23.5 kN/m<sup>3</sup> (normal weight concrete) is  $M_{curb} = 14.2$  kN-m, and the superimposed dead load of an assumed 100 mm wearing surface,  $M_{WS}$ , with a unit weight of 18.9 kN/m<sup>3</sup> (flexible pavement) is  $M_{WS} = 11.2$  kN-m. Therefore, the maximum allowable service live load including impact,  $M_{LL+I}$ , is given by:

$$M_{LL+I} = M_a - M_{curb} - M_{WS} \quad (3.10)$$

such that,  $M_{LL+I} = 86.8$  kN-m. AASHTO (2017) specifies a 33% dynamic load allowance for impact loading (I). Therefore the maximum allowable service load not including impact,  $M_{LL}$ , on the as-built undamaged exterior girder is  $M_{LL} = 65.3$  kN-m (Table 3.4).

The deterioration of the exterior girder (Figure 3.2) resulted in complete loss of the bottom prestressing strand (Figure 3.7). Using Equations 3.4 through 3.10 and neglecting the prestressing force in the bottom strand, the maximum allowable service load of the deteriorated exterior girder,  $M_{LL,damaged}$  is 28.7 kN-m (Table 3.4) without the added compression capacity of the monolithic curb. However, if the monolithic curb is included in the analysis,  $M_{LL,damaged w/curb}$  is 82.4 kN-m, which gives a greater service load capacity than the undamaged state without the curb included. The dimensions of the cross-section including the monolithic curb are included in Figure 3.3, and the geometric properties of the cross-section are summarized in Table 3.3.

**Table 3.3:** C-Channel Section Properties Including Curb.

Area (mm <sup>2</sup> )	210.7 x 10 <sup>3</sup>
Weak Axis Moment of Inertia, $I_{xx}$ (mm <sup>4</sup> )	5.734 x 10 <sup>9</sup>
Strong Axis Moment of Inertia, $I_{yy}$ (mm <sup>4</sup> )	15.77 x 10 <sup>9</sup>
Distance from cgc to top, $y_{top}$ (mm)	340.1
Distance from cgc to bottom, $y_{bottom}$ (mm)	358.4

*Note: Properties assume horizontal axis of bending of a non-symmetrical section*

Although the allowable stress analysis of the deteriorated exterior girder including the compression capability of the monolithic curb demonstrates the flexural capacity without repair is sufficient for service load conditions,  $f_t$  at service levels exceeds 0 MPa, and as previously discussed, the inventory rating of the damaged girder is insufficient without a retrofit that restores prestress losses to reduce dead load effects. In this case study, the inventory rating factor for concrete tensile stress is the controlling inventory rating factor. Equation 3.1 is rewritten in specific terms for the concrete tensile stress as

$$RF = \frac{0\sqrt{f'_c - (F_d + F_p + F_s)}}{F_t} \quad (3.11)$$

where  $C$  from Equation 3.1 becomes  $0\sqrt{f'_c}$  as the tensile stress limit for the concrete, and  $D$  from Equation 3.1 becomes  $(F_d + F_p + F_s)$  where  $F_d$  is the unfactored dead load stress (MPa),  $F_p$  is the unfactored stress due to prestress effects after losses (MPa),  $F_s$  is the unfactored secondary stress due to prestress forces in continuous span elements (MPa), and  $L(1+I)$  from Equation 3.1 becomes  $F_l$  as the unfactored live load stress including impact (MPa). Given that  $C$ ,  $F_d$ , and  $F_s$  cannot be changed, and it is desirable to keep the live load stress unchanged such that the nominal vehicle load remains unchanged, only the prestressing forces after losses,  $F_p$  can be changed to reduce the dead load effect,  $D$ , and increase the residual live load capacity of the member. It is worth noting, that while adding material to increase the section moment of inertia,  $I_{xx}$ , would reduce concrete stresses, the effect is small unless a significant amount of material is added to the section, which also increases  $F_d$  and decreases  $F_l$  resulting in reduced capacity of the bridge.

The values for the variables in Equation 3.11 for the cross-section excluding the curb prior to deterioration (undamaged), and the cross-section excluding the curb after deterioration (damaged) are shown in Table 3.4. In this case study the concrete tensile stress inventory rating factor before losses due to deterioration is 1.0. Equation 3.2 can be modified as:

$$M_{LL,R} = (RF)M_{LL} \quad (3.12)$$

where  $M_{LL,R}$  (kN-m) is the maximum permissible rated live load moment for the given rating criteria.

$M_{LL,R}$  for the inventory rating with a concrete stress limit of 0 MPa is 48.7 kN-m (Table 3.4), which is a 25.4% reduction from the 65.3 kN-m (Table 3.4) rated live load moment based on the concrete stress limit in Equation 3.5. The prestress losses in the deteriorated cross-section drops the inventory rating factor to 0.25, resulting in a  $M_{LL,R,damaged}$  of 12.2 kN-m (Table 3.4). This indicates that any loading condition on the bridge which creates a moment greater than 12.2 kN-m in the deteriorated C-channel results in concrete tensile stresses greater than 0 MPa, and results in incremental damage. Therefore, a complete retrofit solution which sufficiently restores the prestress losses due to deterioration such that the prestress effects after losses of the deteriorated bridge member,  $F_{p,damaged}$ , are equal to the total prestress effects

after losses of the pre-deterioration condition,  $F_{p,undamaged}$ , enables the inventory rating for a deteriorated bridge, such as Bridge 380093, to remain unchanged.

**Table 3.4:** Inventory Rating Summary.

Criteria	Criteria Variables	Undamaged	
		without Curb	Damaged without Curb
Concrete Tension Stress Limit	$F_d$ (MPa)	8.95	8.95
	$0\sqrt{f'_c}$ $F_p$ (MPa)	-17.6	-11.1
	$F_l$ (MPa)	8.60	8.60
	$M_{LL}$ (kN-m)	48.7	48.7
	<b>RF</b>	<b>1.00</b>	<b>0.25</b>
	$M_{LL,R}$ (kN-m)	48.7	12.2
$0.5\sqrt{f'_c}$ Concrete Tension Stress Limit	$F_d$ (MPa)	8.95	8.95
	$F_p$ (MPa)	-17.6	-11.1
	$F_l$ (MPa)	11.50	11.50
	$M_{LL}$ (kN-m)	65.3	65.3
	<b>RF</b>	<b>1.00</b>	<b>0.44</b>
	$M_{LL,R}$ (kN-m)	65.3	28.7

#### Ultimate Limit State

The ultimate nominal moment capacity,  $M_n$ , of the exterior girder Slab S1 is calculated iteratively applying strain compatibility and typical design equations:

$$M_n = A_{ps} \times f_{ps} \times \left( d_{strands} - \frac{a}{2} \right) \quad (3.13)$$

where  $f_{ps}$  is the stress in the prestressing strands,  $d_{strands}$  is the depth to the centroid of the prestressing strand layers, and

$$a = \frac{A_{ps} \times f_{ps}}{0.85 \times f'_c \times b} \quad (3.14)$$

where  $b$  is the effective width of the concrete in compression, taken as the total width of the cross-section in Figure 3.7. Equation 3.13 assumes that  $a$  is less than the depth of the top flange of the section. From strain compatibility

$$\varepsilon_{ps} = \varepsilon_{pe} + \varepsilon_{ce} + \varepsilon_{pc} \quad (3.15)$$

where  $\varepsilon_{ps}$  is the total strain in the prestressing strand at ultimate load,  $\varepsilon_{pe}$  is the strain in the prestressing strand due to prestressing, and  $\varepsilon_{ce}$  is the strain in the prestressing strand due decompression of the concrete as defined in Equations 3.15 and 3.16.

$$\varepsilon_{ce} = \frac{f_c}{E_c} \quad (3.16)$$

and

$$f_c = \frac{P_e}{A} + \frac{P_e \times e^2}{I} \quad (3.17)$$

The Precast Concrete Institute (PCI) allows for  $f_{ps}$  to be calculated using Equations 3.18 and 3.19 (PCI, 2010):

when  $\varepsilon_{ps} \leq 0.0086$

$$f_{ps} = 196500 \times \varepsilon_{ps} \text{ (MPa)} \quad (3.18)$$

and when  $\varepsilon_{ps} > 0.0086$

$$f_{ps} = 1860 - \frac{0.04}{\varepsilon_{ps} - 0.07} \text{ (MPa)} \quad (3.19)$$

Therefore, using Equations 3.12 through 3.19, the undamaged ultimate nominal moment capacity,  $M_n$ , is 300 kN-m (Table 3.4). Using Equations 3.12-3.19, and again neglecting the bottom prestressing strand, the deteriorated ultimate nominal moment capacity,  $M_{n,damaged}$ , is calculated as 205 kN-m (Table 3.4).

This analysis can be incorporated into the specific form of Equation 3.1 for the flexural strength operating rating:

$$RF = \frac{\varphi M_n - (1.3D + S)}{1.3L(1+I)} \quad (3.20)$$

where  $\varphi$  is 1.0 for ASD method,  $M_n$  is the nominal moment capacity of the member (kN-m),  $D$  is the unfactored dead load moment (kN-m),  $S$  is the unfactored prestress secondary moment (kN-m) for continuous spans, and  $L(1+I)$  is the unfactored live load moment including impact factor (kN-m). Using Equation 3.20, the unfactored live load moment excluding the 33% impact factor,  $L$ , for the undamaged cross-section without the curb is 123 kN-m with an operating rating factor of 1.0 (Table 3.5). The reduced  $M_n$  for Bridge 380093 from 300 kN-m to 205 kN-m results in a deteriorated operating rating factor of

0.55 (Table 3.5), reducing the  $M_{LL,R}$  to 67.7 kN-m. This reduced operating rating requires a load posting limit restricting vehicles that produce a live load moment in the deteriorated span which is greater than 67.7 kN-m. Therefore, a complete retrofit solution which is capable of addressing all possible rating criteria must provide increased nominal moment capacity such that the operating rating factor of the deteriorated member with retrofit installed is equal to or greater than 1.0.

**Table 3.5: Operating Rating Summary.**

Criteria	Criteria Variables	Undamaged without Curb	Damaged without Curb
Flexural Strength	$M_n$ (kN-m)	300	205
	$D$ (kN-m)	67.4	67.4
	$S$ (kN-m)	0	0
	$L$ (kN-m)	123	123
	$M_{LL}$ (kN-m)	123	123
	<b><math>RF</math></b>	<b>1.00</b>	<b>0.55</b>
	$M_{LL,R}$ (kN-m)	123	67.7

## Proposed Retrofit Solution

### Background

The challenge is to develop retrofit techniques that are corrosion resistant, easy to install, monitor and maintain, and that may be applied to a range of prestressed concrete beam types with internal DOT resources that do not require capital budget appropriation and DBB project delivery time constraints. Critically, state DOTs must also be able to rate a bridge with the proposed retrofit installed using established AASHTO (2016) inventory and operating rating methods before it may be applied in the field. In many cases the retrofit may be considered temporary because the deteriorated bridge may be scheduled for replacement, but legislative requirements for budgeting and contracting prevent replacement from occurring within a few years, as was the case with Bridge 380093 presented in the case study.

FRP composite materials are corrosion resistant and therefore provide a strengthening system that is durable against marine and agricultural environmental effects. Typical strengthening systems within the current state of practice include those which attach composite laminate materials to the tension face of

flexural elements to provide additional capacity. The laminate materials are attached through external adhesive bonding (Figure 3.8a), mechanical fasteners (Figure 3.8b), or a combination of both (hybrid) (Figure 3.8c). The schematics presented in Figure 3.8 represent a simply supported beam, in positive bending such that the composite material is attached to the tension face of the beam to provide additional tensile reinforcement to the strengthened element. Although not specific to C-channel girders, the systems in Figure 3.8 can be used in a similar manner to strengthen C-channel cross-sections, as presented in the proposed retrofit later in this chapter.

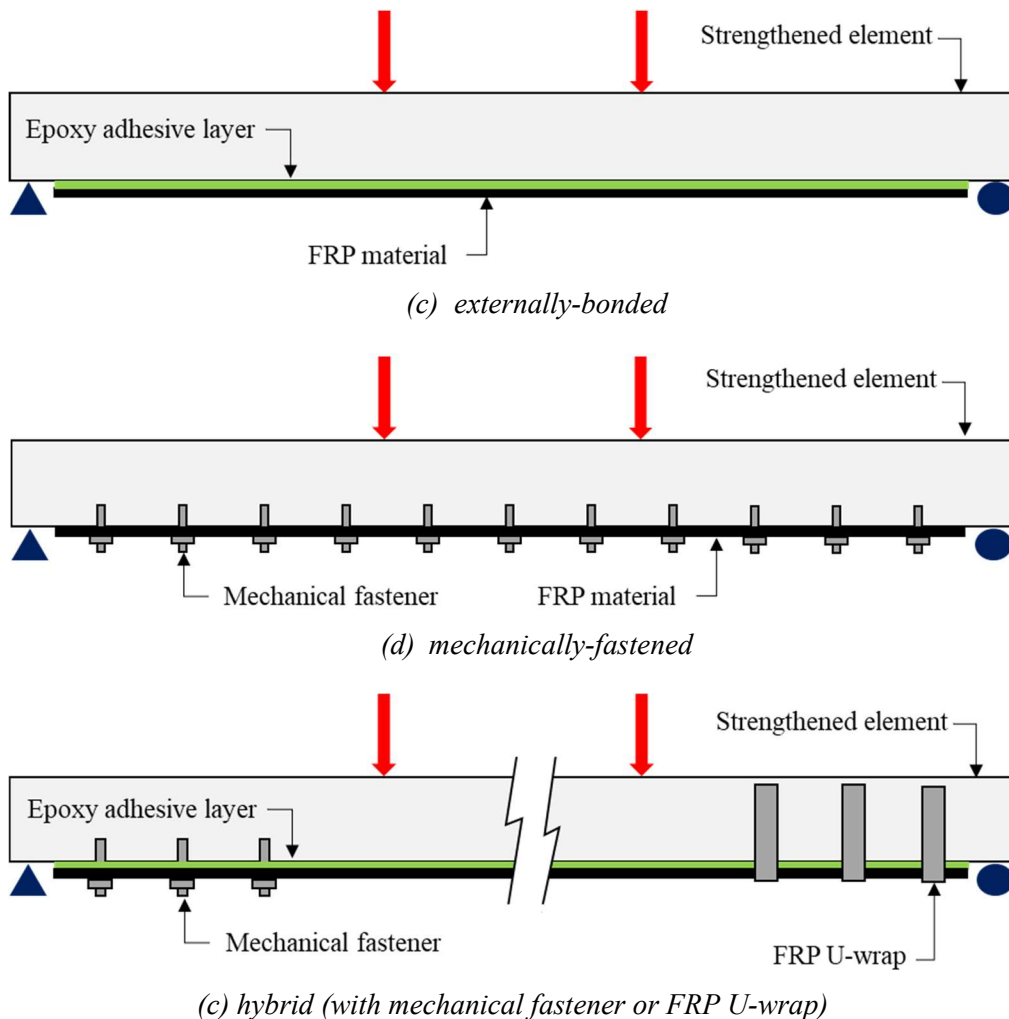


**Figure 3.8:** Types of strengthening with composite laminate materials.

Externally-bonded and hybrid systems (Figures 3.8a and 3.8c), while often effective methods of strengthening, present challenges that do not exist with mechanically-fastened systems. The epoxy cure time to achieve the desired bond adds days to the installation time of the system leading to longer bridge

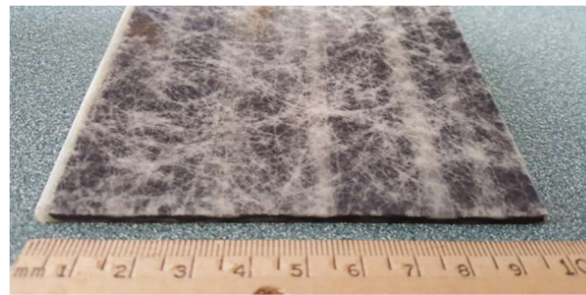
closure time, which increases direct and indirect costs due to extended travel time with delays and detours. Additionally, the quality of the adhesive bond at the bond-critical locations requires extensive surface preparation and is difficult to control and monitor during subsequent bridge inspections.

American Concrete Institute subcommittee 440 (2017) provides a design guide for externally-bonded systems, making these systems more prevalent in practice than mechanically-fastened alternatives, for which there are currently no national design guides available. The effectiveness of externally-bonded systems is critically dependent upon the adhesive bond between the FRP and concrete substrate (ACI 440.2, 2017). These systems often experience premature debonding of the FRP, increasing the need for hybrid systems which incorporate mechanical fasteners or epoxy bonded FRP U-wraps (Figure 3.8c) near the ends of the bonded FRP material to prevent premature debonding and increasing the efficiency of the system. Limited research is available investigating the effectiveness of externally-bonded FRP which is prestressed to reduce concrete tensile stresses (Michels et al. 2014); however, these applications are still subject to premature debonding of the FRP from the substrate. Regardless of application method, the use of adhesive bonding increases preparation, installation, and maintenance labor and time requirements for the system; therefore, the retrofit technique concept proposed in this chapter focuses on the use of mechanical fastening only to present a solution that is reasonably quick to install, is traffic ready upon installation, and the quality of the anchorage (in the form of mechanical fasteners) can be easily inspected at time of installation and during subsequent bridge inspections throughout the life of the system.

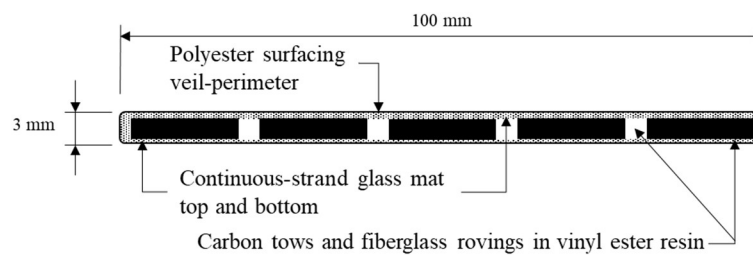
MF-FRP systems (Figure 3.8b) are presented as an effective flexural strengthening technique to increase the AASTHO operational load rating for reinforced concrete elements throughout the literature. Early studies that examine the capability of FRP materials for use in mechanically fastened applications include Lamanna et al. (2001), Bank et al. (2002), Lamanna (2002), and Lamanna et al. (2004). Other studies exist examining the effectiveness of various fastener types, slip effects, and analytical techniques for MF-FRP systems (Elsayed et al., 2009; Lee et al., 2009; and Martinelli et al., 2014). Additional experimental projects for the Wisconsin DOT and Missouri DOT that examine the increased load rating and construction procedures required to strengthen reinforced concrete bridge decks using MF-FRP plates

are presented by Bank (2004). McCoy et al. (2018) presents a summary of available relevant literature including type and size of fastener and testing methodology used.

The relevant literature consistently uses the glass-carbon hybrid FRP plate shown in Figure 3.9 (described in detail in McCoy et al., 2018) which is commercially available and possesses the bolt bearing and longitudinal shear capacity necessary for MF-FRP strengthening systems. The retrofit solution proposed in this chapter is also intended to use the same FRP plate material; however, other FRP plates that possess the necessary bearing and shear capacity could also be used.



(a) FRP plate sample



(b) FRP cross-section (adapted from Strongwell, 2016)

**Figure 3.9:** FRP plate schematic.

### ***Retrofit Concept***

A retrofit solution using MF-FRP plates is an attractive option due to the short duration and minimal labor requirements for installation, durability of FRP, ease of anchor system inspection, and overall cost of the retrofit compared to the cost of detours due to posted limits or closures. Additionally, when compared to the more traditional externally-bonded FRP systems, MF-FRP systems can develop higher strains as they are not susceptible to premature debonding as is the case with externally-bonded systems.

The proposed MF-FRP retrofit concept to restore deteriorated C-channel girders, such as Bridge 380093, is presented in Figure 3.10. FRP plates are attached to the interior of the C-channel stems

(Figures 3.10a and 3.10b) as the stem exteriors are not easily accessible due to the adjacent C-channel girders (shown in Figure 3.5). The FRP is attached using a sufficient number and pattern of stainless-steel bolts and bolted directly to the concrete stem at one end (referred to as the dead-end) of the member and attached to a prestressing mechanism at the opposite end (referred to as the live-end). The prestressing mechanism at the live-end may be a turnbuckle system attached to the FRP plate using the same bolt pattern as the dead-end and attached to the concrete C-channel using a sufficient size and number of bolts to fully develop the capacity of the FRP plate and transfer the force into the concrete substrate without splitting of the concrete due to bearing. Prestressing is applied to the FRP plate by tightening the turnbuckle system such that the internal force in the FRP, which is delivered to the C-channel through the stainless-steel bolts, restores the prestress losses in the deteriorated member.

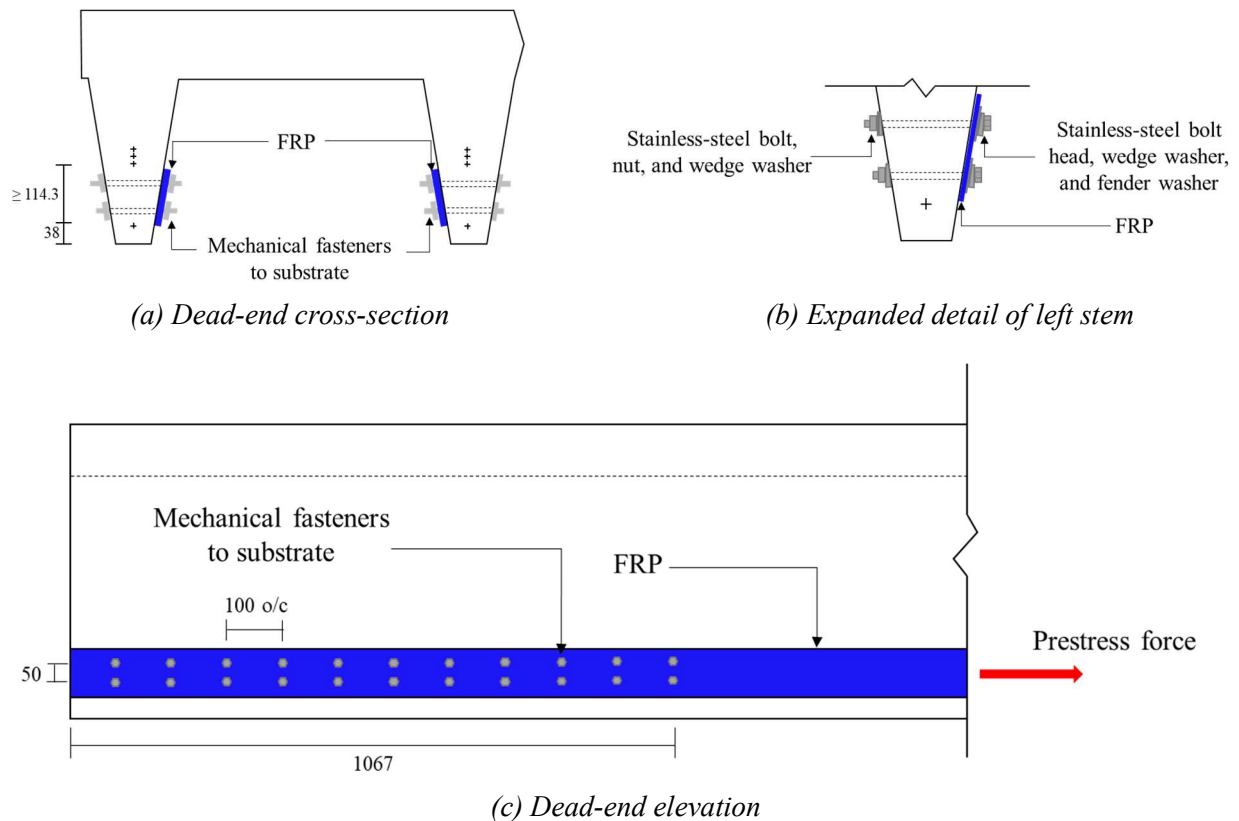


**Figure 3.10:** Proposed MF-FRP retrofit applied to C-channel beam.  
*Note: All dimensions are in millimeters*

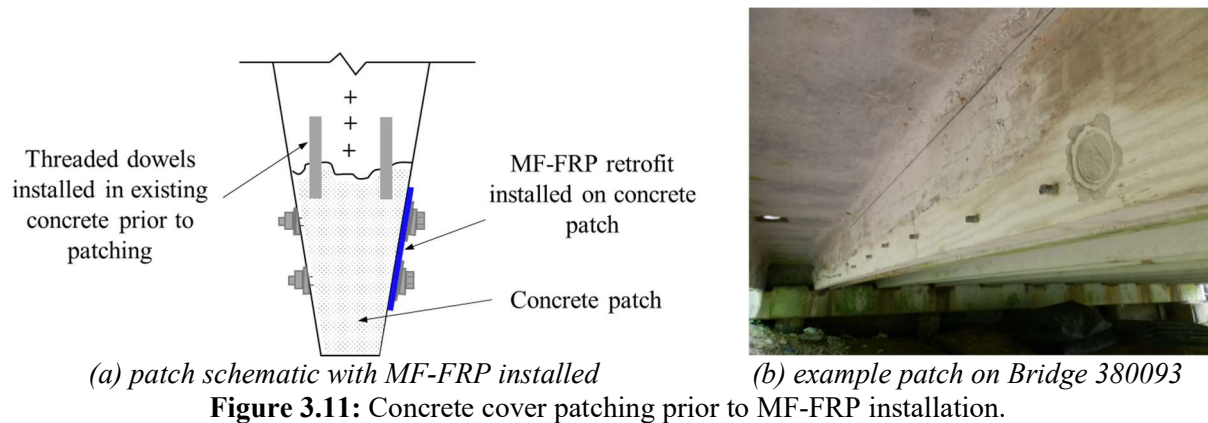
As in Equation 3.6, the effective prestressing force,  $P_e$ , in the C-channel cross-section presented in the case study is taken as 85% of the initial prestressing force,  $P_i$ . The initial prestressing force is 96.5 kN

(Table 3.1), therefore,  $P_e$  for a single prestressing strand without deterioration is 82.0 kN. The prestressed MF-FRP retrofit, must be capable of developing this prestressing force, after losses, for each prestressing strand which experiences total loss due to deterioration. Prestressing strands which experience partial loss may be restored with less prestressing force in the MF-FRP retrofit as appropriate. Because some loss will likely be experienced in the MF-FRP system due to slip and bearing effects between the system and the concrete substrate,  $P_i$  is taken as the target prestressing force for development of the MF-FRP retrofit system, such that a single FRP plate is capable of replacing the total loss of a single prestressing strand. Using  $P_i$  provides an upper bound prestressing capability for the MF-FRP retrofit. The MF-FRP retrofit prestressing force range is considered to be between  $P_e$  and  $P_i$ , or 82.0 kN to 96.5 kN.

While  $P_i$  is 96.5 kN for the case study bridge, it is important to note that this is a typical initial prestressing value for high strength, 7-wire prestressing strands. Applying Equation 3.7 to the range of typical high strength, 7-wire prestressing strand diameters, ranging from 6 mm to 13 mm (PCI, 2010), gives an effective prestressing range of 23.6 kN to 94.5 kN, therefore, the proposed MF-FRP retrofit must be capable of applying an effective prestressing force of 94.5 kN to restore the inventory rating across the range of prestressed concrete member cross-sections and varying prestressing strand configurations.

Initial research findings by McCoy et al. (2018) indicate that a 22-bolt pattern, aligned in 2 rows, provides sufficient bearing resistance to develop an ultimate capacity of approximately 214 kN for the MF-FRP retrofit connection. Therefore, the required initial prestressing force of the MF-FRP retrofit is between 38% and 45% of the ultimate capacity. The re-introduction of the effective prestress force in the C-Channel through the MF-FRP retrofit increases  $F_p$  from Equation 3.11, which reduces the dead load effect,  $D$  (Equation 3.1), and increases the inventory load rating to pre-deterioration levels. The line-of-action of the MF-FRP retrofit at a depth,  $d$ , from the top of the member is intended to be at, or near, the line-of-action of the deteriorated prestress strands. In cases where concrete cover loss prevents the installation near the line-of-action of the original prestressing strand, such as the complete loss in Figure 3.2, cover patching with shear dowels along the cold joint must be done to provide a surface to anchor the

MF-FRP retrofit. Figure 3.11a is a concept schematic of patch concrete cover with dowels installed. Such patching is currently a standard practice for DOTs, as shown in Figure 3.11b as an example illustration of an installed patch on Bridge 380093. This patch must be installed and allowed to cure prior to the MF-FRP installation, which may necessitate a temporary load restriction on the bridge prior to the installation of the MF-FRP retrofit. If patching is not possible, calculations must be done to determine the level of prestressing force necessary for an installed MF-FRP retrofit which is not coincident with the prestressing strand line-of-action such that the inventory rating criteria are satisfied to produce an inventory rating factor of 1.0 or greater.



The residual capacity of the MF-FRP retrofit above the prestressing force is necessary to restore  $\phi M_n$  to pre-deterioration levels in candidate bridges with deteriorated operating rating factors less than 1.0 such that the post-MF-FRP operating rating factor is 1.0 or greater without reducing the nominal vehicle live load. Further material-scale and full-scale testing of the proposed MF-FRP retrofit solution is necessary to quantify the increase in  $\phi M_n$  after the retrofit is installed on a candidate member; however, the residual capacity of the FRP plate after prestressing, 55% to 62% of ultimate capacity, is believed to be sufficient to restore nominal moment capacity losses in deteriorated members.

Additional design considerations for the MF-FRP retrofit solution should include the level of deterioration in the candidate member and longitudinal splitting due to strong axis bending of the FRP plate. The level of deterioration must be considered when determining the number of FRP plates needed to restore the concrete tension to within allowable limits and restore the pre-deterioration flexural capacity

to allow the bridge to remain open without posted limits or closures. Additionally, longitudinal splitting that may occur in the FRP plate due to induced moment from the camber and flexure of the C-channel. This is a consequence of attaching the MF-FRP to the side of the C-channel stem which places the FRP plate in strong axis bending, and is specific to the sample retrofit solution for the C-channel cross-section presented in this study. However, to effectively address all criteria for a complete solution across multiple cross-sections, it is recommended that this behavior be examined during full-scale testing of the MF-FRP retrofit, and the effect of the moment in the FRP plate be accounted for in the retrofit design.

### ***Other Applications and Limitations***

A second study conducted by the NCDOT examined NCDOT Bridge 150035 (Figure 3.1b) which carries United States Highway 70 (US 70) across Ward Creek along the Pamlico Sound in Carteret County, North Carolina (Van Brunt, 2016). The bridge consists of nine 12.2 m hollow core slab spans. The hollow core slab cross-section for Bridge 150035 is shown in Figure 3.12. Five site visits of Bridge 150035 were conducted between December 9<sup>th</sup>, 2013 and February 8<sup>th</sup>, 2014. The inspections during the site visits revealed the greatest deterioration at the end spans of the bridge. This deterioration resulted in partial prestress losses in the bottom layer of prestressing strands in multiple hollow core sections within each of the two end spans. Figure 3.1b is a representative photo of patchwork in place to slow the rate of deterioration; however, patchwork does not restore prestress loss which has already occurred. Figure 3.13 is representative of deterioration with spalled concrete exposing shear reinforcement and prestressing strands, indicating partial prestress loss in the damaged region of the hollow core section.

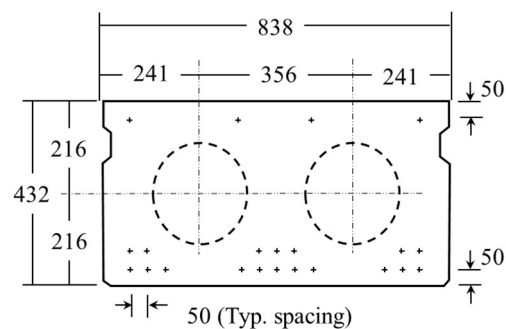


**Figure 3.12:** Bridge 150035 hollow core slab cross-section (adapted from Van Brunt, 2016).

*Note: “+” denotes prestressing strand; all dimensions are in millimeters*



**Figure 3.13:** Example deterioration of hollow core slab.

At the time of the site visits, posted load limits were active for Bridge 150035, due to reduced flexural capacity and excess  $f_t$  in the concrete. Therefore, a similar MF-FRP retrofit is desired for use on hollow core slab cross-sections which experience similar prestress loss due to deterioration in aggressive environments. The retrofit solution for hollow core cross-sections can be applied directly to the tension face of the section (Figure 3.14), placing the MF-FRP system in uniaxial tension. Because of the uniaxial tension behavior in this application, transverse splitting of the FRP due to induced moment in the system is not a concern with hollow core applications.

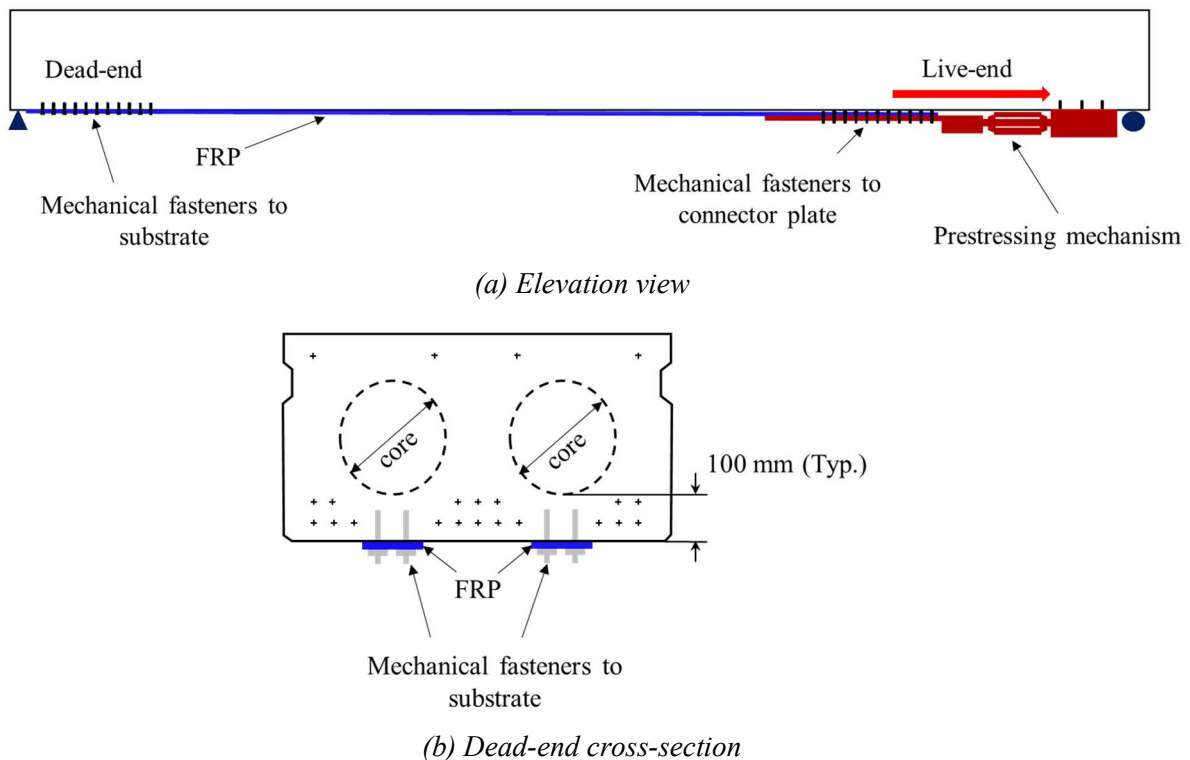


**Figure 3.14:** Proposed MF-FRP retrofit applied to a hollow core slab.

Note: “+” denotes prestressing strand

Equations 3.4 through 3.19, modified for the geometric properties of the hollow core cross-section, conclude that the MF-FRP system with a single FRP plate is capable of restoring prestress losses for a typical prestressing strand and restoring the ultimate moment capacity of the damaged hollow core section. As shown in Figure 3.14b, typical dimensions for concrete cover beneath a single void in the hollow core section is 100 mm. A 50 mm fastener depth develops sufficient capacity for the MF-FRP system to transfer force from the prestressed FRP plate into the concrete substrate. Therefore, sufficient concrete cover exists to fasten the retrofit solution along the center line of each void, avoiding the prestressing strand layout in the section. Further, the 0.9 m long end regions of hollow core slabs are of a solid concrete section. The total length of the proposed anchor system is 1.06 m; therefore, the majority of the dead-end is anchored in solid concrete, and the complete live-end anchor is anchored in solid concrete. As with the C-channel application, the size of the hollow core section and extent of deterioration must be considered when determining the number of FRP plates needed to retrofit the superstructure elements such that the bridge remains open without posted limits or closures.

There are some challenges with applying the proposed retrofit solution to AASHTO I-beams (Figure 3.15a) or bulb-tee girders (Figure 3.15b) typically found on major arterial routes such as the interstate highway system. The larger number and close spacing of prestressing strands at the bottom and in the web of these of long-span girders makes application of the MF-FRP retrofit difficult because the fasteners need to be embedded in concrete without interfering with the prestressing strands. Further, damage in the large AASHTO girders, often due to vehicle strikes, results in a significant loss of prestress (greater than that of one or two prestressing strands). Significant prestress loss would require multiple FRP plates and likely enhanced fastening and prestressing techniques; therefore, the applications of the proposed MF-FRP retrofit do not include large, long-span AASHTO girders, but rather are limited to hollow core and C-channel cross-sections which are typically found on minor arterial routes and state highways.

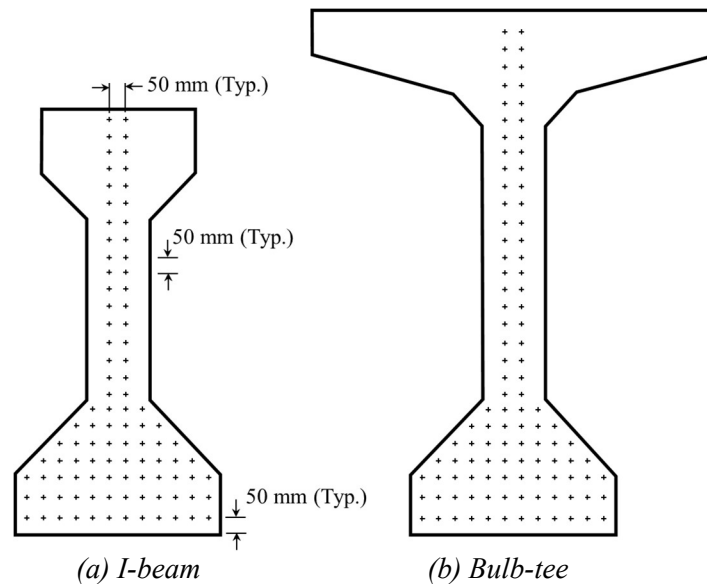


**Figure 3.15:** AASHTO girder examples (adapted from Nawy, 2010).  
*Note: “+” denotes prestressing strand*

Other design considerations for the MF-FRP retrofit solution, regardless of candidate member type, include the bearing and longitudinal shear capacity of the FRP plate at the fastener locations, shear and pullout capacity of each fastener, and the behavior of the concrete due to fastener bearing. Typical design rules to model the capacity of each bolt and the concrete splitting behavior may be used as appropriate. Additionally, fatigue and creep bearing behavior are important design considerations, both of which are the subject of ongoing research to develop a complete MF-FRP retrofit design and implementation methodology.

### Conclusions and Recommendations

Both inventory and operating rating criteria (AASHTO, 2016) must be addressed to remove posted load limits and closures on deteriorated prestressed concrete bridges. While operating rating criteria typically control the overall member rating, a retrofit solution that provides strengthening only, without restoring prestress losses, would likely create a situation in which inventory rating criteria control. Therefore, a complete retrofit solution must also address the concrete stress limits within the inventory rating criteria to effectively remove posted load limits or closure, and allow the bridge to remain in service without restrictions.

The development of analysis and design tools that apply the inventory and operating rating criteria to a range of cross-sections would be useful. These tools must also be capable of incorporating the effects of prestressed MF-FRP retrofit solutions, such as the one presented in this study. Layered-sectional-analysis modeling techniques are recommended for the development of a tool that will enable practicing engineers to design MF-FRP retrofit solutions for candidate bridge superstructures and analyze load rating criteria for bridge retrofitted with the proposed MF-FRP solution.

Initial analysis of the service and ultimate limit states on North Carolina bridge 380093 indicates that the bridge could have been a candidate for the proposed MF-FRP retrofit. Further, hollow core bridge superstructures, such as that in Bridge 150035, experience similar deterioration and prestress losses, would also be a candidate for the MF-FRP retrofit adapted for hollow core members. Initial calculations and early research indicate that the MF-FRP retrofit is capable of restoring prestress losses and reductions in nominal moment capacity due to deterioration, and therefore enable the inventory and operating ratings to remain unchanged such that retrofitted bridges could remain open, without posted load limits or closures, until permanent superstructure placement can be scheduled. Further research is needed to quantify the cost of installation and maintenance of the MF-FRP retrofit; however, the proposed retrofit solution is likely a low-cost alternative to superstructure replacement and can be installed in a shorter period of time compared to externally-bonded, prestressed FRP retrofit alternatives.

Further research is needed to develop the proposed concept. Specifically, small-scale testing to investigate the FRP bearing capacity and tensile behavior with various diameters of mechanical fasteners would be helpful to develop a comprehensive MF-FRP solution. It is also necessary to understand the FRP fatigue and creep bearing behavior with a given anchor pattern to inform the MF-FRP system life-cycle for varying traffic loading conditions. Additionally, full-scale testing of the MF-FRP system on C-channel and hollow core sections is necessary to understand the complete composite behavior of the system and interaction with the concrete substrate. Full-scale testing is also needed to inform installation and inspections procedures and the development of a comprehensive solution which includes design and implementation considerations for the MF-FRP system.

**Acknowledgements**

The authors would like to thank NCDOT for their financial support, Mr. Gichuru Muchane, Assistant State Structures Engineer for the NCDOT, for his technical expertise, and Mr. William (Reese) Briley, NCDOT Division 5 Bridge Maintenance Engineer for providing access to the case study bridge and the appropriate inspection reports and structural drawings.

## **CHAPTER 4: ANCHOR BOLT PATTERNS FOR MECHANICALLY-FASTENED FRP PLATES**

*(ASCE Journal of Composites for Construction, in press)*

Brad C. McCoy, P.E.: Ph.D. Candidate, North Carolina State University, Department of Civil, Construction, and Environmental Engineering, Corresponding Author: [bcmccoy@usma.edu](mailto:bcmccoy@usma.edu)

Zakariya Bourara: MS Student, North Carolina State University, Department of Civil, Construction, and Environmental Engineering

Rudolf Seracino, Ph.D.: Professor, North Carolina State University, Department of Civil, Construction, and Environmental Engineering

Gregory W. Lucier, Ph.D.: Assistant Research Professor, North Carolina State University, Department of Civil, Construction, and Environmental Engineering

### **Abstract**

This chapter examines the results of material testing of hybrid carbon and glass fiber-reinforced polymer (FRP) plates for use in prestressed mechanically-fastened applications. The small-scale material tests were conducted in three phases: 1) uniaxial tension without holes, 2) uniaxial tension with open holes, and 3) uniaxial tension with single- and multi-bolt connections. In all three phases of testing, Digital Image Correlation (DIC) was used to obtain continuous strain data, showing holistic strain field development through failure. A total of 89 tests were conducted across 17 treatment groups to develop an anchor pattern and fastener spacing which is optimized with respect to maximum capacity and behavior under anticipated service load conditions. The tests presented comprise the initial phase of a larger project that aims to employ prestressed Mechanically-Fastened FRP (MF-FRP) plates as a retrofit repair solution for deteriorated prestressed concrete bridge superstructures. Results conclude that 2 lines of 11 each 12.7 mm diameter bolts, with 100 mm longitudinal spacing and 38 mm transverse spacing, provide an end region anchor pattern with an ultimate capacity of 206 kN – 89% of the ultimate capacity for the examined FRP plate with holes.

*Keywords: Strengthening and repair; Mechanically-Fastened FRP; Digital Image Correlation;*

## **Introduction**

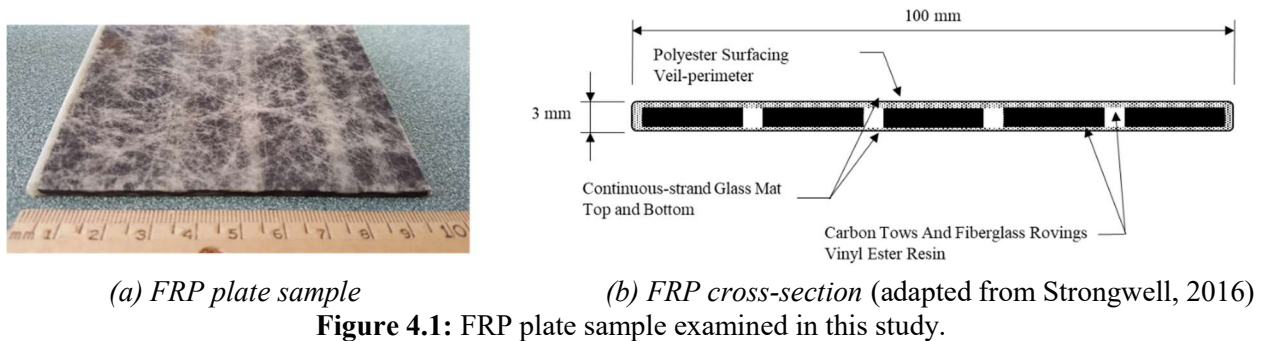
Prestressed concrete is a common construction material used in bridge superstructure systems currently in service across the United States. The North Carolina Department of Transportation (NCDOT) employs the use of prestressed concrete in a variety of shapes and forms including C-channel and hollow core slabs. Many of these superstructure elements are experiencing varying levels of deterioration and must be repaired or replaced to extend the useful life of the bridge. Examples of deteriorated C-channel and hollow core prestressed concrete beams are the subject of earlier research funded by the North Carolina Department of Transportation (NCDOT) to investigate the level of deterioration and potential repair methods (Seliem et al., 2014; and Van Brunt et al., 2016).

Strengthening and repair of deteriorated C-channel and hollow core superstructures to extend the useful life of bridges without posted load limits, or closure, is of interest to the NCDOT. Externally-bonded systems, which transfer shear between the strengthened member and the FRP through an adhesive bond, present bond quality and subsequent bond inspection challenges, as well as bond curing requirements which increase the installation time of the system. These challenges are not present with the application of Mechanically-Fastened Fiber-Reinforced Polymer (MF-FRP) systems. Corrosion of galvanized steel fasteners with MF-FRP systems is of concern where fasteners may come into galvanic contact with carbon fibers; however, the use stainless steel fasteners removes the concern of galvanic reactions. Further, corrosion and section loss in prestressed concrete flexural elements often results in prestress loss and concrete cracking which exceeds the allowable concrete tensile stress limits per the American Association of State Highway and Transportation Officials (AASHTO) Load Resistance and Factor Rating criteria (AASHTO, 2016). Therefore, a prestressed MF-FRP solution which is capable of restoring the cracking moment and reducing the tensile concrete stresses to within allowable is of particular interest.

## **Research Significance**

This chapter examines the anchor pattern and fastener diameter necessary to develop the maximum capacity possible of a commercially available hybrid glass and carbon FRP plate material manufactured

with longitudinal, pultruded carbon fiber tows encased in a random glass fiber mat (Figure 4.1) – hereafter referred to as FRP – typically used in MF-FRP applications. Due to prestressing requirements of the MF-FRP retrofit solution, the optimized anchor pattern must be capable of developing the maximum capacity of the FRP material through a system which mechanically fastens the FRP plate to the substrate exclusively within the end (anchorage) region of the plate. Such an MF-FRP system differs from similar systems published previously, which typically employ mechanical anchors over the full length of the fastened FRP plate (Lamanna et al., 2004b). This chapter presents the behavior of the FRP plate in uniaxial tension with and without holes, and in single-bolt and multi-bolt bearing conditions to develop an optimized mechanically fastened anchor system for the retrofit solution. Additionally, Digital Image Correlation (DIC) is used for each material test condition to develop a continuous strain field data. The location of disturbed regions, and the manner in which they develop, gives the researcher understanding of the most efficient fastener pattern for the FRP material examined in this investigation.



## Background

Strengthening of reinforced concrete bridge decks and girders to increase the Federal Highway Administration (FHWA) load rating using Mechanically-Fastened Fiber-Reinforced Polymer (MF-FRP) plates was the subject of previous research projects (Bank et al., 2002; Lamanna et al., 2004a; Lamanna et al., 2004b; Borowicz, 2002; and Lamanna et al., 2001), which focus on various types of fasteners, and the interactions between the concrete and fasteners. Additional experimental projects for the Wisconsin DOT and Missouri DOT which examine the increased load rating and construction procedures required to strengthen reinforced concrete bridge decks using MF-FRP plates are presented by Bank (2004).

Ebead and Saeed (2014) examined the behavior of reinforced concrete beams strengthened with externally-bonded FRP, MF-FRP, and hybrid solutions that use both adhesive bonding and mechanical fasteners. The available research concludes that MF-FRP solutions, when compared to externally bonded solutions, experience increased shear transfer along the FRP and concrete substrate interface. Further, Elsayed et al. (2009) examined two types of mechanical fasteners and compared the performance to external bonding alone for FRP strengthening of concrete elements. The results of the study conclude that a sufficient number of properly-spaced fasteners enables a higher load to be developed in MF-FRP plates compared to adhesively bonding of the same FRP plates – 86.3 kN and 50.2 kN, respectively. Furthermore, the failure mode observed in the mechanically fastened system with a sufficient number of fasteners was FRP rupture, whereas debonding of the FRP from the strengthened element was observed in the externally-bonded system. This study demonstrates the ability of MF-FRP systems to develop the full capacity of applied FRP material, whereas externally-bonded systems typically fail in debonding prior to FRP rupture, and thus do not develop the full capacity of the FRP material.

Table 4.1 provides a representative summary of the available MF-FRP research with the size and type of fasteners used. The FRP material used in all of the studies presented in Table 4.1 is the same commercially-available FRP plate examined in this chapter. While Table 4.1 does not include all available literature on MF-FRP studies, the studies listed represent the preponderance of available literature specific to MF-FRP systems.

The MF-FRP research presented in Table 4.1 examines the capacity of MF-FRP systems using the same commercially-available FRP material (shown in Figure 4.1) fastened with selected fasteners of three general types: powder-actuated fasteners (PAF), screw anchors, and wedge anchors (Figure 4.2). Bank and Arora (2007) examined the effects of PAF and wedge anchors combined in the same system, as noted in Table 4.1.

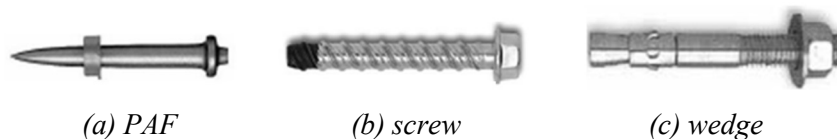


**Figure 4.2:** Types of fasteners used in previous studies (adapted from Martinelli et al., 2014).

Results for each study were reported in various ways – percent increase from a control test, total applied load carried by a strengthened beam in four-point bending, and maximum applied load for uniaxial tension tests. Therefore, it is difficult to draw direct comparisons across the studies presented in Table 4.1. Many of the studies show similar results, however. Those examining PAFs as a means for attaching the FRP to the strengthened member observed fastener pull-out as the primary failure mode in all cases (Borowicz, 2002; Lamanna et al., 2001; Elsayed et al. 2009). This pull-out failure is likely due to a combination of concrete damage during installation of the PAF, to the smooth fastener shank, and to the relatively short fastener length,  $l_f$ , as compared to many of the wedge and screw anchors examined. Studies that examine fastener arrays with a relatively small fastener diameter,  $d_f$ , of less than 12.7 mm, failed in bearing (Figure 4.3) due to the higher bearing stress (Realfonzo et al., 2013; Ebead, 2011; Martinelli et al., 2014; Elsayed et al., 2009; Lamanna et al., 2004b). Martin and Lamanna (2008) used 12.7 mm diameter screw fasteners to attach a single FRP plate to a reinforced concrete beam, and reported a 38.5% increase in strength due to reduced bearing stress with the larger diameter fasteners. Combined failure of bearing (ductile failure) and FRP rupture (brittle failure) is desired to create a ductile but efficient strengthening system, as noted by Lee et al. (2009). These findings indicate that an efficient anchorage which fully develops the capacity of the FRP plate with minimal bearing at each fastener can be obtained with fastener diameters of 12.7 mm or greater; however, this is a current gap in the available knowledge for MF-FRP systems. Detailed research to understand the effect of 12.7 mm (or greater) diameter fasteners is necessary to optimize the capacity of the MF-FRP examined to date in the literature.



**Figure 4.3:** Fastener bearing due to 4.5 mm PAF.  
(Lamanna et al., 2004b)

**Table 4.1:** MF-FRP Literature Summary (adapted from Martinelli et al., 2014).

Source	Type	Fastener		No. lines <sup>1</sup>	Test Type
		$d_f$ (mm)	$l_f$ (mm)		
Borowicz (2002)	PAF	4.45	47.0	2-a	
Ebead (2011)	Screw	4.75	38.1	1-a / 2-a	
Ekenel et al. (2006)	Wedge	9.53	40.6	1-s	
El-Maaddawy (2014)	PAF	3.99	32.0	2-a	
	Wedge	8.00	55.1	1-s	
	Screw	8.00	55.1	1-s	
El-Maaddawy et al. (2013)	PAF	3.99	32.0	1-a / 2-a	
			52.1	1-a / 2-a	
Galati et al. (2007)	Wedge	12.0	99.8	1-s / 2-a	
		3.99	22.0	2-a	
Lamanna (2002)	PAF	3.71	26.9	1-a	4P Bending
		3.71	32.0	1-a	
		3.48	26.9	2-a	
Lamanna et al. (2001)	PAF	3.71	32.0	1-a	
		4.50	32.0	2-a	
Bank et al. (2002)	PAF	4.50	47.0	2-a	
Lamanna et al. (2004b)	PAF	4.50	47.0	2-a	
Lee et al. (2009)	PAF	3.48	25.0	2-a	
		3.48	32.0	2-a	
Bank and Arora (2007)	PAF / Wedge	4.07 / 12.7	44.5 / 69.9	1-a	
Martin and Lamanna (2008)	Screw	12.7	50.8	1-a / 1-s	
Napoli et al. (2013)	Screw	9.53	44.5	1-s	
Dempsey and Scott (2006) <sup>2</sup>	Screw	4.50	50.8	2-a	
Realfonzo et al. (2013)	Screw	5.99	45.0	1-a	Tension
				2-s	
Elsayed et al. (2009)	PAF	3.73	47.0	1-a	
	Screw	4.75	36.8	1-a / 2-a	

Notes: 1) "a" denotes "aligned" lines; "s" denotes "staggered" lines; lines are in the longitudinal direction; 2) MF-FRP applied to timber elements.

The ultimate capacity of the FRP material used in this study with multiple open holes is not known but is necessary to understand the full capacity of the material in uniaxial tension. Testing to examine the behavior of the FRP plate with and without holes fills this gap in the current body of knowledge and provides the maximum capacity for the FRP plate in tension. This open-hole maximum capacity informs the theoretical capacity for the FRP with mechanical fasteners transferring internal load through bearing at each fastener location.

The fastener patterns presented throughout the research are predominantly single- or double-aligned fastener lines. While five of the studies presented in Table 4.1 examine staggered fastener patterns, only Realfonzo et al. (2013) presents a staggered pattern with sufficient transverse spacing for consideration in this study. The remaining four staggered fastener patterns presented in the literature are of systems in which the fastener pattern extends along the length of the FRP, with the holes offset from the centerline only slightly (referred to in most literature as a single-line staggered pattern). Realfonzo et al. (2013) presents a two-line staggered pattern of four (4) total fasteners which fail in bearing in a similar manner to the two-line and single-line fastener patterns presented throughout the literature. Because the predominance of available research examines either single- or two-line aligned fastener patterns, or patterns with only slight staggering, there is a knowledge gap with respect to the behavior of MF-FRP using staggered fastener patterns. This apparent gap in the current research indicates that a study to determine the effect and statistical significance of a staggered fastener pattern on the ultimate anchorage capacity of MF-FRP systems would be useful.

The research presented in this chapter examines the effects of fastener pattern and fastener spacing using a 12.7 mm bolt diameter to quantify the maximum capacity of the FRP plate, and to inform an optimized mechanical fastener system capable of developing the necessary prestress force. The results from 89 individual tests across 17 treatment groups are presented to establish statistical significance at the 90%, or higher, confidence level.

## **Methodology**

### ***Test treatment groups***

To identify the optimal anchor bolt pattern, an experimental program was designed to explore the effects of different anchoring parameters: longitudinal spacing, transverse spacing, number of bolts, and bolt pattern (aligned vs staggered). Therefore, a test matrix (Table 4.2) with a total of 14 tension test treatments was developed with three distinct categories: no-hole, open-hole, and bolted. All treatment groups were tested in uniaxial tension. The no-hole group consisted of 708 mm long FRP plates without holes. The open-hole group consisted of five types of specimens, all 708 mm long, with varying number

of holes, transverse spacing, and hole pattern. The bolted group considered single bolt connections, as well as 16-, 18-, 20-, and 22-bolt connections. ASTM D5766 (2014) specifies a width-to-diameter ratio ( $w/D$ ) of 6 for open-hole tests. However, given the fixed width of the FRP material tested and the desired 12.7 mm bolt diameter, the  $w/D$  ratio for open-hole tests in this study was adjusted to 7 and 3.5 for single-hole and multi-hole test treatments, respectively, corresponding to the nominal specimen width (100 mm) and actual hole diameter (14.2 mm).

**Table 4.2:** Initial Small-Scale Test Matrix.

Specimen ID	No. of Replicates	Treatment Description	ASTM
T	8	No holes	D3039
S-OH	6	Single open hole centered in gauge length	D5766 <sup>1</sup>
DBL4-OH-1.5	6	4 open holes; 2-by-2; 38 mm transverse spacing; 100 mm longitudinal spacing	D5766 <sup>1</sup>
DBL4-OH-2.0	6	4 open holes; 2-by-2; 50 mm transverse spacing; 100 mm longitudinal spacing	D5766 <sup>1</sup>
STG4-OH-1.5	6	4 open holes; staggered with 50 mm offset; 38 mm transverse spacing; 100 mm longitudinal spacing	D5766 <sup>1</sup>
STG4-OH-2.0	6	4 open holes; staggered with 50 mm offset; 50 mm transverse spacing; 100 mm longitudinal spacing	D5766 <sup>1</sup>
S-B-X-1.5	6	Single bolt bearing with 38 mm edge distance excluding threads	D5961
S-B-N-1.5	6	Single bolt bearing with 38 mm edge distance including threads	D5961
S-B-X-4.0	6	Single bolt bearing with 100 mm edge distance excluding threads	NA
S-B-N-4.0	6	Single bolt bearing with 100 mm edge distance including threads	NA
DBL16-B-1.5	6	16 bolts; 12.7 mm diameter; 2-by-2; 38 mm transverse spacing; 100 mm longitudinal spacing	NA
DBL18-B-1.5	6	18 bolts; 12.7 mm diameter; 2-by-2; 38 mm transverse spacing; 100 mm longitudinal spacing	NA
DBL20-B-1.5	6	20 bolts; 12.7 mm diameter; 2-by-2; 38 mm transverse spacing; 100 mm longitudinal spacing	NA
DBL22-B-1.5	6	22 bolts; 12.7 mm diameter; 2-by-2; 38 mm transverse spacing; 100 mm longitudinal spacing	NA

Notes: 1) ASTM D5766 specifies a single hole with  $w/D=6$ , test was adapted to accommodate desired hole diameters for single- and multi-bolt treatment conditions.

#### ***Number of replicates for each test***

To achieve statistical significance, the number of replicates necessary for each group needed to be calculated. It was desired that conclusions be statistically significant at least to the 90% confidence level (CL) with a 5% limit of error ( $e$ ). The CL for a desired test result can be calculated in terms of the coefficient of variation ( $CV$ ) on the tension strength of the material and a sufficient number of sample

replicates using either a student-t distribution (fewer than 30 replicates), or a standard normal distribution (greater than 30 replicates). For the purposes of this study, a student-t distribution was used to determine the sample size ( $n$ ) required for each test to achieve the desired 90% CL. The development of the sample size calculation is shown in Equations 4.1 through 4.3 for  $n$  number of independent and identically distributed (*iid*) samples that follow a standard normal distribution with mean,  $\mu$ , and variance,  $\sigma^2$

$$X_1, \dots, X_n \sim iid N(\mu, \sigma^2) \quad (4.1a)$$

and

$$\hat{\mu} = \bar{x} \quad (4.1b)$$

and

$$\widehat{\sigma^2} = \frac{1}{n-1} \sum_{i=1}^n (x_i - \bar{x})^2 \quad (4.1c)$$

and

$$\hat{\sigma} = \sqrt{\widehat{\sigma^2}} = s \quad (4.1d)$$

where  $\hat{\cdot}$  indicates an estimate of the parameter (i.e.  $\hat{\mu}$  is the estimator for the population mean, which is the sample mean,  $\bar{x}$ ). The 90% CL of  $\mu$  is defined as

$$\hat{\mu} \pm t_{(0.95, df=n-1)} \frac{\hat{\sigma}}{\sqrt{n}} \quad (4.2a)$$

and

$$e = t_{(0.95, df=n-1)} \frac{\hat{\sigma}}{\sqrt{n}} \quad (4.2b)$$

where  $t$  is the critical value that corresponds to the 95<sup>th</sup> percentile on the student-t distribution with  $n-1$  degrees of freedom, and  $e$  is the limit of error that is defined as half of the confidence interval. If  $n$  is sufficiently large, the critical value,  $t_{(0.95, df=n-1)}$ , is approximately 1.7, therefore Equation 4.2b can be re-written in terms of  $s$  as

$$e = 1.7 \frac{s}{\sqrt{n}} \quad (4.2c)$$

The goal is to determine the minimum number of replicates required to achieve the 90% CL and a limit of error of 5%. Therefore, Equation 4.2c is re-written in the following form to solve for  $n$  in terms of

a limit of error that is normalized with respect to the sample mean,  $\bar{x}$ , such that  $e$  is expressed as a percentage,

$$n = \left(1.7 \frac{s}{\bar{x}}\right)^2 \quad (4.2d)$$

and, the normalized standard deviation with respect to the sample mean is known as the coefficient of variation ( $CV$ )

$$CV = \frac{s}{\bar{x}} \quad (4.2e)$$

Substituting  $CV$  in Equation 4.2d gives the following final form of the statistical equation that is routinely used to determine the minimum number of replicates required for a 90% CL

$$n = \left(1.7 \frac{CV}{e}\right)^2 \quad (4.3)$$

where  $CV$  is the coefficient of variation (%) on a material property, and  $e$  is the limit of error (%) desired, typically taken as 0.5 (1 – CL).

The number of replicates required to achieve a CL that is different from 90% can be calculated using the  $t$  critical value which corresponds to the desired CL and degrees of freedom. For example, a 95% CL with 40 degrees of freedom would be calculated using a critical value of approximately 2.0, and a 99% CL would be calculated using a critical value of 2.7.

Material test data from the manufacturer were used to determine the  $CV$  (Equation 4.2e) of the material for various types of behavior – pure tension, open hole tension, and bolt bearing. The material test data available for the FRP used in this study included the mean value for each set of material tests and the design value, which is published as three standard deviations below the mean in accordance with ACI 440.2R (2008). Therefore, the standard deviation for each test was determined as:

$$s_{test} = \frac{mean\ value - design\ value}{3} \quad (4.4)$$

where  $s_{test}$  is the material standard deviation for the given test, *mean value* is the mean test value for a given condition (i.e. mean tensile strength based on a sample size of 20 replicates), and *design value* is the published material design value for a given condition (i.e. design tensile strength).

Equation 4.3 was used to determine the number of replicates needed for each test condition conducted in this study. The material test data provided by the manufacturer is shown in Table 4.3 and the resulting number of replicates required to achieve the 90% CL, with various limits of error, is presented in Table 4.4. Each material test result provided by the manufacturer is based on a sample size of 20, which is sufficiently large to use a student-t distribution to determine the number of replicates needed for each condition tested in the study.

**Table 4.3:** Data Provided by the Manufacturer (adapted from Strongwell, 2016).

Property	No. of Replicates	Mean Value (MPa)	Design Value (MPa)	ASTM
Tensile Strength	20	852	640	D638
Open Hole Strength	20	652	543	D5766
Unclamped Bearing Strength	20	214	180	D5961

**Table 4.4:** Calculated Data and Sample Size for 90% CL.

Property	$s^1$ (MPa)	$CV^2$	No. of Replicates for 90% Confidence Level <sup>3</sup>				
			e	2.5%	5.0%	7.5%	10.0%
Tensile Strength	70.7	8.29%	n	32	8	4	2
Open Hole Strength	36.3	5.57%	n	15	4	2	1
Unclamped Bearing Strength	11.3	5.30%	n	13	4	2	1

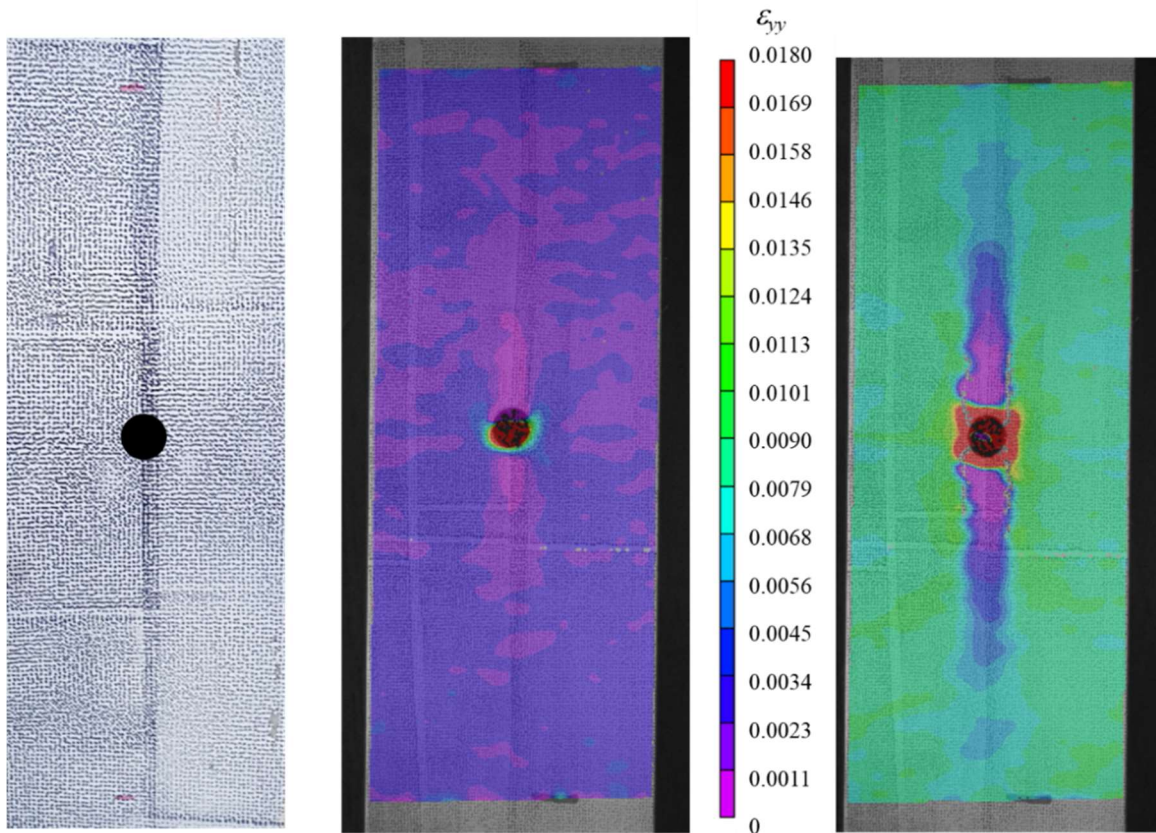
Notes: 1) Calculated using Equation 4.4; 2) Calculated using relationship between Equation 4.2d and Equation 4.3; 3) Calculated using Equation 4.3

The minimum number of replicates for the pure tension tests (no hole condition) in this study is 8 and the minimum number of replicates for tension tests using open hole, unclamped single-bolt bearing, and unclamped multi-bolt bearing conditions is 4 for each condition, all of which correspond to the 90% CL with a 5% limit of error (Table 4.4). In some tests a greater number of replicates (Table 4.2) was used and therefore the actual CL for each test will be discussed later.

### **Instrumentation**

Digital Image Correlation (DIC) techniques are used in this study to develop a continuous strain map over the entire specimen during testing. A detailed description and discussion of DIC is provided by Xie and Kang (2015). The accuracy of DIC compared to conventional strain gauge measurements is a

common topic in the literature with the general understanding that when the system is properly calibrated, the accuracy of strain measurement using DIC is equal to foil strain gauge measurements (Hoult et al., 2013; and Bomarito et al., 2017). The benefits of DIC include the ability to visualize strain (longitudinal, transverse, and shear) over the entire surface of a specimen (Figures 4.4b and 4.4c) rather than only at the location of an applied strain gauge, and the ability to measure strain well beyond the point at which typical strain gauges debond from the surface of the test specimen.



(a) 0.33 mm speckle pattern (b)  $\epsilon_{yy}$  at low strain levels (c)  $\epsilon_{yy}$  after longitudinal shear failure  
**Figure 4.4:** Example DIC strain field and specimen speckle pattern.

DIC uses a series of photos taken of the material surface during testing to measure the relative distance between speckles which are applied to the material before testing. The speckle pattern in this study was applied to each test specimen using an ink roller with a non-uniform pattern and 0.33 mm dot size (Figure 4.4a) which was calibrated to the camera resolution and field of view used during the test. This calibration ensures the accuracy of the commercial DIC system used in this study to within 10 micro-strain and is consistent with the calibration requirements discussed by Hoult et al. (2013) and

Bomarito et al. (2017). The contrast between the specimen and the speckle pattern was achieved by painting the material surface with white spray paint before applying the black ink speckle pattern.

### ***Tension test treatments and specimen preparation***

A universal testing machine (UTM) with an 890 kN +/- 0.25% capacity load cell was used to conduct a series of tension tests using nine different hole patterns – no holes, single hole, 4 holes aligned in two columns, 4 holes staggered, single-bolt bearing, and multi-bolt bearing. All holes had a 14.2 mm nominal diameter to accommodate a 12.7 mm diameter fastener. Statistical analysis of the results presented later in this chapter refers to each test variation as a treatment to be consistent with terminology used in statistical modeling. For each 4-hole treatment, two transverse spacing distances were examined, and for the single-bolt bearing pattern, two edge distances, bearing on threads, and excluding threads were examined. The variations of each pattern created a total of 14 treatment groups. Figure 4.5a shows the no-hole, open-holes, and single-bolt bearing test treatment configurations, and Figure 4.5b shows the multi-bolt treatment configurations. The corresponding specimen identification referenced in the test matrix (Table 4.2) is also shown for each treatment in Figures 4.5a and 4.5b. The results of the statistical analysis for the open-hole treatment groups (discussed in detail later in this chapter) indicates that there is no statistically significant difference between the staggered and aligned hole patterns, and between the 38 mm and 50 mm transverse spacing hole patterns. Therefore, the 38 mm aligned hole patterns were the only patterns used for the multi-bolt treatment conditions shown in Figure 4.5b. Each tension test treatment contains at least the minimum number of replicates to achieve the 90% CL as discussed earlier. The American Society for Testing and Materials (ASTM) standards which apply to each test are also noted in Table 4.3.

Each specimen was cut from one of three rolls of FRP material using a standard water-cooled saw. An equal number of specimens from each roll was taken for each treatment group to ensure variation between rolls was reflected in each sample set. Prior to painting and applying the DIC speckle pattern, 14.2 mm diameter holes were drilled in the samples using a tungsten carbide hole saw per the dimensions in Figure 4.5, and measurements were taken to record the actual thickness, width, and hole diameter for each individual specimen.

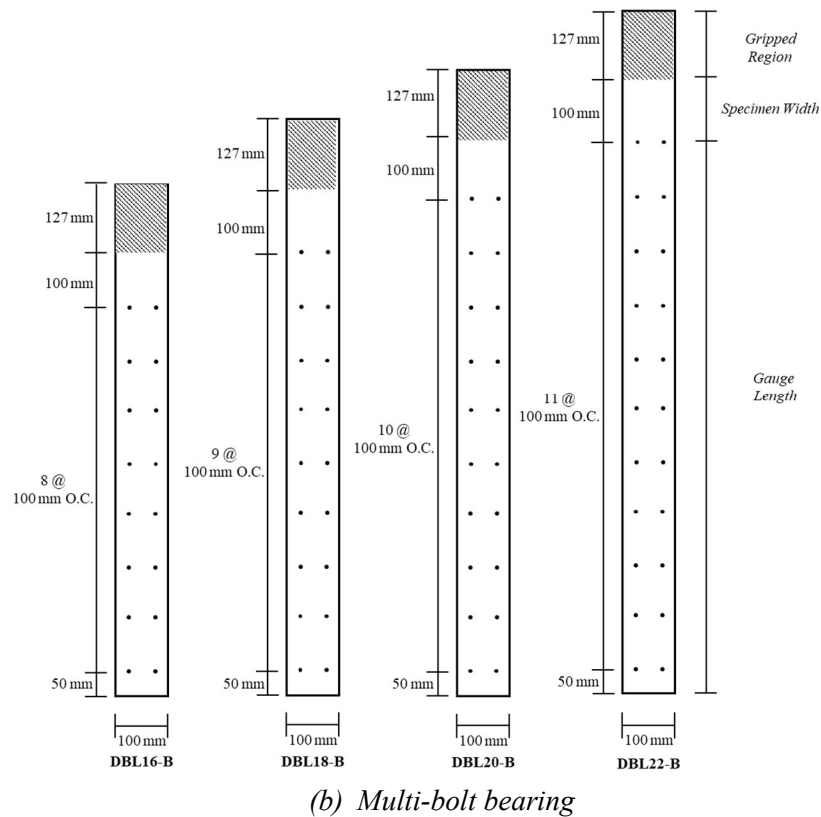
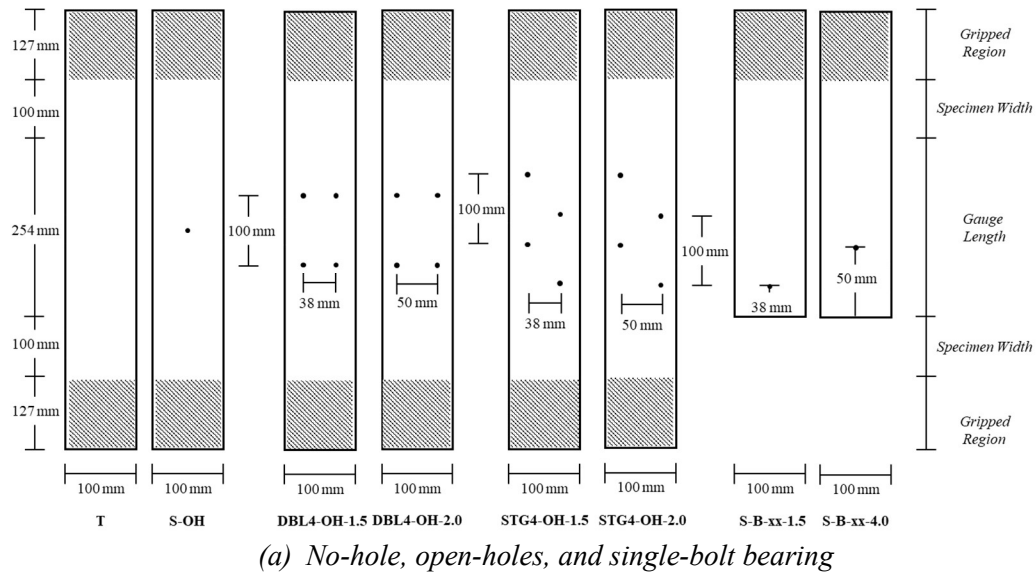


**Figure 4.5:** Test treatment configurations and specimen identification.

### *Universal Testing Machine tension test set-up*

Tensile forces developed in the UTM were transferred to the test specimen through 127 mm by 127 mm knurled, steel wedge grips. Care was taken to ensure each specimen was plumb with the axis of the

UTM to minimize eccentric load effects. Pilot tests were also conducted to determine if the wedge grips of the UTM required alignment, or if tabs needed to be bonded to the FRP material to properly grip each specimen such that rupture in the FRP occurred before slipping at the grips. It was determined that the wedge grips alone were sufficient to develop rupture in the FRP without slipping between the steel grips and the FRP plate, and no local rupture occurred at the grips. An example test set-up with the FRP specimen gripped in the UTM is shown in Figure 4.6a. The UTM setup shown in Figure 4.6a was used for the no-hole and open-hole treatment conditions. Figure 4.6b shows an example of a failed specimen in the no-hole treatment condition.



**Figure 4.6:** UTM setup (no-hole and open-holes) and failed specimen.

Tension tests without holes (specimens T-1 through T-8) were conducted in accordance with ASTM D3039 (2014). Tests with open holes were conducted in general accordance with ASTM D5766 (2014); however,  $w/D$  was adjusted to accommodate a 12.7 mm diameter bolt and multiple hole configurations. Each test specimen had a nominal thickness of 3.175 mm and nominal width of 100 mm. Actual thickness and width were recorded for each specimen prior to testing. Total specimen length (Figure 4.5a) was determined using a 254 mm gauge length, plus 200 mm (2 x plate width), plus 254 mm (127 mm for each grip), as specified in ASTM D3039 (2014). Each specimen was loaded at a constant displacement rate of 1.27 mm/min., and load-displacement data were recorded at a frequency of 1 Hz, in addition to the DIC

strain data for each test. Tests were conducted until rupture, and each failure mode was recorded in accordance with ASTM D3039 (2014) failure codes.

Single-bolt bearing tests were conducted in general accordance with ASTM D5961 (2017) using two edge distances, 38 mm (3 x bolt diameter to be in strict accordance with ASTM D5961) and 100 mm edge distance (corresponding to the longitudinal spacing in the open-hole and multi-bolt treatment conditions). Additionally, tests were conducted to examine the effects of bearing on threads (threads included) and on the bolt shank (threads excluded), as shown in Table 4.2.

A steel plate with an offset in the grip region was designed for the test to ensure the centerline of the FRP test specimen coincided with the centerline of the UTM axial load (Figure 4.7). The plate was also sized to accommodate multiple bolt patterns. Bolts were tightened to 3.4 kN-mm, corresponding to a field specification of “finger tight plus ¼ turn”, for all tests so as not to create a slip-critical connection between the FRP and steel plate. The test was designed as an idealization of the bolted connection, the goal of which was to achieve the maximum capacity of the FRP plate with holes. The steel plate is used in place of the concrete substrate to which the MF-FRP will typically be attached; therefore, concrete failure modes, which can be analyzed using traditional design techniques, are not considered in this test.

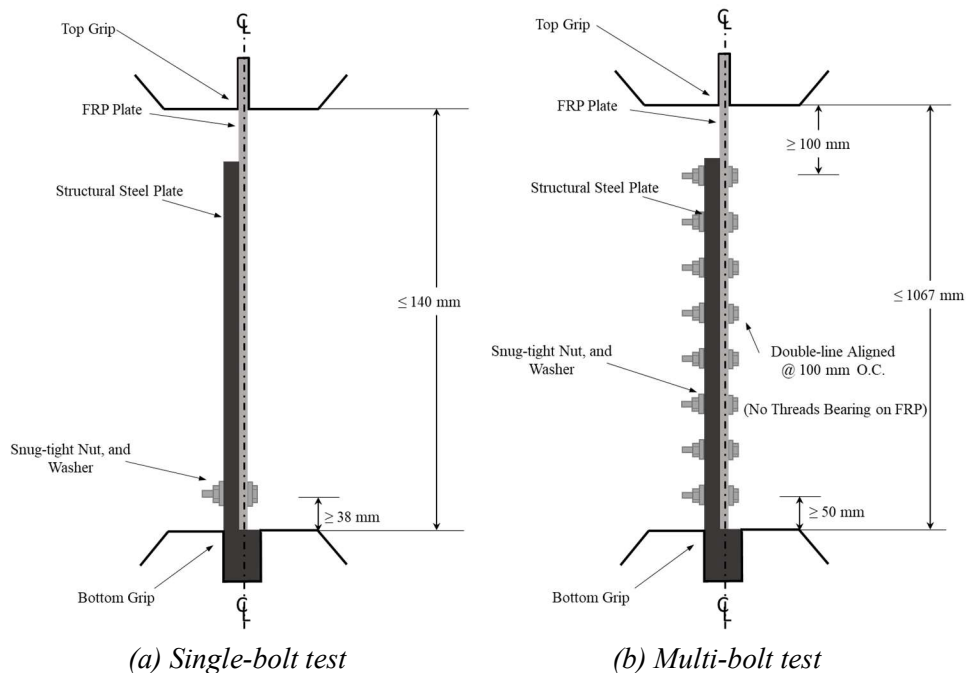


**Figure 4.7:** Bolted connection test schematic.

## Results and Discussion

Summary results for all tests are presented in Table 4.5. Mean peak load was determined directly from available load data and mean peak stress was calculated using the peak load and either a) net cross-sectional area of the test specimen for no-hole and open-hole treatment groups, or b) bolt bearing area, calculated in accordance with ASTM D5961 (2017) for single-bolt and multi-bolt treatment groups. Individual measurements for specimen width, thickness, and hole diameter were taken for each test specimen using a digital caliper (0.025 mm precision). The mean values, standard deviations, and coefficients of variation for these measurements are recorded in Table 4.6. The mean measurement values were used for calculating stress levels for all multi-bolt treatment groups.

**Table 4.5:** Test results summary.

Specimen ID	No. of Replicates	Mean Peak Load (kN)	Mean Peak Stress <sup>2</sup> (MPa)	Sample Peak Stress Standard Deviation (MPa)	Sample Peak Stress <i>CV</i> (%)	CL based on Sample <i>CV</i> (%)	Pop. Peak Stress (MPa)	Pop. Peak Stress <i>CV</i> (%)	CL based on Pop. <i>CV</i> (%)
T	8	340	1010	40.4	3.99	99	852	8.28	90
S-OH	6	296	1040	42.2	4.06	96	652 <sup>2</sup>	5.56	97
DBL4-OH-1.5	6	229	944	30.0	3.18	97	NA	5.56 <sup>1</sup>	97
DBL4-OH-2.0	6	233	909	44.5	4.89	95	NA	5.56 <sup>1</sup>	97
STG4-OH-1.5	5	234	958	15.6	1.63	99	NA	5.56 <sup>1</sup>	93
STG4-OH-2.0	5	228	937	12.6	1.35	99	NA	5.56 <sup>1</sup>	93
S-B-X-1.5	6	13	315	14.9	4.75	95	214	5.37	92
S-B-N-1.5	6	14	324	18.5	5.72	91	NA	5.37 <sup>3</sup>	92
S-B-X-4.0	6	15	349	20.1	5.77	90	NA	5.37 <sup>3</sup>	92
S-B-N-4.0	6	16	385	26.7	6.94	86	NA	5.37 <sup>3</sup>	92
DBL16-B-1.5	6	189	275	7.99	2.91	99	NA	5.37 <sup>3</sup>	92
DBL18-B-1.5	6	202	262	5.10	1.95	99	NA	5.37 <sup>3</sup>	92
DBL20-B-1.5	6	201	234	8.41	3.60	99	NA	5.37 <sup>3</sup>	92
DBL22-B-1.5	6	206	221	3.28	1.48	99	NA	5.37 <sup>3</sup>	92

Notes: 1) Multiple hole Population *CV* values are assumed to follow single hole testing values; 2) ASTM D5766 stress calculation uses gross cross-sectional area, sample peak stress is calculated using net cross-sectional area; 3) All single bolt and multi-bolt population *CV* values are assumed to follow S-B-X-1.5 value for population.

**Table 4.6:** Mean Specimen Measurements.

Specimen Dimension	No. of Measurements	Mean Value (mm)	Sample $s$ (mm)	Sample $CV$ (%)
Width	205	101	0.0962	0.0951
Thickness	207	3.33	0.0525	1.57
Hole Diameter	138	14.1	0.270	1.92

Sample peak stress standard deviations were recorded for each sample set and used to determine the peak stress coefficient of variation within each sample set (Table 4.5). Equation 4.5 was used to calculate the confidence limit for sample sets and the population (defined as the manufacturer provided data):

$$t_{(0.95, df=n-1)} = \frac{e\sqrt{n}}{CV} \quad (4.5)$$

The lowest CL based on population (manufacturer) data was 90% for the no-hole (T) treatment condition; however, all other treatment condition tests resulted in higher CL because of the lower  $CV$  with respect to the number of specimens tested for each treatment group. All multi-bolt treatment conditions obtained results at the 92% CL.

#### ***No hole treatment condition***

A total of eight (8) individual replicates were tested in the no-hole (T) condition (Table 4.2). The material  $CV$  for pure tension is 8.28% (considered the population  $CV$  for this study) per the manufacturer's available data presented in Table 4.3. Therefore, using Equation 4.3, a 90% CL with a 5% limit of error is achieved with a sample size of 8. The mean peak load for the 8 tests was 340 kN, and the mean peak stress for the sample set was 1010 MPa with a sample  $CV$  of 3.99% based on recorded peak loads. The manufacturer data provides a mean peak stress of 852 MPa (Table 4.3) – 18.9% lower than the peak stress from the sample set. This difference is more than double the population  $CV$  value, indicating a significant discrepancy between the sample set tested in this study and the manufacturer's data. It is difficult to determine the source of this difference with certainty, but it is likely due to differences in testing procedures and specimen preparation. The manufacturer's tests were conducted using ASTM D638 (2014), a specification for testing plastic polymers, whereas the standard applied to the tension tests conducted in this study is ASTM D3039 (2014), a specification for testing polymer matrix composite

materials such as the FRP used in the study. The main difference between ASTM D638 (2014) and ASTM D3039 (2014) is the use of specimens with reduced cross-sections in ASTM D638 (2014). This reduced cross-section testing is believed to be the probable source of the mean peak stress and  $CV$  differences. A reduced cross-section for the non-homogeneous FRP plate tested in this study would produce variable results highly dependent upon the longitudinal carbon fibers remaining after the cross-section was cut down in each specimen. It is worth noting the 3.99%  $CV$  yields an actual CL = 99% with  $n = 8$  (Table 4.5), assuming the  $CV$  is representative of the true population  $CV$ . However, without further testing with a greater number of replicates to determine the true population  $CV$  for the FRP material in tension, the assumed population  $CV$  of 8.28% is sufficient to report a mean peak load at the 90% CL. The observed mode of failure for all tests was explosive rupture located near the middle of the gage length (XGM per ASTM D3039, 2014). A photograph of the representative failure mode is shown in Figure 4.6b.

### ***Open-hole treatment conditions***

#### *Single-hole condition*

Six (6) total specimens were tested in the single open-hole condition providing a 97% CL with 5% limit of error (Table 4.5) based on the  $CV$  determined from the manufacturer testing (Table 4.4). The test procedure for this study was adapted from ASTM D5766 (2014) which, as previously described, specifies a  $w/D$  equal to 6. The desired  $w/D$  ratio in this study is 7.1 to incorporate the 14.2 mm hole diameter necessary for a 12.7 mm diameter fastener. Further, the stress calculation using ASTM D5766 (2014) uses the gross cross-sectional area of the test specimen whereas the stress calculation in this study uses the net cross-sectional area. The mean peak load for the single-hole test condition was 296 kN and the mean peak stress using the net cross-sectional area was 1041 MPa. The mean peak stress reported by the manufacturer using  $w/D = 6$  and the gross cross-sectional area is 652 MPa. The calculated mean peak stress using the manufacturer test data and the net cross-sectional area based on  $w/D = 6$  is 786 MPa. The net cross-sectional area mean peak stress for the sample set in this study (1041 MPa) and net cross-sectional area mean peak stress using the manufacturer test data (786 MPa) differs by 32.4% of the

manufacturer mean peak stress using the net cross-sectional area. This difference is likely due to the non-homogeneity of the material and to the exact amount of longitudinal carbon fiber included in the net cross-section for each test specimen – carbon fiber lost from the cross-section due to drilling holes would result in a lower peak stress as compared to the gross section results.

The DIC shear strain results show the development of a disturbed region approximately 50 mm above and below the hole just before a longitudinal shear failure in the glass fibers begins (Figure 4.8a). Therefore, the longitudinal spacing between holes for multiple hole test conditions was selected to be 100 mm (Figure 4.5) to minimize interaction between disturbed regions developing at adjacent holes. Longitudinal shear failure of the glass fibers results in shear splitting which propagates and joins from the holes until ultimate failure occurs with complete shear failure of glass fibers along the length of the test specimen.

#### *Aligned and staggered hole conditions*

Two (2) transverse spacing distances were tested for each of the aligned (DBL4) and staggered (STG4) hole spacing conditions: 38 mm and 50 mm (shown in Figure 4.5a). The mean peak stress for each of the four treatments is 910 MPa, 945 MPa, 958 MPa, and 938 MPa for DBL4-OH-1.5, DBL4-OH-2.0, STG4-OH-1.5, and STG4-OH-2.0, respectively (Table 4.5). Six replicates were tested for each of the 4 treatments; however, one of the STG4 replicates slipped in the UTM wedge grips during testing, creating an extreme outlier result. Therefore, for the STG4 treatment group, only 5 tests were considered in the analysis of the results to eliminate the effects of the slip that occurred during one test.

A Multi-Factor Analysis of Variance (ANOVA) test was conducted to determine if there is a statistically significant difference between the DBL4, STG4, 38 mm and 50 mm treatments. The following null ( $H_0$ ) and alternate ( $H_a$ ) hypotheses were tested:

$$H_{0A}: \alpha_1 = \alpha_2 = 0 \text{ and } H_{0B}: \beta_1 = \beta_2 = 0 \quad (4.6a)$$

and

$$H_{aA}: \text{at least one } \alpha_i \neq 0 \text{ and } H_{aB}: \text{at least one } \beta_i \neq 0 \quad (4.6b)$$

where  $\alpha_i$  is the effect of the hole pattern treatment (DBL4 or STG4) on the mean peak load and  $\beta_i$  is the effect of the transverse spacing treatment on the mean peak load.

The results of the multi-factor ANOVA are shown in Table 4.7. When tested at the 90% CL ( $\alpha = 0.1$ ), the P-value for  $\alpha_i$  is 0.443 and the P-value for  $\beta_i$  is 0.855 (both are greater than  $\alpha$ ); therefore, there is a failure to reject both null hypotheses. This failure to reject both null hypotheses indicates no statistically significant difference exists on the mean peak load for each test (at the 90% CL) due to the effects of both the hole pattern (DBL4 or STG4) and the transverse spacing (38 mm or 50 mm).

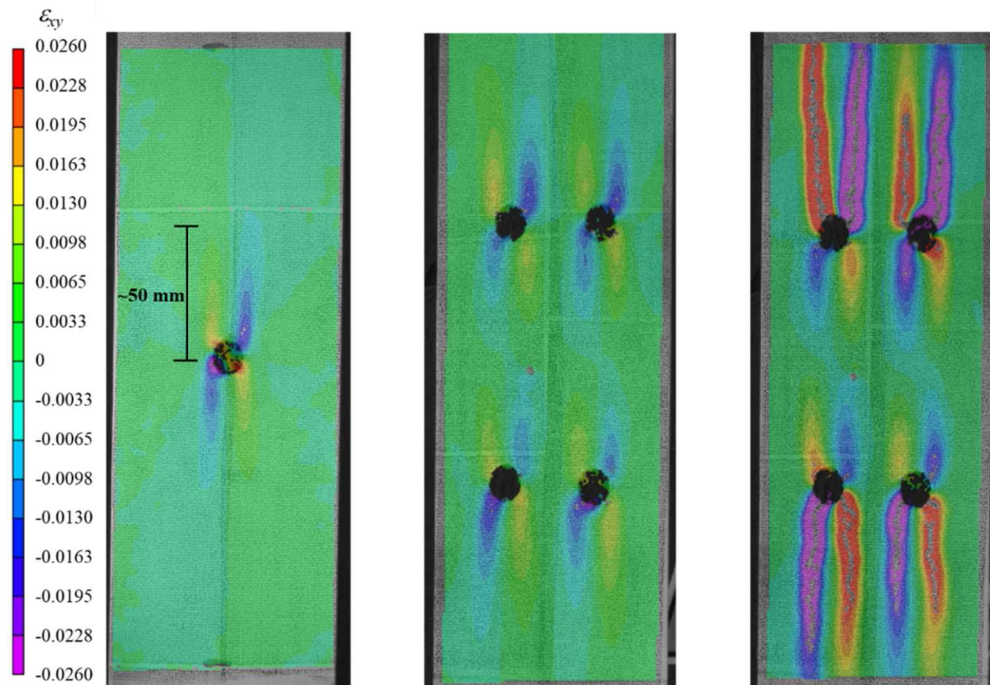
**Table 4.7:** Multi-factor ANOVA results.

<i>Source of Variation</i>	<i>SS</i>	<i>df</i>	<i>MS</i>	<i>F</i>	<i>P-value</i>	<i>F critical</i>
Hole Pattern	22.532	10	2.253	1.097	0.443	2.978
Transverse Spacing	0.072	1	0.072	0.035	0.855	4.965
Error	20.534	10	2.053			
Total	43.137	21				

The results of the ANOVA are consistent with the manner in which the FRP test specimens carry load in the pure tension tests. The tensile forces are carried in the longitudinal carbon fibers of the FRP plate, and the staggered nature of the STG4 treatment does not change the manner in which the longitudinal fibers carry load that is applied in the same direction as the carbon fibers. For the same reason, the transverse spacing between the holes does not affect the capacity of FRP plate in axial tension. The lack of statistical significance between the DBL4 and STG4 treatments provides critical information regarding the behavior of the FRP material tested in this study, which is not examined in the available literature. This finding enables the remainder of this study to focus on a single transverse spacing and single hole pattern; therefore, only 38 mm transverse spacing and aligned (DBL) hole pattern are examined in all multi-bolt treatment conditions.

Figure 4.8 shows the DIC shear strain results for both the S-OH (Figure 4.8a) and the DBL4-OH-1.5 (Figures 4.8b and 4.8c) test treatments. Figures 4.8a and 4.8b illustrate the disturbed regions above and below the holes just prior to initial longitudinal shear splitting (approximately 170 kN). Figure 4.8c

illustrates the shear strain at failure (approximately 230 kN). The 100 mm longitudinal spacing between holes is shown to be sufficient to minimize the interaction of shear strain between each hole.



(a) *S-OH pre-splitting* (b) *DBL4-OH pre-splitting* (c) *DBL4-OH at failure*

**Figure 4.8:** Shear strain map of disturbed regions and shear failure.

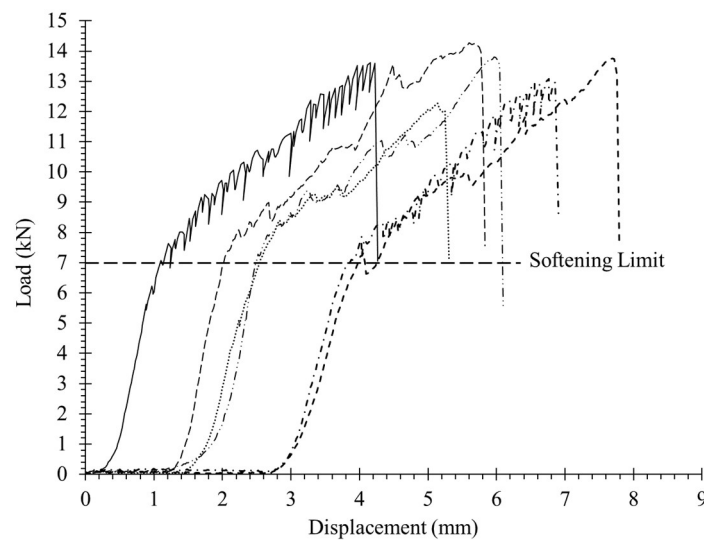
### ***Bolt bearing treatment conditions***

#### *Single-bolt bearing*

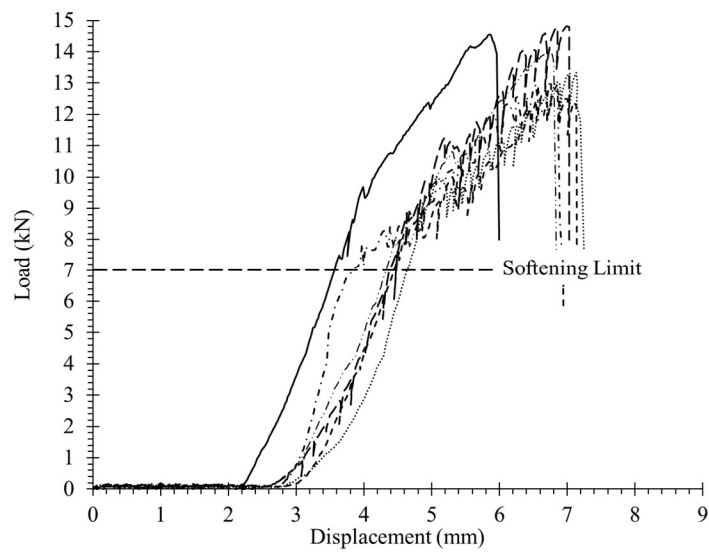
Six (6) tests were conducted for each of the single bolt bearing test treatment conditions (Table 4.2). The difference between the mean peak load for each of the 38 mm edge distance treatment groups (“N” and “X”) is just 3.3% of the total force (Table 4.5). However, there is greater variability in the treatment group excluding threads, which is quantified in the higher standard deviation and lower statistical significance as compared to the treatment group including threads (Table 4.5). Figure 4.9 shows the load-displacement curves for the 38 mm edge distance treatment group with bearing excluding threads (Figure 4.9a) and with bearing including threads (Figure 4.9b). Single factor ANOVA testing confirmed that there is no statistically significant difference between the N and X treatment conditions at the 90% CL.

There are differences, however, between the two treatment groups that are visualized in Figure 4.9. The treatment bearing on threads has a less defined softening region after 7 kN of applied load as

compared to the group bearing with threads excluded. There is also greater variability between the tests for the treatment bearing on threads. This difference is likely due to rotation of the bolt relative to the FRP, which was observed when bearing included threads, but not observed in the condition which excluded threads. This difference is not captured with the ANOVA test because the ANOVA uses only the peak load value to compare the two treatments. All tests were stopped after longitudinal shear failure, which is marked by a severe decrease in load at the end of each load-displacement curve shown in Figure 4.9.



(a) Bearing excluding threads (*S-B-X series*)

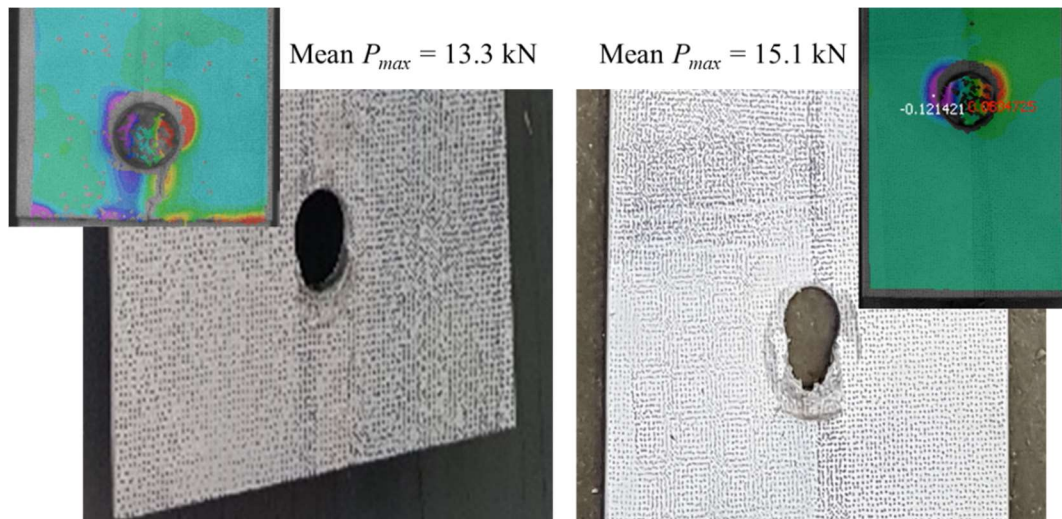


(b) Bearing including threads (*S-B-N series*)

**Figure 4.9:** Load-displacement curves for single-bolt tests with 38 mm edge distance.

Every test experienced some level of slip before the applied load started to increase, as visualized in the initial displacement under minimal load in Figures 4.9a and 4.9b. The maximum theoretical slip possible for the single bolt test is equal to the twice the difference between the hole diameter and bolt diameter. This produces a possible slip range between 0 and 3 mm, due to the 14.3 mm holes in the FRP and steel plates relative to the 12.7 mm diameter bolts.

The 100 mm edge distance treatment group resulted in a mean peak load of 15.1 kN, which is 13.5% higher mean peak load than the 38 mm edge distance mean peak load of 13.3 kN (Table 4.5 and Figure 4.10). However, the behavior during loading for the two treatments was similar with initial softening due to bearing of the bolts against the FRP occurring at approximately 7 kN (Figure 4.9). The lesser peak loads and stresses in the 38 mm edge distance treatment group is due to longitudinal shear failure (shown in the Figure 4.10a DIC inset) that occurred in the 38 mm edge distance group, but not in the 100 mm edge distance treatment group. This shear failure was the primary source of failure in the 38 mm group, whereas failure in the 100 mm edge distance group was a pure bearing failure (Figure 4.10b), resulting in greater displacement at peak load values. Both DIC insets in Figure 4.10 are captured at peak load, which occurred just prior to shear failure in the 38 mm edge distance group and bearing failure in the 100 mm edge distance group.



(a) *S-B-X-1.5 bearing and shear failure*    (b) *S-B-X-4.0 bearing failure*

**Figure 4.10:** Single-bolt bearing failure modes with DIC inset showing shear strain.

As noted in Table 4.5, the sample  $CV$  for both single bolt treatment groups is higher than the other treatment groups examined in this study ranging from 4.75% to 6.94%. This is likely due to the effect of the UTM load cell accuracy when failure load are small relative the error range. However, the increased coefficients of variation for the two single bolt sample sets are sufficient to present the mean results at the 90% CL, with the exception of the S-B-N treatment group which satisfies an 86% CL. The consistency of the single bolt results and the ANOVA results for the two treatment groups are sufficient for the purposes of this investigation; therefore, further investigation of the single bolt  $CV$  range, or the accuracy of the UTM load cell at lower loads is not discussed.

The results of the four single-bolt bearing treatment groups confirm that a 100 mm longitudinal spacing between bolts is sufficient to avoid interaction between the disturbed regions that develop at each bolt, as shown in Figure 4.8. Further, the single-bolt bearing results allow for an initial calculation to be made for the total number of 12.7 mm diameter bolts needed to stay below the softening limit of 7 kN/bolt (Figure 4.9), and below the maximum capacity of 15 kN/bolt (Table 4.5). Assuming all bolts are equally engaged at the softening limit, Equation 4.7 can be used to calculate the number of bolts needed to stay below the softening limit:

$$T_p = n_b F_{b,s} \quad (4.7)$$

where  $n_b$  is the number of bolts,  $T_p$  is the tension force in plate (kN), and  $F_{b,s}$  is the force limit before initial softening (kN/bolt). A maximum value of  $F_{b,s} = 7.0$  kN per bolt was selected to ensure the FRP plate remains in the initial, pre-softening region of the load-displacement curve. The prestress force range (after initial losses) for a typical 11 mm diameter steel prestressing strand is between 80 kN and 98 kN according to NCDOT structural plans for typical C-channel and hollow core sections. Using a maximum live load according to NCDOT vehicle loading configurations (NCDOT, 2018), 32 kN is a conservative estimate for the force increase in the FRP plate applied to a typical candidate hollow core cross-section. The 32 kN estimate assumes full-interaction between the concrete and FRP, which other studies have shown to overestimate the FRP strain by as much as 39% (Lee et al., 2009) for non-prestressed MF-FRP

using powder actuated fasteners. However, for initial calculations in this investigation, this conservative estimate is sufficient. Using the 32 kN force increase and the 98 kN prestress force, the estimated maximum value for  $T_p$  at service load conditions is 130 kN (target prestress force plus projected live load for the retrofit solution). Using Equation 4.7,  $n_b = 18.5$ ; therefore, the projected minimum number of bolts needed to remain in the pre-softening region at service load is 20 (after rounding up to the nearest even number of bolts). Additionally, Equation 4.8 can be used to calculate the number of bolts needed to stay below the maximum capacity:

$$T_o = n_b F_{b,u} \quad (4.8)$$

where  $T_o$  is the open-hole capacity (kN), and  $F_{b,u}$  is the maximum capacity per bolt (kN/bolt). Using  $F_{b,u} = 15$  kN per bolt, the minimum number of bolt needed to stay below  $T_o = 231$  kN (mean capacity for all open-hole treatment groups in Table 4.5) is  $n_b = 15.4$ ; therefore, a minimum of 16 bolts are projected to achieve the open-hole capacity of the plate assuming all 16 bolts are engaged equally throughout the loading of the connection.

#### *Multi-bolt bearing*

Based on the single-bolt bearing results, and initial calculations using Equations 4.7 and 4.8, multi-bolt tests were conducted using 16-, 18-, 20-, and 22-bolt, 2-lines, aligned with 38 mm transverse spacing (DBLxx-B-1.5) configurations shown in Figure 4.5b. These four treatment groups were selected to provide multiple connection configurations at or near the 20- and 16-bolt results from Equations 4.7 and 4.8, respectively. Six tests for each treatment were conducted in accordance with Table 4.2. The mean peak loads were 189, 202, 200, and 206 kN for the DBL16, DBL18, DBL20 and DBL22 treatments, respectively (Table 4.5). The calculated mean bolt bearing stresses for each treatment are 275, 262, 234, and 221 MPa, respectively (Table 4.5). A single factor ANOVA test (Table 4.8) determined at least one of the four treatment conditions (DBL16, DBL18, DBL20, DBL22) is statistically different at the 90% CL (P-value =  $6.89 \times 10^{-5} \ll \alpha = 0.1$ ) when using peak load as a measure. Therefore, a second ANOVA test (Table 4.9) was conducted to confirm that there is no statistically significant difference between the

DBL18, DBL20, and DBL22 treatments at the 90% CL ( $P\text{-value} = 0.168 > \alpha = 0.1$ ). While there is no statistically significant difference between the DBL18, DBL20, and DBL22 treatment groups at the 90% CL, a reduced confidence limit of 80% ( $\alpha = 0.2$ ) would result in a statistically significant difference for at least one of the treatment groups. However, 90% is the desired CL, and therefore, further ANOVA testing is not necessary for the purposes of understanding the ultimate capacities of the four treatment groups.

**Table 4.8:** Single Factor ANOVA Results (DBL16, DBL18, DBL20, DBL22).

<i>Source of Variation</i>	<i>SS</i>	<i>df</i>	<i>MS</i>	<i>F</i>	<i>P-value</i>	<i>F critical</i>
Between Groups (DBL16, DBL18, DBL20, DBL22)	50.098	3	16.69	12.777	$6.89 \times 10^{-5}$	2.380
Within Groups	26.14	20	1.307			
Total	76238	23				

**Table 4.9:** Single Factor ANOVA Results (DBL18, DBL20, DBL22).

<i>Source of Variation</i>	<i>SS</i>	<i>df</i>	<i>MS</i>	<i>F</i>	<i>P-value</i>	<i>F critical</i>
Between Groups (DBL18, DBL20, DBL22)	4.973	2	2.487	2.013	0.168	2.695
Within Groups	18.532	15	1.235			
Total	23.505	17				

Box plots (Figure 4.11) of the peak loads for the four treatments indicate a single statistical outlier for the DBL20 treatment (186 kN); however, the single outlier is within three standard deviations of the lower quartile – commonly referred to as a mild outlier (Devore, 2015). The presence of this mild outlier does not adversely affect the ANOVA results; therefore, no data were discarded in the analysis. Figure 4.11 also serves as a visual representation of the statistically significant difference with the DBL16 treatment peak load when compared to the DBL18, DBL20, and DBL22 treatment peak loads. The higher peak load and reduced variability of the DBL22 treatment group is the reason the ANOVA test results in Table 4.9 indicates a reduced CL would produce a statistically significant difference.

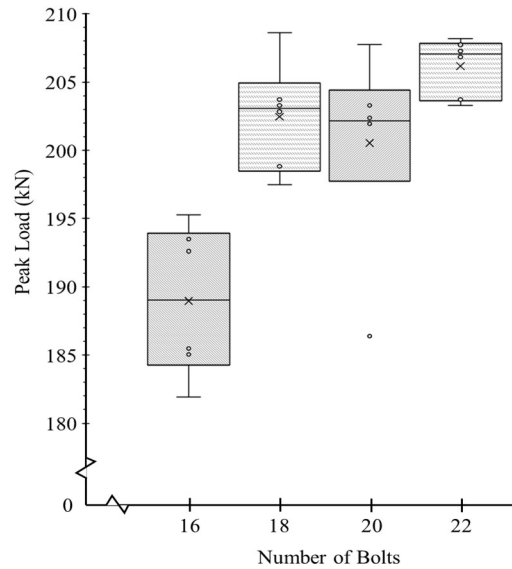


**Figure 4.11:** Box plots of multi-bolt peak load distributions.

The load-displacement curves for the four treatment conditions in Figure 4.12 were produced by performing a multi-parametric regression analysis of the set of curves for each treatment condition using RStudio®, a commercially available statistical software package. The load-displacement curves therefore represent the mean curve for each treatment group. Figure 4.12 shows that the load-displacement behavior for each of the four connections is similar. This indicates that although there is a statistically significant peak load difference between the DBL16 treatment, and the DBL18, DBL20 and DBL22 treatments, the behavior during loading up to ultimate failure for all four treatments is similar. The distinct softening region that is visible in single-bolt bearing (Figure 4.9) is not present in the multi-bolt behavior due to the effect of multiple bolts experiencing bearing throughout the test. The bolts do not experience initial bearing simultaneously, but rather progressively, such that bearing in the first several rows experience greater bearing than the last row of bolts in the connection. Each of the mean load-displacement curves is calculated using six test specimens, as previously discussed, and therefore, the curves are statistically significant at the 90% CL or greater. The upper bound curve shown in Figure 4.12 is the upper limit corresponding to the 90% CL for the population of treatments.

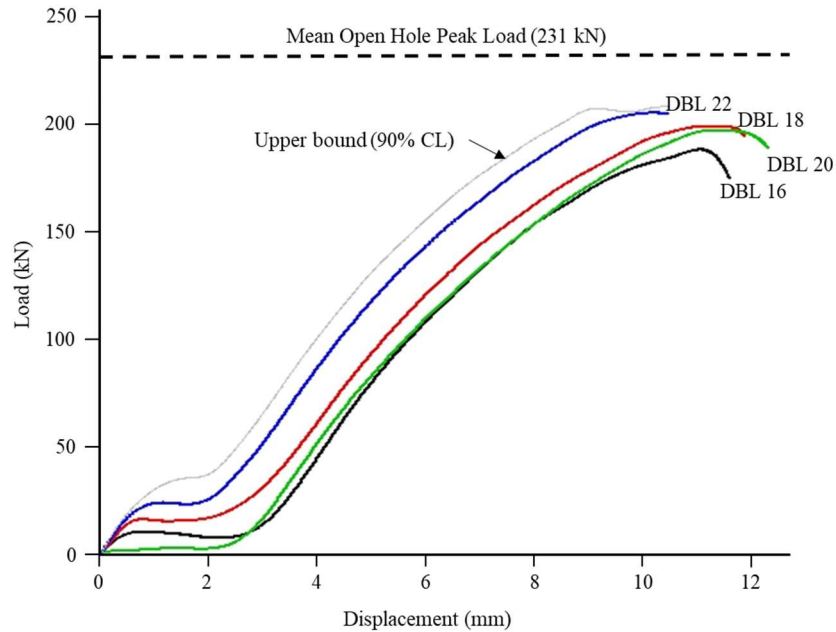


**Figure 4.12:** Mean multi-bolt load-displacement curves (DBL series).

The mean open-hole peak load (231 kN) in Figure 4.12 is the mean peak load for the open-hole treatment conditions, mean value for peak load of all DBL4 and STG4 results in Table 4.5. As previously discussed, this is the theoretical maximum load for the FRP material tested with holes, which was the peak load goal for the multi-bolt testing; however, under the current treatment conditions, the mean peak load for the DBL22 treatment is approximately 89% of the theoretical maximum. This difference in the theoretical maximum is due to shear lag effects which cause longitudinal shear failure to propagate in a progressive manner from the first row of bolts (top two holes for each specimen in Figure 4.13c), rather than uniform shear failure along the length of the specimen.

The longitudinal shear failure shown in Figures 4.13b and 4.13c is representative of the failure mode for every treatment group except the T and S-B-X-4.0 treatments which experienced rupture (Figure 4.13a) and bearing failure (Figure 4.10), respectively, and the multi-bolt treatment groups with fewer than 16 bolts which experienced bearing failure (Figure 4.13d). All open-hole (Figure 4.13b) and all multi-bolt (Figure 4.13c) treatments experienced longitudinal shear failure at the measured peak loads. Therefore, the mean peak load for each of these treatment groups are plotted in Figure 4.14 to show the variation in capacity and failure mode as a function of the bearing surface area, defined as

$$A_b = n_b d_{bolt} t_p \quad (4.9)$$

where  $A_b$  is the total bearing surface area,  $n_b$  is number of bolts,  $d_{bolt}$  is the diameter of the bolt and  $t_p$  is the thickness of the plate. The trendline shown in Figure 4.14 is established using the S-B-X-1.5 and the 16-, 18-, 20-, and 22-bolt treatment groups. Additional testing was then conducted using the supplementary test matrix in Table 4.10 to determine the validity of the trendline to predict mean peak loads for bolt patterns with less than 16 bolts. The mean peak loads for the 10-, 12-, and 14-bolt treatment groups are within 3.0% of the trendline, indicating the curve in Figure 4.14 is sufficient for predicting the capacity of a connection using 12.7 mm diameter bolts and 100 mm longitudinal spacing over the range of bolts from one to 22 at the 90% CL.

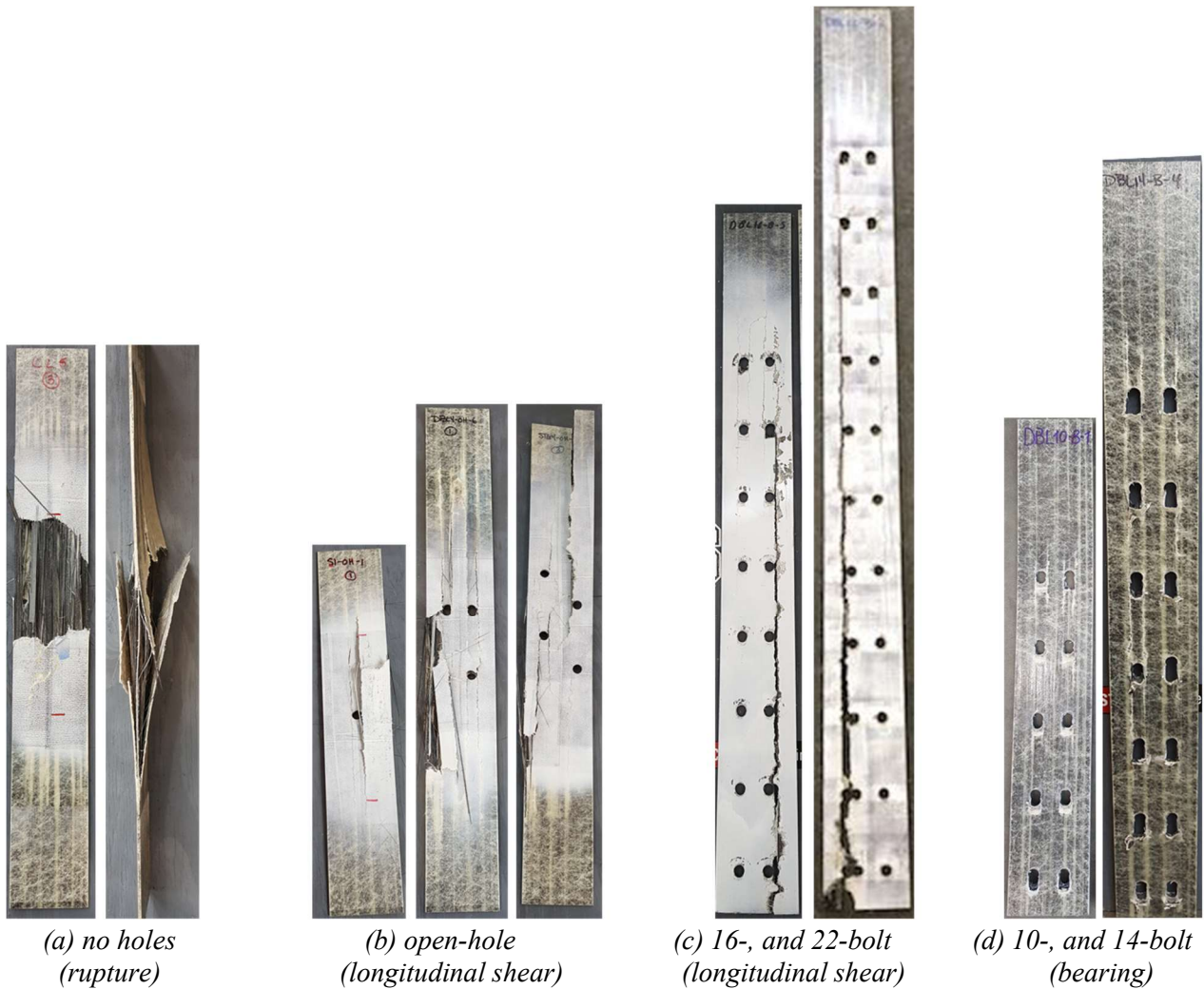


**Figure 4.13:** FRP failure modes.

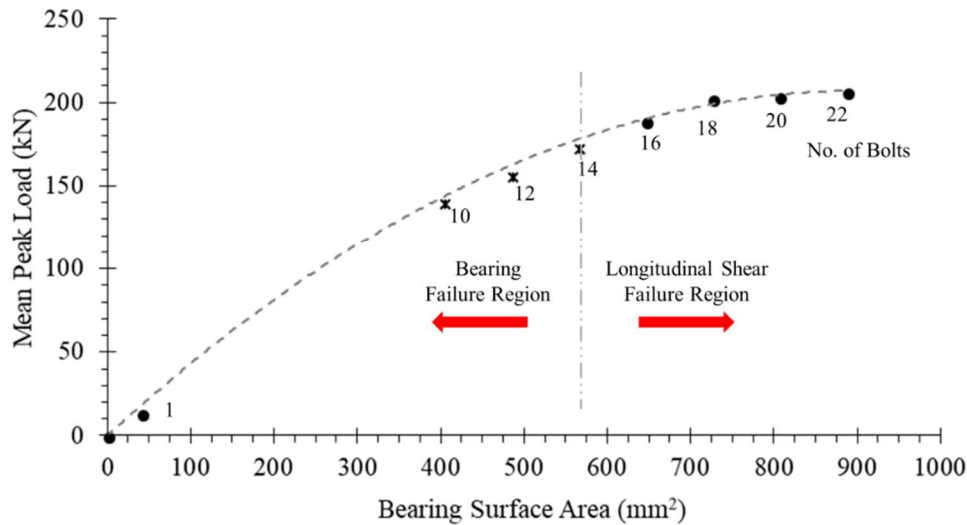


**Figure 4.14:** Variation of mean peak load and FRP failure modes.

**Table 4.10:** Supplementary Test Matrix.

Specimen ID	No. of Replicates	Treatment Description	ASTM
DBL10-B-1.5	1	10 bolts; 12.7 mm diameter; 2-by-2; 38 mm transverse spacing; 100 mm longitudinal spacing	NA
DBL12-B-1.5	1	12 bolts; 12.7 mm diameter; 2-by-2; 38 mm transverse spacing; 100 mm longitudinal spacing	NA
DBL14-B-1.5	1	14 bolts; 12.7 mm diameter; 2-by-2; 38 mm transverse spacing; 100 mm longitudinal spacing	NA

The 10-, 12-, and 14-bolt treatment groups produced a bearing failure (Figure 4.13d) rather than the longitudinal shear failure mode experienced in the 16-, 18-, 20-, and 22-bolt treatment groups. The threshold for this change in failure mode is shown with the vertical dashed line in Figure 4.14. It is necessary to understand the impacts of this critical finding to optimize the capacity of the bolt pattern such that a maximum capacity can be achieved, the theoretical maximum of which is the capacity of the plate with holes gripped and loaded in uniaxial tension (231 kN in Figure 4.12).

The results presented in this chapter indicate that a 22-bolt connection with 12.7 mm diameter bolts in a double-line aligned pattern (DBL22-B in Figure 4.5) is sufficient to develop 89% of the open-hole capacity of the FRP plate (Figure 4.12) and remain below the softening limit at service loads of 130 kN (prestress + live load). While connections with greater than 14-bolts produce a shear failure mode that is more brittle than the bearing failure experienced in connections with 14 or fewer bolts, the progressive

nature of the shear failure provides early warning of impending failure and the number of bolts ensure the connection remains in the pre-softening region at service load levels when applied to a typical hollow core bridge superstructure. Therefore, one prestressed, 22-bolt connection MF-FRP plate, approximately restores the prestress effect of the steel section loss equivalent to one 11 mm diameter strand stressed to 98 kN after initial losses. In situations where a more ductile bearing failure is desired, and a lower capacity is acceptable, bolted connections with 14 or fewer bolts would be acceptable per the failure behavior and connection capacity shown in Figure 4.14.

### **Conclusions and Recommendations**

The following conclusions are drawn from the study presented in this chapter.

- 1) The current work demonstrated that the coefficient of variance for a specific material property published by a supplier can be combined with a small number of laboratory tests to obtain statistically-significant results for a sample of material. This outcome has important consequences for quality-control and validation of as-received FRP material.
- 2) There is not a statistically significant impact (at the 90% CL) on the peak load capacity between the staggered and aligned treatment conditions and between the 38 mm and 50 mm transverse spacing treatment conditions for the tested FRP material under uniaxial tension load conditions. This finding allows the experimental work in subsequent studies to be conducted considering a single configuration of the treatment conditions, i.e. aligned with 38 mm transverse spacing distance.
- 3) Single-bolt bearing test results indicate that bearing failure (crushing) begins at approximately 7 kN per bolt regardless of single-bolt treatment conditions, allowing for initial calculations to determine the number of bolts necessary to prevent bearing at service load conditions.
- 4) There is not a statistically significant impact (at the 90% CL) on the peak load capacity between the 18-, 20-, and 22-bolt treatment conditions.
- 5) The peak load capacity of the 16-bolt treatment condition is statistically different from the 18-, 20-, and 22-bolt treatments. The mean value for the 16-bolt treatment is 8% lower than the mean value for the 18-, 20-, and 22-bolt treatments at the 90% CL.

- 6) The mean peak load for the 18-, 20-, and 22-bolt treatments is approximately 89% of the peak load capacity of the FRP with holes. The 22-bolt treatment is sufficiently optimized considering peak bearing stress (less than 18- and 20-bolt treatments), peak load (equal to 18- and 20-bolt treatments), and total anchor length (100 mm longer than the 20-bolt treatment) given a 12.7 mm diameter fastener and the FRP plate examined.
- 7) Longitudinal shear failure controls the ultimate capacity of the open-hole and multi-bolt treatment conditions with greater than 14 bolts resulting in a progressive, brittle failure.
- 8) Bearing failure controls the ultimate capacity of single-bolt (with  $e > 3D$ ) and multi-bolt treatment conditions with 14 or fewer bolts resulting in a more ductile failure compared to treatments with greater than 14 bolts.

Future research will examine the effects of fatigue loading and sustained loading on the performance of the bolted connection examined in this study. It is necessary to understand the effects of fatigue on the FRP due to bolt bearing in the connection to provide a failure envelope for design engineers to consider across a range of candidate bridges with varying levels of traffic demands. Additionally, the creep bearing behavior of the FRP at the mechanical connection is critical due to the application of a constant prestress force on the MF-FRP system.

### **Acknowledgements**

The authors would like to thank the North Carolina Department of Transportation and the NSF I/UCRC *Center for the Integration of Composites into Infrastructure (CICI)* for funding the research.

## CHAPTER 5: ADDITIONAL MECHANICAL FASTENER DIAMETERS

### Introduction

To provide engineers a suite of solutions for varying situations, additional fastener diameters in varying numbers are included with this research. Building upon the results presented in Chapter 4, and expanding upon available literature presented in Table 2.1 of this thesis, a test matrix to examine 0.375 in. and 0.75 in. (9.53 mm and 19.1 mm) diameter bolts is presented in Table 5.1. All treatment groups examined aligned hole patterns only as the use of staggered holes does not change the capacity of the FRP in uniaxial tension (McCoy et al., 2019a). The coefficient of variation of the material and the desired confidence limit remains the same; therefore, the number of replicates for each treatment group remains the same as those presented in Chapter 4.

**Table 5.1:** Additional Bolt Diameter Test Matrix.

Specimen ID	No. of Replicates	Treatment Description
S-B-X-0.375-1.5	6	1 bolt; 0.375 in. dia.; 4 in. edge distance excluding threads
DBL18-B-0.375-1.5	6	18 bolts; 0.375 in. diameter; 2-by-2; 1.5 in. transverse spacing; 4 in. longitudinal spacing
DBL20-B-0.375-1.5	6	20 bolts; 0.375 in. diameter; 2-by-2; 1.5 in. transverse spacing; 4 in. longitudinal spacing
DBL22-B-0.375-1.5	6	22 bolts; 0.375 in. diameter; 2-by-2; 1.5 in. transverse spacing; 4 in. longitudinal spacing
DBL14-B-4-0.75-1.5	6	14 bolts; 0.75 in. diameter; 2-by-2; 1.5 in. transverse spacing; 4 in. longitudinal spacing
DBL14-B-6-0.75-1.5	6	14 bolts; 0.75 in. diameter; 2-by-2; 1.5 in. transverse spacing; 6 in. longitudinal spacing

*Note: 1 in. = 25.4 mm*

### Methodology

The test methodology, to include number of replicates, specimen preparation and test set up, for the treatment conditions presented in Table 5.1 is identical to the methodology presented in Chapter 4. Figures 4.6a and 4.7 show the test set up for the single bolt and multi-bolt tests. The universal testing machine (UTM) used to execute the tests in Table 5.1 is the same UTM with a 200-kip (890-kN) +/- 0.25% capacity load cell used to conduct the uniaxial tension tests presented in Chapter 4. The Digital Image Correlation setup used in Chapter 4 was also used to examine the surface strain development for

the 0.375 in. diameter bolt treatment groups in Table 5.1. Because the methodology, test setup, and statistical analysis to determine the appropriate number of replicates for each treatment group are discussed in detail in Chapter 4, they are not discussed in detail here.

## Results and Discussion

Summary results for all treatment groups in Table 5.1 are presented in Table 5.2. Mean peak load was determined from measured load data for each test specimen and mean peak stress is a calculated value using bolt bearing area, calculated in accordance with ASTM D5961 (2017). Measurements for specimen width and thickness were taken as the average width and thickness of the 84 test specimens presented in Chapter 4. Three measurements of different hole diameters were taken using a digital caliper (0.001 in. / 0.0254 mm precision) for each specimen. Stress levels in Table 5.2 are calculated using the mean hole diameter, 0.442 in. and 0.884 in. (11.2 mm and 22.5 mm) for 0.375 in. and 0.75 in. (9.53 mm and 19.1 mm) diameter bolts respectively.

**Table 5.2:** Test Results Summary – 0.375 in. and 0.75 in. Diameter Bolts.

Specimen ID	No. of Specimens	Mean Peak Load (kips)	Mean Peak Stress <sup>1</sup> (ksi)	Sample Peak Stress Standard Deviation (ksi)	Sample Peak Stress CV (%)	CL based on Sample CV (%)	Pop. Peak Stress (ksi)	Pop. Peak Stress CV (%)	CL based on Pop. CV (%)
S-B-X-0.375	6	3.01	61.1	3.99	6.53	89	31.0 <sup>1</sup>	5.37	92
DBL18-B-0.375	6	43.0	48.5	2.59	5.34	93	NA	NA	NA
DBL20-B-0.375	6	45.0	45.7	1.24	2.71	99	NA	NA	NA
DBL22-B-0.375	6	48.5	44.7	1.62	3.62	98	NA	NA	NA
DBL14-B-4-0.75	6	30.9	75.9	3.81	5.02	94	NA	NA	NA
DBL14-B-6-0.75	6	36.3	89.0	3.18	3.57	98	NA	NA	NA

Notes: 1) ASTM D5766 stress calculation uses gross cross-sectional area, sample peak stress is calculated using net cross-sectional area; 1 kip = 4.4482 kN; 1 ksi = 6.895 MPa

Equation 4.5 was used to calculate the critical  $t$ -value for each treatment group, from which the confidence limit for sample sets and the population (manufacturer provided data) was determined, using a Student- $t$  distribution with 5 degrees of freedom ( $n-1$ ). All treatment groups except for S-B-X-0.375 resulted in a higher sample CL than the population CL because of the lower  $CV$  with respect to the number of specimens tested. The higher  $CV$  for the S-B-X-0.375 treatment group is visualized in the

variability of the load-displacement curves shown in Figure 5.1. Although the S-B-X-0.375 treatment group has increased variability compared to the other treatment groups, the S-B-X-0.375 treatment group still obtained an 89% CL, which is considered acceptable for the purposes of this research.

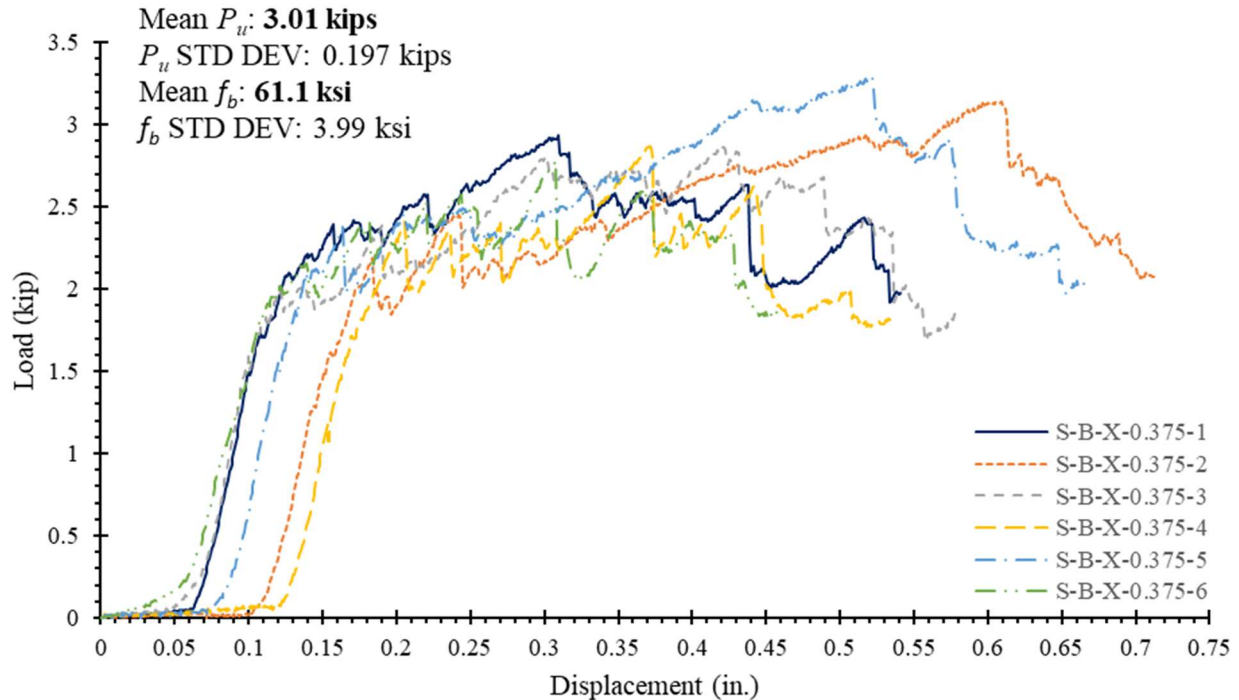


**Figure 5.1:** S-B-X-0.375 load-displacement curves.

Note: 1 kip = 4.4482 kN; 1 ksi = 6.895 MPa

The mean peak loads for the 0.375 in. (9.53 mm) bolt diameter treatment groups are similar to the 0.5 in. (12.7 mm) diameter treatment groups (Tables 5.2 and 4.5, respectively), however, the 0.375 in. (9.53 mm) diameter bolt connections resulted in higher peak stress levels compared to 0.5 in. (12.7 mm) diameter treatment groups (Tables 5.2 and 4.5, respectively) due to the reduced bearing surface area of the 0.375 in. (9.53 mm) diameter fasteners, which resulted in significant bearing in the FRP prior to longitudinal shear failure. Figure 5.2 shows the bearing failure for the DBL20-B-0.375 treatment group compared to that in the DBL20-B treatment group, and DBL14-B-4-0.75 treatment group (discussed later in this chapter). In most specimens, the bearing was followed by longitudinal shear failure similar to that which was observed in the 0.5 in. (12.7 mm) diameter bolt treatments.



**Figure 5.2:** Failure mechanisms for 0.5 in., 0.375 in., and 0.75 in. diameter treatment groups.

This bearing failure prior to longitudinal shear failure resulted in greater displacement in all 0.375 in. (9.53 mm) diameter treatment groups as well (Table 5.3). Figure 5.3 is representative of this increased displacement for all treatment groups (additional load-displacement curves are located in Appendix A). Also seen in the representative load-displacement curves (Figure 5.3) is the greater displacement variability in the 0.375 in. (9.53 mm) bolt diameter treatment groups. Specifically, the mean total displacement for the DBL22-B treatment condition is 0.43 in. (10.9 mm) with a *CV* of 6.38%, whereas the mean total displacement for the DBL22-B-0.375 is 0.75 in. (19.1 mm) with a *CV* of 21.1% (Table

5.3). All 0.375 in. (9.53 mm) bolt diameter treatment groups experienced significantly higher displacement coefficients of variation compared to the 0.5 in. (12.7 mm) bolt diameter treatment groups (Table 5.3). This increased variability is also seen in the wider distribution of data compared to the 0.5 in. diameter bolts shown in Figure 5.3.

**Table 5.3:** Average Maximum Displacement By Treatment Group.

Treatment Group	Mean Maximum Displacement (in.)	Displacement Standard Deviation (in.)	Displacement CV (%)
DBL22-B	0.427	0.0272	6.37%
DBL20-B	0.489	0.0325	6.65%
DBL18-B	0.486	0.0324	6.67%
DBL22-B-0.375	0.749	0.158	21.1%
DBL20-B-0.375	0.667	0.172	25.8%
DBL18-B-0.375	0.746	0.146	19.6%

Note: 1 in. = 25.4 mm

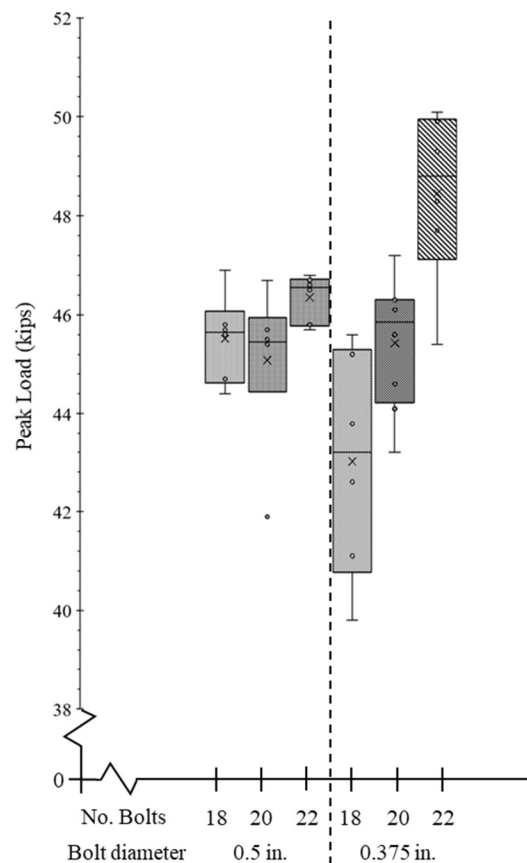


**Figure 5.3:** 0.5 in. and 0.375 in. bolt diameter peak load distribution.

Note: 1 in. = 25.4 mm

Although the greater displacement of the 0.375 in. (9.53 mm) diameter treatment groups provides a perceived increase in ductility (prolonged displacement at peak loads) in the system, and early visual warning of failure through bearing at each bolt, the high *CV* of 21.1%, 25.8%, and 19.6% for DBL22-B-0.375, DBL20-B-0.375, and DBL18-B-0.375 respectively, indicates that the increased displacement is unreliable, and in some test specimens there was no prolonged displacement prior to failure, but rather immediate failure at peak load (Figure 5.4a) similar to that of the 0.5 in. (12.7 mm) bolt diameter treatments (Figure 5.4b). Therefore, future research is recommended to gain increased reliability and decreased variation in the load-displacement behavior of 0.375 in. (9.53 mm) bolt diameter connections before MF-FRP solutions using 0.375 in. (9.53 mm) bolt diameters are used in practice. This research is currently on-going, but is not included in the scope of this research.

In addition to the 0.375 in. (9.53 mm) diameter bolt treatment groups, two treatment groups with 0.75 in. (19.1 mm) diameter bolts were examined to investigate the effects of larger bolt diameters on the behavior of the connection. To keep a similar total bearing surface area as the DBL22-B treatment group, 14 0.75 in. (19.1 mm) diameter bolts were used. As seen in Figure 5.2b, the holes for the 0.5 in. (12.7 mm) and 0.375 in. (9.53 mm) bolt diameter cut through a single carbon tow (Figure 4.1b) for each line of bolts. However, during preparation of the 0.75 in. (19.1 mm) bolt diameter specimens, it was observed that the larger hole diameter resulted in reduction of the transverse glass fibers between the longitudinal carbon tows, which redistribute the stress concentration at each hole, and reduction of the adjacent carbon tows (Figure 5.2c). The reduced area of carbon tows and transverse glass fibers resulted in significant reduction in ultimate load capacity of the connection with a mean maximum capacity of 30.9 kips (137 kN) for the DBL14-B-4-0.75 treatment (Table 5.2).

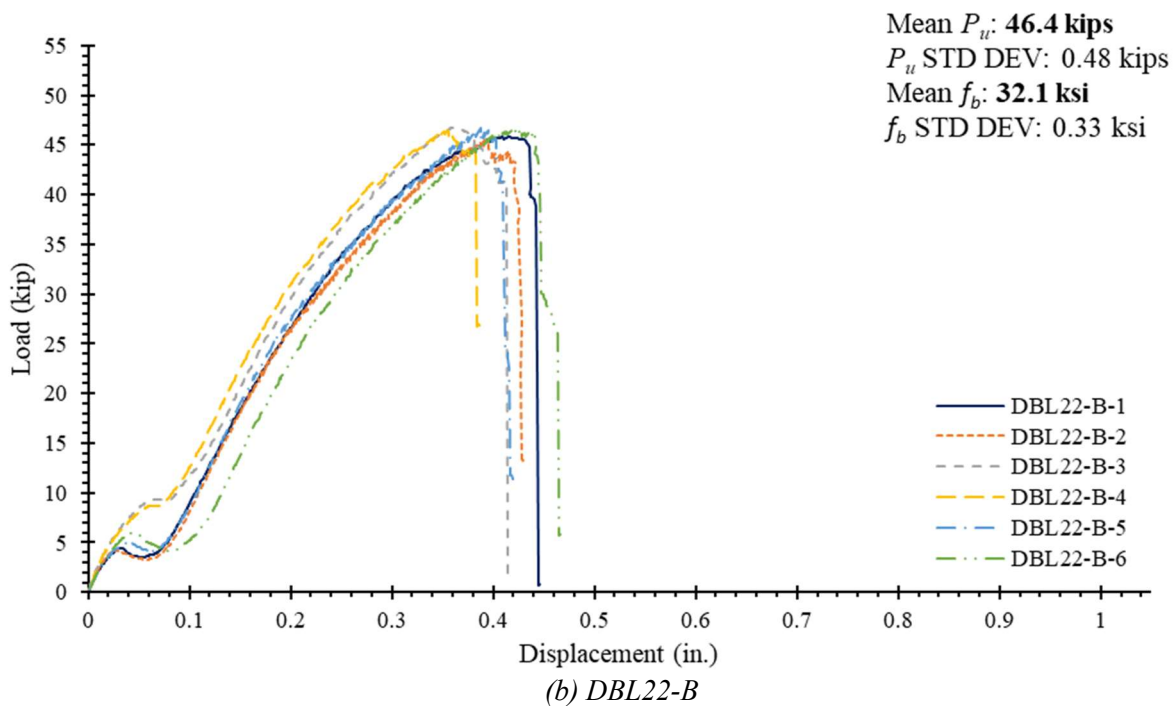
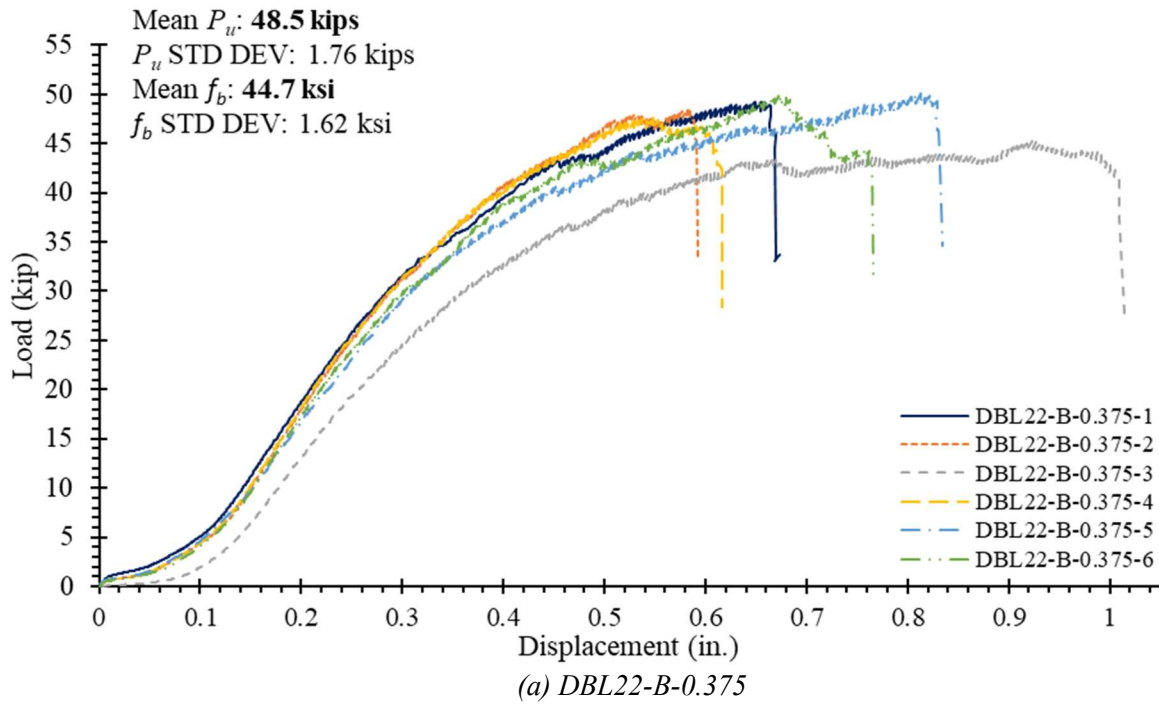


**Figure 5.4:** Load-displacement behavior for DBL22-B and DBL22-B-0.375 treatment groups.

Note: 1 kip = 4.4482 kN; 1 ksi = 6.895 MPa

Figure 5.5 shows the load-displacement behavior for the DBL14-B-4-0.75 specimens. Although the 0.75 in. bolt diameter resulted in less variability than the 0.375 in. treatment (visualized in Figure 5.6), the reduction in mean peak load is a concern for the MF-FRP retrofit solution because the loads in the FRP at operating levels requires greater capacity in the MF-FRP system. This is discussed in detail in Chapter 7.

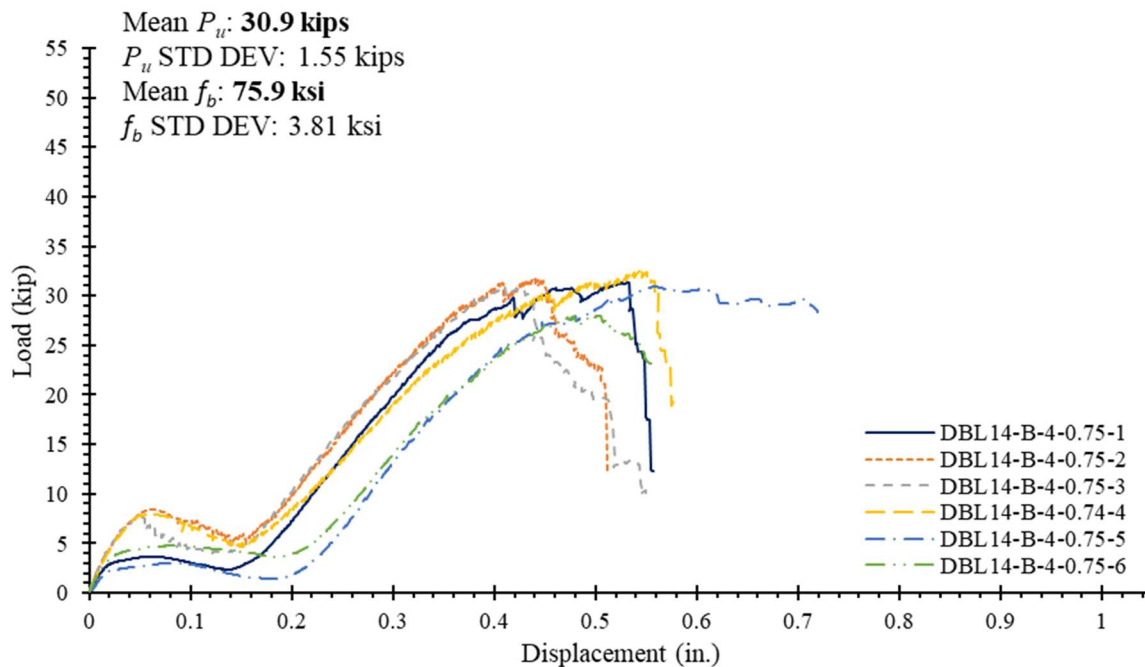


**Figure 5.5:** Load-displacement behavior for DBL14-B-4-0.75 treatment group.

Note: 1 kip = 4.4482 kN; 1 ksi = 6.895 MPa

A similar treatment group with greater longitudinal spacing between holes was also examined to determine the effect of increasing the length of the longitudinal shear failure plane. Increasing the longitudinal spacing by 50% (from 4 in. to 6 in. / 100 mm to 150 mm) increased the peak load on the connection by only 17.5% (from 30.9 kips to 36.3 kips / 137 kN to 161 kN); therefore, the increased longitudinal shear failure plane does result in a sufficiently higher load capacity of the system. However, the load capacity of both 0.75 in. (19.1 mm) bolt diameter treatment groups is significantly less than the load capacity of the 0.5 in. (12.7 mm) and 0.375 in. (9.53 mm) bolt diameter treatment groups with similar bearing surface areas. Therefore, further investigation of 0.75 in. (19.1 mm) bolt diameter (or larger) fasteners is not recommended as larger diameters experience reduced FRP performance and decrease the efficiency of the MF-FRP retrofit.

## Conclusions

The following conclusions are presented.

- 1) The DBL-B-0.375 treatment groups have load capacities similar to that of the DBL-B treatment groups presented in Chapter 4.
- 2) The DBL-B-0.375 treatment group have increased displacement behavior compared to the DBL-B treatment groups; however, with increased variability. This increased displacement of the bearing failure at peak loads occurs prior to longitudinal shear failure, and gives a desirable early warning of failure; however, the high variability of the behavior introduces unpredictability of the fastener patterns with 0.375 in. (9.53 mm) diameter bolts. Therefore, it is recommended that the 0.5 in. (12.7 mm) bolt diameter fasteners be used in the development of the MF-FRP retrofit, and further research be conducted to investigate the causes of the DBL-B-0.375 variability.
- 3) Although the bearing surface area was similar that of the DBL22-B treatment groups, the DBL14-B-0.75 treatment groups experienced significant reduction in load capacity due to the larger diameter hole reducing the cross-sectional area of the carbon tows and transverse glass fibers. However, the DBL14-B-6 treatment group, with a longitudinal shear plane increase of 50% over the DBL14-B-4 treatment group, experienced a 17.5% increase in load capacity. While increased capacity for the 0.75 in. bolt diameter anchor pattern is desired, increasing the longitudinal shear plane requires increased anchor length for the MF-FRP system, which is not desirable for short span (30 – 40 ft.) bridge beams. Therefore, further investigation of anchor bolt patterns with increased anchor zone lengths is not included in this research, and 0.5 in. diameter bolts are used for the MF-FRP retrofit design and full-scale testing presented in Chapter 7.

**CHAPTER 6:  
PRESTRESSED MF-FRP: AN EXPERIMENTAL STUDY OF A RAPID RETROFIT SOLUTION  
FOR DETERIORATED PRESTRESSED C-CHANNEL BEAMS**

*(ASCE Journal of Performance of Constructed Facilities, under review)*

Brad C. McCoy, P.E., ENV SP: Ph.D. Candidate, North Carolina State University, Department of Civil, Construction, and Environmental Engineering, Corresponding Author: [bcmccoy@usma.edu](mailto:bcmccoy@usma.edu)

Zakariya Bourara: MS Student, North Carolina State University, Department of Civil, Construction, and Environmental Engineering

Gregory W. Lucier, Ph.D.: Assistant Research Professor, North Carolina State University, Department of Civil, Construction, and Environmental Engineering

Rudolf Seracino, Ph.D.: Professor, North Carolina State University, Department of Civil, Construction, and Environmental Engineering

Min Liu, Ph.D.: Associate Professor, North Carolina State University, Department of Civil, Construction, and Environmental Engineering

**Abstract**

This chapter presents design and installation details, and full-scale test results for a mechanically-fastened fiber-reinforced polymer (MF-FRP) retrofit solution that restores the original operating and inventory rating of prestressed concrete C-channel bridge superstructures with prestress losses due to deterioration of concrete and steel corrosion. Bridges with deteriorated superstructures require weight restrictions and detours for traffic with vehicle loads in excess of the posted restrictions. These restrictions increase travel time and vehicle operating costs which results in significant impacts on local commerce, public transportation, and emergency services. Departments of transportation must leave bridge restrictions in place until the bridge can be repaired or replaced, which requires time for planning, budgeting and construction. Therefore, a retrofit solution that can be rapidly installed to remove posted restrictions and closures until permanent replacement can occur is desired. The full-scale test results of the examined MF-FRP retrofit solution indicate that the retrofit can be installed on a bridge by a 4-worker DOT maintenance crew in a single 8-hour workday, and is capable of immediately restoring mild to moderate prestress loss due to deterioration of prestressed concrete C-channel beams such that the original operating and inventory ratings are satisfied.

*Keywords: Strengthening and repair; MF-FRP; Prestressed concrete; In-place concrete strength*

## Introduction

Prestressed concrete C-channel beams (referred to hereafter as C-channel beams) are among the common bridge superstructure elements in service across North Carolina (NC) and in many regions of the United States. North Carolina currently has 269 bridges across the state with prestressed concrete C-channel superstructures, of which 226 have load restrictions posted (or are closed) due to superstructure deterioration (NCDOT BMS, 2018). Deterioration of the C-channel beams often results in prestress losses and requires both inventory and operating rating levels to be reduced (McCoy et al., 2019b). These bridge load restrictions are categorized by the American Association of State Highway and Transportation Officials (AASHTO) as: 1) single vehicle (SV); and 2) truck tractor semi-trailer (TTST) (AASHTO, 2018). Table 6.1 provides a summary of the in-service C-channel bridges across NC. An example of a deteriorated prestressed C-channel beam bridge is shown in Figure 6.1. The deterioration in Figure 6.1b is due to agricultural run-off; however, similar deterioration occurs in chloride environments along the coast, resulting in prestress loss from concrete spalling and steel corrosion.

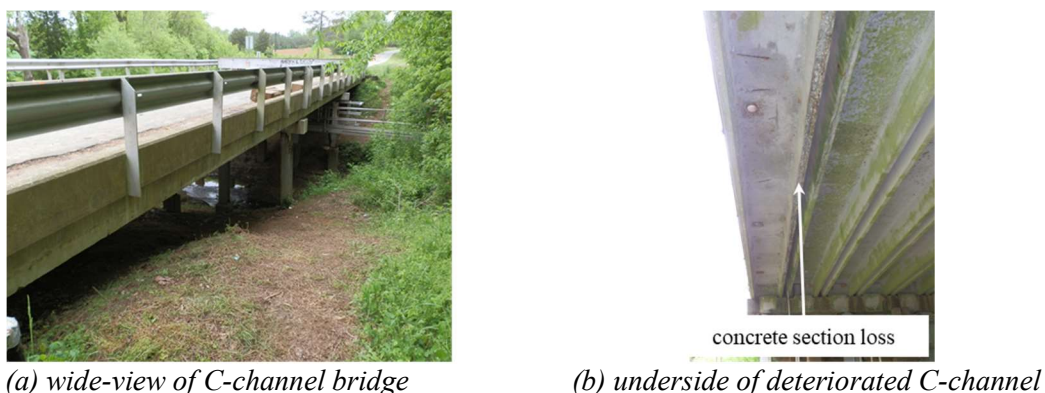


**Figure 6.1:** Example C-channel deterioration.

**Table 6.1:** North Carolina C-channel Bridge Restriction Summary.

	SV	TTST
Total Posted Restrictions	225	208
Percent Posted (%)	83.6	77.3
Average Restriction Value (kN / ton)	227 / 25.5	267 / 30.0
Median Restriction Value (kN / ton)	214 / 24	258 / 29
Minimum Restriction (kN / ton)	44.5 / 5	44.5 / 5
Maximum Restriction (kN / ton)	365 / 41	400 / 45
Total Closures	1	3
Average Detour (km / mi.)	12.6 / 7.8	12.1 / 7.5

Of particular interest is the 12.6 km and 12.1 km (7.8 mi. and 7.5 mi.) average detour length for SV and TTST respectively across the 226 restricted or closed bridges. Detours due to bridge restrictions and closures increase vehicle operating costs (VOC) for industries that routinely use routes with restricted bridges, which can lead to substantial highway customer costs and increased travel time. While not the focus of this chapter, a previous study conducted by the North Carolina Department of Transportation (NCDOT) concluded that the average VOC for vehicles greater than 231 kN (26 tons) is \$1.61/km (\$2.59/mi.) and \$1.16/km (\$1.86/mi.) for vehicles less than 231 kN (26 tons) (Cavalline et al., 2015), meaning these detours are directly costing each vehicle owner approximately \$14-20 each way. Further, the study concluded the average detour speed is 64.5 km/h (40 mph) resulting in an 11.7- minute average detour time for SV and 11.3-minute average detour time for TTST.

The detours due to bridge load restrictions and closures not only impact industry, but public transportation and emergency services as well. Table 6.2 shows the number of C-channel bridges in NC with restrictions that detour a typical Type C School Bus (151 kN / 16 ton), a typical pumper truck fire apparatus (187 kN / 21 ton), and a typical aerial ladder truck fire apparatus (338 kN / 38 ton) (FAMA, 2017). Bridge restrictions that detour fire trucks increase emergency response times in those areas and impact the safety of residents. Using an average emergency vehicle travel speed of 72.5 km/h (45 mph), the response times for pumper trucks and aerial ladder trucks are increased by approximately 9 and 12 minutes, respectively (Table 6.2). These increases alone are more than double the U.S. national benchmark response time of 5 minutes (Ammons, 2001). It is important to note that NC is one of 21 states in the U.S. that do not exempt emergency service vehicles from weight restrictions (FAMA, 2017). Therefore, it is reasonable to include bridge restriction detours in emergency service response times in NC (and in all non-exempt states).

**Table 6.2:** Total C-channel Bridge Restrictions Impacting Public Service Vehicles.

	SV	TTST	Avg. Detour Length (km / mi.)	Avg. Detour Time (min.)
Type C School Bus	13	NA	24 / 15	22.5
Pumper Truck Fire Apparatus	68	NA	11 / 6.8	9.1
Aerial Ladder Truck Fire Apparatus	NA	177	14 / 8.7	11.6

The 226 C-channel bridge restrictions and closures across NC increase travel time, VOC, and emergency response capabilities, significantly impacting commerce and the lives of residents. Current solutions available to address bridge superstructure deterioration include immediate bridge replacement, temporary posted restrictions or closures until bridge replacement can be scheduled, and long-term restrictions or closures. In most cases in NC, the scheduling process for bridge replacement takes 3-5 years, including the time required for capital project funding and the design-bid-build or design-build project delivery cycles. Therefore, a retrofit solution is desired which can be installed rapidly, can be easily inspected and maintained, and is capable of restoring prestress losses due to deterioration for a service-life period of 3-5 years. Such a system would allow deteriorated C-channel beams to remain in service without posted load restrictions or closures while a permanent superstructure replacement is scheduled and completed.

AASHTO (2018) requires bridges be rated for two categories – operating and inventory rating. McCoy et al. (2019b) describes in detail the requirements and impacts for each rating criteria. Inventory rating criteria establish the maximum load level which can be applied to the bridge without damage for an indefinite period of time and an indefinite number of cycles. Inventory ratings are typically based on elastic stress limit states. Operating rating criteria establish a load level that can be applied safely to a bridge for an extended period of time, but may cause incremental damage with each loading. The operating rating is based on strength limit states and is typically a specified factor of the ultimate strength capacity. In most cases, the operating rating controls bridge capacity and load restrictions; however, to adequately remove posted load restrictions from deteriorated prestressed concrete bridge superstructures, both operating and inventory rating criteria must be addressed.

A feasible retrofit solution must restore prestress losses such that concrete stress limits at service load levels are within AASHTO (2018) allowable limits:

$$f_{t,allow} = 0.5\sqrt{f'_c} \text{ (MPa)} \quad (6.1a)$$

or

$$f_{t,allow} = 6\sqrt{f'_c} \text{ (psi)} \quad (6.1b)$$

where  $f_{t,allow}$  is the allowable concrete tensile stress, and  $f'_c$  is the concrete design compressive strength. Equation 6.1 is the controlling inventory rating criteria for prestressed C-channel beams (McCoy et al., 2019b). Many bridge owners, in accordance with AASHTO (2018) provisions, further reduce  $f_{t,allow}$  to  $0.25\sqrt{f'_c}$  MPa or  $3\sqrt{f'_c}$  psi, or 0 depending upon environmental conditions. Therefore, to address the most conservative tensile stress limits, a desirable retrofit solution must be capable of limiting concrete tensile stress to zero at inventory rating levels, and must be capable of restoring the ultimate strength capacity such that the operating rating of a deteriorated C-channel beam is equal to or greater than the original operating rating.

McCoy et al. (2019b) presents a retrofit solution concept using mechanically fastened-fiber reinforced polymer (MF-FRP) that addresses inventory and operating rating requirements to allow deteriorated C-channel bridges to remain in service without restrictions or closures. The MF-FRP retrofit solution can be designed for rapid installation, eliminating detours and decreasing VOC, travel time, and emergency response time.

### **Research Significance**

This chapter presents a proof-of-concept for two MF-FRP retrofit designs and unique data which describes the behavior of the MF-FRP retrofit on previously in service, full-scale C-channel beams tested to failure in flexure. The behavior of beams strengthened with the proposed MF-FRP retrofit are presented for damaged (deteriorated) and undamaged C-channel sections, and are useful for the ongoing development of a field-ready MF-FRP retrofit solution for Departments of Transportation (DOTs) to address prestress loss in deteriorated C-channel beams. Additionally, the results of the full-scale tests presented here can be used to develop other MF-FRP retrofit solutions which restore minor to moderate prestress losses in deteriorated superstructure elements across a range of cross-sections. The MF-FRP retrofit solution examined in this study is post-tensioned to restore prestress losses and to satisfy inventory rating requirements. The proposed MF-FRP system differs from non-post-tensioned MF-FRP in

the literature because non-post-tensioned systems strengthen, but cannot effectively restore lost prestress effects.

### Experimental Program

Six 9.14 m (30 ft.) long C-channel beams were tested as part of this investigation. Two C-channel beams were tested without the MF-FRP retrofit installed, one undamaged (U), and one damaged (D), to determine a control baseline prior to strengthening for each condition. Four C-channel beams were tested with the MF-FRP retrofit installed on the interior face of each stem, two undamaged (MF-FRP-U1 and MF-FRP-U2), and two damaged (MF-FRP-D1 and MF-FRP-D2). All C-channel beams were removed in relatively good condition from an existing structure and were damaged as required in the lab by cutting the bottom prestressing strand in each stem at mid-span (Figure 6.2). The induced damage was used to simulate field deterioration with moderate prestress loss at the point of maximum moment.

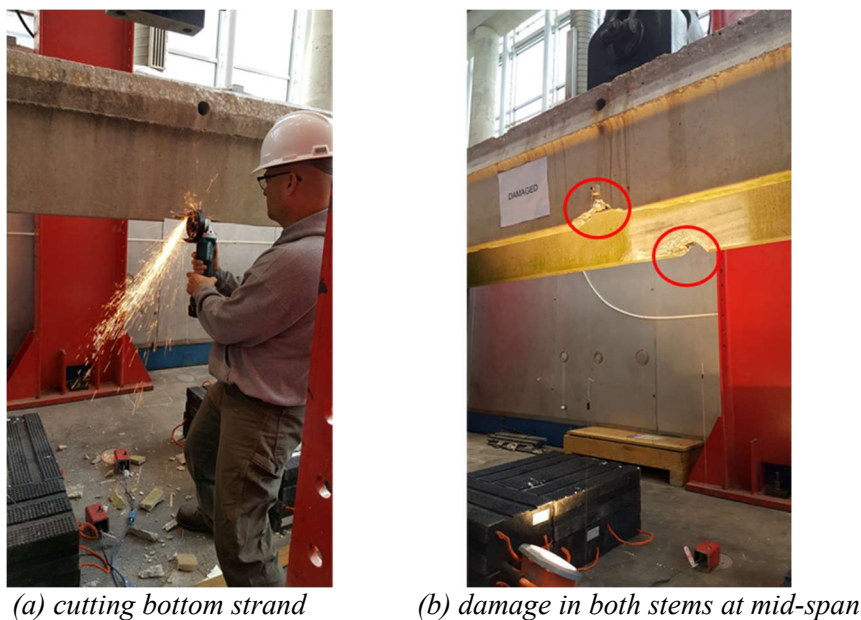
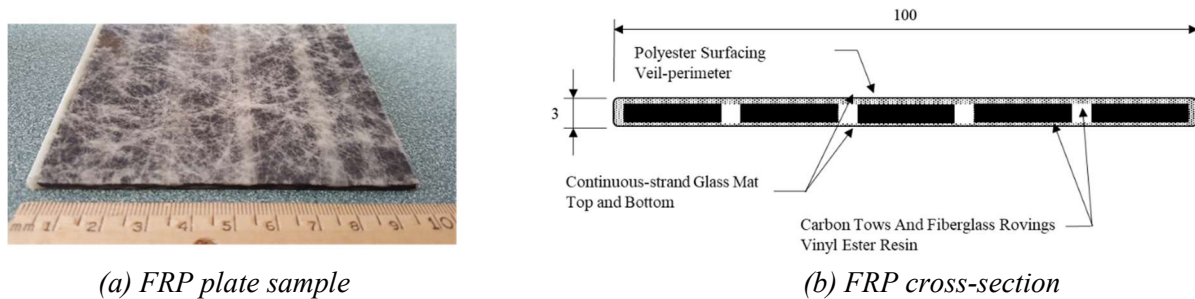


**Figure 6.2:** Damaged C-channel beam.

Specimens MF-FRP-U1 and MF-FRP-D1 were tested with the initial MF-FRP connection design (MF-FRP 1.0), and MF-FRP-U2 and MF-FRP-D2 were tested with an improved connection design (MF-FRP 2.0) that eliminates internal moment in the FRP due to fixity in the connection. All MF-FRP specimens used one commercially-available FRP plate per C-channel stem, shown in Figure 6.3 and discussed in detail in McCoy et al. (2019a). MF-FRP 1.0 and MF-FRP 2.0 connections are discussed in

detail later in this chapter. Table 6.3 presents a summary of the test matrix for the six tested C-channel beams.



(a) FRP plate sample

(b) FRP cross-section

**Figure 6.3:** FRP plate examined (McCoy et al., 2019a).

Note: all dimensions are in millimeters, 1 in. = 25.4 mm.

**Table 6.3:** C-channel Test Matrix

Specimen ID	Specimen Description
U	Undamaged Control
D	Damaged (deteriorated) Control
MF-FRP-U1	Undamaged with first version retrofit (MF-FRP 1.0) installed on both stems
MF-FRP-U2	Undamaged with improved retrofit (MF-FRP 2.0) installed on both stems
MF-FRP-D1	Damaged with MF-FRP 1.0 installed on both stems
MF-FRP-D2	Damaged with MF-FRP 2.0 installed on both stems

### *C-channel beam description*

The six C-channel beams tested in this program were removed from NC Bridge 380093 which carries State Route 1156 (SR1156) across Owen Creek in Granville County, NC. All beams selected for testing were interior, undamaged girders in serviceable condition. These nominally-identical girders allowed for controlled damage of selected specimens to be implemented in the lab such that results could be compared across all test specimens. NC Bridge 380093 is the subject of a case study that served as the impetus for the MF-FRP retrofit concept proposed by McCoy et al. (2019b) and is examined in detail in this chapter.

Figure 6.4 shows the cross-section of the 9.14 m (30 ft.) long C-channel beams. The beams were prestressed with 11.1 mm (7/16 in.) diameter high-strength (HS), stress-relieved strands with an ultimate tension capacity of 1860 MPa (270 ksi) (Table 6.4). The bottom HS strand in each stem is oriented parallel to the bottom of the stem; however, the three HS strands near mid-height of each stem are harped

90.4 mm (3.60 in.) at the mid-span. All strands were stressed by the manufacturer with an initial reported prestressing force,  $P_i$ , of 96.5 kN (21.7 kips) (NCDOT, 1966). The C-channel beams were approximately 45 years old (400,000+ hours) at time of testing. Therefore, losses due to relaxation of the stress-relieved HS strands (not low-relaxation) can be estimated using the following (Nawy, 2009),

$$\Delta f_{pR} = f'_{pi} \frac{\log}{10} \left( \frac{f'_{pi}}{f_{py}} - 0.55 \right) \quad (6.2)$$

where  $\Delta f_{pR}$  is the change in stress due to relaxation,  $t$  is time since initial applied prestress (hours),  $f'_{pi}$  is the stress in the HS strand immediately after transfer – taken as 98% of  $f_{pi}$  to account for 6 hours of HS strand relaxation, and  $f_{py}$  is the yield strength of the HS strand. Using Equation 6.2,  $\Delta f_{pR}$  at time of transfer,  $\Delta f_{pR,transfer}$ , is 27.5 MPa (4 ksi), assuming transfer occurs at 6 hours, and  $\Delta f_{pR}$  at 400,000 hours after transfer,  $\Delta f_{pR,400k}$ , is 153 MPa (22.2 ksi). Using the AASHTO (2017) lump sum approach, the predicted total prestress loss,  $\Delta f_{pT}$ , due to elastic shortening, shrinkage, and creep is 243 MPa (35.3 ksi). After total prestress loss, the effective prestress force at time of testing,  $P_{eff,400k}$ , is expected to be 77.6 kN (17.4 kips) and can be calculated using

$$P_{eff,400k} = (f'_{pi} - \Delta f_{pT}) A_{ps} \quad (6.3)$$

Material properties (Table 6.4) and structural detailing information (Figure 6.4) were extracted from structural drawings provided by the NCDOT (1966).

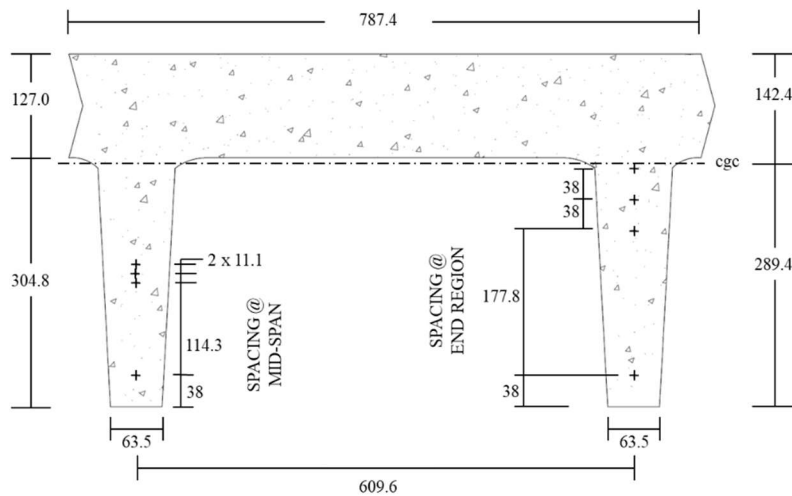


**Figure 6.4:** C-channel cross-section details (adapted from NCDOT, 1966).

*Note: All dimensions are in millimeters, 1 in. = 25.4 mm; “+” denotes a single prestressing strand*

**Table 6.4:** C-channel Specified Material Properties (adapted from NCDOT, 1966).

Concrete Details	
Design Compressive Strength, $f'_c$ (MPa / psi)	35.5 / 5000
Compressive Strength at Transfer of Prestress Force, $f_{ci}$ (MPa / psi)	27.6 / 4000
Compressive Strength at Time of Testing, $f_c$ (MPa / psi) <sup>1</sup>	68.9 / 10000
Cross-sectional Area (mm <sup>2</sup> / in. <sup>2</sup> )	170970 / 265
Strong Axis Moment of Inertia, $I_{yy}$ (mm <sup>4</sup> / in. <sup>4</sup> )	119 x 10 <sup>8</sup> / 28600
Prestressing Strand Details	
Ultimate Strength, $f_{pu}$ (MPa / ksi)	1860 / 270
Yield Strength, $f_{py}$ (MPa / ksi)	1580 / 230
Initial Stress, $f_{pi}$ (MPa / ksi)	1300 / 189
Transfer Stress, $f'_{pi}$ (MPa / ksi)	1273 / 185
Diameter (mm / in.)	11.1 / 0.4375
Area, $A_{ps}$ (mm <sup>2</sup> / in. <sup>2</sup> )	75.3 / 0.1167
Ultimate Prestress Force, $P_u$ (kN / kips) <sup>2</sup>	138 / 31.5
Initial Prestress Force, $P_i$ (kN / kips) <sup>3</sup>	96.5 / 21.7
Effective Prestress Force at 400,000 hours, $P_{eff,400k}$ (kN / kips) <sup>4</sup>	82.3 / 18.5
Number of Strands	8

Notes: 1) calculated from cores removed at time of testing; 2) calculated with  $f_{pu}$  and  $A_{ps}$ ; 3) calculated with  $f_{pi}$  and  $A_{ps}$ ; 4) calculated with Equation 6.3

### **Test set-up and instrumentation**

The test set-up, shown in Figure 6.5, was modeled after a previous study which examined the behavior of similar C-channel beams strengthened with externally-bonded FRP (Rosenboom and Rizkalla, 2008). All C-channel beams were loaded in 3-point bending with a 980 kN (220 kip) +/- 0.25% capacity load cell and hydraulic actuator mounted on a steel frame at the beam mid-span. The load was applied with a 250 mm x 510 mm (10 in. x 20 in.) steel bearing plate in accordance with AASHTO (2017) bearing area requirements for wheel loading. Neoprene bearing pads on concrete blocks were used at the supports to simulate field conditions. The bearing width of each neoprene pad was 190 mm (7.5 in.), creating a span length of 8.95 m (29.4 ft.) (Figure 6.5). Prior to testing, all specimens were instrumented with string potentiometers at each quarter-span point and mid-span point of the front stem, and at the mid-span point of the rear stem. Additionally, two linear potentiometers were used to measure vertical displacement at the supports. Electric resistance strain gauges were attached to all FRP plates at

mid-span along the centroidal axis of the FRP plate to measure axial strain throughout the test. Digital image correlation (DIC) was also used to provide a continuous strain map at the 22-bolt FRP-to-concrete connection for MF-FRP 1.0 specimens and the 22-bolt FRP-to-connector plate connection for MF-FRP 2.0 connections. The DIC results were then compared to DIC results from uniaxial tension testing of the 22-bolt FRP connection (McCoy et al., 2019a) to categorize the FRP behavior and failure mode for each MF-FRP connection. All specimens were tested to failure under displacement-controlled conditions at a load rate of 6.4 mm (0.25 in.) per minute from 0 kN (0 kips) to 71.3 kN (16.0 kips) of applied load, after which the load rate was increased to 12.7 mm (0.5 in.) per minute through failure. The 71.3 kN (16.0 kips) applied load corresponds to an internal moment of 163 kN-m (120.3 k-ft.), which is the live load moment generated by the HS-15 vehicle loading condition, including impact, along a single wheel line for a 9.1 m (30 ft.) span length (AASHTO, 2018). The HS-15 is the original load rating for the C-channel beams examined in this study (NCDOT, 1966), and the HS-15 live load moment assumes no load-transfer occurs between adjacent beams in accordance with AASHTO (2018) load rating analysis guidelines.

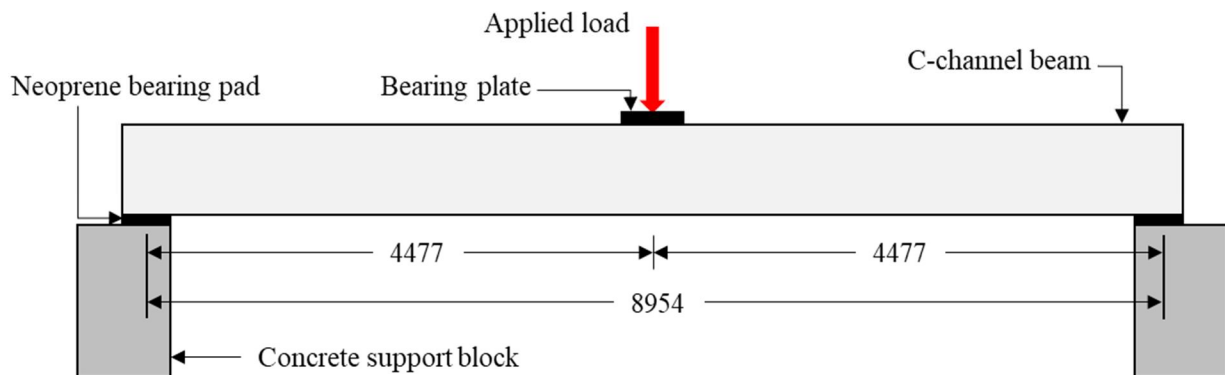


**Figure 6.5:** Test set-up.

*Note: All dimensions are in millimeters, 1 in. = 25.4 mm*

## MF-FRP Retrofit Design

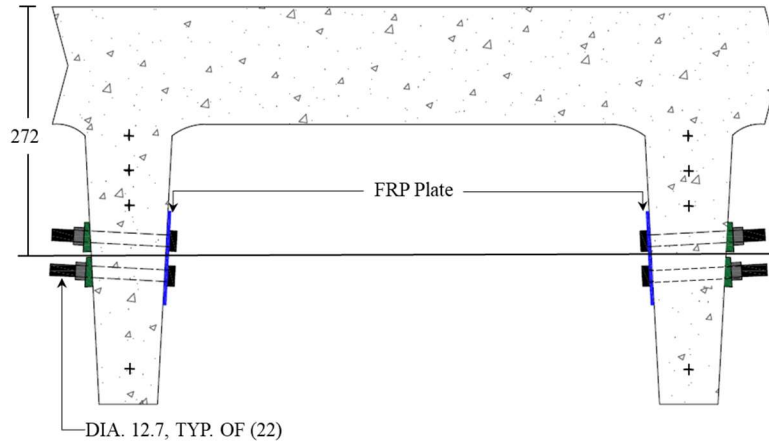
### ***MF-FRP 1.0***

McCoy et al. (2019a) presents a 22-bolt anchor pattern, shown in Figures 6.6c and 6.6d, using 12.7 mm (0.5 in.) diameter bolts arranged in 2 aligned, 11-bolt rows with 38 mm (1.5 in.) transverse spacing between rows. This pattern was proven sufficient to develop approximately 90% of the full-capacity of

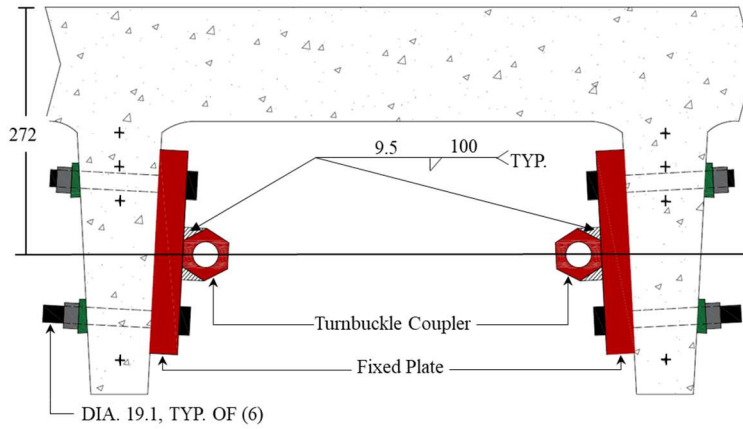
the FRP plate with holes, and is sufficiently optimized with respect to the number of bolts and peak bearing stress in the FRP plate. The capacity of the 22-bolt anchor pattern presented by McCoy et al. (2019a) is 200 kN (45 kips).

The MF-FRP 1.0 connection design shown in Figures 6.6 and 6.7 (C-channel beams MF-FRP-U1 and MF-FRP-D1) incorporates the 22-bolt anchor pattern by attaching the FRP plate directly to the concrete on the interior of each C-channel stem at one end (dead-end) (Figures 6.6a, 6.6c and 6.7a). The MF-FRP retrofit is attached to the interior only because adjacent beams in the field prevent access to the stem exteriors. The FRP plate is attached to a steel connector plate at the opposite end (live-end) (Figures 6.6d and 6.7b) using the same 22-bolt anchor pattern. The steel connector plate at the live-end is joined to a steel fixed plate through a welded coupler and turnbuckle system (Figure 6.6b), and the fixed plate is connected to the concrete interior of the C-channel stem through six 18.8 mm (0.75 in.) diameter bolts (Figure 6.6b). All components of the MF-FRP 1.0 connection are designed in accordance with American Institute of Steel Construction (AISC) design guidelines (AISC, 2015) such that the design strength exceeds the 200 kN (45 kip) capacity of the 22-bolt FRP connection.

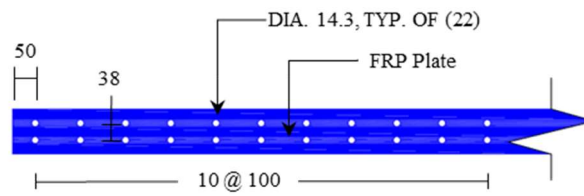
MF-FRP 1.0 requires 28 holes drilled per stem for the 22-bolt FRP connection at the dead-end, and the 6-bolt steel connection at the live-end. Prior to drilling, a commercially-available pachometer was used to locate the HS strands and shear reinforcement within the MF-FRP 1.0 anchor zones on each stem. All holes were drilled using a commercially-available hammer drill, and although care was taken to minimize spalling due to drilling, moderate concrete spalling occurred at each hole during drilling. This spalling was repaired at the dead-end with a high strength grout to create a flat surface for the 22-bolt FRP-to-concrete connection (Figure 6.7a). At the live-end, the spalling was not repaired because it was determined that sufficient concrete remained at each hole to give the required bearing surface area at each bolt, and the spalled surface did not impact the installation of the steel base plate. All steel-to-concrete bolts in all connections extend through the entire stem thickness with wedge washers used to provide even force distribution against the tapered side of the C-channel stems (Figures 6.6a and 6.6b).



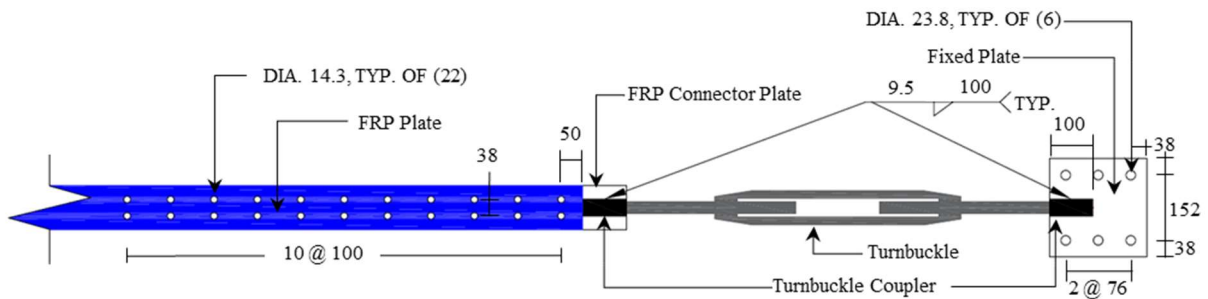
(a) dead-end cross-section detail



(b) live-end cross section detail



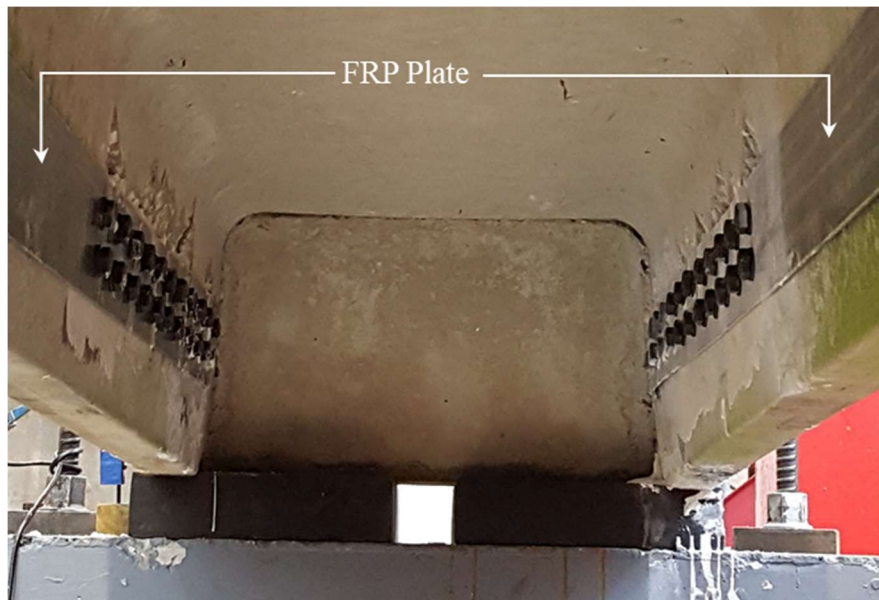
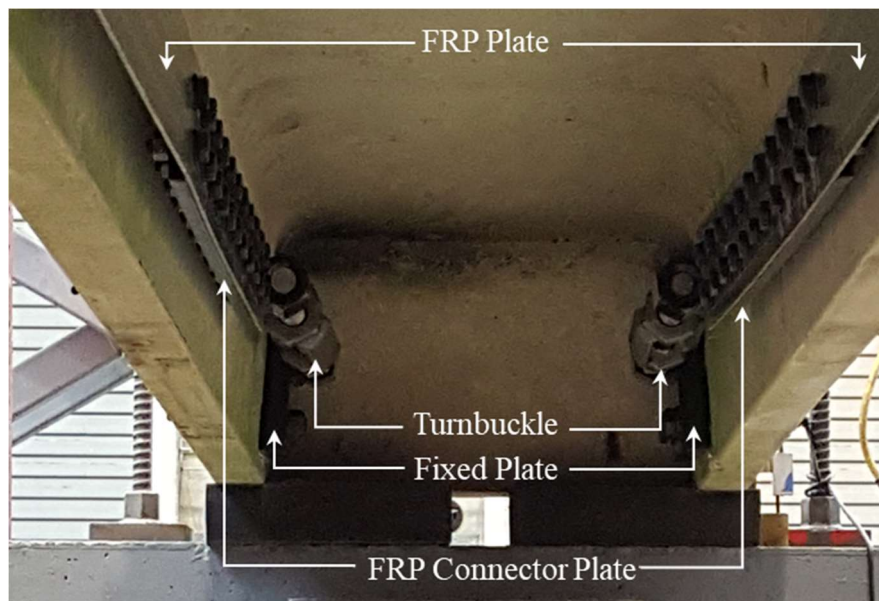
(c) dead-end elevation detail



(d) live-end elevation detail

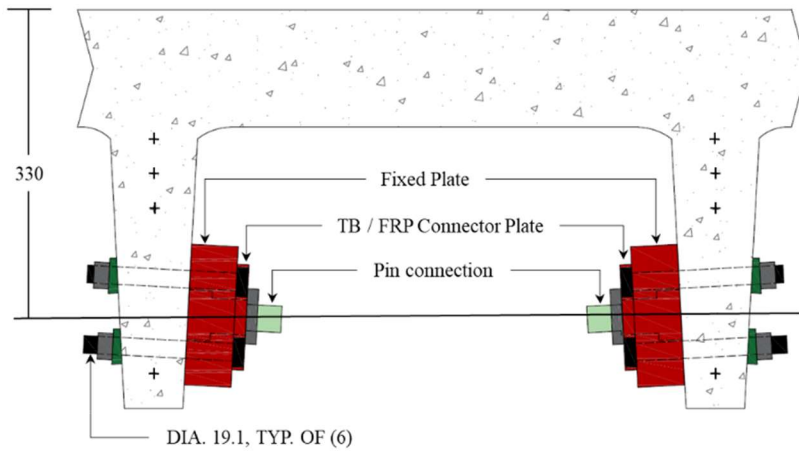
**Figure 6.6:** MF-FRP 1.0 design details.

Note: All dimensions are in millimeters, 1 in. = 25.4 mm; "+" denotes a single prestressing strand

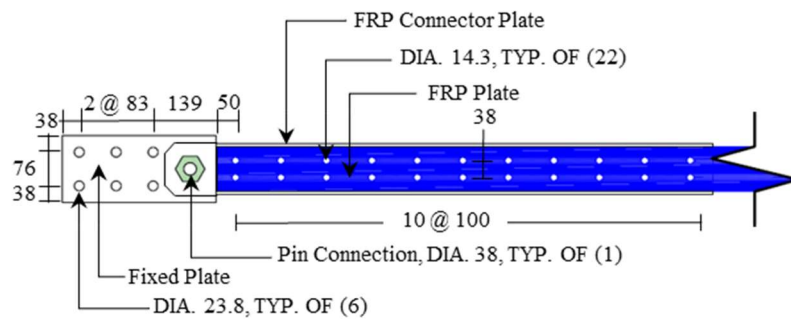
(a) *dead-end*(b) *live-end***Figure 6.7:** MF-FRP 1.0 connection photos.***MF-FRP 2.0***

The performance of MF-FRP 1.0 presents two critical observations, which are discussed in more detail later in this chapter: 1) drilling 28 holes in each stem of the C-channel beam is labor intensive and requires a great deal of time, and 2) the 22-bolt dead-end connection creates a fixity that results in an in-plane moment about the strong-axis of the FRP plate as the beam deflects, developing transverse stresses

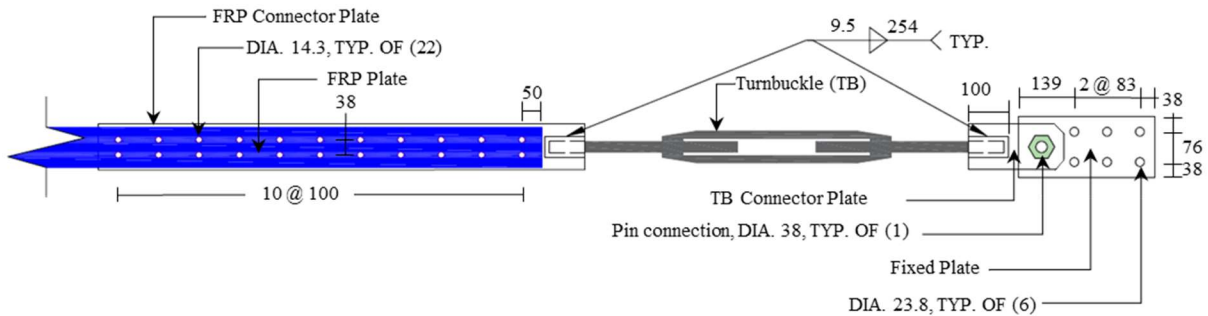
in the FRP plate along the bolted connection and reducing the capacity of the MF-FRP system. Therefore, a second MF-FRP (MF-FRP 2.0) design was developed to reduce field drilling requirements and to allow the FRP plate to remain in uniaxial tension throughout the test. Details of MF-FRP 2.0 are presented in Figures 6.8 and 6.9.



(a) dead- and live-end cross-section detail



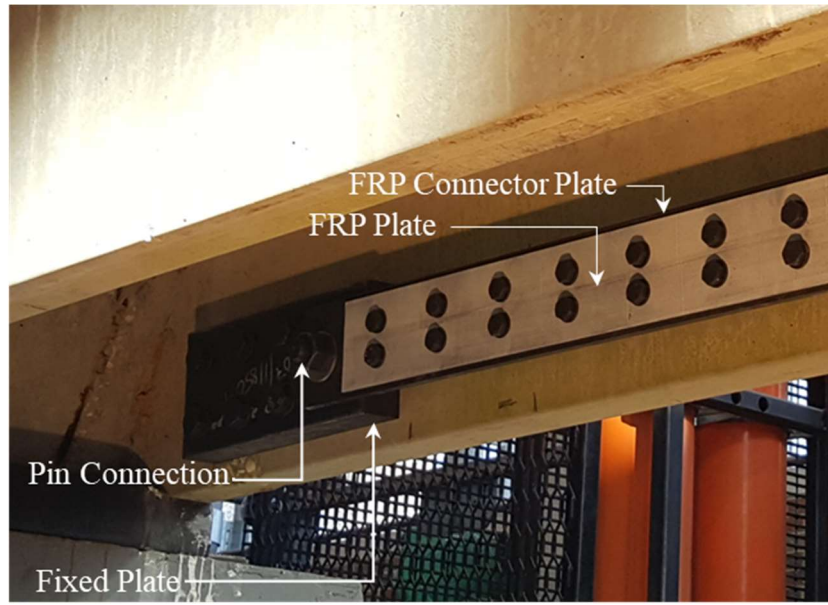
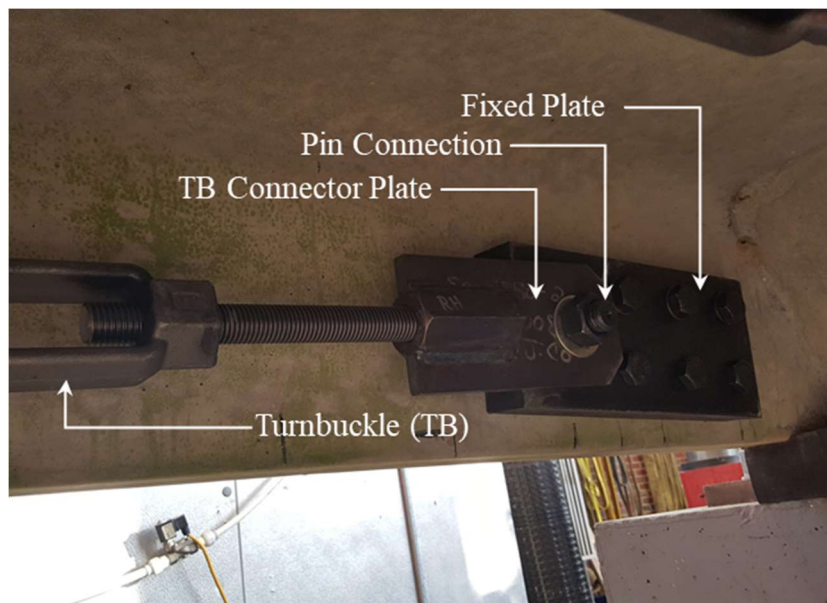
(b) dead-end elevation detail



(c) live-end elevation detail

**Figure 6.8:** MF-FRP 2.0 design details.

Note: All dimensions are in millimeters, 1 in. = 25.4 mm; "+" denotes a single prestressing strand

(a) *dead-end*(b) *live-end***Figure 6.9:** MF-FRP 2.0 connection photos.

MF-FRP 2.0 uses a fixed plate connection at each end of the C-channel beam to transfer the forces between the MF-FRP system and the beam. Forces are transferred through six 18.8 mm (0.75 in.) diameter bolts at each end of the C-channel beam (Figures 6.8 and 6.9), similar to the live-end of MF-FRP 1.0. The transverse spacing between the fixed plate bolts is reduced to 76 mm (3.0 in.) (Figures 6.8b and 6.8c) to optimize concrete splitting behavior and reduce the weight of the 50 mm (2 in.) fixed plate

such that one worker can feasibly lift the plate into place during installation. The fixed plate is connected to an FRP connector plate at the dead-end (Figure 6.9a) and a turnbuckle (TB) connector plate at the live-end (Figure 6.9b) through a pin connection to allow rotation and prevent internal moment in the FRP plate as the beam deflects under applied loads. The TB connector plate connects to the turnbuckle and FRP connector plates at the live-end through a welded connection (Figures 6.8b and 6.9b) configured so that the centerline of the turnbuckle and connector plates are aligned to minimize internal moment due to eccentricity. Additionally, the depth of the FRP centerline with respect to the beam cross-section is 272 mm (11 in.) in MF-FRP 1.0 (Figures 6.6a and 6.6b) and 330 mm (13 in.) in MF-FRP 2.0 (Figure 6.8a). This 21% increase in depth increases effectiveness of the FRP, reducing the FRP tensile force required for the same level of strengthening compared to MF-FRP 1.0.

MF-FRP 2.0 is optimized in accordance with AISC (2015) design guidelines with a design strength of 222 kN (50 kips) – 10% greater than the ultimate strength of the FRP plate in uniaxial tension. The controlling limit state of the MF-FRP 2.0 steel connection components is bolt bearing on the steel plate at the pin connection on both the dead- and live-end.

Factors other than design strength influence the thickness of the fixed plate in both connection designs. The thickness of the fixed plate for MF-FRP 1.0 is 32 mm (1.25 in.) to provide clearance between the concrete stem and turnbuckle such that the body of the turnbuckle can be rotated. The thickness of the fixed plate for MF-FRP 2.0 is due to the shoulder length (38 mm / 1.5 in.) and head thickness (25 mm / 1.0 in.) of the commercially-available shoulder bolt that is used as the pin connection in Figures 6.8 and 6.9. A custom turnbuckle or pin connection could be designed to further reduce the thickness of the fixed plate if desired.

#### *Concrete splitting*

Design guides that model concrete splitting behavior due to mechanical fasteners can be used to check the capacity of the concrete at each bolt. Equation 6.4 is a model presented by Oehlers (2001) that determines the minimum concrete splitting force for shear studs and bolted connections in composite steel and concrete elements where the length of the fastener is greater than  $1.8d_{bolt}$ :

$$P_{split} \approx 7\pi c d_{bolt} f_t \left(1 - \frac{d_{bolt}}{2c}\right)^{-2} \quad (6.4)$$

where  $P_{split}$  is the minimum force at which splitting occurs,  $d_{bolt}$  is the diameter of the bolt,  $c$  is the concrete cover to the side of the bolt, and  $f_t$  is the splitting tensile strength of the concrete in the strengthened member. Using 12.7 mm (0.5 in.) diameter bolts, a minimum concrete cover of 19 mm (0.75 in.), and concrete splitting tensile strength of 2.92 MPa (425 psi),  $P_{split}$  for a typical C-channel section with the retrofit installed is 35.1 kN (7.9 kips) per bolt at the dead-end of MF-FRP 1.0. Assuming uniform distribution of force in the FRP plate at ultimate load conditions, the maximum force per bolt is 10.2 kN (2.3 kips), which is below the splitting force. Therefore, force transfer between the FRP plate and the concrete substrate at the dead-end of MF-FRP 1.0 will not result in concrete splitting.

Using Equation 6.4 to check concrete splitting at the live-end of MF-FRP 1.0, the minimum  $P_{split}$  is 87.6 kN (19.7 kips) per bolt, and the maximum force per bolt, assuming uniform distribution at ultimate load conditions, is 33.4 kN (8.3 kips) per bolt; therefore, the bearing force at the bolts on the live-end of MF-FRP 1.0 and both ends of MF-FRP 2.0 will not result in concrete splitting.

The 76.2 mm (3.0 in.) transverse spacing and 82.6 mm (3.25 in.) longitudinal spacing of bolts at the dead- and live-end of MF-FRP 2.0 (Figure 6.8) are designed using Equations 6.5 and 6.6:

$$s_L \geq 1.4b_{eff} \quad (6.5)$$

and

$$s_T \geq b_{eff} \quad (6.6)$$

where  $s_L$  is the center-to-center longitudinal spacing of bolts (mm / in.),  $s_T$  is the edge-to-edge transverse spacing of bolts (mm / in.), and  $b_{eff}$  is the effective width of the connection (mm / in.). Using an initial effective connection width of 57.2 mm (2.25 in.) – center-to-center spacing minus  $d_{bolt}$ , the minimum  $s_L$  is 80.0 mm (3.15 in.) and minimum  $s_T$  is 57.2 mm (2.25); therefore, 82.6 mm (3.25 in.) and 76.2 mm (2.25 in.) were selected for  $s_L$  and  $s_T$ , respectively.

### ***Post-tensioning***

Restoration of prestress losses due to deterioration of the C-channel beam is achieved through post-tensioning of the FRP plate. The post-tensioning is delivered through the turnbuckle system at the live-end of the MF-FRP system (Figures 6.6d and 6.8c). To simulate field applications, the applied prestressing force in each FRP plate is determined through an application of Hooke's Law using Equations 6.7 and 6.8:

$$P_{FRP} = \frac{(\Delta L_p)(A_{FRP})(E_{FRP})}{L_g} \quad (6.7)$$

and

$$\Delta L_{TOT} = \Delta L_p + \Delta L_{slip} \quad (6.8)$$

where  $\Delta L_p$  is the change in length of the FRP plate due to the applied prestress force,  $L_g$  is the gauge length over which  $\Delta L_p$  is measured,  $A_{FRP}$  is the cross-sectional area of the FRP,  $E_{FRP}$  is the elastic modulus of the FRP,  $P_{FRP}$  is the prestress force in the FRP,  $\Delta L_{slip}$  is the axial displacement of the FRP plate to account for bolt slip in the connections, and  $\Delta L_{TOT}$  is the total axial displacement required to achieve the desired  $P_{FRP}$ . For the FRP plate used in this study,  $A_{FRP}$  is 300 mm<sup>2</sup> (0.5 in.<sup>2</sup>), and  $E_{FRP}$  is provided by the manufacturer as 62,190 MPa (9.02 x 10<sup>6</sup> psi) (Strongwell, 2016). Hooke's Law is an appropriate application at prestress load levels based on the linear behavior of the FRP presented by McCoy et al. (2019a).

Prior to post-tensioning, an indicator was affixed to the FRP and a mark was placed on the interior of the stem near the live-end. A second mark was placed on the stem at the desired  $\Delta L_{TOT}$  distance from the first mark (Figure 6.10). The gauge length,  $L_g$  was measured on each test specimen from the mid-point of the 22-bolt anchor zone at the dead-end to the indicator affixed to the FRP plate. The mid-point of the anchor zone was used because the elongation of the FRP plate through the 22-bolt anchor region is assumed to linearly decrease through the anchor region toward the end of the FRP plate. The measured  $L_g$  for each MF-FRP 1.0 specimen was 3785 mm (149 in.), and the desired  $P_{FRP}$  was 82.3 kN (18.5 kips) to restore  $P_e$  for the HS strand that was cut to simulate moderate deterioration. Therefore, using Equation

6.7, the desired  $\Delta L_p$  was 15.5 mm (0.61 in.). The effect of bolt slip between the FRP and steel plate, and the fixed plate and the concrete was also included.  $\Delta L_{slip}$  was taken as the difference between the hole and bolt diameters. Therefore,  $\Delta L_{slip}$  for MF-FRP 1.0 was 9.5 mm (0.375 in.). Using Equation 6.8,  $\Delta L_{TOT}$  for the MF-FRP 1.0 specimens was 25 mm (1 in.). The measured  $L_g$  for the MF-FRP 2.0 specimens was 5080 mm (200 in.), and the desired  $P_{FRP}$  remained 82.3 kN (18.5 kips).  $\Delta L_{slip}$  for MF-FRP 2.0 was 10.3 mm (0.406 in.) and, using Equation 6.7,  $\Delta L_p$  was 24.3 mm (0.958 in.). Thus,  $\Delta L_{TOT}$  for MF-FRP 2.0 was approximately 35 mm (1.38 in.). The marks for the  $\Delta L_{TOT}$  measurement for MF-FRP 2.0 are shown in Figure 6.10.

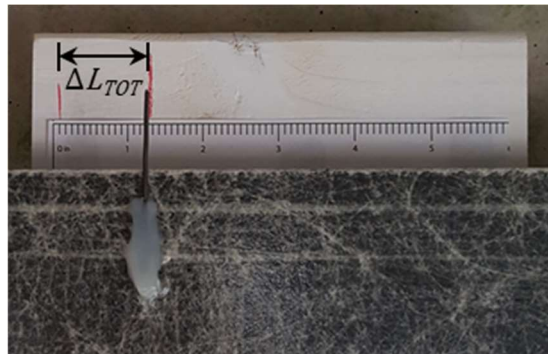


**Figure 6.10:**  $\Delta L_{TOT}$  measurement marks for MF-FRP 2.0 at  $P_{FRP} = 82.3$  kN (18.5 kips).  
*Note: scale in figure is in inches; 1 in. = 25.4 mm*

Throughout the post-tensioning process for all test specimens, FRP strain at mid-span was monitored using electric resistance strain gauges. The strain gauge measurement was used to maintain consistency between test specimens and to confirm the application of Hooke's Law for determining  $P_{FRP}$  in the field where strain gauges are not normally practical as a method for measuring the level of applied prestress force. Post-tensioning of the FRP was stopped when the measured strain in the FRP,  $\epsilon_{FRP}$ , reached 4100  $\mu\epsilon$ , the FRP strain which corresponds to  $P_{FRP} = 82.3$  kN (18.5 kips), at which point  $\Delta L_{TOT}$  was confirmed with the marks on the FRP and concrete stem (see Figure 6.10).

All steel plate components for MF-FRP 1.0 and MF-FRP 2.0 are constructed of A572 Grade 50 steel, and A325 Grade 8 bolts are used for all bolted connections. However, for long-term durability in corrosive environments, such as bridges in coastal regions, it is recommended that connection

components be constructed of stainless steel to resist corrosion and to increase durability, bearing in mind that a service life of in the order of 5 years is typically expected for the application under consideration.

## Results and Discussion

### Test results

Table 6.5 provides a summary of test results, including ultimate load capacity and failure mode for all C-channel test specimens. Specimen U failed by concrete crushing (CC) at an applied load of 132 kN (29.6 kips). This ultimate capacity is 185% of the HS-15 internal live load moment, and serves as a benchmark for the MF-FRP-D1 and MF-FRP-D2 test specimens.

**Table 6.5:** C-channel Test Results Summary.

Specimen ID	U	D	MF-FRP-U1	MF-FRP-U2	MF-FRP-D1	MF-FRP-D2
HS-15 Live Load, kN (kips)	71.3 (16.0)	71.3 (16.0)	71.3 (16.0)	71.3 (16.0)	71.3 (16.0)	71.3 (16.0)
Ultimate Load, kN (kips)	132 (29.6)	83.6 (18.8)	156 (35.1)	166 (37.3)	123 (27.6)	116 (26.1)
Percent increase from U, %	--	-36.6	18.1	25.8	-6.85	-12.1
Percent capacity of HS-15, %	185	117	219	233	172	163
Maximum measured FRP tensile strain, $\mu\epsilon$	--	--	7380	6425	7980	6712
Maximum FRP tensile force, <sup>1</sup> kN (kips)	--	--	148 (33.2)	128 (29.0)	160 (36.0)	135 (30.3)
Failure Mode <sup>2</sup>	CC	CC	LS/R, CC	CC	LS/R, CC	CC

Notes: 1) obtained from strain gauge and application of Hooke's Law; 2) LS is longitudinal splitting, R is rupture, CC is concrete crushing

Specimen D, with the bottom HS strand in each stem cut at mid-span, also failed by concrete crushing at an applied load of 83.4 kN (18.7 kips). The induced damage to simulate moderate deterioration in the field resulted in a 37% reduction in capacity compared to Specimen U, that is undamaged and unstrengthened.

MF-FRP-U1 experienced an 18% increase in flexural capacity over U and failed by FRP longitudinal splitting (LS) and rupture (R), followed by concrete crushing. MF-FRP-D1 experienced a 47% increase over control Specimen D, but failed to reach the full undamaged capacity, achieving 93% of the ultimate capacity of control Specimen U. MF-FRP-D1 also failed by FRP longitudinal splitting and rupture followed by concrete crushing. Although the MF-FRP 1.0 retrofit system did not restore the full

undamaged capacity of the C-channel beam, the system did increase the capacity of the damaged beam such that it exceeded the HS-15 live load by approximately 52 kN (12 kips) – a factor of safety of 1.7; whereas, the unstrengthened, damaged beam failed at just 12 kN (3 kips) above the HS-15 live load – a factor of safety of 1.2.

The mid-span load-deflection behavior for all tests is shown in Figure 6.11. Mid-span deflection was determined by averaging the deflection at each stem measured by the two string potentiometers, and subtracting the average vertical displacement at the supports measured by the vertical potentiometers. The progressive FRP longitudinal splitting and rupture failure of MF-FRP-D1 is visualized in the load-deflection curves (Figure 6.11) with the “step-wise” decrease after ultimate load due to progressive loss in FRP cross-sectional area. MF-FRP-U1 did not experience incremental FRP rupture, but rather instantaneous longitudinal splitting and rupture failure just before concrete crushing, visualized as the instantaneous drop in load at approximately 200 mm of mid-span deflection.

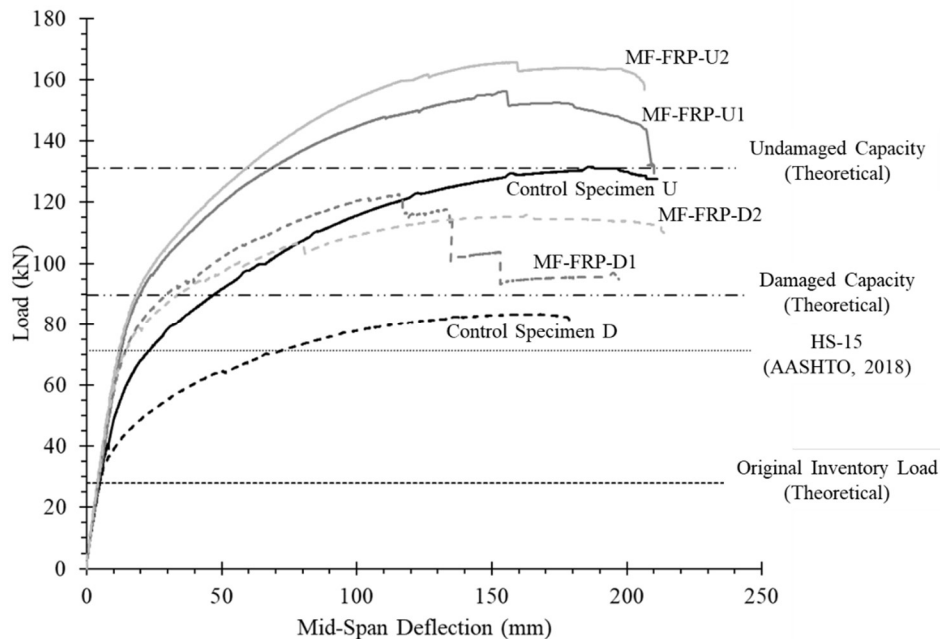


**Figure 6.11:** Full-scale C-channel beam load-deflection results.

*Note: 1 kip = 4.4482 kN; 1 in. = 25.4 mm*

The load-deflection behavior in Figure 6.11 is also compared to the theoretical inventory load, theoretical undamaged ultimate capacity, and theoretical damaged ultimate capacity. The theoretical inventory load is determined by calculating the internal moment at which concrete tensile stress is 0 for

an undamaged C-channel beam. Therefore, using the calculations presented by McCoy et al. (2019b), an internal live load moment, including impact, of 64.1 kN-m (47.3 k-ft.) is considered the inventory load for a candidate bridge in a coastal region (the most conservative inventory load situation), which corresponds to an applied load of 28 kN (6.3 kips). This is shown in Figure 6.11, and lies well within the elastic region of the load-deflection curves for all test specimens, which indicates the beam would experience no damage from continued loading over an extended period of time at this inventory load. The calculations for the theoretical undamaged and theoretical damaged nominal maximum moment capacities are also presented in detail by McCoy et al. (2019b). The theoretical undamaged nominal moment capacity,  $M_{n,undamaged}$  is 300 kN-m (221 k-ft.) and the theoretical damaged nominal moment capacity,  $M_{n,damaged}$  is 205 kN-m (151 k-ft.), which corresponds to an applied load of 131 kN (29.5 kips) and 89.4 kN (20.1 kips), respectively (Figure 6.11). The maximum applied load for control Specimen U coincides very well with the theoretical undamaged capacity at 101% of  $M_{n,undamaged}$ , and the applied load for control Specimen D is 94% of  $M_{n,damaged}$  (see Table 6.5 and Figure 6.11).

The applied load that generates the HS-15 live load moment, including impact, (AASHTO, 2018) is also shown in Figure 6.11. For control Specimen U, the load-deflection curve intersects with the HS-15 live load just beyond the elastic region at approximately 25 mm (1 in.) of mid-span deflection. This indicates that incremental damage may occur at this load, which corresponds to the definition of the operating rating (AASHTO, 2018). Although the maximum load for MF-FRP-D1 is 93% of the maximum load for control Specimen U, the load-deflection curve for MF-FRP-D1 intersects with the HS-15 live load at approximately 10 mm (0.4 in.), which is less than 50% of the HS-15 live load deflection for control Specimen U and is just within the elastic region of the strengthened damaged section. This indicates that the MF-FRP 1.0 system is capable of restoring the HS-15 live load capacity of the beam. However, the failure mode of MF-FRP-D1 was initiated with longitudinal splitting of the FRP, therefore, a modified MF-FRP retrofit system that prevents FRP failure and allows the beam to fail by concrete crushing is desired, which lead to the development of MF-FRP 2.0 as previously described.

During the MF-FRP-U1 and MF-FRP-D1 tests, bending of the FRP plate about its strong axis at the dead-end was observed as can be seen in Figure 6.12a. This is due to the fixity condition of the 22-bolt dead-end connection and the side-stem application of the FRP, resulting in the combination of flexural and axial tensile stresses in the FRP causing longitudinal splitting failure of the FRP plate (Figures 6.12b and 6.12c). McCoy et al. (2019a) determined that the capacity of the 22-bolt connection in uniaxial tension is 200 kN (45 kips); however, the FRP plates on MF-FRP-U1 and MF-FRP-D1 ruptured at 148 kN (33 kips) and 160 kN (36 kips), respectively, well below the expected ultimate capacity for the connection. The FRP rupture at a lower capacity is due to the longitudinal splitting at the dead-end. To reduce this increased stress due to flexure in the FRP plate, the MF-FRP 2.0 connection design uses a pin connection (Figures 6.8 and 6.9) to allow rotation at each end of the C-channel such that the FRP plate remains in uniaxial tension throughout the loading of the C-channel eliminating the development of flexural stresses in the FRP. This prevents longitudinal splitting rupture of the FRP and increases the efficiency of the MF-FRP system.

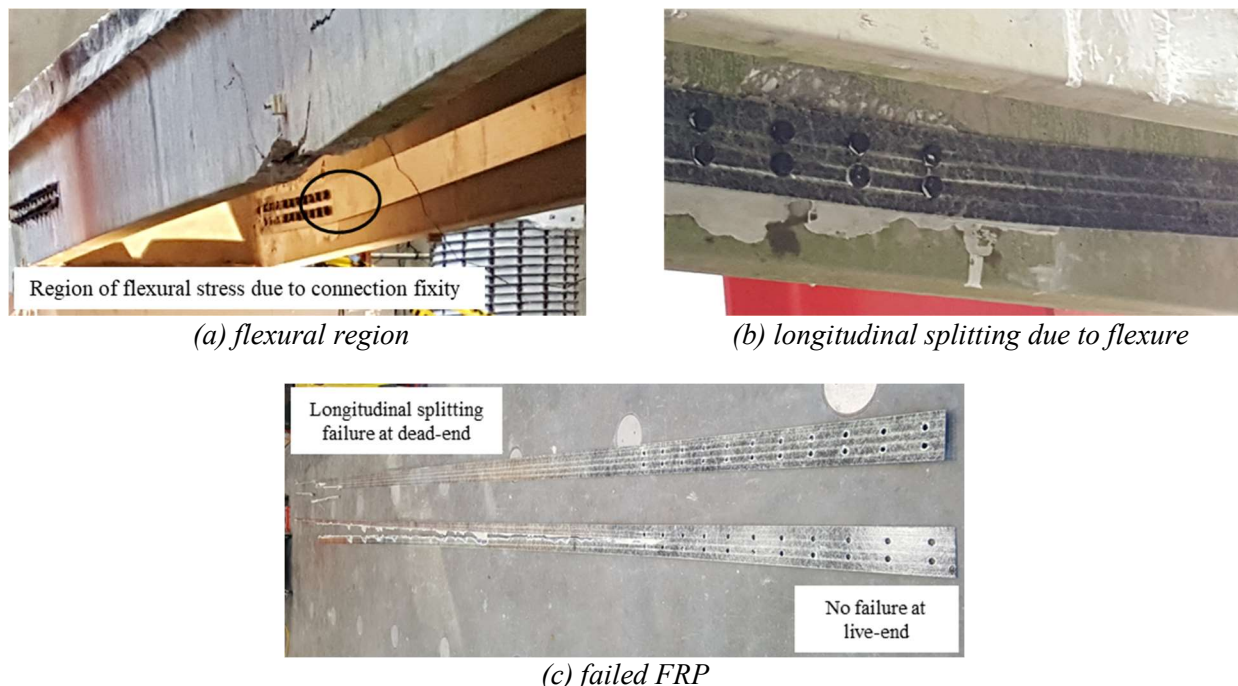


**Figure 6.12:** FRP failure mode for MF-FRP 1.0.

MF-FRP-U2 experienced a 26% increase in ultimate capacity compared to control Specimen U, and the ultimate load capacity for MF-FRP-D2 was 88% of the ultimate capacity for control Specimen U and

94% of the ultimate capacity of MF-FRP-D1. The reduction in ultimate capacity of MF-FRP-D2 compared to MF-FRP-D1 is due to the greater reduction in effective depth of the FRP as the beam deflects during the test, and the lack of moment developed in the FRP plate. However, although the ultimate capacity of MF-FRP-D2 is less than MF-FRP-D1, the MF-FRP 2.0 system increases the damaged stiffness and capacity of the C-channel such that the HS-15 operating load is within the elastic region of the load-deflection curve (Figure 6.11), and therefore, the MF-FRP 2.0 system restores both the inventory and operating ratings of the damaged C-channel specimen to pre-damaged levels, which allows for posted load restrictions and detours to be removed.

Both MF-FRP-U2 and MF-FRP-D2 failed by concrete crushing only (Table 6.5). The FRP in MF-FRP-U2 and MF-FRP-D2 did not experience longitudinal splitting or rupture, as in MF-FRP-U1 and MF-FRP-D1, and, therefore, provided for a more ductile failure of MF-FRP-D2 compared to that of MF-FRP-D1. This ductile failure of the MF-FRP 2.0 system design, visualized in the extended load plateau of MF-FRP-D2 (Figure 6.11), is similar to that of control Specimen U and is a more desirable failure than the brittle failure caused by the longitudinal splitting and rupture of the FRP in MF-FRP-D1. Additionally, the un-failed FRP in MF-FRP 2.0 achieved a maximum tensile force of 128 kN (29.0 kips) and 135 kN (30.3 kips) for MF-FRP-U2 and MF-FRP-D2 (Table 6.5), respectively, leaving an FRP reserve capacity of approximately 67 kN (15 kips) for the MF-FRP 2.0 system, or 33% of the 200 kN (45 kips) ultimate capacity. This reserve capacity in the FRP allows for a higher prestress force to be applied, if necessary, up to 98 kN (22 kips) based on the behavior presented by McCoy et al. (2019a), to achieve restoration of inventory and operating ratings of the deteriorated C-channel.

The MF-FRP 1.0 and MF-FRP 2.0 systems experienced some minor local concrete splitting near the fixed plate connection. The local splitting occurred in-line with bottom prestressing strand in the stem, and is due to the reduced concrete cover at the location of the prestressing strand. In all cases, the local splitting allows for the prestressing strand to debond from the concrete, but did not impact the overall performance of the MF-FRP retrofit solution. The debonding of the bottom prestressing strand is not of concern, as the purpose of the MF-FRP retrofit solution is to restore the prestressing effects that would be

lost due to deterioration in the field. In many field cases, the bottom prestressing strand is not present, and the concrete section is restored with a plain concrete patch (McCoy et al., 2019b).

### ***Retrofit Installation***

The 28 holes per stem required for the installation of the MF-FRP 1.0 retrofit requires extensive drilling in each concrete stem, and the spalled concrete due to drilling at the dead-end requires patchwork to provide a smooth surface to attach the FRP. The installation time for all field-level tasks (those tasks which must be completed at the bridge site in the field) was recorded to compare the installation efficiency of the two MF-FRP retrofit designs. The times presented in Table 6.6 shows the time to install the MF-FRP retrofit system on both stems of a single C-channel, and categorizes the total time for each task into working time, contributing time, and not working time. Working time (W) is time spent performing the actual task (i.e. drilling), contributing time (C) is time spent performing a supporting task (i.e. moving the dust collector during drilling), and not working time (NW) is all other time spent on the project (i.e. rest breaks).

**Table 6.6:** MF-FRP Retrofit Installation Times for a Single C-channel.

Task	Installation Time (labor-hrs.)							
	MF-FRP 1.0				MF-FRP 2.0			
	W	C	NW	TOTAL	W	C	NW	TOTAL
Locate steel	0.3	0.1	0	<b>0.4</b>	0.2	0.1	0	<b>0.3</b>
Drill live-end	0.8	0.5	0.8	<b>2.0</b>	0.5	0.5	0.3	<b>1.3</b>
Drill dead-end	1.0	1.0	1.0	<b>3.0</b>	0.5	0.5	0.3	<b>1.3</b>
Attach live-end	0.5	0.3	0.2	<b>1.0</b>	0.3	0.2	0	<b>0.4</b>
Attach dead-end	0.2	0.3	0	<b>0.7</b>	0.2	0.1	0	<b>0.3</b>
Post-tension FRP	0.4	0.5	0.4	<b>1.2</b>	0.3	0.3	0.0	<b>0.7</b>
<b>TOTAL</b>	<b>3.1</b>	<b>2.7</b>	<b>2.5</b>	<b>8.3</b>	<b>1.9</b>	<b>1.7</b>	<b>0.5</b>	<b>4.1</b>
<b>Percent of Total, %</b>	<b>37.7</b>	<b>32.7</b>	<b>29.6</b>	<b>100</b>	<b>46.9</b>	<b>40.8</b>	<b>12.2</b>	<b>100</b>

For both MF-FRP systems, a pachometer was used to locate the HS strands and shear reinforcement prior to drilling, and the placement of the MF-FRP system was adjusted to avoid the HS strands and reinforcement in the C-channel stems. All holes were drilled using a commercially-available hammer drill. A portable dust collection system with a snorkel attachment in accordance with Occupational Safety and Health Administration (OSHA 29 CFR 1926, 2017) requirements was used to mitigate the effects of

respirable crystalline silica dust during drilling operations. For MF-FRP 1.0, holes were drilled from the exterior of the stem due to size of the hammer drill and length of available bits. However, in a field installation, holes on interior stems would be drilled from the interior of the stem because adjacent beams would prevent access to the exterior of the stems with a hammer drill. Access, however, is sufficient for installation of washers and nuts on the exterior of the stem. Therefore, a compact hammer drill and bits were purchased for the installation of MF-FRP 2.0 such that holes could be drilled from the interior of the C-channel to replicate a field installation. Drilling holes from the interior of the stem also eliminates the need for grout at the dead-end, as previously mentioned; therefore, grout installation at the dead-end is not included in the time analysis in Table 6.6.

MF-FRP 2.0 reduces the total number of field-level drilled holes per beam by more than 50% from 56 to 24, which reduces the time to drill the dead-end by 1.7 labor-hours (Table 6.6). With MF-FRP 2.0, the FRP plate is not attached directly to the stem reducing the number of bolts placed in the field at the dead-end which also reduces the time to attach the live-end for MF-FRP 2.0 by 0.6 labor-hours. Additionally, the concrete drilling process for the dead- and live-ends of MF-FRP 2.0 was optimized through the use of shop-prepared templates and drilling a 9.5 mm (0.125 in.) diameter pilot hole for each bolt followed by incrementally increased diameters of 12.7 mm (0.5 in.), 19.1 mm (0.75 in.) and 22.2 mm (0.875 in.) to achieve the desired, over-sized hole diameter for the 19.1 mm (0.75 in.) diameter bolts. Incrementally increasing the hole diameter allowed for increased efficiency and a less labor-intensive drilling process, resulting in less break time (non-working time). Further, incrementally increasing the diameter of each hole significantly reduced concrete spalling on the exterior of the stem, increasing the available bearing surface of concrete at each bolt. The reductions in installation time not only reduces labor costs, but also reduces muscle exertion and noise exposure, which leads to reduced worker fatigue, fewer errors, and fewer safety risks.

The time required to post-tension the FRP installed on both stems remains the same for both MF-FRP 1.0 and MF-FRP 2.0. During post-tensioning, a large wrench was used to rotate the turnbuckle. A second wrench was used to hold the FRP connector plates to prevent the plates from rotating while the turnbuckle

was tightened. To maintain symmetry of internal forces on the C-channel stems, post-tensioning was applied in equal increments, alternating on each stem. If possible, it would also be appropriate to post-tension the FRP plates simultaneously.

An additional consideration with the MF-FRP 2.0 design is the weight of individual components. The weight and total length of the live-end for MF-FRP 1.0 – fixed plate, turnbuckle, and FRP connector plate (Figure 6.6d) was greater than 23.1 kg (51 lb.), the maximum recommended weight limit (RWL) for a single-person two-handed lift (NIOSH, 1994), and therefore required two people to lift the system into place during installation. However, MF-FRP 2.0 was designed such that the fixed plates could be installed individually, without the FRP connector plates or turnbuckle attached. After the fixed plate is installed, the FRP or turnbuckle connector plates can be hung from the connector pin. The total weight of the fixed plate is approximately 19.5 kg (43 lb.), which is less than the RWL under ideal conditions (NIOSH, 1994), allowing for a single-worker two-handed lift and increasing efficiency in the field.

Shop-level tasks such as cutting and drilling holes in the FRP plate, and attaching the FRP plate to the FRP connector plates in MF-FRP 2.0 are not included in the installation time as they would be accomplished prior to crew-mobilization. It is expected that DOT field maintenance personnel would take pre-cut and pre-drilled FRP plates, pre-attached to steel FRP connector plates (MF-FRP 2.0) to the bridge site for installation. Therefore, only the tasks listed in Table 6.6 would be necessary at the bridge site, minimizing field labor time and costs.

Figure 6.13 provides a visual representation of the working, contributing, and not working times presented in Table 6.6. The complete process optimization for the installation of MF-FRP 2.0 reduced the total field-level installation time from 8.3 labor-hours for MF-FRP 1.0 to 4.1 labor-hours for MF-FRP 2.0 (Table 6.6) – a 53% reduction. The percentage of working time is increased from 38% of the total time for MF-FRP 1.0 to 47% of the total time for MF-FRP 2.0 (Table 6.6). Additionally, the percentage of not working time is reduced from 30% to 12% with the MF-FRP 2.0 design (Table 6.6). It is important to note, however, that installation time analysis is based on novice-level labor in a laboratory environment using 2 workers. Further optimization may be possible with increased experience and number of workers.

Therefore, it is recommended that field installation time analysis be included in future research planned for installation of MF-FRP 2.0 on in-service candidate bridges, with DOT maintenance personnel. It is also recommended that a 4-worker crew size be employed in the field to allow the dead- and live-end activities to occur in parallel, providing greater optimization and a greater reduction in installation time.

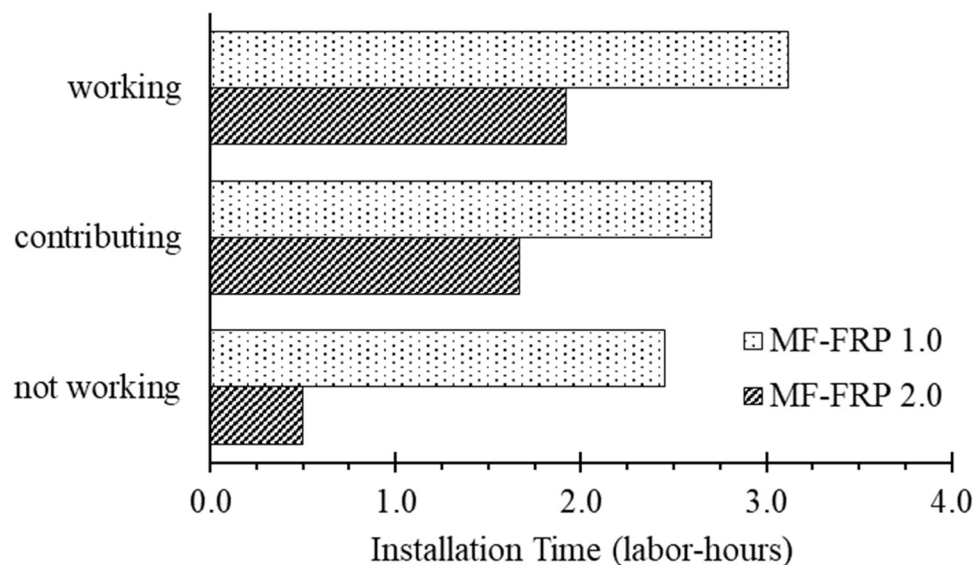


**Figure 6.13:** Installation time comparison of MF-FRP 1.0 and MF-FRP 2.0 by time category.

All installation times presented are for a single C-channel beam. Deteriorated C-channel bridges often have between two and four deteriorated beams per span, with the greatest deterioration occurring on the exterior girders, as in the case study bridge presented by McCoy et al. (2019a). In candidate bridges with four deteriorated C-channel beams, the total installation time for MF-FRP 2.0 (excluding mobilization and demobilization of installation personnel) would be 16.4 labor-hours. A typical 4-worker DOT maintenance crew has a total of 32 available labor-hours per 8-hour work day; therefore, it is feasible for a single span bridge with 4 deteriorated C-channel beams to be retrofitted with the MF-FRP 2.0 design in a single 8-hour work day, including mobilization and demobilization.

### ***Concrete strength***

The specified concrete compressive strength,  $f'_c$ , of the C-channel beams examined in this study was 34.5 MPa (5000 psi) (NCDOT, 1966). However, the equivalent in-place concrete compressive strength,

$f'_{c,eq}$ , of the beams at time of testing was desired to account for the actual concrete capacity. Cores were drilled from the flange of three of the six tested beams (MF-FRP-D1, MF-FRP-U2, and MF-FRP-D2) to determine  $f'_{c,eq}$ . A total of 8 cores were drilled using a 100 mm (4 in.) outer diameter coring bit. The cores were drilled and prepared in accordance with ASTM C42 (2018) and ACI 214.4 (2010) and tested in accordance with ASTM C39 (2018). Individual core strengths,  $f_{core}$ , were adjusted to account for variability due to damage during drilling, moisture conditioning, and geometric properties of the core. Adjusted core strengths are then considered the individual in-place strength of concrete,  $f_{ci}$ , at the location the core was extracted from in the C-channel beam (ACI 214.4, 2010). Using the ACI 214.4 Alternate Method (2010),  $f'_{c,eq}$  is 56.6 MPa (8210 psi) at the 90% confidence limit; therefore,  $f'_{c,eq} = 56.5$  MPa (8200 psi) is appropriate for design purposes. Differences between  $f'_c$  and  $f'_{c,eq}$  are not uncommon in practice, and are due to a number of factors including concrete strength gain with maturity, concrete batch plant considerations, and high early concrete strength requirements during casting. Therefore, it is recommended that  $f'_{c,eq}$  be determined and incorporated into design and analysis for all candidate bridges prior to the installation of the MF-FRP retrofit.

Using  $f'_{c,eq}$  determined from cores taken from the flange of the beams assumes the concrete strength in the stem of the C-channel is consistent with the strength in the flange. This should be verified through appropriate concrete evaluation techniques in field applications where deterioration of the stems may be inconsistent with the flange, but is not of concern for the purposes of this investigation because the C-channel beams tested were received in good condition with no deterioration. Individual core strengths and in-place strengths for the 8 extracted cores are presented in Table 6.7.

**Table 6.7:** C-channel Concrete Core Data.

Specimen	Core	$f_{core}$ , MPa (psi)	Strength Correction Factors (ACI 214.4, 2010)				Adjusted $f_{core}$ MPa (psi)
			$F_{ga}$ <sup>1</sup>	$F_{dia}$ <sup>2</sup>	$F_{mc}$ <sup>3</sup>	$F_d$ <sup>4</sup>	
MF-FRP-D1	C1	73.4 (10650)	0.95	1.0	0.96	1.06	74.0 (10730)
	C2	84.4 (12240)	0.94	1.0	0.96	1.06	84.3 (12220)
	C3	72.0 (10440)	0.94	1.0	0.96	1.06	71.4 (10360)
	C4	84.2 (12210)	0.95	1.0	0.96	1.06	84.3 (12230)
MF-FRP-U2	C5	68.7 (9960)	0.92	1.0	0.96	1.06	67.1 (9730)
	C6	55.2 (8000)	0.92	1.0	0.96	1.06	53.8 (7810)
MF-FRP-D2	C7	62.0 (8990)	0.92	1.0	0.96	1.06	60.3 (8750)
	C8	78.5 (11380)	0.92	1.0	0.96	1.06	77.6 (11260)

Notes: 1) length-to-diameter ratio; 2) core diameter; 3) moisture content; 4) damage during coring

## Conclusions and Recommendations

This research presents unique results related to the restoration of deteriorated prestressed concrete C-channel beams retrofitted with two designs for a post-tensioned MF-FRP retrofit solution. The test results and retrofitted C-channel behavior are compared to damaged (deteriorated) and undamaged control C-channel beams. The research presents the following conclusions:

- 1) MF-FRP 1.0 and MF-FRP 2.0 retrofit designs sufficiently restore a damaged C-channel with moderate deterioration at the location of maximum moment such that the retrofitted C-channel is capable of supporting the original operating and inventory ratings. However, MF-FRP 1.0 allows an in-plane moment in the FRP plate to develop near the dead-end anchor zone, which introduces flexural stresses not present in uniaxial tension loading. This in-plane moment causes longitudinal splitting and rupture of the FRP plate at 69% of the uniaxial tension capacity.
- 2) MF-FRP 2.0 retrofit design fails in concrete crushing only resulting in a more ductile failure mode compared to that of MF-FRP 1.0. The residual capacity of the FRP plate at concrete crushing is 33% of the ultimate FRP capacity. This residual capacity in the FRP plate, gives engineers

flexibility to increase the prestress force beyond the 82.3 kN (18.5 kips) applied in this investigation, up to 98 kN (22 kips), which would further increase the inventory and operating ratings of the retrofitted C-channel beams.

- 3) MF-FRP 1.0 has a total installation time of 8.3 labor-hours for a single C-channel beam, with 30% non-working time. MF-FRP 2.0 reduces the total installation time to 4.1 labor-hours for single C-channel beam, of which only 12% is non-working time. The installation time for MF-FRP 2.0 is 49% of the MF-FRP 1.0 installation time, and is sufficiently reduced such that a 4-worker maintenance crew can install the retrofit on a deteriorated bridge within an 8-hour workday.
- 4) Both MF-FRP 1.0 and MF-FRP 2.0 require the concrete in the C-channel stems to be of sound concrete at the location where the retrofit is attached to the concrete substrate (fixed plates in MF-FRP 2.0). This should be verified through appropriate field inspection techniques (discussed in Appendix D) prior to installation of the MF-FRP retrofit.
- 5) The turnbuckle prestressing mechanism for both MF-FRP 1.0 and MF-FRP 2.0 remains in place, allowing for the prestress level in the system to be increased or decreased at a later time if necessary. This also allows for the prestress in the retrofit to be increased, or completely removed to either remove the MF-FRP retrofit system or replace the FRP plate, if necessary, to extend the life of the retrofit solution. Further, it should be noted that the connection hardware in the MF-FRP system can be re-used in future applications, increasing the value of the system and any life-cycle cost analysis.

Future research to examine the behavior of the MF-FRP retrofit solution on a variety of prestressed concrete superstructure cross-sections, to include hollow core slabs, is recommended. Current research is on-going to examine the long-term performance of the retrofit solution under sustained and fatigue loading. Additionally, research to examine the long-term behavior of the retrofit system on in-service bridges is expected.

**Acknowledgements**

The authors would like to thank the NCDOT and the NSF I/UCRC *Center for the Integration of Composites into Infrastructure* (CICI) for funding the research. Additionally, the authors would like to acknowledge Cleveland City Forge for providing the turnbuckles used in MF-FRP 1.0 and MF-FRP 2.0 system designs, Mr. William Briley at the NCDOT Division 5 Bridge Maintenance Division for providing the C-channel beams for testing.

## **CHAPTER 7: CONCLUSIONS AND RECOMMENDATIONS FOR FUTURE RESEARCH**

### **Conclusions**

Both inventory and operating rating criteria (AASHTO, 2016) must be addressed to remove posted load limits and closures on deteriorated prestressed concrete bridges. While operating rating criteria typically control the overall member rating, a retrofit solution that provides strengthening only, without restoring prestress losses, would likely create a situation in which inventory rating criteria control. Therefore, a complete retrofit solution must also address the concrete stress limits within the inventory rating criteria to effectively remove posted load limits or closure, and allow the bridge to remain in service without restrictions. The following conclusions are presented as a result of this research.

- 1) The methodology and experimental program presented in Chapters 3 through 6 successfully address the challenges that are fundamental to rapid restoration of deteriorated prestressed concrete superstructures such that inventory and operating rating limits can be restored to the original level and posted load restrictions removed.
- 2) The conclusions presented in Chapters 4 and 5 are specific to the commercially-available FRP plate examined in this research. If an FRP plate material is used other than the one examined in this research, an experimental program similar to those in Chapters 4 and 5 should be used to investigate the capabilities and behavior of the FRP within the context of the desired MF-FRP retrofit solution.
- 3) Given the FRP plate examined in this study:
  - a. The mean peak load for the 0.5 in. (12.7 mm) 18-, 20-, and 22-bolt treatments is approximately 89% of the peak load capacity of the FRP plate with holes. The 22-bolt treatment is sufficiently optimized considering peak bearing stress (less than 18- and 20-bolt treatments), peak load (equal to 18- and 20-bolt treatments), and total anchor length (100 mm longer than the 20-bolt treatment) given a 12.7 mm diameter fastener. Longitudinal shear failure controls the ultimate capacity of the open-hole and multi-bolt treatment conditions with greater than 14 bolts resulting in a progressive brittle failure, and bearing failure controls

- the ultimate capacity of single-bolt (with  $e > 3D$ ) and multi-bolt treatment conditions with 14 or fewer bolts resulting in a more ductile failure compared to treatments with greater than 14 bolts.
- b. The DBL-B-0.375 treatment groups presented in Chapter 5 have load capacities similar to that of the DBL-B treatment groups presented in Chapter 4. The DBL-B-0.375 treatment group have increased displacement behavior compared to the DBL-B treatment groups; however, with significantly increased variability. This increased displacement of the bearing failure at peak loads which occurs prior to longitudinal failure and gives a desirable early warning of failure; however, the high variability of the behavior introduces unpredictability of the fastener patterns with 0.375 in. (9.53 mm) diameter bolt. Therefore, it is recommended that the 0.5 in. (12.7 mm) bolt diameter fasteners be used in the MF-FRP retrofit, and further research, if desired, is recommended to reduce the variability of the DBL-B-0.375 treatment groups.
  - c. Although the bearing surface area was similar that of the DBL22-B treatment groups, the DBL14-B-0.75 treatment groups experienced significant reduction in load capacity due to the larger diameter hole reducing the cross-sectional area of the carbon tows and transverse glass fibers. However, the DBL14-B-6 treatment group, with a longitudinal shear plane increase of 50% over the DBL14-B-4 treatment group, only experienced a 17.5% increase in load capacity. Therefore, future research to investigate the impacts of increasing the longitudinal spacing of fasteners (and thus, the longitudinal shear plane of the FRP) on other fastener diameters is recommended if further optimization is desired.
- 4) MF-FRP 1.0 and MF-FRP 2.0 retrofit designs sufficiently restore a damaged C-channel with moderate deterioration at the location of maximum moment such that the retrofitted C-channel is capable of supporting the original operating and inventory loads. However, MF-FRP 1.0 allows an in-plane moment in the FRP plate to develop near the dead-end anchor zone, which introduces flexural

stresses not present in uniaxial tension loading. This in-plane moment causes longitudinal splitting and rupture of the FRP plate at 69% of the uniaxial tension capacity.

- 5) MF-FRP 2.0 retrofit design fails in concrete crushing only resulting in a more ductile failure mode compared to that of MF-FRP 1.0. The residual capacity of the FRP plate at concrete crushing is 33% of the ultimate FRP capacity. This residual capacity in the FRP plate, gives engineers flexibility to increase the prestress force beyond the 82.3 kN (18.5 kips) applied in this investigation, up to 98 kN (22 kips), which would further increase the inventory and operating ratings of the retrofitted C-channel beams.
- 6) MF-FRP 1.0 has a total installation time of 8.3 labor-hours for a single C-channel beam, with 30% non-working time. MF-FRP 2.0 reduces the total installation time to 4.1 labor-hours for single C-channel beam, of which only 12% is non-working time. The installation time for MF-FRP 2.0 is 49% of the MF-FRP 1.0 installation time, and is sufficiently reduced such that a 4-worker maintenance crew can install the retrofit on a deteriorated bridge within an 8-hour workday.
- 7) Both MF-FRP 1.0 and MF-FRP 2.0 require the concrete in the C-channel stems to be of sound concrete at the location where the retrofit is attached to the concrete substrate (fixed plates in MF-FRP 2.0). This should be verified through appropriate field inspection techniques (discussed in Appendix D) prior to installation of the MF-FRP retrofit.
- 8) The turnbuckle prestressing mechanism for both MF-FRP 1.0 and MF-FRP 2.0 remains in place, allowing for the prestress level in the system to be increased or decreased at a later time if necessary. This also allows for the prestress in the retrofit to be increased, or completely removed to either remove the MF-FRP retrofit system or replace the FRP plate, if necessary, to extend the life of the retrofit solution. Further, it should be noted that the connection hardware in the MF-FRP system can be re-used in future applications, increasing the value of the system and any life-cycle cost analysis.
- 9) Limited quantitative analysis, including maintenance crew cost and MF-FRP material cost for the DOT and VOC for detoured vehicles, estimates that the direct cost to the DOT is likely to be between \$25000 and \$75000 per repaired bridge, depending upon the extent of deterioration and length of the

bridge, and the VOC varies between \$270 and \$14000 per day depending upon the volume of traffic and detour length for a bridge with a posted weight restriction. These estimated values indicate that a break-even duration between DOT direct costs and customer VOC can be as little as just a few days in the case of a high traffic volume bridge with an above average detour length, or as long as 4 to 5 months with a low traffic volume bridge and below average detour length. Detailed analysis to provide a complete cost-benefit analysis is possible for specific candidate bridges using available BMS information and detailed labor and material costs.

### **Future Research**

The following recommendations for future research are presented.

- 1) The effects of fatigue loading and sustained loading on the performance of the bolted connections examined in this thesis is also of interest for a comprehensive MF-FRP retrofit solution. It is necessary to understand the effects of fatigue on the FRP due to bolt bearing in the connection to provide a failure envelope for design engineers to consider across a range of candidate bridges with varying levels of traffic demands. Additionally, the creep behavior of the FRP at the mechanical connection is critical due to the application of a constant prestress force on the MF-FRP system.
- 2) Future research is necessary to examine the effects of bolt torque on the MF-FRP system connection, and the variability of the 0.375 in (9.5 mm) diameter bolt pattern such that additional options are available within the suite of solutions for the MF-FRP retrofit.
- 3) Future research is needed to develop an analytical model to predict the behavior of various cross-sections with the MF-FRP retrofit solution installed. The model would be useful to engineers to determine the appropriate MF-FRP retrofit with respect to number and diameter of mechanical fasteners and number of FRP plates to restore deteriorated superstructures. Additional design considerations might also include FRP rupture due to longitudinal shear failure, FRP bearing, concrete splitting at the connection and crushing behavior in the compression region of the beam, and yielding of the connection and bolt shear.

- 4) The development of analysis and design tools that apply the inventory and operating rating criteria to a range of cross-sections would be useful. These tools must also be capable of incorporating the effects of prestressed MF-FRP retrofit solutions, such as the one presented in this study. Layered-sectional-analysis modeling techniques are recommended for the development of a tool that will enable practicing engineers to design MF-FRP retrofit solutions for candidate bridge superstructures and analyze load rating criteria for bridge retrofitted with the proposed MF-FRP solution.
- 5) Case-study research of the MF-FRP retrofit on in-service deteriorated C-channel bridges is recommended to include environmental effects which are not included in the laboratory results presented in this study. Further, analysis of installation procedures of the MF-FRP retrofit on in-service bridges using DOT maintenance personnel is recommended to validate the presented procedure and allow for further improvement for maximum labor efficiency and reduced retrofit installation time.
- 6) Research which examines current NCDOT utility functions and BMS detour data that combine vehicle operating costs for deteriorated bridges with detour lengths due to posted restrictions or closures would be useful. VOC utility functions provide the basis for cost-sensitivity analysis, and aides in the formation of cost-benefit analyses and decision-making processes for DOT personnel to identify and prioritize MF-FRP retrofit candidate bridges.
- 7) Further research is needed to quantify the cost of installation and maintenance of the MF-FRP retrofit to aide in complete life-cycle-cost analysis. The proposed retrofit solution is likely a low-cost alternative to superstructure replacement and can be installed in a shorter period of time compared to existing externally-bonded, prestressed FRP retrofit alternatives.
- 8) Further research is necessary to extend the application of the MF-FRP retrofit solution to hollow core slab superstructures and other cross-sections. Research on various cross-sections should include full-scale lab testing of undamaged and deteriorated elements as well as long-term field studies on bridges currently in service, which are scheduled for replacement in 3 -5 years. After the in-service case study

elements are removed from service, full-scale tests in the lab would be useful to examine fatigue loading and environmental effects on the restoration of the deteriorated flexural element.

## REFERENCES

- AASHTO (2018). *The Manual for Bridge Evaluation, 3<sup>rd</sup> Ed.* American Association of State Highway and Transportation Officials, Washington, DC, 674.
- AASHTO (2017). *LRFD Bridge Design Specifications, 8<sup>th</sup> Ed.* American Association of State Highway and Transportation Officials, Washington, D.C., 1780.
- AASHTO (2016). *The Manual for Bridge Evaluation, 2<sup>nd</sup> Ed.* American Association of State Highway and Transportation Officials, Washington, D.C., 674.
- AASHTO (2013). *Manual for Bridge Element Inspection, 1<sup>st</sup> Ed.* American Association of State Highway and Transportation Officials, Washington, D.C., 406.
- ACI 214.4R (2010). "Guide for Obtaining Cores and Interpreting Compressive Strength Results," American Concrete Institute, Farmington Hills, MI, 17.
- ACI 318 (2014). "Building Code Requirements for Structural Concrete and Commentary," American Concrete Institute, Farmington Hills, MI, 520.
- ACI 440.2R (2017). "Guide for the Design and Construction of Externally Bonded FRP Systems for Strengthening of Concrete Structure." American Concrete Institute, Farmington Hills, MI, 2017, 116.
- ACI 562-16 (2016). "Code Requirements for Assessment, Repair, and Rehabilitation of Existing Concrete Structures and Commentary." American Concrete Institute, Farmington Hills, MI, 2016, 88.
- AISC (2015). *Steel Construction Manual, 14<sup>th</sup> Ed.* American Institute of Steel Construction Inc., Chicago, IL, 2192.
- Ammons, D. N. (2001). *Municipal Benchmarks: Assessing Local Performance and Establishing Community Standards, 2<sup>nd</sup> Ed.* Sage Publications Inc., Thousand Oaks, CA, 501.
- ASTM C42 (2018). "Standard Test Method for Obtaining and Testing Drilled Cores and Sawed Beams of Concrete," ASTM International, West Conshohocken, PA, 7.
- ASTM D3039 (2014). "Standard Test Method for Tensile Properties of Polymer Matrix Composite Materials." ASTM International, West Conshohocken, PA, 13.
- ASTM D5766 (2011). "Standard Test Method for Open-Hole Tensile Strength of Polymer Matrix Composite Laminates." ASTM International, West Conshohocken, PA, 7.
- ASTM D5961 (2017). "Standard Test Method for Bearing Response of Polymer Matrix Composite Laminates." ASTM International, West Conshohocken, PA, 31.
- ASTM D638 (2014). "Standard Test Method for Tensile Properties of Plastics." ASTM International, West Conshohocken, PA, 17.
- Bank, L. C. (2004). "Mechanically-fastened FRP (MF-FRP) – a viable alternative for strengthening RC members." *FRP Composites in Civil Engineering – CICE 2004*, R. Seracino (ed.), Taylor and Francis Group, London, 3-15.

- Bank, L. C., and Arora, D. (2007). "Analysis of RC beams strengthened with mechanically fastened FRP (MF-FRP) strips." *Composite Structures*, 79(2), 180-191.
- Bank, L. C., Lamanna, A. J., Ray, J. C., and Velazquez, G. I. (2002). "Rapid strengthening of reinforced concrete beams with mechanically fastened, fiber-reinforced polymeric composite strips." *Rep No. ERDC/GSL TR-02-4*, U.S. Army Corps of Engineers Engineer Research and Development Center, Vicksburg, MS, 99.
- Bartlett, F. M., and MacGregor, J. G. (1995). "Equivalent Specified Concrete Strength from Core Test Data," *Concrete International*, March, 52-58.
- Bartlett, F. M., and MacGregor, J. G. (1996). "Statistical Analysis of the Compressive Strength of Concrete in Structures," *ACI Materials Journal*, 93(1), 158-168.
- Bartlett, F. M. (2016). "Evolution of ACI 562 Code – Part 6: Quantification of in-place concrete strength using core tests," *Concrete International*, July, 36-39.
- Bomarito, G. F., Hochhalter, J. D., Ruggles, T. J., and Cannon, A. H. (2017). "Increasing accuracy and precision of digital image correlation through pattern optimization." *Optics and Lasers in Engineering*, 91, 73-85.
- Borowicz, D. T. (2002). "Rapid strengthening of concrete beams with powder-actuated fastening systems and fiber reinforced polymer (FRP) composite materials". M.S. Thesis, University of Wisconsin-Madison, Madison, WI.
- Borowicz, D. T., and Bank, L. C. (2013). "Effect of web reinforcement on the behavior of pultruded fiber-reinforced polymer beams subjected to concentrated loads." *Construction and Building Materials*, 47 347-357.
- Cavalline, T., Whelan, M., Tempest, B., Goyal, R., and Ramsey, J. (2015). "Determination of Bridge Deterioration Models and Bridge User Costs for the NCDOT Bridge Management System." *Technical Report No. FHWA/NC/2014-07*, North Carolina Department of Transportation, October, 188.
- Cleveland City Forge (2018). "Turnbuckles and Assemblies Specifications." Online at [www.clevelandcityforge.com](http://www.clevelandcityforge.com) [accessed December 20, 2018].
- Dempsey, D., D., and Scott, D. W. (2006). "Wood Members Strengthened with Mechanically Fastened FRP Strips." *Journal of Composites for Construction*, 10(5), 392-398.
- Devore, J. L. (2015). *Probability and Statistics for Engineering and the Sciences*, 9<sup>th</sup> Ed. Cengage Learning, Boston, 715.
- Diab, H., Wu, Z., and Iwashita, K. (2009). "Short and long-term bond performance of prestressed FRP sheet anchorages." *Engineering Structures*, 31(5), 1241-1249.
- Ebead, U. (2011). "Hybrid Externally Bonded/Mechanically Fastened Fiber-Reinforced Polymer for RC Beam Strengthening." *ACI Structural Journal*, 108(6), 669-678.
- Ebead, U., and Saeed, H. (2014). "Flexural and Interfacial Behavior of Externally Bonded/Mechanically Fastened Fiber-Reinforced Polymer-Strengthened Reinforced Concrete Beams." *ACI Structural Journal; Farmington Hills*, 111(4), 741-751.

- Efron, B., and Tibshirani, R. J. (1994). *An introduction to the bootstrap*, CRC Press, New York, NY, 437.
- Ekenel, M., Rizzo, A., Myers, J. J., and Nanni, A. (2006). "Flexural Fatigue Behavior of Reinforced Concrete Beams Strengthened with FRP Fabric and Precured Laminate Systems." *Journal of Composites for Construction*, 10(5), 433-442.
- El-Maaddawy, T. A. (2014). "Mechanically Fastened Composites for Retrofitting Corrosion-Damaged Reinforced-Concrete Beams: Experimental Investigation." *Journal of Composites for Construction*, 18(2), doi:10.1061/(ASCE)CC.1943-5614.0000447.
- El-Maaddawy, T., Nessabi, A., and El-Dieb, A. (2013). "Flexural Response of Corroded Reinforced Concrete Beams Strengthened with Powder-Actuated Fastened Composites." *Journal of Composites for Construction*, 17(6), doi:10.1061/(ASCE)CC.1943-5614.0000395.
- Elsayed, W. E., Ebead, U. A., and Neale, K. W. (2009). "Studies on Mechanically Fastened Fiber-Reinforced Polymer Strengthening Systems." *ACI Structural Journal; Farmington Hills*, 106(1), 49-59.
- FAMA (2017). "Emergency Vehicle Size and Weight Guide." *Technical Committee Report No TC009-1*, Fire Apparatus Manufacturers' Association, 20.
- Galati, D., Rizzo, A., and Micelli, F. (2007). "Comparison of reinforced concrete beams strengthened with FRP pre-cured laminate systems and tested under flexural loading." In *Proceeding of the FRPRCS-8*, Patras, Greece, 16-18 July.
- Hamrat, M., Boulekbache, B., Chemrouk, M., and Amziane, S. (2016). "Construction & building materials." 106(Supplement C), 678-692.
- Hindo, K. R., and Bergstrom, W. R. (1985). "Statistical evaluation of the in-place compressive strength of concrete," *Concrete International*, 7(2), 44-48.
- Hoult, N. A., Take, W. A., Lee, C., and Dutton, M. (2013). "Experimental accuracy of two-dimensional strain measurements using Digital Image Correlation." *Engineering Structures*, 46, doi: 10.1016/j.engstruct.2012.08.018.
- Huang, Y. H., Liu, L., Sham, F. C., Chan, Y. S., and Ng, S. P. (2010). "Optical strain gauge vs. traditional strain gauges for concrete elasticity modulus determination." *Optik - International Journal for Light and Electron Optics*, 121(18), 1635-1641.
- Knudson, K., Schexnayder, C. J., Fiori, C. M., and Mayo, R. E. (2009). *Construction Management Fundamentals, 2<sup>nd</sup> Ed.* McGraw-Hill, New York, 697.
- Lamanna, A. J. (2002). "Flexural strengthening of reinforced concrete beams with mechanically fastened fiber reinforced polymer strips". Ph.D. Thesis, University of Wisconsin-Madison, Madison, WI.
- Lamanna, A. J., Bank, L. C., and Borowicz, D. T. (2004a). "Mechanically Fastened FRP Strengthening of Large Scale RC Bridge T Beams." *Advances in Structural Engineering*, 7(6), 525-538.
- Lamanna, A. J., Bank, L. C., and Scott, D. W. (2001). "Flexural strengthening of RC beams using fasteners and FRP strips." *ACI Structural Journal*, 98(3), 368-376.

- Lamanna, A. J., Bank, L. C., and Scott, D. W. (2004b). "Flexural Strengthening of Reinforced Concrete Beams by Mechanically Attaching Fiber-Reinforced Polymer Strips." *Journal of Composites for Construction*, 8(3), 203-210.
- Lee, H. L., Lopez, M. M., and Bakis, C. E. (2009). "Flexural behavior of reinforced concrete beams strengthened with mechanically fastened FRP strips." In Proceeding of the FRPRCS-8, Patras, Greece, 16-18 July.
- Lee, J. H., Lopez, M. M., and Bakis, C. E. (2009). "Slip effects in reinforced concrete beams with mechanically fastened FRP strip." *Cement and Concrete Composites*, 31(7), 496-504.
- Martin, J. A., and Lamanna, A. J. (2008). "Performance of Mechanically Fastened FRP Strengthened Concrete Beams in Flexure." *Journal of Composites for Construction*, 12(3), 257-265.
- Martinelli, E., Napoli, A., Nunziata, B., and Realfonzo, R. (2014). "A 1D finite element model for the flexural behaviour of RC beams strengthened with MF-FRP strips." *Composite Structures*, 107, 190-204.
- McCoy, B. C., Bourara, Z., Seracino, R., and Lucier, G. W. (2019a). "Anchor Bolt Patterns for Mechanically-Fastened FRP Plates." *Journal of Composites for Construction*, American Society of Civil Engineers, Washington DC, in-press, doi: 10.1061/(ASCE)CC.1943-5614.0000951.
- McCoy, B. C., Seliem, H. M., Seracino, R., and Lucier, G. W. (2019b). "Addressing Superstructure Load Rating Criteria for Deteriorated Prestressed Concrete Members Using a Proposed MF-FRP Retrofit." *Journal for the Performance of Constructed Facilities*, American Society of Civil Engineers, Washington DC, under review.
- McMaster-Carr (2018). "Product Details." Online at [www.mcmaster.com](http://www.mcmaster.com) [accessed December 20, 2018].
- Michels, J., Martinelli, E., Czaderski, C., and Motavalli, M. (2014). "Prestressed CFRP Strips with Gradient Anchorage for Structural Concrete Retrofitting: Experiments and Numerical Modeling." *Polymers*, 6, 114-131.
- Napoli, A., Matta, F., Martinelli, E., Nanni, A., and Realfonzo, R. (2010). "Modelling and verification of response of RC slabs strengthened in flexure with mechanically fastened FRP laminates." *Magazine of Concrete Research*, 62(8), 593-605.
- Nawy, E. G. (2010). *Prestressed Concrete: A Fundamental Approach, 5<sup>th</sup> Ed.* Pearson Education, Inc., Upper Saddle River, New Jersey, 949.
- NCDOT (2018a). "North Carolina Bridge Management System." NCDOT database accessed December 12, 2018.
- NCDOT (2018b). "Prestressed Concrete Channel Beam Bridges." Online at [www.connect.ncdot.gov](http://www.connect.ncdot.gov) [accessed January 8, 2019].
- NCDOT (2018c). *Standard Specifications for Roads and Structures*, North Carolina Department of Transportation, January, 829.
- NCDOT (1966). "Standard Prestressed Concrete Channels 20 ft.-, 25 ft.-, and 30 ft.-Spans, 24 ft.-, 29 ft.-, and 34 ft.-Roadways, Standard BMD-13." State Highway Commission, North Carolina Department of Transportation, August, 1.

- NIOSH (1994). "Applications Manual for the Revised NIOSH Lifting Equation." U.S. Department of Health and Human Services, National Institute for Occupational Safety and Health, Cincinnati, OH, 164.
- Oehlers, D. J. (2001). "Development of design rules for retrofitting by adhesive bonding or bolting either FRP or steel plates to RC beams of slabs in bridges and buildings." *Composites Part A: Applied Science and Manufacturing*, 32, 1345-1355.
- Oehlers, D. J., and Bradford, M. A. (1995). *Composite Steel and Concrete Structural Members: Fundamental Behavior*. Elsevier, Kidlington, U.K., 549.
- Oehlers, D. J., and Seracino, R. (2004). *Design of FRP and Steel Plated RC Structures: Retrofitting Beams and Slabs for Strength, Stiffness, and Ductility*. Elsevier, Kidlington, U.K., 228.
- OSHA 29 CFR 1926 (2018). "Construction Industry Regulations." U.S. Department of Labor Occupational Safety and Health Administration, Springfield, MO, Online at <https://www.osha.gov/laws-regs/regulations/standardnumber/1926> [accessed September 12, 2018].
- PCI (2010). *PCI Design Handbook, 7<sup>th</sup> Ed.* Precast Concrete Institute, Chicago, 814.
- Peters W. F., and Ranson W. F. (1982). "Digital imaging techniques in experimental stress analysis." *Optical Engineering*, 21(3), 427-431.
- R, version 3.2.5 (2016). The R Foundation for Statistical Computing.
- Rahman, A. H., Kingsley, C., Richard, J., and Crimi, J. (1998). "Experimental investigation of the mechanism of deterioration of FRP reinforcement for concrete." *Fiber Composites in Infrastructure, Proceedings of the Second International Conference on Fibre Composites in Infrastructure*, ICCI-98, Tucson, AZ, Vol. 2, 501-511.
- Ramos, T., Braga, D. F. O., Eslami, S., Tavares, P. J., and Moreira, P M G P. (2015). "Comparison Between Finite Element Method Simulation, Digital Image Correlation and Strain Gauges Measurements in a 3-Point Bending Flexural Test." *Procedia Engineering*, 114, 232-239.
- Realfonzo, R., Martinelli, E., Napoli, A., and Nunziata, B. (2013). "Experimental investigation of the mechanical connection between FRP laminates and concrete." *Composites Part B: Engineering*, 45(1), 341-355.
- Roper, K. O., and Payant, R. P. (2014). *The Facility Management Handbook, 4<sup>th</sup> Ed.* American Management Association, New York, 675.
- Rosenboom, O., and Rizkalla, S. H. (2008). "Experimental Study of Intermediate Crack Debonding in Fiber-Reinforced Polymer Strengthened Beams." *ACI Structural Journal*, American Concrete Institute, Farmington Hills, MI, 41-50.
- Seliem, H., Lucier, G., Seracino, R. (2014). "Structural Assessment and Repair of Deteriorated Exterior Precast Prestressed Concrete Channel Girders." *Technical Report No. RD-14-03*, North Carolina Department of Transportation, March, 43.

- Sena-Cruz, J. M., Barrow, J. A. O., Coelho, M. R. F., and Silva, L. F. F. T. (2012). "Efficiency of different techniques in flexural strengthening of RC beams under monotonic and fatigue loading." *Construction and Building Materials*, 29, 175-182.
- Shapack, G., Seracino, R., Lucier, G., and Rizkalla, S. (2016). "CFRP Strands in Prestressed Cored Slab Units." *Technical Report No. FHWA/NC/2014-09*, North Carolina Department of Transportation, February, 133.
- Sokoli, D., Shekarchi, W., Buenrostro, E., and Ghannoum, W. M. (2014). "Advancing behavioral understanding and damage evaluation of concrete members using high-resolution digital image correlation data." *Earthquakes and Structures*, 7(5), 609-626.
- Sutton M. A., Wolters W. J., Peters W. H., Ranson W. F., and McNeill S. F. (1983). "Determination of displacements using an improved digital correlation method." *Image and Vision Computing*, 1(3), 133-139.
- Strongwell (2016) "SAFSTRIP® Fiber Reinforced Strengthening Strip." Online at [www.strongwell.com](http://www.strongwell.com) [accessed 11/13/2017].
- Triantafillou, T. C., and Deskovic, N. (1991). "Innovative Prestressing with FRP Sheets: Mechanics of Short-Term Behavior." *Journal of Engineering Mechanics*, 117(7), 1652-1672.
- Van Brunt, Z., Seracino, R., Lucier, G., and Pour-Ghaz, M. (2016). "Assessment of Deteriorated Cored Slabs: Bridges No. 150035 and 150039." *Technical Report No. FHWA/NC/2014.35*, North Carolina Department of Transportation, February, 233.
- Xie, H., and Kang, Y. (2015). "Digital image correlation technique." *Optics and Lasers in Engineering*, 65, 1-2.
- Yang, Y., Yang, C., and Huang, C. (2015). "Thin crack observation in a reinforced concrete bridge pier test using image processing and analysis." *Advances in Engineering Software*, 83, 99-108.

**APPENDICES**

## Appendix A: Small-scale Test Matrix and Detailed Test Data

Appendix A contains data and charts for mean peak load, mean peak stress, and load-displacement behavior for all small-scale material tests. Table A.1 presents the consolidated test matrix for all small-scale treatment groups, presented separately in Chapters 4 and 5 of this work.

**Table A.1:** Small-scale FRP Material Test Matrix.

Specimen ID	No. of Replicates	Treatment Description	ASTM
T	8	No holes	D3039
S-OH	6	Single open hole centered in gauge length	D5766 <sup>1</sup>
DBL4-OH-1.5	6	4 open holes; 2-by-2; 1.5 in. transverse spacing; 4.0 in. longitudinal spacing	D5766 <sup>1</sup>
DBL4-OH-2.0	6	4 open holes; 2-by-2; 2.0 in. transverse spacing; 4.0 in. longitudinal spacing	D5766 <sup>1</sup>
STG4-OH-1.5	6	4 open holes; staggered with 2.0 in. offset; 1.5 in. transverse spacing; 4.0 in. longitudinal spacing	D5766 <sup>1</sup>
STG4-OH-2.0	6	4 open holes; staggered with 2.0 in. offset; 2.0 in. transverse spacing; 4.0 in. longitudinal spacing	D5766 <sup>1</sup>
S-B-X-1.5	6	Single bolt bearing with 1.5 in. edge distance excluding threads	D5961
S-B-N-1.5	6	Single bolt bearing with 1.5 in. edge distance including threads	D5961
S-B-X-4.0	6	Single bolt bearing with 4.0 in. edge distance excluding threads	NA
S-B-N-4.0	6	Single bolt bearing with 4.0 in. edge distance including threads	NA
DBL10-B-1.5	1	10 bolts; 0.5 in. diameter; 2-by-2; 1.5 in. transverse spacing; 4.0 in. longitudinal spacing	NA
DBL12-B-1.5	1	12 bolts; 0.5 in. diameter; 2-by-2; 1.5 in. transverse spacing; 4.0 in. longitudinal spacing	NA
DBL14-B-1.5	1	14 bolts; 0.5 in. diameter; 2-by-2; 1.5 in. transverse spacing; 4.0 in. longitudinal spacing	NA
DBL16-B-1.5	6	16 bolts; 0.5 in. diameter; 2-by-2; 1.5 in. transverse spacing; 4.0 in. longitudinal spacing	NA
DBL18-B-1.5	6	18 bolts; 0.5 in. diameter; 2-by-2; 1.5 in. transverse spacing; 4.0 in. longitudinal spacing	NA
DBL20-B-1.5	6	20 bolts; 0.5 in. diameter; 2-by-2; 1.5 in. transverse spacing; 4.0 in. longitudinal spacing	NA
DBL22-B-1.5	6	22 bolts; 0.5 in. diameter; 2-by-2; 1.5 in. transverse spacing; 4.0 in. longitudinal spacing	NA
S-B-X-0.375-4.0	6	Single bolt; 0.375 in. dia.; 4.0 in. edge distance excluding threads	D5961
DBL18-B-0.375-1.5	6	18 bolts; 0.375 in. diameter; 2-by-2; 1.5 in. transverse spacing; 4.0 in. longitudinal spacing	NA
DBL20-B-0.375-1.5	8	20 bolts; 0.375 in. diameter; 2-by-2; 1.5 in. transverse spacing; 4.0 in. longitudinal spacing	NA
DBL22-B-0.375-1.5	6	22 bolts; 0.375 in. diameter; 2-by-2; 1.5 in. transverse spacing; 4.0 in. longitudinal spacing	NA
DBL14-B-4-0.75-1.5	6	14 bolts; 0.75 in. diameter; 2-by-2; 1.5 in. transverse spacing; 4.0 in. longitudinal spacing	NA
DBL14-B-6-0.75-1.5	6	14 bolts; 0.75 in. diameter; 2-by-2; 1.5 in. transverse spacing; 6.0 in. longitudinal spacing	NA

Notes: 1) ASTM D5766 stress calculation uses gross cross-sectional area, sample peak stress is calculated using net cross-sectional area; 1 kip = 4.4482 kN; 1 ksi = 6.895 MPa

Table A.2 presents a summary of all small-scale treatment group test results to include sample standard deviations and coefficients of variation as an inference on the population parameters.

**Table A.2: Small-scale FRP Material Test Results Summary.**

Specimen ID	Mean Peak Load (kips)	Mean Peak Stress <sup>2</sup> (ksi)	Sample Peak Stress Standard Deviation (ksi)	Sample Peak Stress CV (%)	CL based on Sample CV (%)	Pop. Peak Stress (ksi)	Pop. Peak Stress CV (%)	CL based on Pop. CV (%)
T	76.5	147	5.87	3.99	99	124	8.28	90
S-OH	66.5	151	6.13	4.06	96	94.6 <sup>2</sup>	5.56	97
DBL4-OH-1.5	51.5	137	4.36	3.18	97	NA	5.56 <sup>1</sup>	97
DBL4-OH-2.0	52.3	132	6.46	4.89	95	NA	5.56 <sup>1</sup>	97
STG4-OH-1.5	52.5	139	2.26	1.63	99	NA	5.56 <sup>1</sup>	93
STG4-OH-2.0	51.3	136	1.83	1.35	99	NA	5.56 <sup>1</sup>	93
S-B-X-1.5	3.00	45.7	2.17	4.75	95	31	5.37	92
S-B-N-1.5	3.10	47.0	2.69	5.72	91	NA	5.37 <sup>3</sup>	92
S-B-X-4.0	3.40	50.6	2.92	5.77	90	NA	5.37 <sup>3</sup>	92
S-B-N-4.0	3.70	55.9	3.88	6.94	86	NA	5.37 <sup>3</sup>	92
DBL10-B-1.5	31.5	48.0	NA	NA	NA	NA	5.37 <sup>3</sup>	92
DBL12-B-1.5	35.2	44.7	NA	NA	NA	NA	5.37 <sup>3</sup>	92
DBL14-B-1.5	39.0	42.4	1.56	3.68	99	NA	5.37 <sup>3</sup>	92
DBL16-B-1.5	42.5	39.9	1.16	2.91	99	NA	5.37 <sup>3</sup>	92
DBL18-B-1.5	45.5	38.5	0.74	1.92	99	NA	5.37 <sup>3</sup>	92
DBL20-B-1.5	45.1	33.9	1.22	3.60	99	NA	5.37 <sup>3</sup>	92
DBL22-B-1.5	46.4	32.1	0.476	1.48	99	NA	5.37 <sup>3</sup>	92
DBL18-B-0.375-1.5	43.0	48.5	2.59	5.34	94	NA	5.37 <sup>3</sup>	92
DBL20-B-0.375-1.5	45.4	46.1	1.36	2.95	99	NA	5.37 <sup>3</sup>	96
DBL22-B-0.375-1.5	48.4	44.7	1.62	3.62	99	NA	5.37 <sup>3</sup>	92
DBL14-B-4-0.75-1.5	30.9	75.9	3.81	5.02	94	NA	5.37 <sup>3</sup>	92
DBL14-B-6-0.75-1.5	36.3	89.0	3.16	3.55	99	NA	5.37 <sup>3</sup>	92

Notes: 1) Multiple hole population CV values are assumed to follow single hole testing values; 2) ASTM D5766 stress calculation uses gross cross-sectional area, sample peak stress is calculated using net cross-sectional area; 3) All single bolt and multi-bolt population CV values are assumed to follow S-B-X-1.5 value for population. 1 kip = 4.4482 kN; 1 ksi = 6.895 MPa.

Table A.3 is the detailed data for 137 individual small-scale test specimens. Geometric properties, peak load, and calculated peak stresses are presented.

**Table A.3: Detailed FRP Material Test Result Data.**

Specimen ID	Test Results					Geometric Properties																		
	Anchored Length (in)	Peak Load (kips)	Mean Peak Load (kips)	Ultimate Stress (ksi)	Mean Ultimate Stress (ksi)	t (in)	t (in)	t (in)	t <sub>avg</sub> (in)	w (in)	w (in)	w (in)	w <sub>avg</sub> (in)	A <sub>avg</sub> (in <sup>2</sup> )	d (in)	d (in)	d (in)	d <sub>avg</sub> (in)	A <sub>hole</sub> (in <sup>2</sup> )	A <sub>net</sub> (in <sup>2</sup> )	W/D	d <sub>bolt</sub> (in)	No. of bolts	A <sub>bearing</sub> (in <sup>2</sup> )
T-1	NA	77.3		147.8		0.132	0.132	0.130	0.131	3.983	3.984	3.983	3.983	0.523	NA	NA	NA	NA	0.000	0.523	NA	NA	NA	NA
T-2	NA	75.3		145.7		0.129	0.130	0.130	0.130	3.985	3.984	3.984	3.984	0.517	NA	NA	NA	NA	0.000	0.517	NA	NA	NA	NA
T-3	NA	73.5		142.6		0.129	0.130	0.129	0.129	3.984	3.986	3.986	3.985	0.515	NA	NA	NA	NA	0.000	0.515	NA	NA	NA	NA
T-4 (SG)	NA	72.8	76.5	140.5	147.4	0.130	0.130	0.130	0.130	3.984	3.984	3.984	3.984	0.518	NA	NA	NA	NA	0.000	0.518	NA	NA	NA	NA
T-5 (SG)	NA	75.8		145.1		0.132	0.131	0.130	0.131	3.986	3.988	3.986	3.987	0.522	NA	NA	NA	NA	0.000	0.522	NA	NA	NA	NA
T-6 (SG)	NA	76.4		145.3		0.132	0.132	0.132	0.132	3.984	3.985	3.985	3.985	0.526	NA	NA	NA	NA	0.000	0.526	NA	NA	NA	NA
T-7 (SG)	NA	80.0		156.0		0.130	0.128	0.128	0.129	3.987	3.986	3.986	3.986	0.513	NA	NA	NA	NA	0.000	0.513	NA	NA	NA	NA
T-8 (SG)	NA	81.2		156.6		0.130	0.131	0.129	0.130	3.987	3.987	3.987	3.987	0.518	NA	NA	NA	NA	0.000	0.518	NA	NA	NA	NA
S1-OH-1	NA	65.9		149.4		0.129	0.128	0.130	0.129	3.983	3.982	3.984	3.983	0.514	0.561	0.562	0.562	0.562	0.072	0.441	7.09	NA	NA	NA
S1-OH-2	NA	68.9		156.1		0.129	0.128	0.130	0.129	3.985	3.983	3.984	3.984	0.514	0.562	0.561	0.562	0.562	0.072	0.441	7.09	NA	NA	NA
S1-OH-3	NA	61.6	66.5	139.5	150.5	0.129	0.128	0.130	0.129	3.983	3.984	3.984	3.984	0.514	0.562	0.562	0.562	0.562	0.072	0.441	7.09	NA	NA	NA
S1-OH-4	NA	66.3		149.3		0.130	0.129	0.130	0.130	3.982	3.985	3.985	3.984	0.517	0.562	0.563	0.562	0.562	0.073	0.444	7.08	NA	NA	NA
S1-OH-5	NA	67.5		152.9		0.129	0.128	0.130	0.129	3.984	3.989	3.984	3.986	0.514	0.562	0.562	0.562	0.562	0.072	0.442	7.09	NA	NA	NA
S1-OH-6	NA	68.6		155.7		0.130	0.128	0.128	0.129	3.985	3.988	3.985	3.986	0.513	0.562	0.561	0.563	0.562	0.072	0.441	7.09	NA	NA	NA
STG4-OH-1.5-1	NA	53.7		143.8		0.13	0.131	0.131	0.131	3.984	3.984	3.984	3.984	0.521	0.563	0.561	NA	0.562	0.147	0.374	3.54	NA	NA	NA
STG4-OH-1.5-2	NA	52.7		142.1		0.129	0.130	0.129	0.129	3.989	3.989	3.990	3.989	0.516	0.560	0.560	NA	0.560	0.145	0.371	3.56	NA	NA	NA
STG4-OH-1.5-3	NA	51.1	52.5	137.8	139.3	0.130	0.129	0.129	0.129	3.987	3.989	3.987	3.988	0.516	0.559	0.560	NA	0.560	0.145	0.371	3.56	NA	NA	NA
STG4-OH-1.5-4	NA	52.3		139.9		0.130	0.129	0.132	0.130	3.988	3.986	3.988	3.987	0.520	0.559	0.560	NA	0.560	0.146	0.374	3.56	NA	NA	NA
STG4-OH-1.5-5	NA	48.1		130.9		0.130	0.129	0.129	0.129	3.990	3.989	3.987	3.989	0.516	0.574	0.575	NA	0.575	0.149	0.367	3.47	NA	NA	NA
STG4-OH-1.5-6	NA	52.8		141.3		0.131	0.131	0.130	0.131	3.990	3.990	3.989	3.990	0.521	0.564	0.565	NA	0.565	0.148	0.374	3.53	NA	NA	NA
STG4-OH-2.0-1	NA	51.3		135.5		0.13	0.133	0.132	0.132	3.960	3.990	3.990	3.980	0.524	0.550	0.555	NA	0.553	0.145	0.379	7.20	NA	NA	NA
STG4-OH-2.0-2	NA	51.4		137.4		0.129	0.129	0.129	0.129	3.990	3.990	3.990	3.990	0.515	0.550	0.540	NA	0.545	0.141	0.374	7.32	NA	NA	NA
STG4-OH-2.0-3	NA	52.2	51.3	132.8	135.5	0.136	0.13	0.131	0.132	3.980	3.980	3.980	3.980	0.527	0.500	0.510	NA	0.505	0.134	0.393	7.88	NA	NA	NA
STG4-OH-2.0-4	NA	51.2		136.9		0.127	0.13	0.131	0.129	3.990	3.980	3.980	3.983	0.515	0.546	0.546	NA	0.546	0.141	0.374	7.30	NA	NA	NA
STG4-OH-2.0-5	NA	43.9		112.6		0.138	0.137	0.132	0.136	3.990	3.980	3.990	3.987	0.541	0.562	0.550	NA	0.556	0.151	0.390	7.17	NA	NA	NA
STG4-OH-2.0-6	NA	50.6		134.7		0.13	0.131	0.129	0.130	3.990	3.990	3.980	3.987	0.518	0.548	0.550	NA	0.549	0.143	0.376	7.26	NA	NA	NA
DBL4-OH-1.5-1	NA	52.3		139.9		0.131	0.130	0.131	0.131	3.984	3.984	3.983	3.984	0.521	0.562	0.562	NA	0.562	0.147	0.374	3.54	NA	NA	NA
DBL4-OH-1.5-2	NA	48.5		130.3		0.129	0.130	0.130	0.130	3.984	3.987	3.988	3.986	0.517	0.557	0.557	NA	0.557	0.144	0.372	3.58	NA	NA	NA
DBL4-OH-1.5-3	NA	52.9	51.5	139.8	136.8	0.132	0.130	0.134	0.132	3.985	3.989	3.986	3.987	0.526	0.558	0.559	NA	0.559	0.147	0.379	3.57	NA	NA	NA
DBL4-OH-1.5-4	NA	50.2		132.3		0.131	0.134	0.132	0.132	3.989	3.990	3.989	3.989	0.528	0.560	0.560	NA	0.560	0.148	0.380	3.56	NA	NA	NA
DBL4-OH-1.5-5	NA	52.4		139.0		0.131	0.132	0.131	0.131	3.990	3.987	3.988	3.988	0.524	0.559	0.560	NA	0.560	0.147	0.377	3.56	NA	NA	NA
DBL4-OH-1.5-6	NA	52.4		139.8		0.131	0.131	0.130	0.131	3.989	3.988	3.987	3.988	0.521	0.558	0.561	NA	0.560	0.146	0.375	3.56	NA	NA	NA
DBL4-OH-2.0-1	NA	53.8		143.5		0.131	0.132	0.131	0.131	3.988	3.981	3.984	3.984	0.523	0.576	0.554	NA	0.565	0.148	0.375	3.53	NA	NA	NA
DBL4-OH-2.0-2	NA	51.4		137.2		0.130	0.130	0.131	0.130	3.980	3.980	3.980	3.980	0.519	0.552	0.554	NA	0.553	0.144	0.375	3.60	NA	NA	NA
DBL4-OH-2.0-3	NA	50.9	52.3	133.6	138.7	0.132	0.130	0.134	0.132	3.990	3.980	3.980	3.983	0.526	0.543	0.554	NA	0.549	0.145	0.381	3.63	NA	NA	NA
DBL4-OH-2.0-4	NA	51.0		135.7		0.132	0.130	0.131	0.131	3.980	3.980	3.980	3.980	0.521	0.558	0.554	NA	0.556	0.146	0.376	3.58	NA	NA	NA
DBL4-OH-2.0-5	NA	55.4		146.1		0.134	0.130	0.130	0.131	3.986	3.993	3.982	3.987	0.524	0.546	0.554	NA	0.550	0.144	0.379	3.62	NA	NA	NA
DBL4-OH-2.0-6	NA	51.0		135.7		0.131	0.130	0.131	0.131	3.980	3.980	3.980	3.980	0.520	0.550	0.554	NA	0.552	0.144	0.376	3.61	NA	NA	NA

Note: 1 kip = 4.4482 kN; 1 ksi = 6.895 MPa

Table A.3: (continued)

Specimen ID	Anchored Length (in)	Peak Load (kips)	Mean Peak Load (kips)	Ultimate Stress (ksi)	Mean Ultimate Stress (ksi)	t (in)	t (in)	t (in)	t <sub>avg</sub> (in.)	w (in.)	w (in.)	w (in.)	w <sub>avg</sub> (in.)	A <sub>avg</sub> (in. <sup>2</sup> )	d (in.)	d (in.)	d (in.)	d <sub>avg</sub> (in.)	A <sub>hole</sub> (in. <sup>2</sup> )	A <sub>net</sub> (in. <sup>2</sup> )	W/D	d <sub>bol</sub> (in.)	No. of bolts	A <sub>scaring</sub> (in. <sup>2</sup> )
S-B-X-1.5-1	NA	3.06	3.03	46.6	45.7	0.13	0.133	0.131	0.131	3.980	3.987	3.988	3.985	0.523	0.560	0.557	0.555	0.557	0.073	0.450	7.15	0.500	1	0.066
S-B-X-1.5-2	NA	2.76		41.8		0.131	0.132	0.133	0.132	3.987	3.985	3.984	3.986	0.526	0.556	0.557	0.556	0.556	0.073	0.453	7.16	0.500	1	0.066
S-B-X-1.5-3	NA	3.09		46.7		0.132	0.133	0.132	0.132	3.994	3.985	3.984	3.988	0.528	0.530	0.549	0.562	0.547	0.072	0.455	7.29	0.500	1	0.066
S-B-X-1.5-4	NA	2.94		44.5		0.132	0.134	0.13	0.132	3.988	3.986	3.985	3.986	0.526	0.560	0.561	0.555	0.559	0.074	0.452	7.14	0.500	1	0.066
S-B-X-1.5-5	NA	3.21		47.6		0.132	0.135	0.138	0.135	3.991	3.986	3.984	3.987	0.538	0.550	0.558	0.546	0.551	0.074	0.464	7.23	0.500	1	0.068
S-B-X-1.5-6	NA	3.10		47.1		0.131	0.131	0.133	0.132	3.993	3.986	3.988	3.989	0.525	0.554	0.530	0.538	0.541	0.071	0.454	7.38	0.500	1	0.066
S-B-N-1.5-1	NA	3.27	3.1	48.9	47.0	0.131	0.135	0.135	0.134	3.986	3.987	3.986	3.986	0.533	0.555	0.546	0.560	0.554	0.074	0.459	7.20	0.500	1	0.067
S-B-N-1.5-2	NA	2.99		45.0		0.135	0.132	0.132	0.133	3.997	3.985	3.987	3.990	0.531	0.551	0.559	0.548	0.553	0.074	0.457	7.22	0.500	1	0.067
S-B-N-1.5-3	NA	2.87		42.9		0.1333	0.133	0.135	0.134	3.986	3.988	3.988	3.987	0.533	0.546	0.551	0.546	0.548	0.073	0.460	7.28	0.500	1	0.067
S-B-N-1.5-4	NA	3.14		47.0		0.132	0.135	0.134	0.134	3.984	3.985	3.985	3.985	0.533	0.561	0.560	0.565	0.562	0.075	0.457	7.09	0.500	1	0.067
S-B-N-1.5-5	NA	3.33		50.3		0.13	0.134	0.133	0.132	3.985	3.987	3.989	3.987	0.528	0.526	0.552	0.546	0.541	0.072	0.456	7.37	0.500	1	0.066
S-B-N-1.5-6	NA	3.17		47.8		0.131	0.1332	0.134	0.133	3.991	3.988	3.986	3.988	0.529	0.547	0.545	0.550	0.547	0.073	0.457	7.29	0.500	1	0.066
S-B-X-4.0-1	NA	3.80	3.7	57.9	55.9	0.130	0.133	0.131	0.131	3.980	3.987	3.988	3.985	0.523	0.560	0.557	0.555	0.557	0.073	0.450	7.15	0.500	1	0.066
S-B-X-4.0-2	NA	3.70		56.1		0.131	0.132	0.133	0.132	3.987	3.985	3.984	3.986	0.526	0.556	0.557	0.556	0.556	0.073	0.453	7.16	0.500	1	0.066
S-B-X-4.0-3	NA	3.30		49.9		0.132	0.133	0.132	0.132	3.994	3.985	3.984	3.988	0.528	0.530	0.549	0.562	0.547	0.072	0.455	7.29	0.500	1	0.066
S-B-X-4.0-4	NA	3.50		53.0		0.132	0.134	0.13	0.132	3.988	3.986	3.985	3.986	0.526	0.560	0.561	0.555	0.559	0.074	0.452	7.14	0.500	1	0.066
S-B-X-4.0-5	NA	3.90		57.8		0.132	0.135	0.138	0.135	3.991	3.986	3.984	3.987	0.538	0.550	0.558	0.546	0.551	0.074	0.464	7.23	0.500	1	0.068
S-B-X-4.0-6	NA	4.00		60.8		0.131	0.131	0.133	0.132	3.993	3.986	3.988	3.989	0.525	0.554	0.530	0.538	0.541	0.071	0.454	7.38	0.500	1	0.066
S-B-N-4.0-1	NA	3.10	3.4	46.4	50.6	0.131	0.135	0.135	0.134	3.986	3.987	3.986	3.986	0.533	0.555	0.546	0.560	0.554	0.074	0.459	7.20	0.500	1	0.067
S-B-N-4.0-2	NA	3.20		48.1		0.135	0.132	0.132	0.133	3.997	3.985	3.987	3.990	0.531	0.551	0.559	0.548	0.553	0.074	0.457	7.22	0.500	1	0.067
S-B-N-4.0-3	NA	3.50		52.3		0.133	0.133	0.135	0.134	3.986	3.988	3.988	3.987	0.533	0.546	0.551	0.546	0.548	0.073	0.460	7.28	0.500	1	0.067
S-B-N-4.0-4	NA	3.60		53.9		0.132	0.135	0.134	0.134	3.984	3.985	3.985	3.985	0.533	0.561	0.560	0.565	0.562	0.075	0.457	7.09	0.500	1	0.067
S-B-N-4.0-5	NA	3.30		49.9		0.130	0.134	0.133	0.132	3.985	3.987	3.989	3.987	0.528	0.526	0.552	0.546	0.541	0.072	0.456	7.37	0.500	1	0.066
S-B-N-4.0-6	NA	3.50		52.7		0.131	0.133	0.134	0.133	3.991	3.988	3.986	3.988	0.529	0.547	0.545	0.550	0.547	0.073	0.457	7.29	0.500	1	0.066
DBL10-B-1.5-1	16	31.5	31.5	48.0	48.0			0.131				3.986	0.524				0.554	0.073	0.451	3.60	0.500	10	0.657	
DBL12-B-1.5-1	20	35.2	35.2	44.7	44.7			0.131				3.986	0.524				0.554	0.073	0.451	3.60	0.500	12	0.788	
DBL14-B-1.5-1	24	39.0	39.0	42.4	42.4			0.131				3.986	0.524				0.554	0.073	0.451	3.60	0.500	14	0.920	
DBL14-B-1.5-2	16	37.6		40.9		0.131			3.986	0.524				0.554	0.073	0.451	3.60	0.500	14	0.920				
DBL14-B-1.5-3	16	38.4		41.8		0.131			3.986	0.524				0.554	0.073	0.451	3.60	0.500	14	0.920				
DBL14-B-1.5-4	16	37.7		41.0		0.131			3.986	0.524				0.554	0.073	0.451	3.60	0.500	14	0.920				
DBL14-B-1.5-5	16	41.2		44.8		0.131			3.986	0.524				0.554	0.073	0.451	3.60	0.500	14	0.920				
DBL14-B-1.5-6	16	40.2		43.7		0.131			3.986	0.524				0.554	0.073	0.451	3.60	0.500	14	0.920				
DBL16-B-1.5-1	28	43.3	42.5	41.2	40.4			0.131				3.986	0.524				0.554	0.073	0.451	3.60	0.500	16	1.051	
DBL16-B-1.5-2	28	41.6		39.6		0.131			3.986	0.524				0.554	0.073	0.451	3.60	0.500	16	1.051				
DBL16-B-1.5-3	28	41.7		39.7		0.131			3.986	0.524				0.554	0.073	0.451	3.60	0.500	16	1.051				
DBL16-B-1.5-4	28	40.9		38.9		0.131			3.986	0.524				0.554	0.073	0.451	3.60	0.500	16	1.051				
DBL16-B-1.5-5	28	43.9		41.8		0.131			3.986	0.524				0.554	0.073	0.451	3.60	0.500	16	1.051				
DBL16-B-1.5-6	28	43.5		41.4		0.131			3.986	0.524				0.554	0.073	0.451	3.60	0.500	16	1.051				

Note: 1 kip = 4.4482 kN; 1 ksi = 6.895 MPa

Table A.3: (continued)

Specimen ID	Test Results					Geometric Properties																		
	Anchored Length (in)	Peak Load (kips)	Mean Peak Load (kips)	Ultimate Stress (ksi)	Mean Ultimate Stress (ksi)	t (in)	t (in)	t (in)	t <sub>avg</sub> (in.)	w (in.)	w (in.)	w (in.)	w <sub>avg</sub> (in.)	A <sub>avg</sub> (in. <sup>2</sup> )	d (in.)	d (in.)	d (in.)	d <sub>avg</sub> (in.)	A <sub>hole</sub> (in. <sup>2</sup> )	A <sub>net</sub> (in. <sup>2</sup> )	W/D	d <sub>bolt</sub> (in.)	No. of bolts	A <sub>bearing</sub> (in. <sup>2</sup> )
DBL18-B-1.5-1	32	44.7		37.8					0.131				3.986	0.524				0.554	0.073	0.451	3.60	0.500	18	1.182
DBL18-B-1.5-2	32	46.9		39.7					0.131				3.986	0.524				0.554	0.073	0.451	3.60	0.500	18	1.182
DBL18-B-1.5-3	32	45.6	45.5	38.6	38.5				0.131				3.986	0.524				0.554	0.073	0.451	3.60	0.500	18	1.182
DBL18-B-1.5-4	32	45.7		38.7					0.131				3.986	0.524				0.554	0.073	0.451	3.60	0.500	18	1.182
DBL18-B-1.5-5	32	44.4		37.6					0.131				3.986	0.524				0.554	0.073	0.451	3.60	0.500	18	1.182
DBL18-B-1.5-6	32	45.8		38.7					0.131				3.986	0.524				0.554	0.073	0.451	3.60	0.500	18	1.182
DBL20-B-1.5-1	36	45.7		34.8					0.131				3.986	0.524				0.554	0.073	0.451	3.60	0.500	20	1.314
DBL20-B-1.5-2	36	41.9		31.9					0.131				3.986	0.524				0.554	0.073	0.451	3.60	0.500	20	1.314
DBL20-B-1.5-3	36	45.3	45.7	34.5	34.3				0.131				3.986	0.524				0.554	0.073	0.451	3.60	0.500	20	1.314
DBL20-B-1.5-4	36	45.4		34.6					0.131				3.986	0.524				0.554	0.073	0.451	3.60	0.500	20	1.314
DBL20-B-1.5-5	36	45.5		34.6					0.131				3.986	0.524				0.554	0.073	0.451	3.60	0.500	20	1.314
DBL20-B-1.5-6	36	46.7		35.6					0.131				3.986	0.524				0.554	0.073	0.451	3.60	0.500	20	1.314
DBL22-B-1.5-1	40	45.8		31.7					0.131				3.986	0.524				0.554	0.073	0.451	3.60	0.500	22	1.445
DBL22-B-1.5-2	40	45.7		31.6					0.131				3.986	0.524				0.554	0.073	0.451	3.60	0.500	22	1.445
DBL22-B-1.5-3	40	46.8	46.4	32.4	32.1				0.131				3.986	0.524				0.554	0.073	0.451	3.60	0.500	22	1.445
DBL22-B-1.5-4	40	46.5		32.2					0.131				3.986	0.524				0.554	0.073	0.451	3.60	0.500	22	1.445
DBL22-B-1.5-5	40	46.7		32.3					0.131				3.986	0.524				0.554	0.073	0.451	3.60	0.500	22	1.445
DBL22-B-1.5-6	40	46.6		32.2					0.131				3.986	0.524				0.554	0.073	0.451	3.60	0.500	22	1.445
S-B-X-0.375-4.0-1	NA	2.9		59.7					0.131				3.986	0.524	0.441	0.440	0.441	0.441	0.058	0.466	4.52	0.375	1	0.049
S-B-X-0.375-4.0-2	NA	3.2		65.0					0.131				3.986	0.524	0.442	0.436	0.438	0.439	0.058	0.466	4.54	0.375	1	0.049
S-B-X-0.375-4.0-3	NA	2.9	3.01	58.9	61.0				0.131				3.986	0.524	0.443	0.445	0.440	0.443	0.058	0.465	4.50	0.375	1	0.049
S-B-X-0.375-4.0-4	NA	2.9		58.9					0.131				3.986	0.524	0.439	0.442	0.444	0.442	0.058	0.466	4.51	0.375	1	0.049
S-B-X-0.375-4.0-5	NA	3.3		67.0					0.131				3.986	0.524	0.439	0.440	0.445	0.441	0.058	0.466	4.52	0.375	1	0.049
S-B-X-0.375-4.0-6	NA	2.8		56.8					0.131				3.986	0.524	0.440	0.439	0.438	0.439	0.058	0.466	4.54	0.375	1	0.049
DBL18-B-0.375-1.5-1	36	41.1		46.4					0.131				3.986	0.524	0.452	0.450	0.452	0.452	0.059	0.464	4.41	0.375	18	0.887
DBL18-B-0.375-1.5-2	36	45.2		51.0					0.131				3.986	0.524	0.466	0.467	0.446	0.460	0.060	0.463	4.34	0.375	18	0.887
DBL18-B-0.375-1.5-3	36	43.8	43.0	49.4	48.5				0.131				3.986	0.524	0.449	0.448	0.459	0.452	0.059	0.464	4.41	0.375	18	0.887
DBL18-B-0.375-1.5-4	36	39.8		44.9					0.131				3.986	0.524	0.445	0.440	0.447	0.444	0.058	0.465	4.49	0.375	18	0.887
DBL18-B-0.375-1.5-5	36	45.6		51.4					0.131				3.986	0.524	0.449	0.449	0.447	0.448	0.059	0.465	4.45	0.375	18	0.887
DBL18-B-0.375-1.5-6	36	42.6		48.0					0.131				3.986	0.524	0.453	0.447	0.463	0.454	0.060	0.464	4.39	0.375	18	0.887

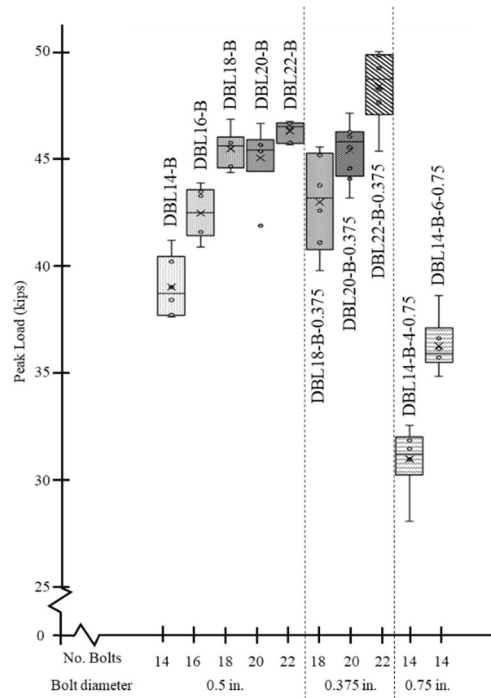
Note: 1 kip = 4.4482 kN; 1 ksi = 6.895 MPa

Table A.3: (continued)

Specimen ID	Test Results					Geometric Properties																		
	Anchored Length (in)	Peak Load (kips)	Mean Peak Load (kips)	Ultimate Stress (ksi)	Mean Ultimate Stress (ksi)	t (in)	t (in)	t (in)	t <sub>avg</sub> (in.)	w (in.)	w (in.)	w (in.)	w <sub>avg</sub> (in.)	A <sub>avg</sub> (in. <sup>2</sup> )	d (in.)	d (in.)	d (in.)	d <sub>avg</sub> (in.)	A <sub>hole</sub> (in. <sup>2</sup> )	A <sub>net</sub> (in. <sup>2</sup> )	W/D	d <sub>bolt</sub> (in.)	No. of bolts	A <sub>bearing</sub> (in. <sup>2</sup> )
DBL20-B-0.375-1.5-1	40	44.1		44.8					0.131				3.986	0.524	0.450	0.446	0.444	0.447	0.059	0.465	4.46	0.375	20	0.985
DBL20-B-0.375-1.5-2	40	45.6		46.3					0.131				3.986	0.524	0.444	0.440	0.442	0.442	0.058	0.466	4.51	0.375	20	0.985
DBL20-B-0.375-1.5-3	40	43.2		43.8					0.131				3.986	0.524	0.438	0.439	0.440	0.439	0.058	0.466	4.54	0.375	20	0.985
DBL20-B-0.375-1.5-4	40	46.1	45.0	46.8	45.7				0.131				3.986	0.524	0.442	0.438	0.440	0.440	0.058	0.466	4.53	0.375	20	0.985
DBL20-B-0.375-1.5-5	40	46.3		47.0					0.131				3.986	0.524	0.437	0.442	0.441	0.440	0.058	0.466	4.53	0.375	20	0.985
DBL20-B-0.375-1.5-6	40	44.6		45.3					0.131				3.986	0.524	0.438	0.437	0.439	0.438	0.058	0.466	4.55	0.375	20	0.985
DBL20-B-0.375-1.5-7	40	46.3		47.0					0.131				3.986	0.524	0.442	0.440	0.441	0.441	0.058	0.466	4.52	0.375	20	0.985
DBL20-B-0.375-1.5-8	40	47.2		47.9					0.131				3.986	0.524	0.440	0.439	0.441	0.440	0.058	0.466	4.53	0.375	20	0.985
DBL22-B-0.375-1.5-1	44	49.3		45.5					0.131				3.986	0.524	0.435	0.438	0.438	0.437	0.057	0.466	4.56	0.375	22	1.084
DBL22-B-0.375-1.5-2	44	48.3		44.6					0.131				3.986	0.524	0.433	0.438	0.436	0.436	0.057	0.466	4.57	0.375	22	1.084
DBL22-B-0.375-1.5-3	44	45.4	48.5	41.9	44.7				0.131				3.986	0.524	0.433	0.431	0.438	0.434	0.057	0.467	4.59	0.375	22	1.084
DBL22-B-0.375-1.5-4	44	47.7		44.0					0.131				3.986	0.524	0.435	0.433	0.437	0.435	0.057	0.466	4.58	0.375	22	1.084
DBL22-B-0.375-1.5-5	44	50.1		46.2					0.131				3.986	0.524	0.437	0.447	0.434	0.439	0.058	0.466	4.54	0.375	22	1.084
DBL22-B-0.375-1.5-6	44	49.9		46.0					0.131				3.986	0.524	0.432	0.431	0.436	0.433	0.057	0.467	4.60	0.375	22	1.084
DBL14-B-4-0.75-1.5-1	24	31.4		77.1					0.131				3.986	0.524	0.884	0.884	0.884	0.884	0.116	0.407	2.25	0.750	14	1.379
DBL14-B-4-0.75-1.5-2	24	31.8		78.0					0.131				3.986	0.524	0.884	0.884	0.884	0.884	0.116	0.407	2.25	0.750	14	1.379
DBL14-B-4-0.75-1.5-3	24	30.9	30.9	75.8	75.9				0.131				3.986	0.524	0.884	0.884	0.884	0.884	0.116	0.407	2.25	0.750	14	1.379
DBL14-B-4-0.75-1.5-4	24	32.5		79.8					0.131				3.986	0.524	0.884	0.884	0.884	0.884	0.116	0.407	2.25	0.750	14	1.379
DBL14-B-4-0.75-1.5-5	24	30.9		75.8					0.131				3.986	0.524	0.884	0.884	0.884	0.884	0.116	0.407	2.25	0.750	14	1.379
DBL14-B-4-0.75-1.5-6	24	28.0		68.7					0.131				3.986	0.524	0.884	0.884	0.884	0.884	0.116	0.407	2.25	0.750	14	1.379
DBL14-B-6-0.75-1.5-1	36	35.7		87.6					0.131				3.986	0.524	0.884	0.884	0.884	0.884	0.116	0.407	2.25	0.750	14	1.379
DBL14-B-6-0.75-1.5-2	36	34.8		85.4					0.131				3.986	0.524	0.884	0.884	0.884	0.884	0.116	0.407	2.25	0.750	14	1.379
DBL14-B-6-0.75-1.5-3	36	36.6	36.3	89.8	89.0				0.131				3.986	0.524	0.884	0.884	0.884	0.884	0.116	0.407	2.25	0.750	14	1.379
DBL14-B-6-0.75-1.5-4	36	38.6		94.7					0.131				3.986	0.524	0.884	0.884	0.884	0.884	0.116	0.407	2.25	0.750	14	1.379
DBL14-B-6-0.75-1.5-5	36	36.1		88.6					0.131				3.986	0.524	0.884	0.884	0.884	0.884	0.116	0.407	2.25	0.750	14	1.379
DBL14-B-6-0.75-1.5-6	36	35.7		87.6					0.131				3.986	0.524	0.884	0.884	0.884	0.884	0.116	0.407	2.25	0.750	14	1.379

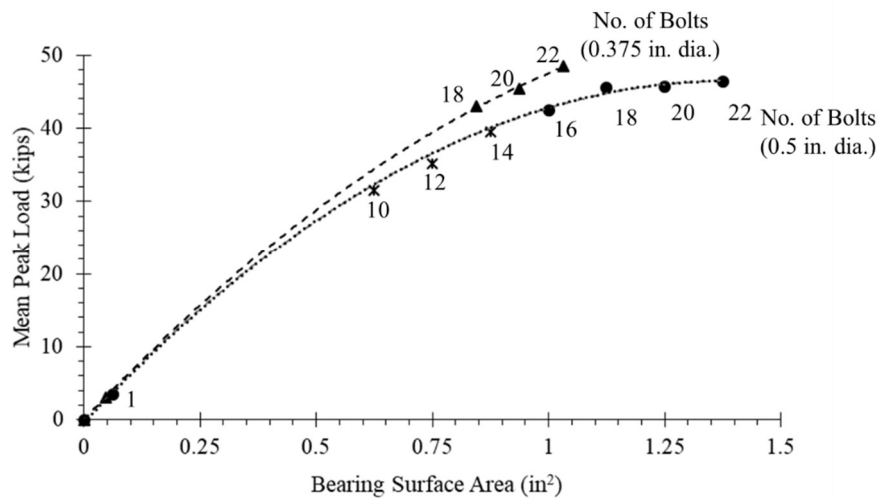
Note: 1 kip = 4.4482 kN; 1 ksi = 6.895 MPa

Figure A.1 shows the peak load distribution for the 10 multi-bolt treatment groups tested. Load distributions are presented separately in Chapters 4 and 5, but consolidated here for comparison across the groups. Figure A.2 presents the mean peak load in relation to total bearing surface area for the 0.5 in. and 0.375 in. diameter treatment groups.



**Figure A.1:** Box plots of all multi-bolt peak load distributions.

*Note: 1 in. = 25.4 mm; 1 kip = 4.4482 kN*



**Figure A.2:** Variation of mean peak load vs. bearing surface area for 0.5 in. and 0.375 in. bolts.

*Note: 1 in.<sup>2</sup> = 645 mm<sup>2</sup>; 1 kip = 4.4482 kN*

Figures A.3 and A.4 present load-displacement curves for the single-bolt small-scale FRP uniaxial tension tests for the 0.5 in. diameter (excluding threads) treatment group (Figure A.3), and the 0.375 in. diameter bolt (excluding threads) treatment groups (Figure A.4). Single-bolt tests were not conducted for the 0.75 in. diameter bolt treatment groups.

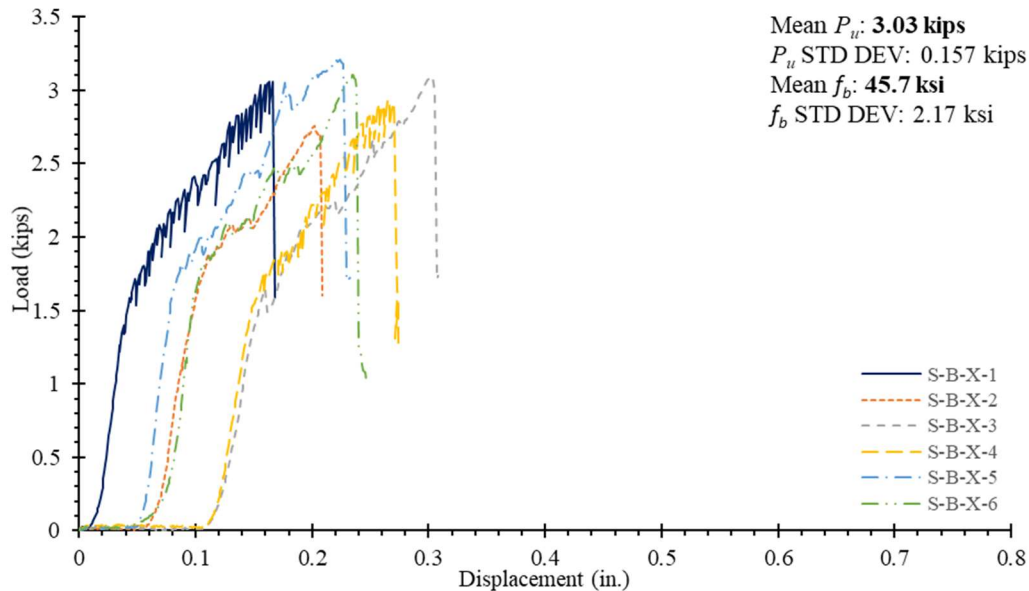


**Figure A.3:** S-B-X load-displacement curves.

Note: 1 in. = 25.4 mm; 1 kip = 4.4482 kN

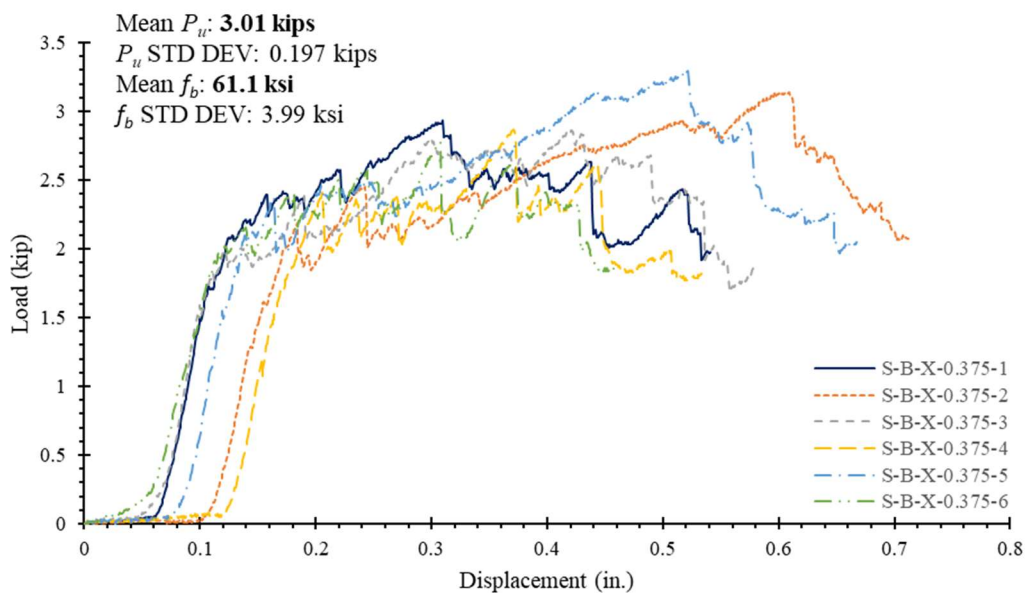


**Figure A.4:** S-B-X-0.375 load-displacement curves.

Note: 1 in. = 25.4 mm; 1 kip = 4.4482 kN

Figures A.5 and A.6 present the load displacement-behavior for the 0.5 in. diameter, 14- and 16-bolt treatment groups treatment groups.

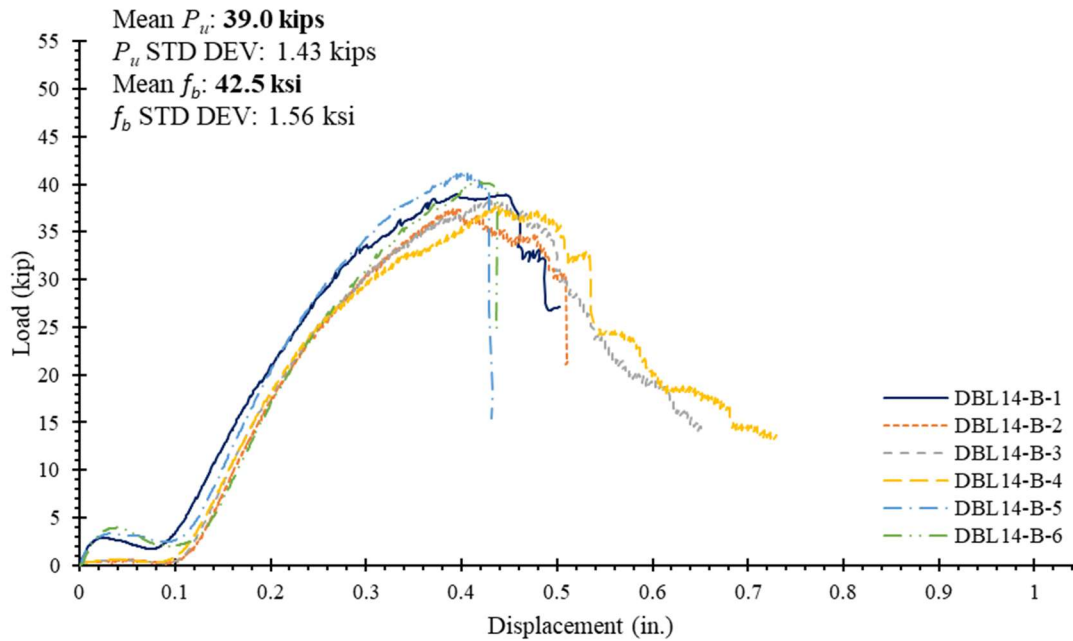


**Figure A.5:** DBL14-B load-displacement curves.

*Note: 1 in. = 25.4 mm; 1 kip = 4.4482 kN*

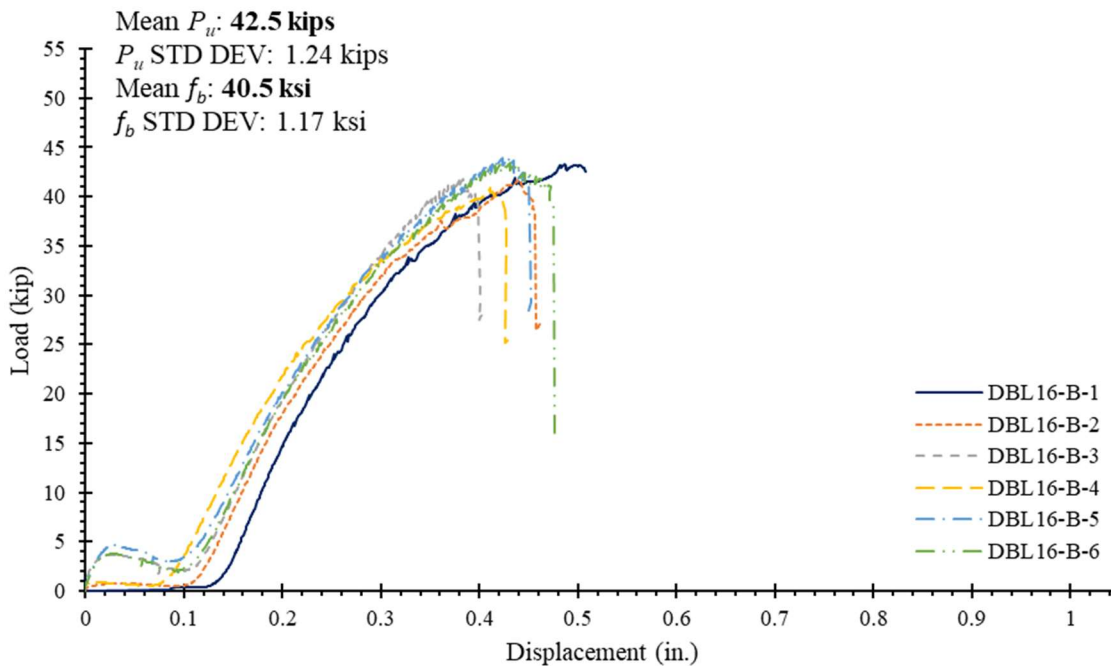


**Figure A.6:** DBL16-B load-displacement curves.

*Note: 1 in. = 25.4 mm; 1 kip = 4.4482 kN*

Figures A.7 through A.12 present the load-displacement behavior for the 18-, 20-, and 22-bolt configurations of the 0.5 in. and 0.375 in. treatment groups. Like configurations are presented on the same page for comparison between the 0.5 in. and 0.375 in. treatments

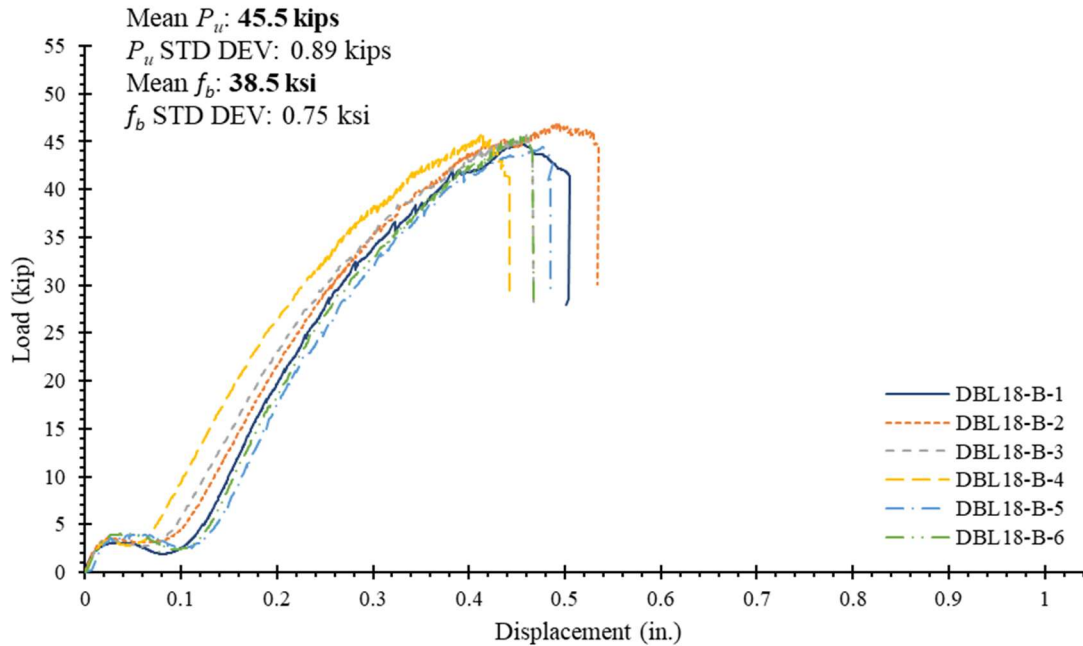


**Figure A.7:** DBL18-B load-displacement curves.

*Note: 1 in. = 25.4 mm; 1 kip = 4.4482 kN*

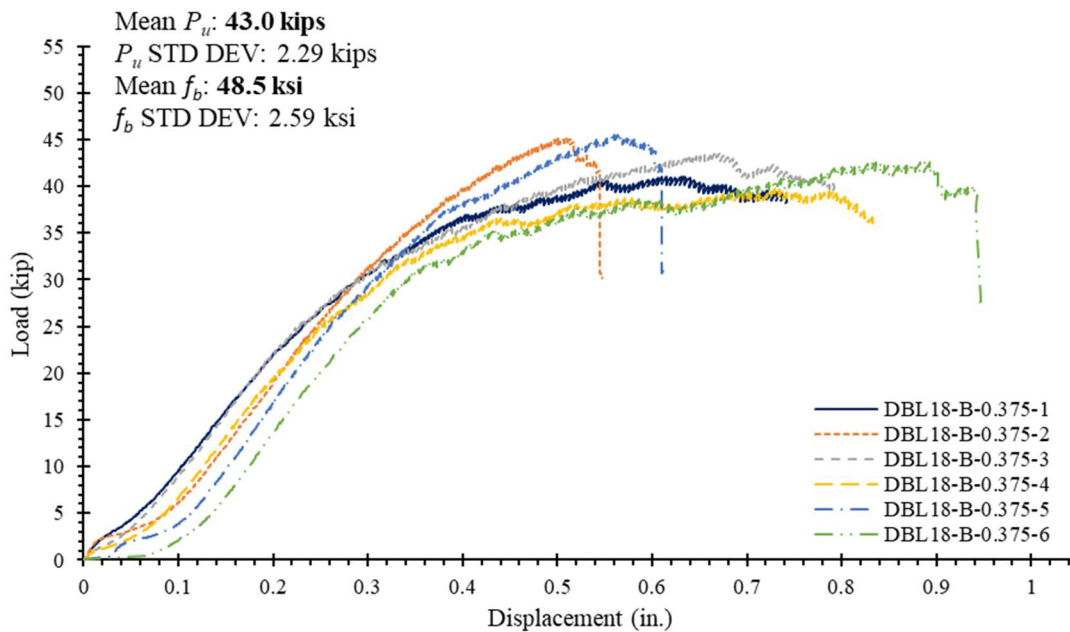


**Figure A.8:** DBL18-B-0.375 load-displacement curves.

*Note: 1 in. = 25.4 mm; 1 kip = 4.4482 kN*

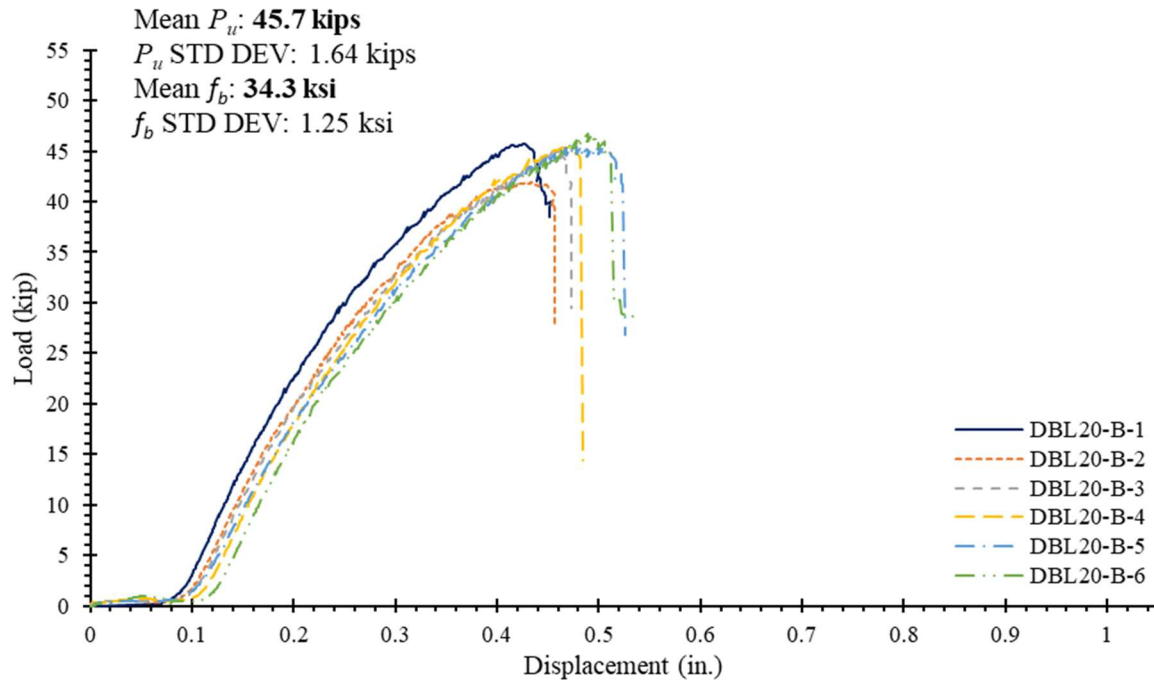


**Figure A.9:** DBL20-B load-displacement curves.

Note: 1 in. = 25.4 mm; 1 kip = 4.4482 kN

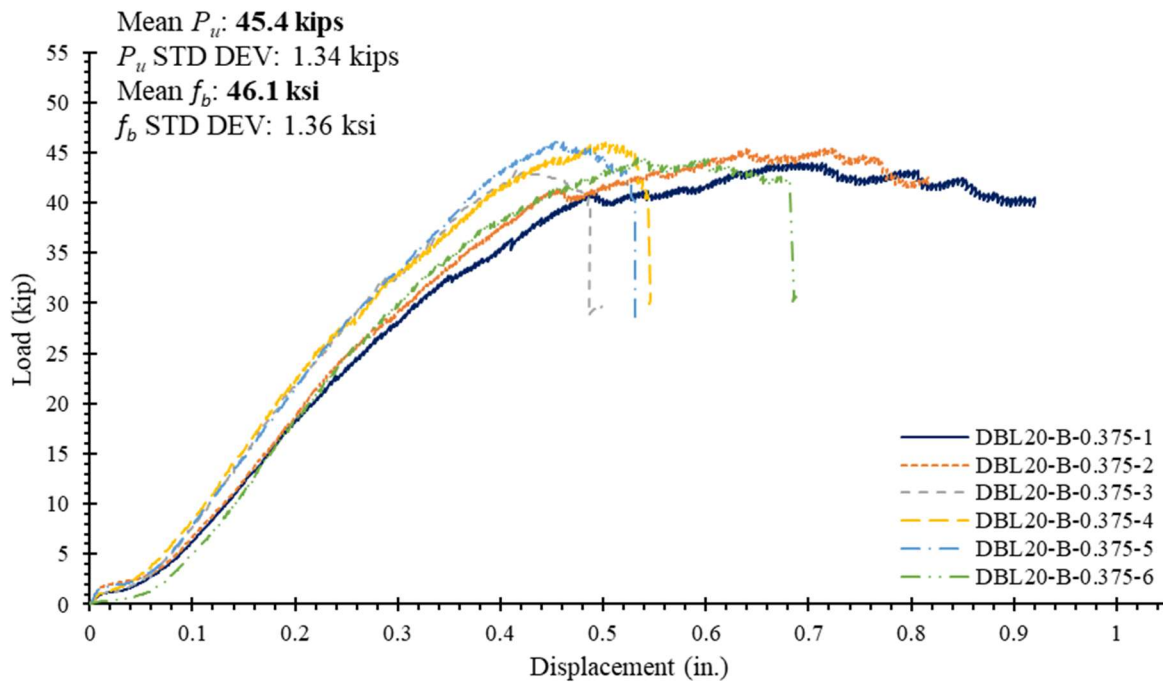


**Figure A.10:** DBL20-B-0.375 load-displacement curves.

Note: 1 in. = 25.4 mm; 1 kip = 4.4482 kN

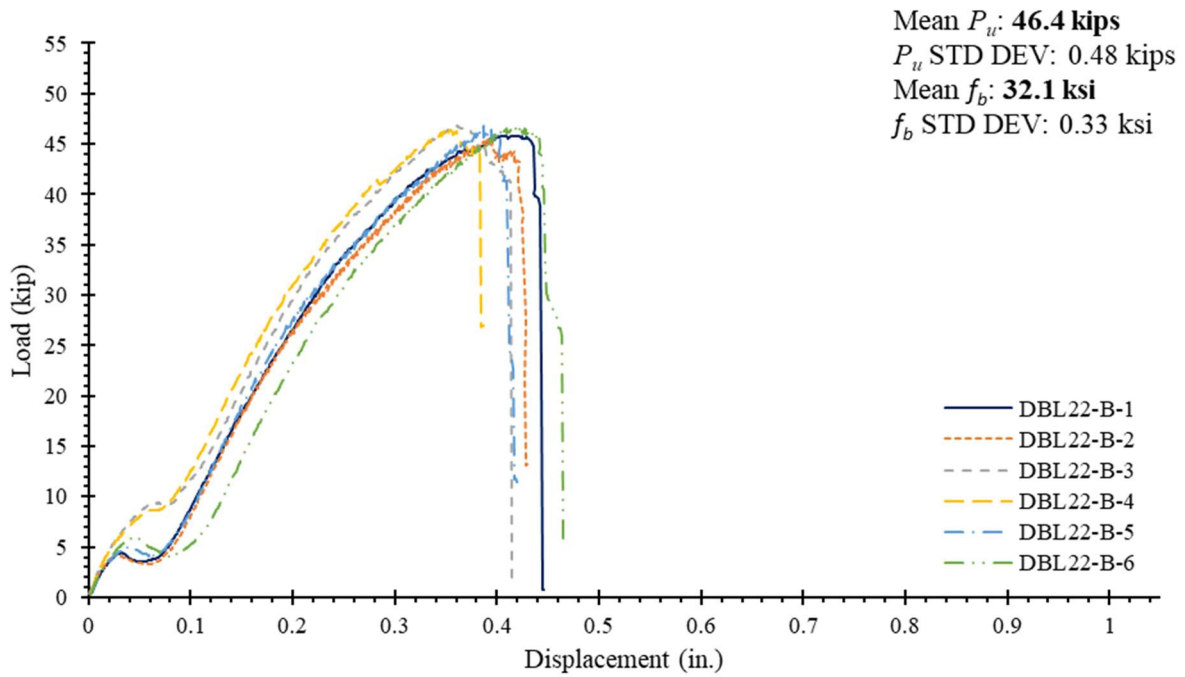


**Figure A.11:** DBL22-B load-displacement curves.  
 Note: 1 in. = 25.4 mm; 1 kip = 4.4482 kN

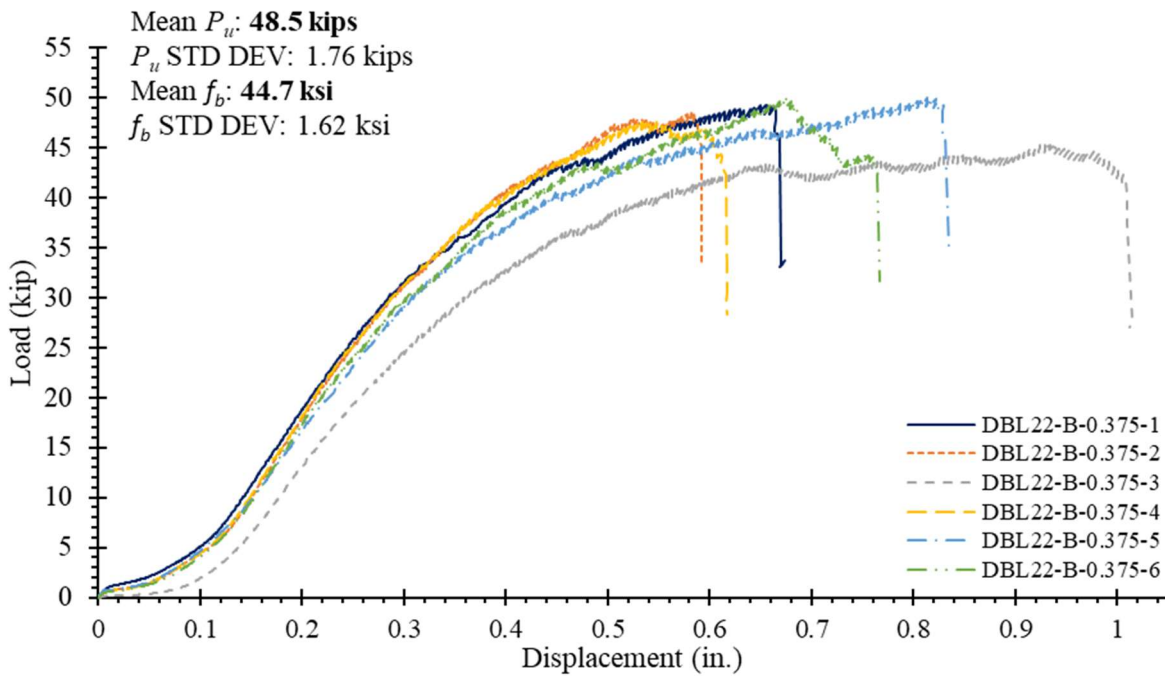


**Figure A.12:** DBL22-B-0.375 load-displacement curves.  
 Note: 1 in. = 25.4 mm; 1 kip = 4.4482 kN

Figures A.13 and A.14 present the load-displacement behavior for the 0.75 in. diameter bolt treatment groups. Figure A.13 is the 14-bolt configuration with 4 in. longitudinal spacing, and Figure A.14 is the 14-bolt configuration with 6 in. longitudinal spacing.

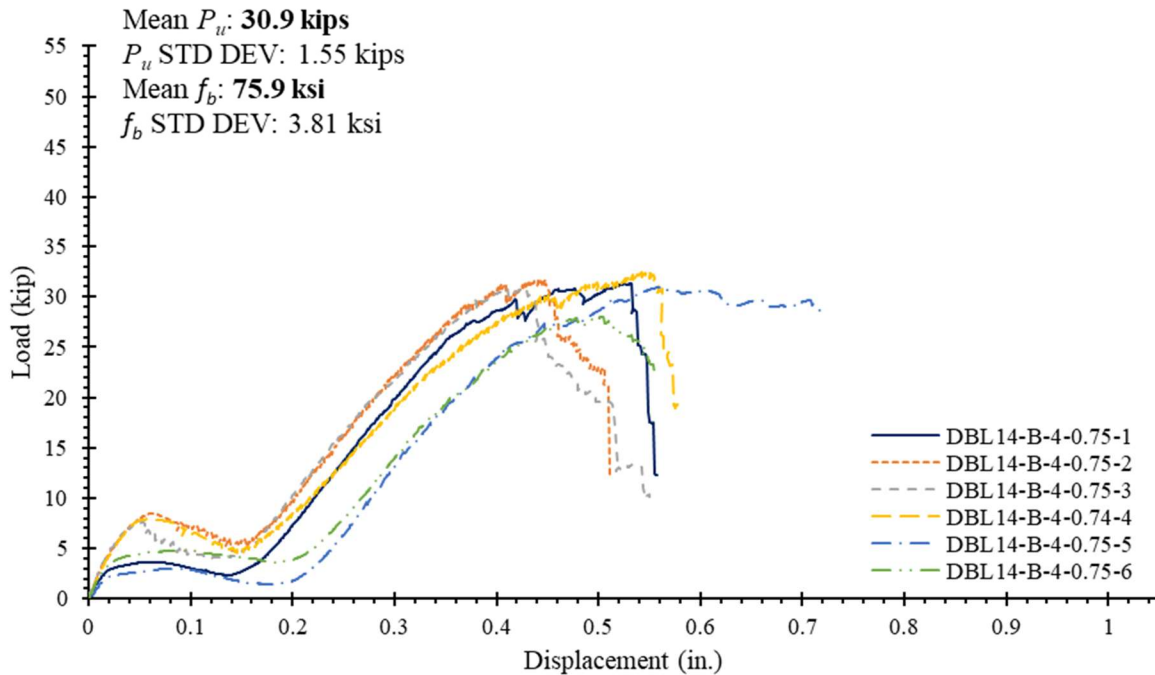


**Figure A.13:** DBL14-B-4-0.75 load-displacement curves.

Note: 1 in. = 25.4 mm; 1 kip = 4.4482 kN

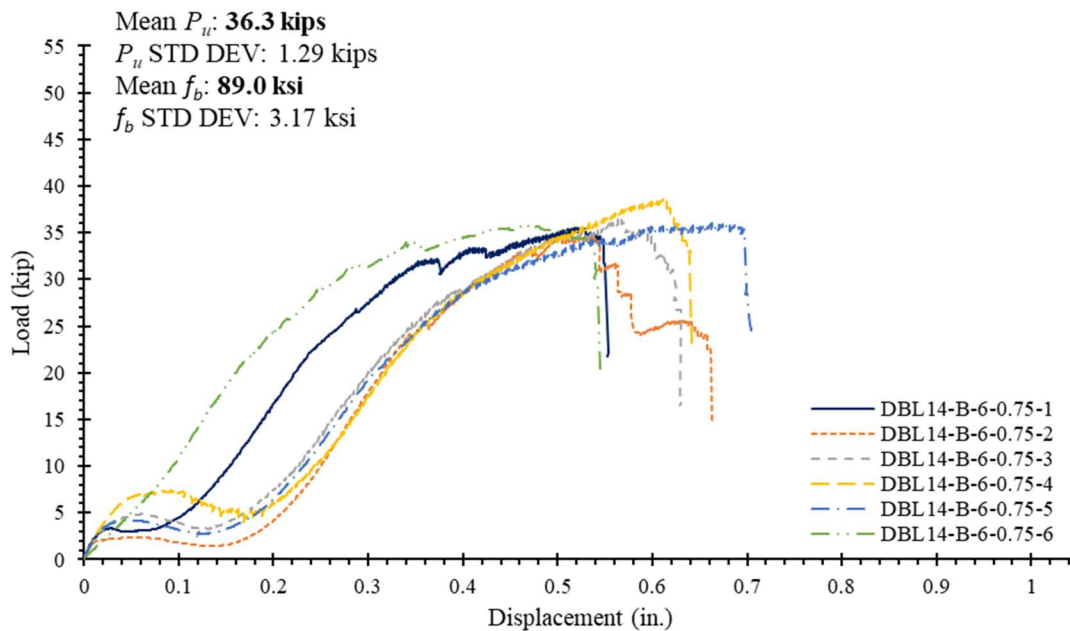


**Figure A.14:** DBL14-B-6-0.75 load-displacement curves.

Note: 1 in. = 25.4 mm; 1 kip = 4.4482 kN

## Appendix B: Bridge 380093 Supporting Calculations

Appendix B contains supporting calculations for the case study bridge, NC Bridge 380093, presented in Chapter 3. The calculation spreadsheets are a collaborative effort with the co-authors of the Chapter 3 journal paper.

### Inventory and Ultimate Load Capacities

The following calculation results (Tables B.1 through B.10) use Equations 3.4 through 3.10 for each load condition and level of prestress loss due to elastic shortening, shrinkage, creep, and relaxation.

**Table B.1:** Undamaged Inventory Load – 15% losses,  $f_t \leq 6\sqrt{f'_c}$  (psi).

<b>MATERIAL PROPERTIES</b>							
$f'_c$ (psi)	5000	$f_{ci}$ (psi)	4000	$f_{pu}$ (ksi)	270	$f'_{pi}$ (ksi)	185
				$A_{strand}$ (in <sup>2</sup> )	0.1167	$f_{pi}$ (ksi)	189
<b>SECTION DEFINITION</b>							
A (in <sup>2</sup> )	264.675	$I_x$ (in <sup>4</sup> )	5238.777	$I_y$ (in <sup>4</sup> )	28593.247	$Y_{top}$ (in)	5.606
						$S_{top}$ (in <sup>3</sup> )	934.495
						$Y_{bot}$ (in)	11.394
						$S_{bot}$ (in <sup>3</sup> )	459.784
<b>PRESTRESSING</b>							
$P_{1-i}$ (kip)	21.56	$e_1$ (in)	4.519	Losses (%)	15	$P_{1-e}$ (kip)	18.33
$P_{2-i}$ (kip)	21.56	$e_2$ (in)	4.957			$P_{2-e}$ (kip)	18.33
$P_{3-i}$ (kip)	21.56	$e_3$ (in)	5.394			$P_{3-e}$ (kip)	18.33
$P_{4-i}$ (kip)	21.56	$e_4$ (in)	9.894			$P_{4-e}$ (kip)	18.33
<b>MOMENT DUE TO OWN WEIGHT</b>							
Span (ft)	30	$W_{ow}$ (k/ft)	0.276	$M_{ow}$ (k-ft)	31.02		
<b>STRESSES AT SERVICE STAGE</b>							
TOP STRESSES (psi)			Allowable Comp. Stresses (psi)		-3000	0.6	x $f'_c$
$P_e/A$	$P_{e-e}/S_{top}$	$M_{ow}/S_{top}$	$M_a/S_{top}$	$f_{top}$ (psi)	$M_{a-1}$ (k-ft)	235.10	
-554	971	-398	-3019	-3000			
BOT STRESSES (psi)			Allowable Tens. Stresses (psi)		424	6	x $\sqrt{f'_c}$
$P/A$	$P_{e-e}/S_{bot}$	$M_{ow}/S_{bot}$	$M_a/S_{bot}$	$f_{bot}$ (psi)	$M_{a-2}$ (k-ft)	82.10	
-554	-1974	810	2143	424			
<b>APPLIED MOMENTS</b>							
Curb:	$M_{curb}$ (k-ft)	10.46	Wearing Surface:	$W_{ws}$ (k/ft)	0.120	$M_{ws}$ (k-ft)	8.25
Live Load Moment Including Impact:			$M_{LL+I}$ (k-ft)	63.39	IM (%)	33	
Live Load Moment <u>NOT</u> Including Impact:			$M_{LL}$ (k-ft)	47.66			

**Table B.2:** Undamaged Inventory Load – 15% losses,  $f_t \leq 0\sqrt{f'_c}$  (psi).

<b>MATERIAL PROPERTIES</b>									
$f'_c$ (psi)	5000	$f_{ci}$ (psi)	4000	$f_{pu}$ (ksi)	270	$f'_{pi}$ (ksi)	185		
				$A_{strand}$ (in <sup>2</sup> )	0.1167				
<b>SECTION DEFINITION</b>									
A (in <sup>2</sup> )	264.675	$I_x$ (in <sup>4</sup> )	5238.777	$I_y$ (in <sup>4</sup> )	28593.247	$Y_{top}$ (in)	5.606	$Y_{bot}$ (in)	11.394
						$S_{top}$ (in <sup>3</sup> )	934.495	$S_{bot}$ (in <sup>3</sup> )	459.784
<b>PRESTRESSING</b>									
$P_{1-i}$ (kip)	21.59	$e_1$ (in)	4.519	Losses (%)	15	$P_{1-e}$ (kip)	18.35		
$P_{2-i}$ (kip)	21.59	$e_2$ (in)	4.957			$P_{2-e}$ (kip)	18.35		
$P_{3-i}$ (kip)	21.59	$e_3$ (in)	5.394			$P_{3-e}$ (kip)	18.35		
$P_{4-i}$ (kip)	21.59	$e_4$ (in)	9.894			$P_{4-e}$ (kip)	18.35		
<b>MOMENT DUE TO OWN WEIGHT</b>									
Span (ft)	30	$W_{ow}$ (k/ft)	0.276	$M_{ow}$ (k-ft)	31.02				
<b>STRESSES AT SERVICE STAGE</b>									
TOP STRESSES (psi)			Allowable Comp. Strsses (psi)			-3000	0.6	x $f'_c$	
$P_e/A$	$P_e \cdot e/S_{top}$	$M_{ow}/S_{top}$	$M_a/S_{top}$	$f_{top}$ (psi)		$M_{a-1}$ (k-ft)	235.15		
-555	973	-398	-3020	-3000					
BOT STRESSES (psi)			Allowable Tens. Strsses (psi)			0	0	x $\sqrt{f'_c}$	
$P/A$	$P_e/S_{bot}$	$M_{ow}/S_{bot}$	$M_a/S_{bot}$	$f_{bot}$ (psi)		$M_{a-2}$ (k-ft)	65.98		
-555	-1977	810	1722	0					
<b>APPLIED MOMENTS</b>									
Curb:	$M_{curb}$ (k-ft)	10.46		Wearing Surface:	$W_{ws}$ (k/ft)	0.120	$M_{ws}$ (k-ft)	8.25	
Live Load Moment Including Impact:				$M_{LL+I}$ (k-ft)	47.27	IM (%)	33		
Live Load Moment <u>NOT</u> Including Impact:				$M_{LL}$ (k-ft)	35.54				

**Table B.3:** Undamaged Inventory Load – 22% losses,  $f_t \leq 6\sqrt{f'_c}$  (psi).

<b>MATERIAL PROPERTIES</b>									
$f'_c$ (psi)	5000	$f_{ci}$ (psi)	4000	$f_{pu}$ (ksi)	270	$f'_{pi}$ (ksi)	185		
				$A_{strand}$ (in <sup>2</sup> )	0.1167	$f'_{pi}$ (ksi)	189		
<b>SECTION DEFINITION</b>									
A (in <sup>2</sup> )	264.675	$I_x$ (in <sup>4</sup> )	5238.777	$I_y$ (in <sup>4</sup> )	28593.247	$Y_{top}$ (in)	5.606	$Y_{bot}$ (in)	11.394
						$S_{top}$ (in <sup>3</sup> )	934.495	$S_{bot}$ (in <sup>3</sup> )	459.784
<b>PRESTRESSING</b>									
$P_{1-i}$ (kip)	21.56	$e_1$ (in)	4.519	Losses (%)	22	$P_{1-e}$ (kip)	16.82		
$P_{2-i}$ (kip)	21.56	$e_2$ (in)	4.957			$P_{2-e}$ (kip)	16.82		
$P_{3-i}$ (kip)	21.56	$e_3$ (in)	5.394			$P_{3-e}$ (kip)	16.82		
$P_{4-i}$ (kip)	21.56	$e_4$ (in)	9.894			$P_{4-e}$ (kip)	16.82		
<b>MOMENT DUE TO OWN WEIGHT</b>									
Span (ft)	30	$W_{ow}$ (k/ft)	0.276	$M_{ow}$ (k-ft)	31.02				
<b>STRESSES AT SERVICE STAGE</b>									
TOP STRESSES (psi)			Allowable Comp. Strsses (psi)			-3000	0.6	x $f'_c$	
$P_e/A$	$P_e \cdot e/S_{top}$	$M_{ow}/S_{top}$	$M_a/S_{top}$	$f_{top}$ (psi)		$M_{a-1}$ (k-ft)	232.45		
-508	891	-398	-2985	-3000					
BOT STRESSES (psi)			Allowable Tens. Strsses (psi)			424	6	x $\sqrt{f'_c}$	
$P/A$	$P_e/S_{bot}$	$M_{ow}/S_{bot}$	$M_a/S_{bot}$	$f_{bot}$ (psi)		$M_{a-2}$ (k-ft)	74.12		
-508	-1811	810	1934	424					
<b>APPLIED MOMENTS</b>									
Curb:	$M_{curb}$ (k-ft)	10.46		Wearing Surface:	$W_{ws}$ (k/ft)	0.120	$M_{ws}$ (k-ft)	8.25	
Live Load Moment Including Impact:				$M_{LL+I}$ (k-ft)	55.41	IM (%)	33		
Live Load Moment <u>NOT</u> Including Impact:				$M_{LL}$ (k-ft)	41.66				

**Table B.4:** Undamaged Inventory Load – 22% losses,  $f_t \leq 0\sqrt{f'_c}$  (psi).

<b>MATERIAL PROPERTIES</b>										
$f'_c$ (psi)	5000	$f_{ci}$ (psi)	4000	$f_{pu}$ (ksi)	270	$f'_{pi}$ (ksi)	185			
				$A_{strand}$ (in <sup>2</sup> )	0.1167					
<b>SECTION DEFINITION</b>										
A (in <sup>2</sup> )	264.675	$I_x$ (in <sup>4</sup> )	5238.777	$I_y$ (in <sup>4</sup> )	28593.247	$Y_{top}$ (in)	5.606	$Y_{bot}$ (in)	11.394	
							$S_{top}$ (in <sup>3</sup> )	934.495	$S_{bot}$ (in <sup>3</sup> )	459.784
<b>PRESTRESSING</b>										
$P_{1-i}$ (kip)	21.59	$e_1$ (in)	4.519	Losses (%)	22	$P_{1-e}$ (kip)	16.84			
$P_{2-i}$ (kip)	21.59	$e_2$ (in)	4.957			$P_{2-e}$ (kip)	16.84			
$P_{3-i}$ (kip)	21.59	$e_3$ (in)	5.394			$P_{3-e}$ (kip)	16.84			
$P_{4-i}$ (kip)	21.59	$e_4$ (in)	9.894			$P_{4-e}$ (kip)	16.84			
<b>MOMENT DUE TO OWN WEIGHT</b>										
Span (ft)	30	$W_{ow}$ (k/ft)	0.276	$M_{ow}$ (k-ft)	31.02					
<b>STRESSES AT SERVICE STAGE</b>										
TOP STRESSES (psi)					Allowable Comp. Strsses (psi)		-3000	0.6	x $\sqrt{f'_c}$	
$P_e/A$	$P_e \cdot e/S_{top}$	$M_{ow}/S_{top}$	$M_a/S_{top}$	$f_{top}$ (psi)			$M_{a-1}$ (k-ft)	232.50		
-509	893	-398	-2986	-3000						
BOT STRESSES (psi)					Allowable Tens. Strsses (psi)		0	0	x $\sqrt{f'_c}$	
$P/A$	$P_e/S_{bot}$	$M_{ow}/S_{bot}$	$M_a/S_{bot}$	$f_{bot}$ (psi)			$M_{a-2}$ (k-ft)	58.00		
-509	-1814	810	1514	0						
<b>APPLIED MOMENTS</b>										
Curb:	$M_{curb}$ (k-ft)	10.46	Wearing Surface:		$W_{ws}$ (k/ft)	0.120	$M_{ws}$ (k-ft)	8.25		
Live Load Moment Including Impact:			$M_{LL+I}$ (k-ft)	39.29	IM (%)	33				
Live Load Moment <u>NOT</u> Including Impact:			$M_{LL}$ (k-ft)	29.54						

**Table B.5:** Undamaged Ultimate Capacity.

<b>MATERIAL PROPERTIES</b>									
$f_c'$ (psi)	5000	$f_{ci}$ (psi)	4000	$f_{pu}$ (ksi)	270	$f_{pi}$ (ksi)	189		
$E_c$ (ksi)	4030.5	$E_{ps}$ (ksi)	28500	$A_{strand}$ (in <sup>2</sup> )	0.1167	$f_{pe}$ (ksi)	160.7		
$\beta$	0.80			Losses (%)	15				
<b>1- <math>\epsilon_{pe}</math></b>									
A (in <sup>2</sup> )	264.675	$I_x$ (in <sup>4</sup> )	5238.777	$I_y$ (in <sup>4</sup> )	28593.247	$Y_{top}$ (in)	5.606	$Y_{bot}$ (in)	11.394
<b>PRESTRESSING</b>									
$P_{1-i}$ (kip)	21.70	$e_1$ (in)	4.519	$P_{1-e}$ (kip)	18.45				
$P_{2-i}$ (kip)	21.70	$e_2$ (in)	4.957	$P_{2-e}$ (kip)	18.45				
$P_{3-i}$ (kip)	21.70	$e_3$ (in)	5.394	$P_{3-e}$ (kip)	18.45				
$P_{4-i}$ (kip)	21.70	$e_4$ (in)	9.894	$P_{4-e}$ (kip)	18.45				
<b>1- <math>\epsilon_{pe}</math></b>									
	$\epsilon_{pe} = 5.637E-03$								
<b>2- <math>\epsilon_{ce}</math></b>									
At centroid of top 3 strands				At centroid of bottom strand					
$P_e/A$	$P_e \cdot e \cdot e/l$	$f_{c1}$ (psi)	$\epsilon_{pe1}$	$P_e/A$	$P_e \cdot e \cdot e/l$	$f_{c1}$ (psi)	$\epsilon_{pe2}$		
558	864	1422	3.528E-04	558	1725	2283	5.664E-04		
<b>3- <math>\epsilon_{pc}</math> (Compatibility)</b>									
<b>First Iteration:</b>									
Assumed Stress	$f_{ps1}$ (ksi)	172.0	$T_1$ (kip)	120.4	$f_{ps2}$ (ksi)	185.0	$T_2$ (kip)	43.2	
Equilibrium:	a (in)	1.24	c (in)	1.55					
Strain Compatibility:	$\epsilon_{pc1}$	1.741E-02			$\epsilon_{pc2}$	2.696E-02			
Total Strain:	$\epsilon_{ps1}$	2.340E-02			$\epsilon_{ps2}$	3.316E-02			
Strand Stress	$f_{ps1}$ (ksi)	267.6			$f_{ps1}$ (ksi)	268.5			
<b>Second Iteration:</b>									
Assumed Stress	$f_{ps1}$ (ksi)	265.8	$T_1$ (kip)	186.1	$f_{ps2}$ (ksi)	267.5	$T_2$ (kip)	62.4	
Equilibrium:	a (in)	1.89	c (in)	2.36					
Strain Compatibility:	$\epsilon_{pc1}$	1.044E-02			$\epsilon_{pc2}$	1.672E-02			
Total Strain:	$\epsilon_{ps1}$	1.643E-02			$\epsilon_{ps2}$	2.292E-02			
Strand Stress	$f_{ps1}$ (ksi)	265.8			$f_{ps1}$ (ksi)	267.5			
<b>Nominal Moment Capacity (<math>M_n</math>)</b>									
$M_{n1}$ (kip-ft)		$M_{n2}$ (kip-ft)		<b><math>M_n</math> (kip-ft)</b>					
149.2		75.7		<b>224.9</b>					

**Table B.6:** Damaged Inventory Load – 15% losses,  $f_t \leq 6\sqrt{f'_c}$  (psi).

<b>MATERIAL PROPERTIES</b>									
$f'_c$ (psi)	5000	$f_{ci}$ (psi)	4000	$f_{pu}$ (ksi)	270	$f_{pi}$ (ksi)	185		
				$A_{strand}$ (in <sup>2</sup> )	0.1167				
<b>SECTION DEFINITION</b>									
A (in <sup>2</sup> )	264.675	$I_x$ (in <sup>4</sup> )	5238.777	$I_y$ (in <sup>4</sup> )	28593.247	$Y_{top}$ (in)	5.606	$Y_{bot}$ (in)	11.394
				$S_{top}$ (in <sup>3</sup> )	934.495	$S_{bot}$ (in <sup>3</sup> )	459.784		
<b>PRESTRESSING</b>									
$P_{1-i}$ (kip)	21.59	$e_1$ (in)	4.519	Losses (%)	15	$P_{1-e}$ (kip)	18.35		
$P_{2-i}$ (kip)	21.59	$e_2$ (in)	4.957			$P_{2-e}$ (kip)	18.35		
$P_{3-i}$ (kip)	21.59	$e_3$ (in)	5.394			$P_{3-e}$ (kip)	18.35		
$P_{4-i}$ (kip)	0.00	$e_4$ (in)	9.894			$P_{4-e}$ (kip)	0.00		
<b>MOMENT DUE TO OWN WEIGHT</b>									
Span (ft)	30	$W_{ow}$ (k/ft)	0.276	$M_{ow}$ (k-ft)	31.02				
<b>STRESSES AT SERVICE STAGE</b>									
TOP STRESSES (psi)					Allowable Comp. Strsses (psi)	-3000	0.6	x $fc'$	
$P_e/A$	$P_e \cdot e/S_{top}$	$M_{ow}/S_{top}$	$M_a/S_{top}$	$f_{top}$ (psi)	$M_{a-1}$ (k-ft)	215.70			
-416	584	-398	-2770	-3000					
BOT STRESSES (psi)					Allowable Tens. Strsses (psi)	424	6	x $\nu fc'$	
$P/A$	$P_e/S_{bot}$	$M_{ow}/S_{bot}$	$M_a/S_{bot}$	$f_{bot}$ (psi)	$M_{a-2}$ (k-ft)	46.65			
-416	-1187	810	1218	424					
<b>APPLIED MOMENTS</b>									
Curb:	$M_{curb}$ (k-ft)	10.46	Wearing Surface:		$W_{ws}$ (k/ft)	0.120	$M_{ws}$ (k-ft)	8.25	
Live Load Moment Including Impact:			$M_{LL+I}$ (k-ft)	27.94	IM (%)	33			
Live Load Moment <u>NOT</u> Including Impact:			$M_{LL}$ (k-ft)	21.01					

**Table B.7:** Damaged Inventory Load – 15% losses,  $f_t \leq 0\sqrt{f'_c}$  (psi).

<b>MATERIAL PROPERTIES</b>									
$f'_c$ (psi)	5000	$f_{ci}$ (psi)	4000	$f_{pu}$ (ksi)	270	$f_{pi}$ (ksi)	185		
				$A_{strand}$ (in <sup>2</sup> )	0.1167				
<b>SECTION DEFINITION</b>									
A (in <sup>2</sup> )	264.675	$I_x$ (in <sup>4</sup> )	5238.777	$I_y$ (in <sup>4</sup> )	28593.247	$Y_{top}$ (in)	5.606	$Y_{bot}$ (in)	11.394
				$S_{top}$ (in <sup>3</sup> )	934.495	$S_{bot}$ (in <sup>3</sup> )	459.784		
<b>PRESTRESSING</b>									
$P_{1-i}$ (kip)	21.59	$e_1$ (in)	4.519	Losses (%)	15	$P_{1-e}$ (kip)	18.35		
$P_{2-i}$ (kip)	21.59	$e_2$ (in)	4.957			$P_{2-e}$ (kip)	18.35		
$P_{3-i}$ (kip)	21.59	$e_3$ (in)	5.394			$P_{3-e}$ (kip)	18.35		
$P_{4-i}$ (kip)	0.00	$e_4$ (in)	9.894			$P_{4-e}$ (kip)	0.00		
<b>MOMENT DUE TO OWN WEIGHT</b>									
Span (ft)	30	$W_{ow}$ (k/ft)	0.276	$M_{ow}$ (k-ft)	31.02				
<b>STRESSES AT SERVICE STAGE</b>									
TOP STRESSES (psi)					Allowable Comp. Strsses (psi)	-3000	0.6	x $fc'$	
$P_e/A$	$P_e \cdot e/S_{top}$	$M_{ow}/S_{top}$	$M_a/S_{top}$	$f_{top}$ (psi)	$M_{a-1}$ (k-ft)	215.70			
-416	584	-398	-2770	-3000					
BOT STRESSES (psi)					Allowable Tens. Strsses (psi)	0	0	x $\nu fc'$	
$P/A$	$P_e/S_{bot}$	$M_{ow}/S_{bot}$	$M_a/S_{bot}$	$f_{bot}$ (psi)	$M_{a-2}$ (k-ft)	30.40			
-416	-1187	810	793	0					
<b>APPLIED MOMENTS</b>									
Curb:	$M_{curb}$ (k-ft)	10.46	Wearing Surface:		$W_{ws}$ (k/ft)	0.120	$M_{ws}$ (k-ft)	8.25	
Live Load Moment Including Impact:			$M_{LL+I}$ (k-ft)	11.69	IM (%)	33			
Live Load Moment <u>NOT</u> Including Impact:			$M_{LL}$ (k-ft)	8.79					

**Table B.8:** Damaged Inventory Load – 22% losses,  $f_t \leq 6\sqrt{f'_c}$  (psi).

<b>MATERIAL PROPERTIES</b>									
$f'_c$ (psi)	5000	$f_{ci}$ (psi)	4000	$f_{pu}$ (ksi)	270	$f_{pi}$ (ksi)	185		
				$A_{strand}$ (in <sup>2</sup> )	0.1167				
<b>SECTION DEFINITION</b>									
A (in <sup>2</sup> )	264.675	$I_x$ (in <sup>4</sup> )	5238.777	$I_y$ (in <sup>4</sup> )	28593.247	$Y_{top}$ (in)	5.606	$Y_{bot}$ (in)	11.394
						$S_{top}$ (in <sup>3</sup> )	934.495	$S_{bot}$ (in <sup>3</sup> )	459.784
<b>PRESTRESSING</b>									
$P_{1-i}$ (kip)	21.59	$e_1$ (in)	4.519	Losses (%)	22	$P_{1-e}$ (kip)	16.84		
$P_{2-i}$ (kip)	21.59	$e_2$ (in)	4.957			$P_{2-e}$ (kip)	16.84		
$P_{3-i}$ (kip)	21.59	$e_3$ (in)	5.394			$P_{3-e}$ (kip)	16.84		
$P_{4-i}$ (kip)	0.00	$e_4$ (in)	9.894			$P_{4-e}$ (kip)	0.00		
<b>MOMENT DUE TO OWN WEIGHT</b>									
Span (ft)	30	$W_{ow}$ (k/ft)	0.276	$M_{ow}$ (k-ft)	31.02				
<b>STRESSES AT SERVICE STAGE</b>									
TOP STRESSES (psi)			Allowable Comp. Strsses (psi)			-3000	0.6	x $f_c'$	
$P_e/A$	$P_e \cdot e/S_{top}$	$M_{ow}/S_{top}$	$M_a/S_{top}$	$f_{top}$ (psi)		$M_{a-1}$ (k-ft)	214.60		
-382	536	-398	-2756	-3000					
BOT STRESSES (psi)			Allowable Tens. Strsses (psi)			424	6	x $v f_c'$	
$P/A$	$P_e/S_{bot}$	$M_{ow}/S_{bot}$	$M_a/S_{bot}$	$f_{bot}$ (psi)		$M_{a-2}$ (k-ft)	41.60		
-382	-1089	810	1086	424					
<b>APPLIED MOMENTS</b>									
Curb:	$M_{curb}$ (k-ft)	10.46		Wearing Surface:	$W_{ws}$ (k/ft)	0.120	$M_{ws}$ (k-ft)	8.25	
Live Load Moment Including Impact:				$M_{LL+I}$ (k-ft)	22.89	IM (%)	33		
Live Load Moment <u>NOT</u> Including Impact:				$M_{LL}$ (k-ft)	17.21				

**Table B.9:** Damaged Inventory Load – 22% losses,  $f_t \leq 0\sqrt{f'_c}$  (psi).

<b>MATERIAL PROPERTIES</b>									
$f'_c$ (psi)	5000	$f_{ci}$ (psi)	4000	$f_{pu}$ (ksi)	270	$f_{pi}$ (ksi)	185		
				$A_{strand}$ (in <sup>2</sup> )	0.1167				
<b>SECTION DEFINITION</b>									
A (in <sup>2</sup> )	264.675	$I_x$ (in <sup>4</sup> )	5238.777	$I_y$ (in <sup>4</sup> )	28593.247	$Y_{top}$ (in)	5.606	$Y_{bot}$ (in)	11.394
						$S_{top}$ (in <sup>3</sup> )	934.495	$S_{bot}$ (in <sup>3</sup> )	459.784
<b>PRESTRESSING</b>									
$P_{1-i}$ (kip)	21.59	$e_1$ (in)	4.519	Losses (%)	22	$P_{1-e}$ (kip)	16.84		
$P_{2-i}$ (kip)	21.59	$e_2$ (in)	4.957			$P_{2-e}$ (kip)	16.84		
$P_{3-i}$ (kip)	21.59	$e_3$ (in)	5.394			$P_{3-e}$ (kip)	16.84		
$P_{4-i}$ (kip)	0.00	$e_4$ (in)	9.894			$P_{4-e}$ (kip)	0.00		
<b>MOMENT DUE TO OWN WEIGHT</b>									
Span (ft)	30	$W_{ow}$ (k/ft)	0.276	$M_{ow}$ (k-ft)	31.02				
<b>STRESSES AT SERVICE STAGE</b>									
TOP STRESSES (psi)			Allowable Comp. Strsses (psi)			-3000	0.6	x $f_c'$	
$P_e/A$	$P_e \cdot e/S_{top}$	$M_{ow}/S_{top}$	$M_a/S_{top}$	$f_{top}$ (psi)		$M_{a-1}$ (k-ft)	214.60		
-382	536	-398	-2756	-3000					
BOT STRESSES (psi)			Allowable Tens. Strsses (psi)			0	0	x $v f_c'$	
$P/A$	$P_e/S_{bot}$	$M_{ow}/S_{bot}$	$M_a/S_{bot}$	$f_{bot}$ (psi)		$M_{a-2}$ (k-ft)	25.35		
-382	-1089	810	662	0					
<b>APPLIED MOMENTS</b>									
Curb:	$M_{curb}$ (k-ft)	10.46		Wearing Surface:	$W_{ws}$ (k/ft)	0.120	$M_{ws}$ (k-ft)	8.25	
Live Load Moment Including Impact:				$M_{LL+I}$ (k-ft)	6.64	IM (%)	33		
Live Load Moment <u>NOT</u> Including Impact:				$M_{LL}$ (k-ft)	4.99				

**Table B.10: Damaged Ultimate Capacity.****MATERIAL PROPERTIES**

$f'_c$ (psi) <b>5000</b>	$f_{ci}$ (psi) <b>4000</b>	$f_{pu}$ (ksi) <b>270</b>	$f_{pi}$ (ksi) <b>189</b>
$E_c$ (ksi) <b>4030.5</b>	$E_{ps}$ (ksi) <b>27000</b>	$A_{strand}$ (in <sup>2</sup> ) <b>0.1167</b>	$f_{pe}$ (ksi) <b>145.2</b>
$\beta$ <b>0.80</b>		Losses (%) <b>23.2</b>	

**1-  $\epsilon_{pe}$** 

A (in <sup>2</sup> ) <b>264.675</b>	$I_x$ (in <sup>4</sup> ) <b>5238.777</b>	$I_y$ (in <sup>4</sup> ) <b>28593.247</b>	$Y_{top}$ (in) <b>5.606</b>	$Y_{bot}$ (in) <b>11.394</b>
			$S_{top}$ (in <sup>3</sup> ) <b>934.495</b>	$S_{bot}$ (in <sup>3</sup> ) <b>459.784</b>

**PRESTRESSING**

$P_{1-i}$ (kip) <b>21.70</b>	$e_1$ (in) <b>4.519</b>	$P_{1-e}$ (kip) <b>16.67</b>
$P_{2-i}$ (kip) <b>21.70</b>	$e_2$ (in) <b>4.957</b>	$P_{2-e}$ (kip) <b>16.67</b>
$P_{3-i}$ (kip) <b>21.70</b>	$e_3$ (in) <b>5.394</b>	$P_{3-e}$ (kip) <b>16.67</b>
$P_{4-i}$ (kip) <b>0.00</b>	$e_4$ (in) <b>9.894</b>	$P_{4-e}$ (kip) <b>0.00</b>

**1-  $\epsilon_{pe}$** 

$$\epsilon_{pe} = 5.376E-03$$

**2-  $\epsilon_{ce}$** 

At centroid of top 3 strands				At centroid of bottom strands			
$P_e/A$	$P_e \cdot e \cdot e/I$	$f_{c1}$ (psi)	$\epsilon_{pe1}$	$P_e/A$	$P_e \cdot e \cdot e/I$	$f_{c1}$ (psi)	$\epsilon_{pe2}$
378	469	847	2.101E-04	378	936	1314	3.260E-04

**3-  $\epsilon_{pc}$  (Compatibility)****First Iteration:**

Assumed Stress	$f_{ps1}$ (ksi) <b>260.0</b>	$T_1$ (kip) <b>182.1</b>	$f_{ps2}$ (ksi) <b>0.0</b>	$T_2$ (kip) <b>0.0</b>
Equilibrium:	$a$ (in) <b>1.38</b>	$c$ (in) <b>1.73</b>		
Strain Compatibility:	$\epsilon_{pc1}$ <b>1.535E-02</b>		$\epsilon_{pc2}$ <b>2.392E-02</b>	
Total Strain:	$\epsilon_{ps1}$ <b>2.093E-02</b>		$\epsilon_{ps2}$ <b>2.962E-02</b>	
Strand Stress	$f_{ps1}$ (ksi) <b>267.1</b>		$f_{ps1}$ (ksi) <b>268.2</b>	

**Second Iteration:**

Assumed Stress	$f_{ps1}$ (ksi) <b>267.0</b>	$T_1$ (kip) <b>187.0</b>	$f_{ps2}$ (ksi) <b>0.0</b>	$T_2$ (kip) <b>0.0</b>
Equilibrium:	$a$ (in) <b>1.42</b>	$c$ (in) <b>1.77</b>		
Strain Compatibility:	$\epsilon_{pc1}$ <b>1.487E-02</b>		$\epsilon_{pc2}$ <b>2.322E-02</b>	
Total Strain:	$\epsilon_{ps1}$ <b>2.045E-02</b>		$\epsilon_{ps2}$ <b>2.892E-02</b>	
Strand Stress	$f_{ps1}$ (ksi) <b>267.0</b>		$f_{ps1}$ (ksi) <b>268.2</b>	

**Nominal Moment Capacity ( $M_n$ )**

$M_{n1}$ (kip-ft)	$M_{n2}$ (kip-ft)	<b><math>M_n</math> (kip-ft)</b>
153.5	0.0	<b>153.5</b>

### AASHTO Lump Sum Results

Equations B.1 through B.6 represent the calculations required for the AASHTO (2017) lump sum approach for determining total prestress losses at time  $t$  hours due to elastic shortening, creep, shrinkage, and relaxation.

$$\Delta f_{pT} = \Delta f_{pES} + \Delta f_{pLT} \quad (\text{B.1})$$

in which,

$$\Delta f_{pES} = \frac{A_{ps} f_{pi} (I_g + e_m^2 A_g) - e_m M_{sw} A_g}{A_{ps} (I_g + e_m^2 A_g) + \frac{A_g I_g E_{ci}}{E_p}} \quad (\text{B.2})$$

and

$$\Delta f_{pLT} = 10.0 \frac{f_{pi} A_{ps}}{A_g} \gamma_h \gamma_{st} + 12.0 \gamma_h \gamma_{st} + \Delta f_{pR} \quad (\text{B.3})$$

and

$$\gamma_h = 1.7 - 0.01H \quad (\text{B.4})$$

and

$$\gamma_{st} = \frac{5}{(1 + f_{ci})} \quad (\text{B.5})$$

and

$$\Delta f_{pR} = f'_{pi} \frac{\log t}{10} \left( \frac{f'_{pi}}{f_{py}} - 0.55 \right) \quad (\text{B.6})$$

where  $\Delta f_{pT}$  is the total prestress loss (MPa / ksi),  $\Delta f_{ES}$  is the change in stress due to elastic shortening of concrete (MPa / ksi),  $\Delta f_{pLT}$  is the prestress loss due to long-term shrinkage and creep of concrete,  $A_{ps}$  is the area of prestressing steel ( $\text{mm}^2 / \text{in.}^2$ ),  $f_{pi}$  is the initial prestress in the steel – taken as 70% of the ultimate stress,  $f_{pu}$  (MPa / ksi),  $I_g$  is the gross moment of inertia of the concrete section neglecting reinforcement ( $\text{mm}^4 / \text{in.}^4$ ),  $e_m$  is the average steel eccentricity at midspan (mm / in.),  $A_g$  is the gross area

of the section ( $\text{mm}^2 / \text{in.}^2$ ),  $M_{sw}$  is the self-weight moment at midspan ( $\text{N-mm} / \text{kip-in.}$ )  $E_{ci}$  is the concrete elastic modulus at transfer ( $\text{MPa} / \text{ksi}$ ),  $E_p$  is the prestressing steel elastic modulus ( $\text{MPa} / \text{ksi}$ ),  $\gamma_h$  is a correction factor for the relative humidity of the ambient air,  $\gamma_{st}$  is a correction factor for specified concrete strength at time of prestress transfer to the concrete member,  $H$  is the average annual ambient relative humidity (%) – taken as 70% for North Carolina,  $f_{ci}$  is concrete compressive strength at time of transfer ( $\text{MPa}$ ,  $\text{ksi}$ ), and  $P_i$  is the initial prestress force ( $\text{kN} / \text{kips}$ ). Using Equation 2g,  $\Delta f_{pR}$  after 400,000 hours is 181 MPa (26.2 ksi). Therefore, using Equations 2b through 2f,  $\Delta f_{pT}$  is 271 MPa (39.3 ksi), and the effective prestress force at 400,000 hours. Table B.11 provides a summary of the results for Equations B.1 through B.6.

**Table B.11:** AASHTO Lump Sum Results.

$\Delta f_{pES}$	0.259 ksi	1.78 MPa	
$\Delta f_{pLT}$	35.046 ksi	241 MPa	
$\Delta f_{pT}$	35.304 ksi	243 MPa	
$A_{ps}$	0.1167 in.2		
$E_{ci}$	3605 ksi		
$E_p$	29000 ksi		
$e_m$	6.191 in.		
$f_{ci}$	4000 psi		
$I_g + e_m^2 A_g$	38738 in.4		
$\gamma_h$	1		
$\gamma_{sh}$	1		
$\Delta f_{pR,0-6 \text{ hours}}$	4.0 ksi	27.53 MPa	relaxation loss at transfer
$\Delta f_{pR,6-400k \text{ hours}}$	22.2 ksi	153 MPa	relaxation loss between transfer and 400k hours
$f_{pi}$	185 ksi	1273 MPa	effective prestress at transfer
$f_{py}$	230 ksi	1585 MPa	
$f_{pe,400k}$	149 ksi	1030 MPa	
$P_{eff,400k}$	17.4 kips	77.6 kN	

### Appendix C: MF-FRP 2.0 Design Calculations and Detail Drawings

Appendix C provides a limit state summary for the MF-FRP 2.0 design calculations followed by design equations, variables for each design equation, and the detailed drawings for the MF-FRP 2.0 components. All components are designed such that  $\phi R_n > 50 \text{ kips}$ . Tables C.1 and C.2 provide the design variable values and material properties for MF-FRP 2.0.

**Limit state summary** ( $\phi = 0.75$  except where otherwise noted)

*Bolt shear:*

1/2" dia. A325:	$\phi R_n = 7.06 \frac{k}{bolt} > V_{bolt} = 2.27 \frac{k}{bolt}$	OK
3/4" dia. A325:	$\phi R_n = 15.9 \frac{k}{bolt} > V_{bolt} = 8.3 \frac{k}{bolt}$	OK
1-1/2" dia. shoulder:	$\phi R_n = 83.6 \frac{k}{bolt} > V_{bolt} = 50 \frac{k}{bolt}$	OK

*Bolt moment* ( $\phi = 0.90$ ):

1-1/2" dia. shoulder:	$\phi R_n = 126 \text{ ksi} > \sigma_{bolt} = 113 \text{ ksi}$	OK
-----------------------	--	----

*Combined tension and shear:*

1-1/2" dia. shoulder:	$\phi R_n = 97.8 \text{ k} > 50 \text{ k}$	OK
-----------------------	--	----

*Bearing at bolt holes:*

1/2" dia. A325:	$\phi R_n = 22.5 \frac{k}{bolt} > V_{bolt} = 2.27 \frac{k}{bolt}$	OK
3/4" dia. A325:	$\phi R_n = 135 \frac{k}{bolt} > V_{bolt} = 8.3 \frac{k}{bolt}$	OK
1-1/2" dia. shoulder:	$\phi R_n = 51 \frac{k}{bolt} > V_{bolt} = 50 \frac{k}{bolt}$	OK

*Steel yielding* ( $\phi = 0.90$ ):

Fixed Plate:	$\phi R_n = 540 \text{ k} > 50 \text{ k}$	OK
FRP Connector Plates:	$\phi R_n = 101 \text{ k} > 50 \text{ k}$	OK
Turnbuckle Connector Plate:	$\phi R_n = 72 \text{ k} > 50 \text{ k}$	OK

*Steel rupture:*

Fixed Plate:	$\phi R_n = 205 \text{ k} > 50 \text{ k}$	OK
FRP Connector Plate 1:	$\phi R_n = 77.5 \text{ k} > 50 \text{ k}$	OK
FRP Connector Plate 2:	$\phi R_n = 113 \text{ k} > 50 \text{ k}$	OK
Turnbuckle Connector Plate:	$\phi R_n = 113 \text{ k} > 50 \text{ k}$	OK

*Weld rupture:*

FRP and TB Plates:	$\phi R_n = 66.8 \text{ k} > 50 \text{ k}$	OK
--------------------	--	----

*Concrete splitting:*

3/4" dia. bolts:	$\phi R_n = 108 \text{ k} > 50 \text{ k}$	OK
------------------	---	----

*Concrete bearing:*

3/4" dia. bolts:	$\phi R_n = 57.2 \text{ k} > 50 \text{ k}$	OK
------------------	--	----

## Design equations

$\phi R_n$  = design strength for each limit state, and  $\phi = 0.75$  except where otherwise noted

*Bolt shear:*  $R_n = F_{nv}A_b$  (AISC, 2015 – J3-1)

where

$F_{nv}$  = nominal shear stress, ksi (MPa)

$A_b$  = nominal body area of bolt, in.<sup>2</sup> (mm<sup>2</sup>)

*Bolt moment ( $\phi = 0.90$ ):*  $R_n > \frac{My}{I}$

where

$M$  = applied moment, k-in. (N-mm)

$y$  = radius of bolt, in. (mm)

$I$  = bolt moment of inertia, in.<sup>4</sup> (mm<sup>4</sup>)

*Combined tension and shear:*  $R_n = F'_{nt}A_b$  (AISC, 2015 – J3-2)

where

$F'_{nt}$  = nominal tensile stress modified to include effects of shear stress, ksi (MPa)

$F'_{nt} = 1.3F_{nt} - \frac{F_{nt}}{\phi F_{nv}} f_v \leq F_{nt}$  (AISC, 2015 – J3-3a)

$F_{nt}$  = nominal tensile stress, ksi (MPa)

$F_{nv}$  = nominal shear stress, ksi (MPa)

$f_v$  = required shear stress, ksi (MPa)

*Bearing at bolt holes:*  $R_n = 1.2L_c t F_u \leq 2.4d_b t F_u$  (AISC, 2015 – J3-6a)

where

$L_c$  = clear distance, in the direction of force, between the edge of hole and edge of adjacent hole or edge of material, in. (mm)

$t$  = thickness of connected material, in. (mm)

$F_u$  = specified minimum tensile strength of connected material, ksi (MPa)

$d_b$  = nominal bolt diameter, in. (mm)

*Steel yielding ( $\phi = 0.90$ ):*  $R_n = F_y A_g$  (AISC, 2015 – J4-1)

where

$F_y$  = specified tensile yield strength of material, ksi (MPa)

$A_g$  = gross cross-sectional area of connected element, in.<sup>2</sup> (mm<sup>2</sup>)

*Steel rupture:*  $R_n = F_u A_e$  (AISC, 2015 – J4-2)

where

$A_e$  = effective net cross-sectional area, in.<sup>2</sup> (mm<sup>2</sup>)

*Weld rupture:*  $R_n = F_w A_w$  (AISC, 2015 – J2-3)

where

$F_w$  = nominal strength of weld per unit area, ksi (MPa)

$F_w = 0.60F_{EXX}$

$A_w$  = effective area weld, in.<sup>2</sup> (mm<sup>2</sup>)

(AISC, 2015 – Tbl. J2.5)

$A_w = \left(\frac{\sqrt{2}}{2}\right) t_w l$

$t_w$  = weld thickness, in. (mm)

$l$  = weld length, in. (mm)

$$\text{Concrete splitting:} \quad R_n = F_{split} = 7\pi c d_{bolt} f_t \left(1 - \frac{d_{bolt}}{2c}\right)^{-2} \quad (\text{Oehlers, 2001})$$

where

$F_{split}$  = minimum concrete splitting force, lbf (N)

$c$  = concrete cover to the side of the bolt, in. (mm)

$d_{bolt}$  = bolt diameter, in. (mm)

$f_t$  = tensile strength of concrete, psi (MPa)

$f_t = 6\sqrt{f_c}$  (psi) or  $0.5\sqrt{f_c}$  (MPa) (Oehlers and Bradford, 1995)

$f_c$  = concrete compressive strength, psi (MPa)

$$\text{Concrete bearing:} \quad R_n = F_{bearing} = f_c A_{bearing}$$

where

$F_{bearing}$  = minimum concrete bearing force, kip (kN)

$A_{bearing}$  = concrete bearing surface area in. (mm)

$A_{bearing} = \frac{\pi d_b}{2} h_a$

**Table C.1:** MF-FRP 2.0 Variables.

Limit State	Component	Variable	Value	Units	
bolt shear	1/2" A325 bolt	$F_{nv}$	48	ksi	
		$A_b$	0.196	in. <sup>2</sup>	
	3/4" A325 bolt	$F_{nv}$	48	ksi	
		$A_b$	0.442	in. <sup>2</sup>	
	bolt moment	shoulder bolt	$F_{nv}$	63	ksi
			$A_b$	1.8	in. <sup>2</sup>
shoulder bolt		$M$	37.5	k-in.	
		$y$	0.75	in.	
		$I$	0.248	in. <sup>4</sup>	
combined tension and shear	shoulder bolt	$F'_{nt}$	73.7	ksi	
		$F_{nt}$	105	ksi	
		$F_{nv}$	63	ksi	
		$f_v$	28.25	ksi	
		$L_c$	1.5	in.	
		$t$	0.5	in.	
bearing at holes	1/2" A325 bolt	$F_u$	50	ksi	
		$d_b$	0.5	in.	
		$L_c$	1.5	in.	
		$t$	2.0	in.	
	3/4" A325 bolt	$F_u$	50	ksi	
		$d_b$	0.75	in.	
		$L_c$	2.25	in.	
		$t$	0.5	in.	
	shoulder bolt	$F_u$	50	ksi	
		$d_b$	1.5	in.	

**Table C.1:** (continued)

steel yielding	Fixed Plate	$F_y$	50	ksi
		$A_g$	12.0	in. <sup>2</sup>
	FRP Connector Plates	$F_y$	50	ksi
		$A_g$	2.25	in. <sup>2</sup>
	Turnbuckle Connector Plate	$F_y$	50	ksi
		$A_g$	2.5	in. <sup>2</sup>
steel rupture	Fixed Plate	$F_u$	65	ksi
		$A_e$	6.75	in. <sup>2</sup>
	FRP Connector Plate 1	$F_u$	65	ksi
		$A_e$	1.59	in. <sup>2</sup>
	FRP Connector Plate 2	$F_u$	65	ksi
		$A_e$	1.75	in. <sup>2</sup>
	Turnbuckle Connector Plate	$F_u$	65	ksi
		$A_e$	1.75	in. <sup>2</sup>
weld rupture	FRP and TB Connector Plates	$F_w$	42	ksi
		$F_{EXX}$	70	ksi
		$A_w$	2.12	in. <sup>2</sup>
		$t_w$	0.375	in.
		$l$	8	in.
		$c$	1.5	in.
concrete splitting	3/4" A325 bolt	$d_{bolt}$	0.75	in.
		$f_t$	540	psi
concrete bearing	3/4" A325 bolt	$A_{bearing}$	2.35	in. <sup>2</sup>
		$f_c$	8200	psi

Note: 1 in. = 25.4 mm; 1 ksi = 6.895 MPa

**Table C.2:** MF-FRP Retrofit Material Properties.

Component	Material Type	Yield Strength (MPa / ksi)	Ultimate Strength (MPa / ksi)	Elastic Modulus (GPa / Mpsi)	Shear Strength (MPa / ksi)
FRP <sup>2</sup>	glass and carbon fiber	N.A.	640 / 92.9 <sup>1</sup>	62.2 / 9.02	N.A.
Plate steel <sup>3</sup>	A572 Gr. 50 Steel	345 / 50	448 / 65	200 / 29	N.A.
Bolts <sup>4</sup>	A325 Gr. 8 Steel	634 / 92	827 / 120	200 / 29	586 / 85
Turnbuckle Coupler <sup>4</sup>	12L14 Carbon Steel	414 / 60	not available	200 / 29	not available
Turnbuckle <sup>5</sup>	C1035 Steel	370 / 53.7	585 / 84.8	200 / 29	not available
MF-FRP 2.0 pin <sup>4</sup>	Alloy Steel	not available	965 / 140	200 / 29	579 / 84

Notes: 1) Design strength in accordance with ACI 440.2R (2008); 2) Strongwell (2016); 3) AISC (2015); 4) McMaster-Carr (2018); 5) Cleveland City Forge (2018)

Figures C.1 through C.5 provide design drawing details for MF-FRP 2.0.

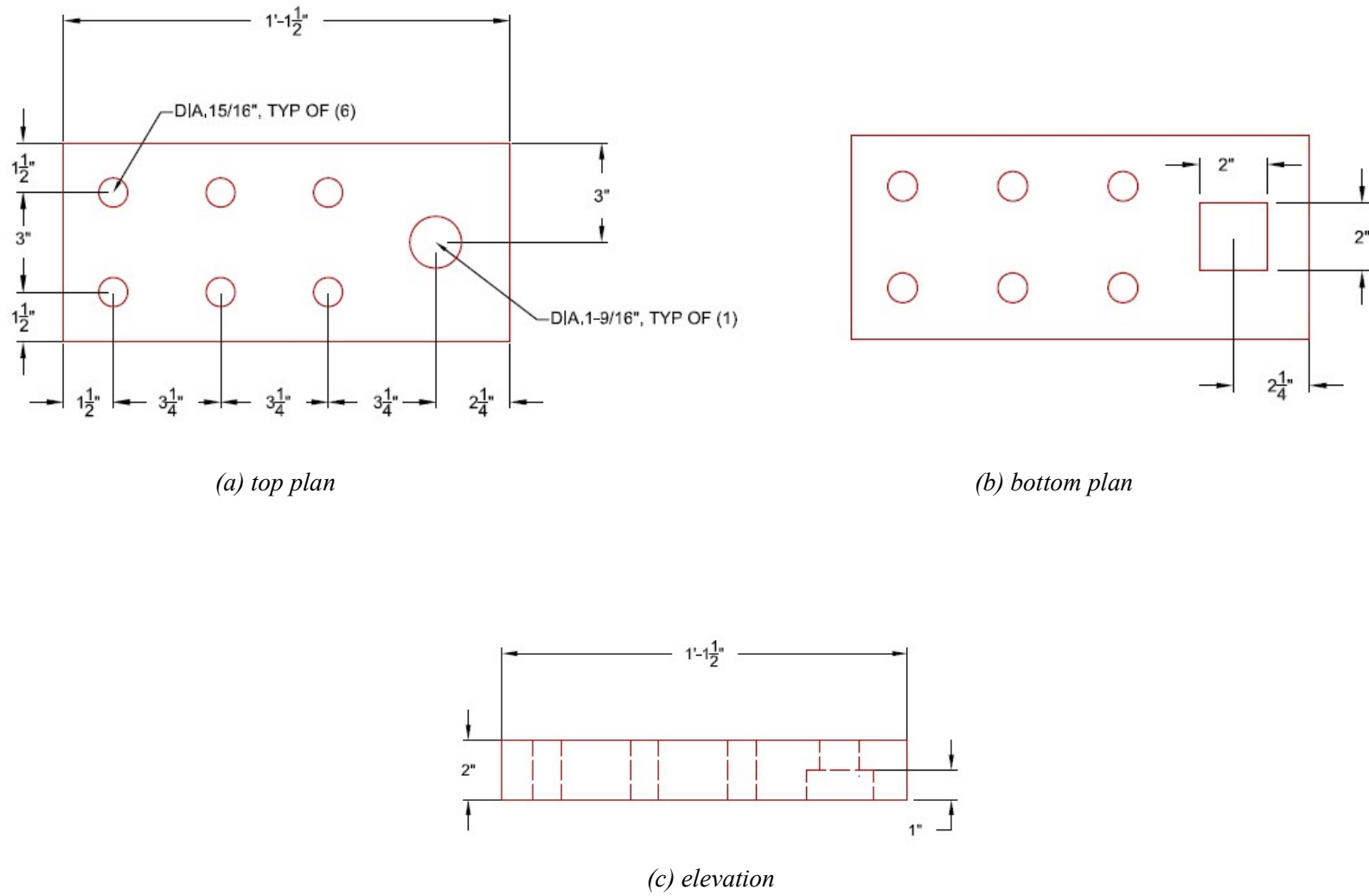
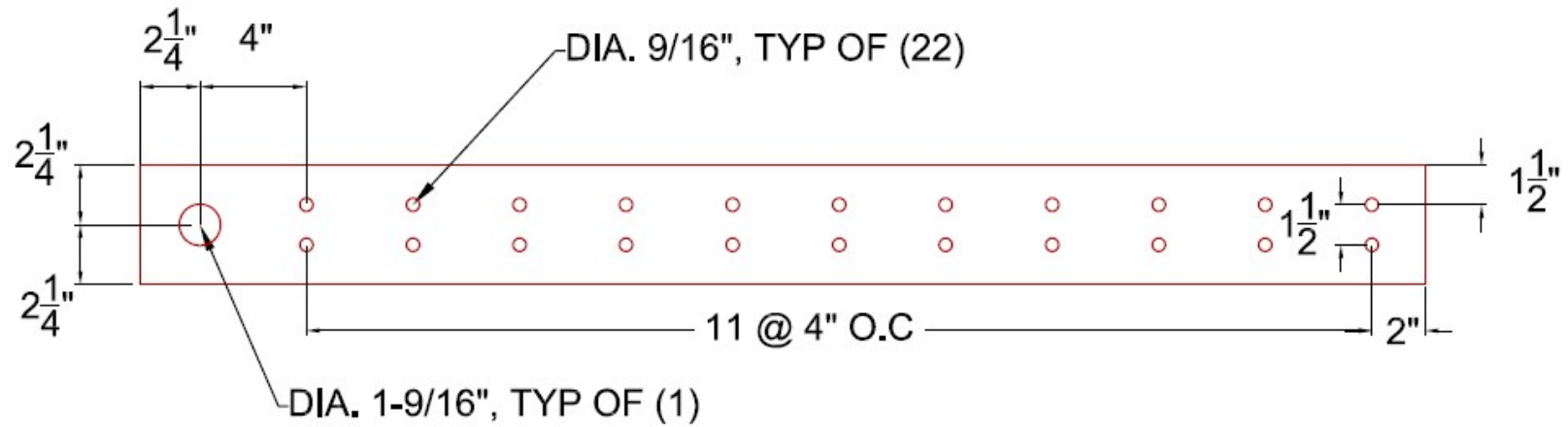
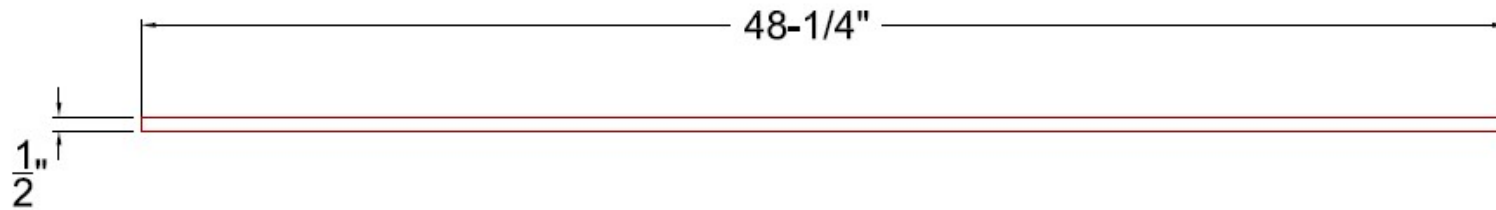


**Figure C.1:** Fixed plate design detail.  
 Note: All dimensions in inches; 1 in. = 25.4 mm



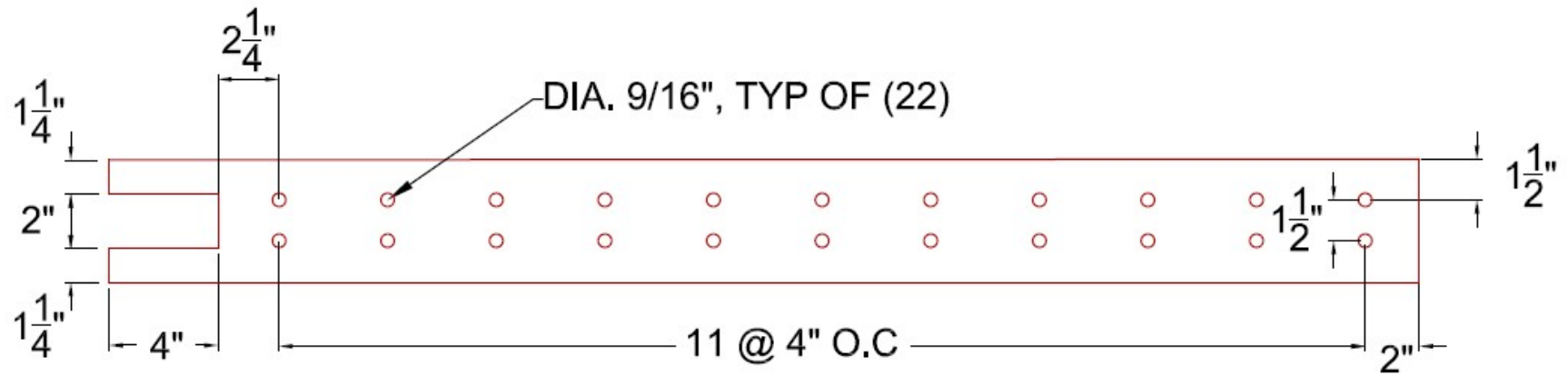
(a) plan



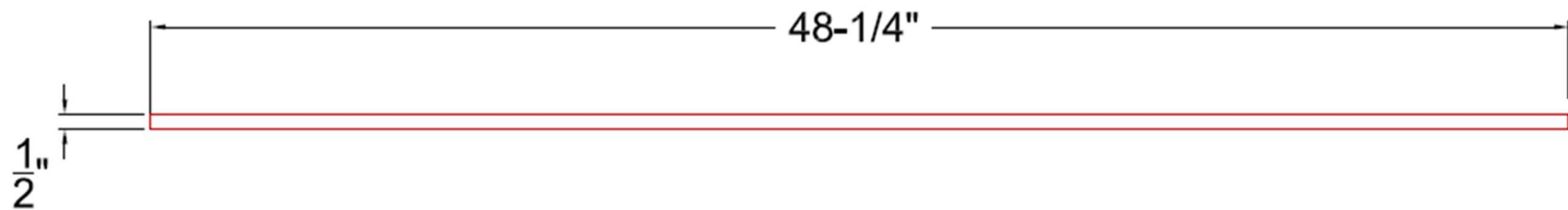
(b) elevation

**Figure C.2:** FRP connector plate 1 design detail.

Note: All dimensions in inches; 1 in. = 25.4 mm



(a) plan



(b) elevation

**Figure C.3:** FRP connector plate 2 design detail.

Note: All dimensions in inches; 1 in. = 25.4 mm

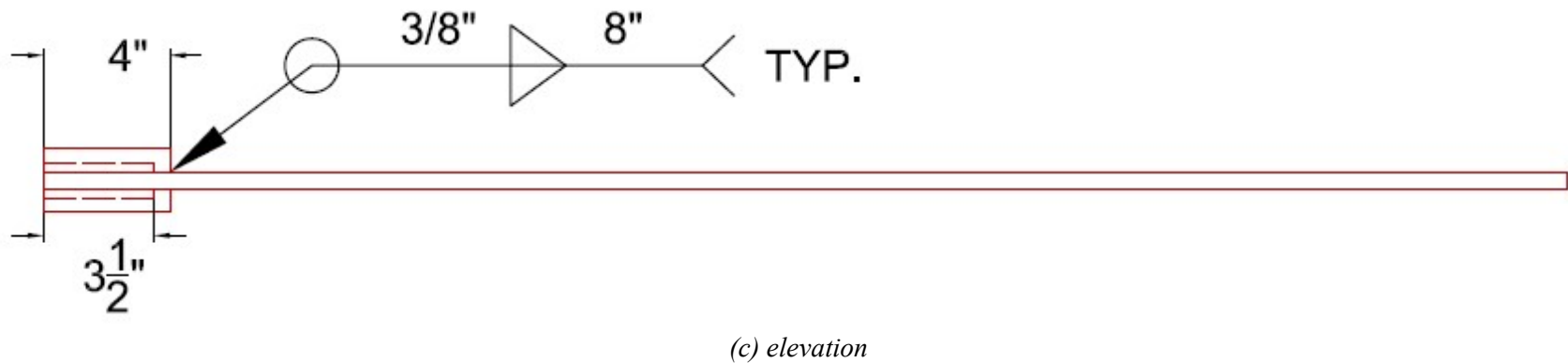
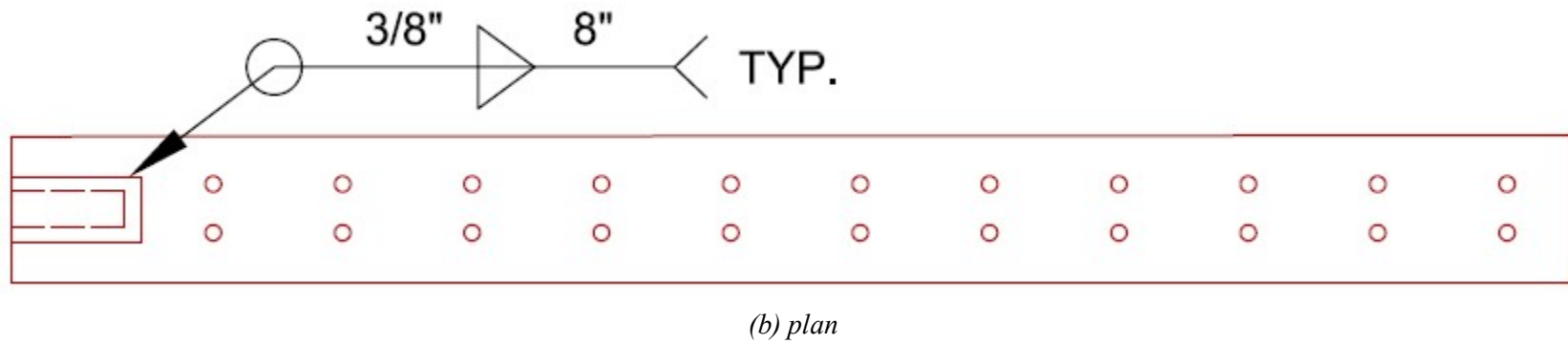
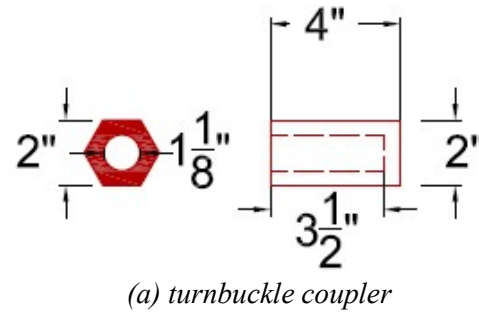
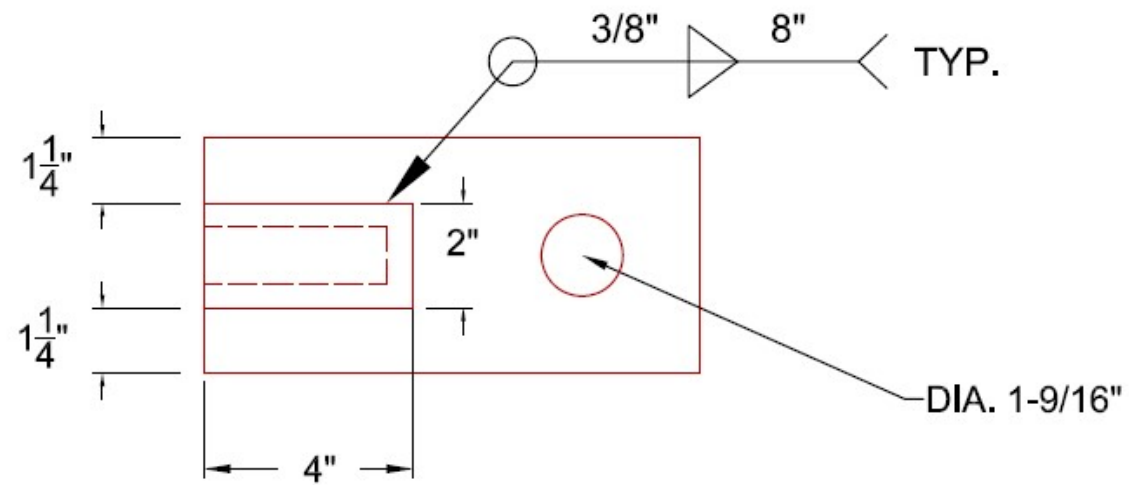
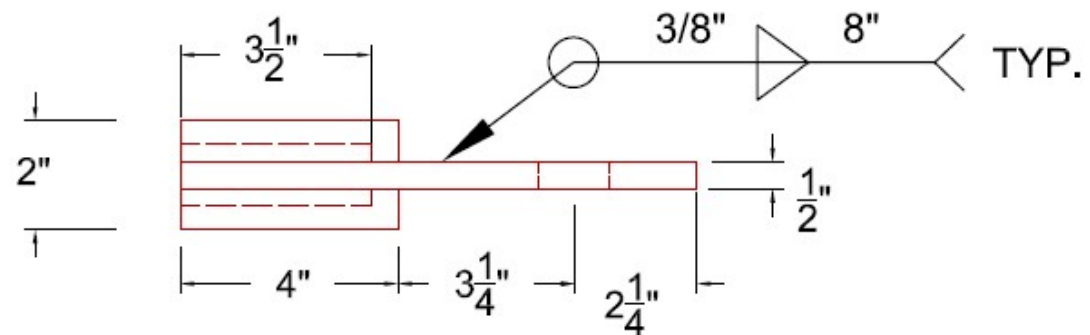


**Figure C.4:** FRP connector plate 2 with design weld detail.  
 Note: All dimensions in inches; 1 in. = 25.4 mm



(a) plan



(b) elevation

**Figure C.5:** Turnbuckle plate with design weld detail.

Note: All dimensions in inches; 1 in. = 25.4 mm



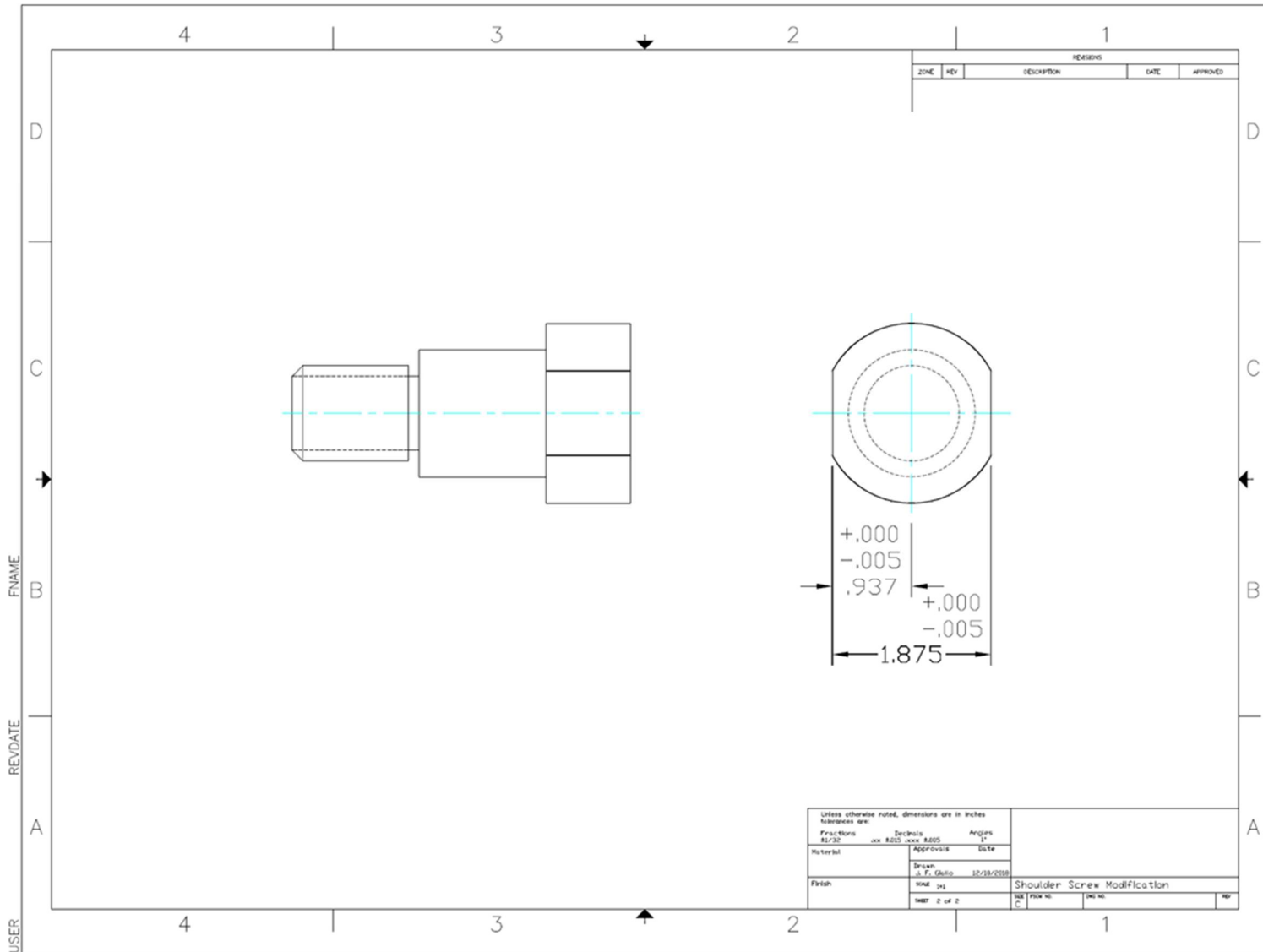


**Figure C.7:** Shoulder bolt (pin) machinist as-built detail.

*Note: All dimensions in inches; 1 in. = 25.4 mm*



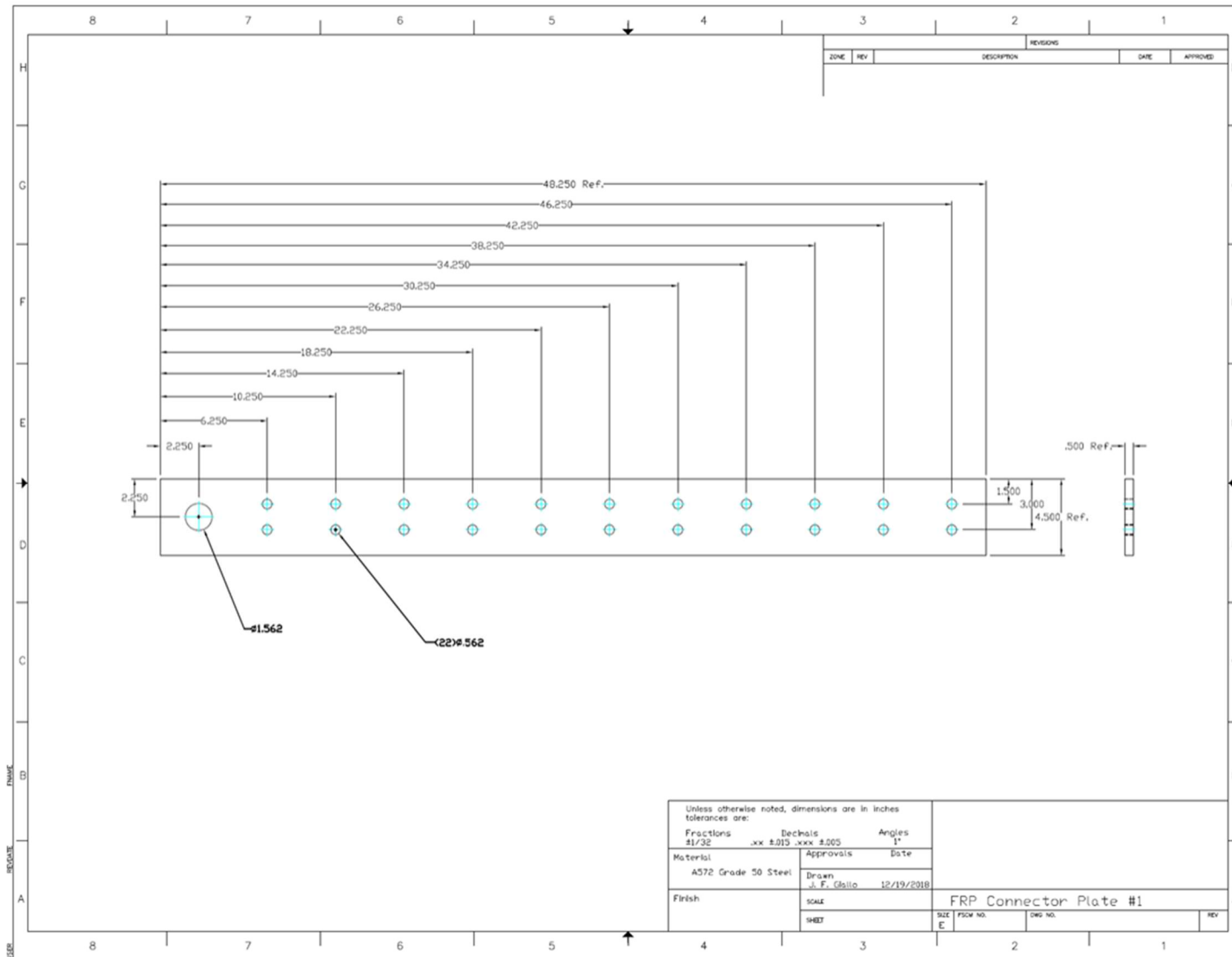


**Figure C.9:** FRP connector plate 1 machinist as-built drawing.  
 Note: All dimensions in inches; 1 in. = 25.4 mm

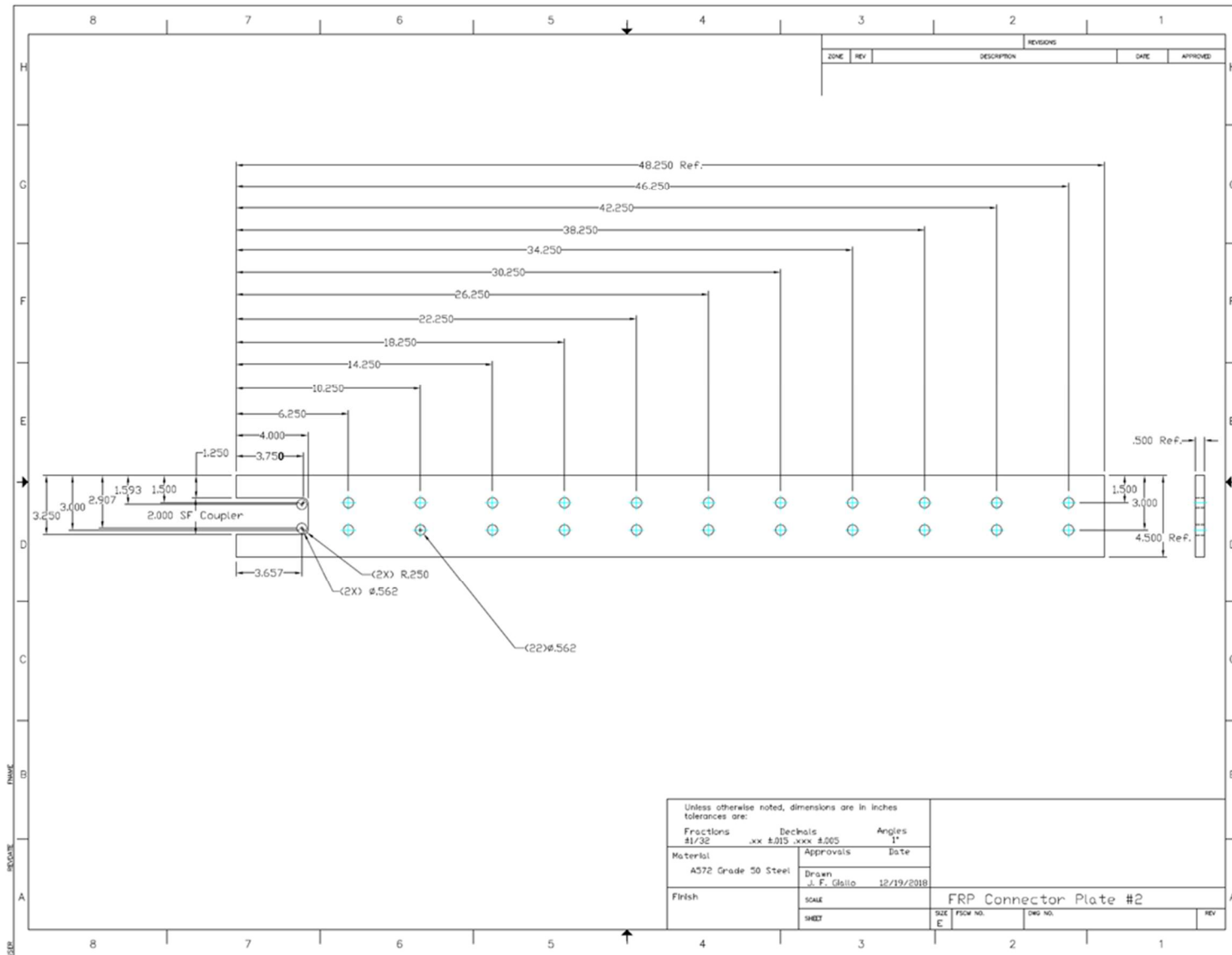


**Figure C.10: FRP connector plate 2 machinist as-built drawing.**

*Note: All dimensions in inches; 1 in. = 25.4 mm*

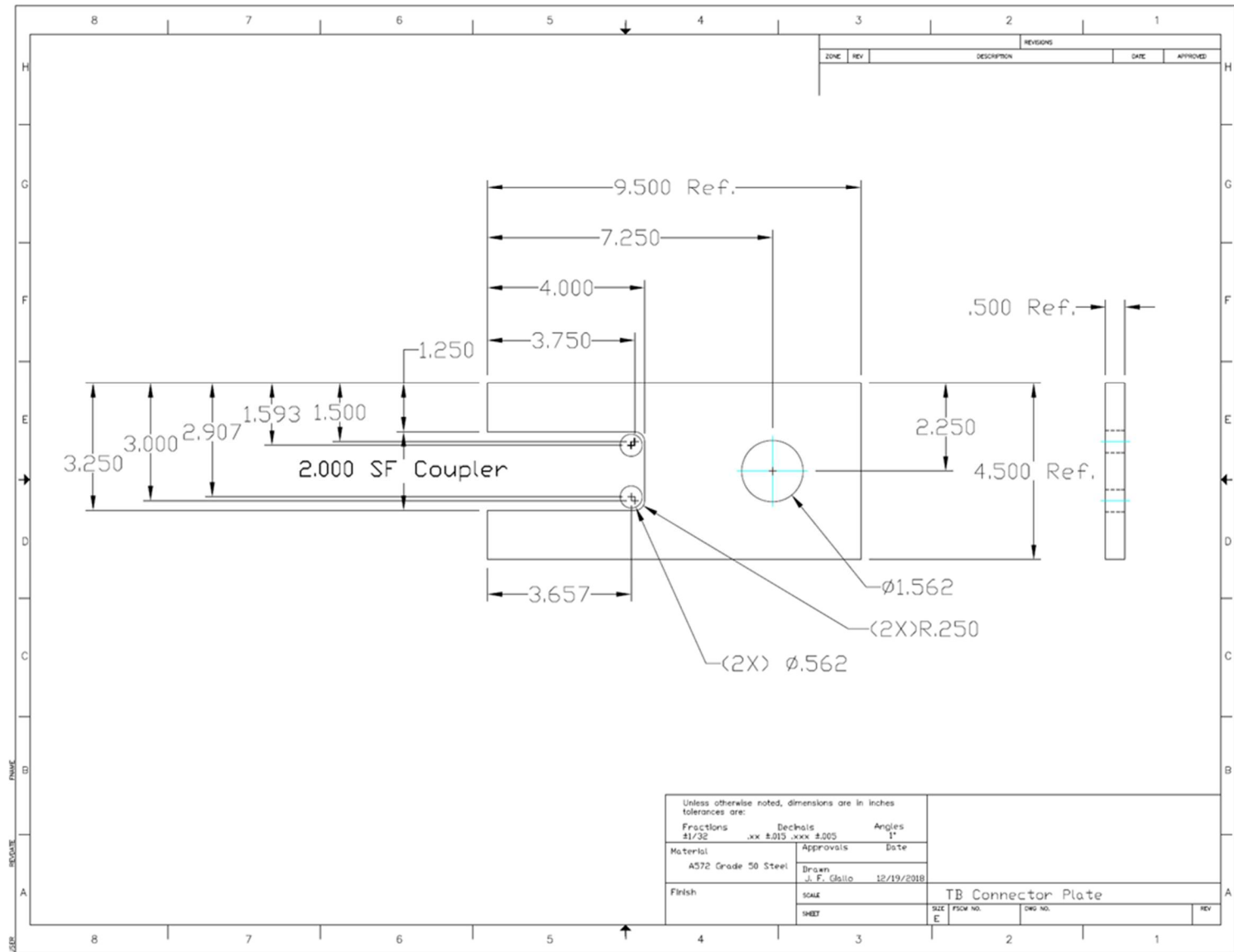


**Figure C.11: Turnbuckle (TB) plate machinist as-built drawing.**

*Note: All dimensions in inches; 1 in. = 25.4 mm*

### Appendix D: Overview of MF-FRP Retrofit Field Installation Activities

Appendix D presents an overview of field-level installation activities for DOT maintenance personnel consideration. It is recommended that DOT maintenance personnel correlate equivalent in-place concrete strength obtained from cores (Activity 2.3 in Table D.1) removed from candidate C-channel flanges with appropriate non-destructive evaluation techniques, such as shear wave tomography or other appropriate methods, to determine the quality of the concrete in the MF-FRP anchor region of the C-channel stems. Further, candidate bridge assessment and the acceptability of the MF-FRP methodology for restoration (Activity 1.1 in Table D.1) should be conducted to determine the level and location of deterioration. The MF-FRP methodology is intended to restore mild to moderate deterioration (complete loss of 1-2 prestressing strands), and the candidate member must have sound concrete (original or patched) at the anchor zone for the retrofit solution.

Correlation between primary wave pulse velocity,  $C_p$ , (if used) and  $f_c$  should be conducted using the ratios in Equation D.1.

$$\frac{C_{p@location\ u}}{C_{p,core}} = \sqrt{\frac{E_{c@location\ u}}{E_{c,core}}} = \sqrt[4]{\frac{f_{c@location\ u}}{f_{c,core}}} \quad (D.1)$$

where  $C_{p@location\ u}$  is the primary wave velocity at location  $u$ ,  $C_{p,core}$  is the primary wave velocity of a core,  $E_{c@location\ u}$  is the modulus of elasticity at location  $u$ ,  $E_{c,core}$  is the modulus of elasticity of a core,  $f_{c@location\ u}$  is the concrete compressive strength at location  $u$ , and  $f_{c,core}$  is the concrete compressive strength of a core. Because the relationship between  $C_p$  and  $E_c$  depends on the specimen geometry and Poisson's Ratio of the material, and the relationship between  $E_c$  and  $f_c$  is empirical and varies with raw materials, it is typically best to use the ratios in Equation D.1 to estimate the compressive strength of concrete in different sections of the beam. Non-destructive testing (NDT) readings should be taken prior to coring for a specific location correlation and to examine special distribution of material properties (if visual inspection suggests it is necessary).

The activity summary presented in Table D.1 does not present activity durations, as the duration for specific field-level tasks presented in Chapter 6 are for comparison of MF-FRP 1.0 and MF-FRP 2.0

designs only, and must be validated by experienced DOT maintenance personnel in the field. However, the activities presented in Table D.1 are intended to provide DOT planners and maintenance supervisors with the appropriate level of detail to schedule installation resources for the MF-FRP retrofit solution presented in this thesis.

**Table D.1:** Installation Activity Summary List.

Activity ID	Activity Name
<b>1</b>	<b>Determine extent of damage, especially in anchor zones, based on visual assessment supported by NDT analysis, as necessary</b>
1.1	Asses acceptability of MF-FRP methodology as appropriate means for addressing prestress losses (based on extent and location of deterioration)
<b>2</b>	<b>Evaluate concrete quality</b>
2.1	Estimate concrete strength
2.1.1	If NDT (eg. impact echo or shear wave tomography) is used, measure $C_p$ before cutting core
2.1.2	If possible, take at least one core in the stem
2.2	Determine equivalent in-place concrete strength from cores
2.3	Correlate strength of flange to stem using appropriate NDT method
<b>3</b>	<b>Design MF-FRP fixed plate connection to accommodate concrete splitting behavior</b>
3.1	Design calculations to determine fixed plate bolt size and pattern using appropriate design guides
<b>4</b>	<b>Prepare FRP for installation</b>
4.1	Measure beams for MF-FRP installation
4.2	Cut FRP to appropriate length and number for bridge
4.3	Drill holes in FRP
4.4	Attach FRP to FRP Connector Plates
<b>5</b>	<b>Installation Activities</b>
5.1	Mobilization
5.2	Locate Steel
5.3	Drill Dead-end
5.4	Drill Live-end
5.5	Install Dead-end Fixed Plates
5.6	Install Live-end Fixed Plates
5.7	Attach FRP Connector Plate to Dead-end Fixed Plate
5.8	Attach FRP Connector Plate to turnbuckle
5.9	Attach turnbuckle to turnbuckle connector plate
5.10	Attach turnbuckle connector plate to live-end fixed plate
5.11	Remove FRP slack
5.12	Mark mid-span witness marks on FRP and C-channel stem
5.13	Mark elongation witness mark for desired prestress level on C-channel stem
5.14	Install brace to prevent FRP plate rotation during prestressing
5.15	Prestress MF-FRP retrofit
5.16	Demobilization

### Appendix E: ACI 214.4 Calculations and Concrete Core Data

Appendix E presents detailed data for the concrete cores taken from specimens MF-FRP-D1, MF-FRP-D2, and MF-FRP-U2. Values for each variable presented in the ACI 214.4 (2010) Alternate Method (Chapters 2 and 6) are presented in Table E.1. Adjustment factors used to determine the equivalent in-place concrete strength are presented in Table E.2, and concrete core data is presented in Table E.3.

**Table E.1:** ACI 214.4 Alternate Method results.

ACI214.4 Alternate Method	
Variable	Value (psi)
$f'_{c,eq}$	<b>8210</b>
$\bar{f}_c$	10380
$(\bar{f}_c)_{CL}$	9440
$s_c$	1580
$s_a$	400
$T$	1.41
$n$	10
$Z$	1.28
$V_{l/d}$	0.0147
$V_{dia}$	0
$V_{mc}$	0.025
$V_d$	0.025
$C$	0.87

**Table E.2:** In-place Strength Adjustment Factors.

Core ID	$l/d$	$\alpha$	Correction Factors (ACI 214.4, 2010)				Adjusted $f_{core}$ (psi)
			$F_{l/d}$	$F_{dia}$	$F_{mc}$	$F_d$	
C1	1.29	3.00E-06	0.95	1.00	1.00	1.06	10730
C2	1.21	3.00E-06	0.94	1.00	1.00	1.06	12220
C3	1.19	3.00E-06	0.94	1.00	1.00	1.06	10360
C4	1.23	3.00E-06	0.95	1.00	1.00	1.06	12230
C5	1.11	3.00E-06	0.92	1.00	1.00	1.06	9730
C6	1.13	3.00E-06	0.92	1.00	1.00	1.06	7810
C7	1.11	3.00E-06	0.92	1.00	1.00	1.06	8750
C8	1.17	3.00E-06	0.93	1.00	1.00	1.06	11260

**Table E.3:** Concrete Core Data.

Specimen	Core ID	dia. <sub>1</sub> (in.)	dia. <sub>2</sub> (in.)	dia. <sub>3</sub> (in.)	dia. <sub>AVG</sub> (in.)	Area (in <sup>2</sup> )	$l_1$ (in.)	$l_2$ (in.)	$l_3$ (in.)	$l_{AVG}$ (in.)	Volume (in <sup>3</sup> )	Peak Load (kip)	$f_{core}$ (ksi)
MF-FRP-D1	C1	3.68	3.70	3.68	3.69	10.67	4.78	4.75	4.75	4.76	50.81	113.70	10.650
	C2	3.74	3.74	3.73	3.74	10.97	4.52	4.52	4.55	4.53	49.68	134.20	12.240
	C3	3.73	3.73	3.73	3.73	10.93	4.44	4.45	4.45	4.45	48.59	114.10	10.440
	C4	3.72	3.72	3.73	3.72	10.89	4.59	4.58	4.61	4.59	50.01	132.90	12.210
MF-FRP-U2	C5	3.74	3.74	3.72	3.73	10.94	4.16	4.16	4.17	4.16	45.49	108.90	9.960
	C6	3.73	3.73	3.72	3.73	10.91	4.21	4.24	4.23	4.23	46.11	87.30	8.000
MF-FRP-D2	C7	3.75	3.72	3.74	3.74	10.97	4.12	4.15	4.14	4.14	45.42	98.60	8.990
	C8	3.73	3.73	3.72	3.73	10.91	4.33	4.34	4.36	4.34	47.40	124.20	11.380

**APPENDIX F:  
METHODOLOGY AND EXAMPLE OF ALTERNATE METHOD FOR DETERMINING IN-  
PLACE CONCRETE STRENGTH**

Appendix F presents the methodology and an example result for a method of obtaining reasonable values of in-place concrete strength using maximum likelihood estimation (MLE). The MLE methodology is an alternate method to the more common methods described in ACI 214.4 (2010), discussed in Chapters 2 and 6 of this thesis. The MLE methodology is currently the subject of future research and planned publication to present the methodology as an additional tool available to practicing engineers. The methodology is presented here because it is relevant, with further development, to determining a statistically valid estimate of the concrete strength in concrete superstructure elements which are candidates for the MF-FRP retrofit solution presented in this study.

**Background – Probabilities of Strength Tests in Acceptance Testing**

ACI 318 (2014), requires the average strength of the concrete as delivered to be no less than the larger of Equations F.1a and F.1b:

$$f'_{cr} \geq f'_c + 2.33s - 500 \quad (\text{F.1a})$$

and

$$f'_{cr} \geq f'_c + 1.34s \quad (\text{F.1b})$$

where  $f'_{cr}$  is the minimum required average compressive strength (psi) and  $s$  is the standard deviation of strength tests from previous acceptance testing, adjusted when less than 30 but at least 15 tests are available. The average strength must be high enough that the probability does not exceed 1% that a test fails either of the acceptance test criteria on which Equations F.1a and F.1b are based.

The minimum average required strength specified in ACI 318 (2014) is a statistically based function of the standard deviation of tests from previous acceptance testing and performance requirements for acceptance testing, an approach that has been in place for over 40 years. The minimum average strength requirements given in Equations F.1a and F.1b are established to limit the probability to no more than 1% that a single acceptance test or three (3) sequential acceptance tests, respectively, fail to meet either of the two acceptance criteria, where a single test is defined as the average of at least two (2) cylinder strengths.

The criteria for acceptance testing in the field are that each individual (IND) strength test shall equal or exceed the specified strength minus 500 psi [ $f'_c - 500$ ] (or  $0.9f'_c$  if  $f'_c > 5000$  psi) and that the moving average of 3 (MA3) single, sequential tests shall equal or exceed the specified strength. The 2.33 coefficient in Equation F.1a is the one-sided, 99% critical value,  $z$ , for a standard normal distribution. A test result falling more than 500 psi lower than the specified strength is considered a structural concern to be investigated further (ACI 318, 2014). The 1.34 coefficient in Equation F.1b equals  $2.33/\sqrt{3}$ , since the average is over 3 consecutive tests. This criterion therefore limits the average of 3 sequential strength tests to no more than 1% falling below  $f'_{cr}$ . A MA3 test result falling below the specified strength is considered a process problem and is structurally acceptable.

The value of 1.34 is also approximately the one-sided, 91% critical value,  $z$ , for a normally distributed population for any single test. This means that acceptance testing of a concrete mixture with the minimum average strength established using Equation F.1a and F.1b will result in about 9% or 10% of the single acceptance test results falling below the specified strength. This observation forms the basis for using the 10<sup>th</sup> percentile value from a sample distribution as the approximate value of the specified strength of that sample of cores.

The multiplicative coefficients for the standard deviation in Equation F.1a and F.1b effectively establish thresholds for acceptance. The percentage of core strengths falling below  $f'_c$  will be termed the “threshold percentage” and the corresponding coefficient termed the “threshold coefficient” in the MLE methodology presented in this appendix.

### **Maximum Likelihood Estimation Methodology**

The distribution of in-place concrete strengths in existing structures is routinely assumed to be normal (Bartlett and MacGregor, 1995) unless control at the time of construction was very poor. In-place strengths from cores may be assumed to be independently and identically distributed (*iid*). Assume there are  $n$ , *iid* observations,  $X_1, \dots, X_n$  of equivalent in-place concrete strengths, that is, after the core strengths

have been adjusted for damage due to drilling, moisture condition at testing, core diameter and length to diameter ratio as described in ACI 214.4 (2010).

### MA3 Criterion

At this point, assume that  $f'_c$  will be selected to conform to a model in which no more than 9% of the strength data will be less than  $f'_c$ , that is, consistent with the requirements of ACI 318 (2014). Using Equation F.1b, it therefore can be stated that

$$X_1, \dots, X_n \stackrel{iid}{\sim} N(f'_c + 1.34\sigma, \sigma^2) \quad (F.3)$$

where the unknown parameters are  $f'_c$  and  $\sigma$ . Here  $f'_c$  is the parameter of interest and  $\sigma$ , the population standard deviation, will be treated as a “nuisance parameter.” The set of possible values of  $f'_c$  and  $\sigma$  is given by  $\Theta = \{3000, 4000, 5000\} \times (\sigma_1, \sigma_2)$  (psi). The density of a random variable  $X$  distributed as  $X \sim N(\mu, \sigma^2)$  is given by

$$f_X(x) = \frac{1}{\sqrt{2\pi}\sigma} \exp\left\{-\frac{1}{2\sigma^2}(x - \mu)^2\right\}; x \in \mathbb{R} \quad (F.4)$$

The likelihood function corresponding to this problem is therefore given by

$$\begin{aligned} L(f'_c, \sigma | X_1 = x_1, \dots, X_n = x_n) &= \prod_{i=1}^n f_{X_i}(x_i) \\ &= \prod_{i=1}^n \frac{1}{\sqrt{2\pi}\sigma} \exp\left\{-\frac{1}{2\sigma^2}(x_i - f'_c - 1.34\sigma)^2\right\} \\ &= (2\pi)^{-\frac{n}{2}} \sigma^{-n} \exp\left\{-\frac{1}{2\sigma^2} \sum_{i=1}^n (x_i - f'_c - 1.34\sigma)^2\right\} \end{aligned} \quad (F.5)$$

The log-likelihood function is analyzed for computational efficiency since the argument that maximizes the likelihood function also maximizes the log-likelihood function. The log-likelihood function is given by

$$\begin{aligned} l(f'_c, \sigma | X_1 = x_1, \dots, X_n = x_n) &= \log [L(f'_c, \sigma | X_1 = x_1, \dots, X_n = x_n)] \\ &= -\frac{n}{2} \log(2\pi) - n \log(\sigma) - \frac{1}{2\sigma^2} \sum_{i=1}^n (x_i - f'_c - 1.34\sigma)^2 \end{aligned} \quad (F.6)$$

A separate log-likelihood function is evaluated for each specific value of  $f'_c$ . Let the values of the MLEs be given by  $f'_c{}^{MLE}$  and  $s^{MLE}$ . By definition,

$$(f_c^{MLE}, s^{MLE}) = \arg \max_{(f_c', s) \in \Theta} l(f_c', s | X_1 = x_1, \dots, X_n = x_n) \quad (\text{F.7})$$

In continuous MLE analysis, the numerical value of each log-likelihood function is typically determined by setting the first derivative of the function to 0 and solving the equation for the parameter of interest.

Since  $f_c'$  is fixed for each of the log-likelihood functions, the derivative would be taken over the standard deviation, the “nuisance” parameter. The second derivative of the log-likelihood must be  $< 0$  for a maximum.

The derivatives are not required to identify the most likely specified strength, however. Equations F.6 and F.7 can be implemented in a spreadsheet for a reasonable range of values of the standard deviation and the maximum of each log-likelihood function determined numerically. Equation F.7 can also be evaluated using R™, an open-source, software package developed for applications to statistical analysis and available without charge.

The log-likelihood function for each separate candidate value of  $f_c'$  is calculated over a range of standard deviations. The candidate specified strength associated with the largest of the discrete log-likelihood functions will be that corresponding to the most likely value of  $f_c'$ .

### ***IND Criterion***

The MLE analysis using IND criteria for compressive strengths of 5000 psi or less is similar to that using MA3 criterion. Using Equation F.1a, Equation F.3 can be modified such that

$$X_1, \dots, X_n \stackrel{iid}{\sim} N((f_c' - 500) + 2.33\sigma, \sigma^2) \quad (\text{F.8})$$

Development of Equation F.9 for the IND criteria is determined similarly to Equation F.6.

$$\begin{aligned} l((f_c' - 3.4), \sigma | X_1 = x_1, \dots, X_n = x_n) &= \log [L((f_c' - 500), \sigma | X_1 = x_1, \dots, X_n = x_n)] \\ &= -\frac{n}{2} \log(2\pi) - n \log(\sigma) - \frac{1}{2\sigma^2} \sum_{i=1}^n (x_i - f_c' + 500 - 2.33\sigma)^2 \quad (\text{F.9}) \end{aligned}$$

The log-likelihood function is evaluated numerically for IND criterion using the method described for MA3 criteria. Equation F.9 must be modified when compressive strengths are greater than 5000 psi by replacing  $f_c' - 500$  (psi) with  $0.9f_c'$ .

### ***MLE Visualization***

Graphical solutions provide important information in the behavior of the log-likelihood functions over the range of interest of the standard deviation. A plot of each log-likelihood function versus standard deviation will either increase or decrease monotonically or have a maximum at the point of inflection. The graphical solution also provides information regarding the sensitivity of the MLE to different values of the standard deviation, an important result considering the concerns with variability of the strengths discussed above.

The limits of the standard deviation used in each of the discrete likelihood functions can be conveniently set as  $\sigma_1 = 300$  and  $\sigma_2 = 700$  psi. The standard deviation will not be less than 300 psi in practical situations. Table 4.3 of ACI 214.4 (2010) indicates that 700 psi is the lower limit for “Poor” control, a likely maximum in practice, at least in commercial construction in many areas. Other ranges of the standard deviation may be used, however, as determined by the engineer of record.

### **Applications and Examples**

#### ***Data for Examples***

Table F.1 shows data for an example set of in-place strengths taken from cores. Unadjusted core strengths and the equivalent in-place strengths are presented. The cores are assumed to each have a length to diameter ratio of exactly 2, a diameter of exactly 4 inches and to have been tested in the as-received moisture condition. The only correction factor to the mean is therefore for damage during drilling, 1.06, according to ACI 214.4 (2010). Strengths are reported to appropriate significant figures. The example data are hypothetical but not unreasonable and the equivalent in-place strengths are intentionally simple in value for convenience in reviewing.

**Table F.1:** Example Compressive Strength Data.

Core ID	unadjusted core strength (psi)	adjusted core: equivalent in-place cylinder strength (psi)
1	4810	5100
2	4620	4900
3	4430	4700
4	4250	4500
5	4250	4500
6	4150	4400
7	3960	4200
8	3770	4000
9	3508	3800
10	3400	3600

*Notes: 1 psi = 6.895 x 10<sup>-3</sup> MPa.*

### ***MLE Example Analysis and Discussion***

The standard deviation of the adjustments ( $s_a$ ) for this combination of factors can be shown to be 155 psi using Equation 2.5 from Chapter 2 of this thesis. If the cores were taken from several structurally similar members of cast-in-place concrete and a confidence level of 90% were used for  $T$ ,  $Z$ , and  $C$ , the CL recommended in ACI 214.4,  $f'_{c,eq}$  for this set of cores based on ACI 214.4 analysis is 3400 psi. The MLE (MA3) method was used to analyze the adjusted core strengths in Table F.1 using candidate specified strengths of 3000, 4000, and 5000 psi for standard deviations of 300, 310, 320, ... 790, and 800 psi in the spreadsheet analysis. Results of the numerical analysis are shown in Figure F.1.

It is clear from the MLE (MA3) analysis (Figure F.1) that the most likely value of the specified strength of the concrete used to place the elements from which the cores were taken is 4000 psi, but the curves of log-likelihood functions with 3000 and 4000 psi intersect at a standard deviation of approximately 650 psi, much greater than the 476 psi calculated standard deviation. This hypothetical data set provides several points that should be examined further. The maximum log-likelihood over the entire standard deviation range is associated with a specified strength of 4000 psi, but Figure F.1 suggests that using a range significantly different from the 300 to 700 psi in the analysis could lead to a different conclusion. In this particular example, concluding that 3000 psi is a more appropriate classification would

only be reasonable if there were indications that the standard deviation of the concrete in the element was much greater than about 700 psi, an unlikely condition in many situations. In the absence of external information, such as from NDT analysis or other site investigation reports, the calculated standard deviation, although based on only 10 samples, suggests that consideration of standard deviation values past the 650 psi intercept is not justified in this case.

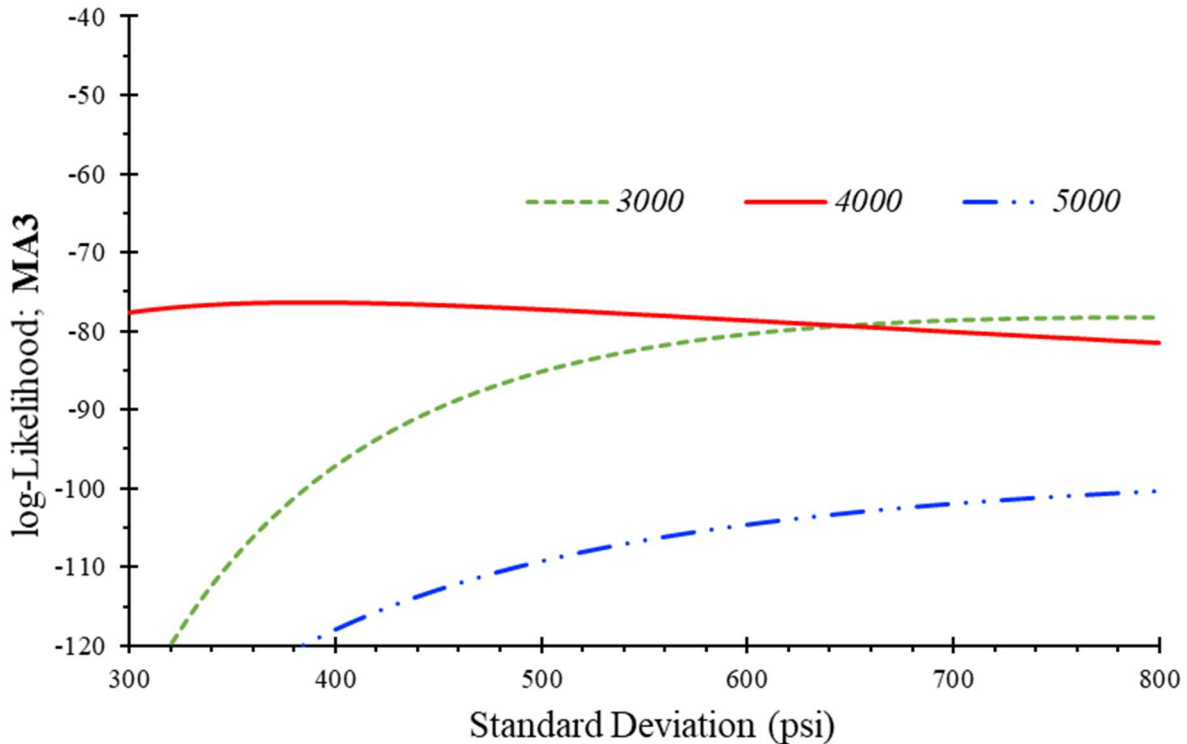


**Figure F.1:** Graphical MLE (MA3) Analysis, Example 1; Threshold Coefficient = 1.34.

Tables F.2 through F.4 provide the numerical results of the MLE methodology for each candidate strength (3000, 4000, and 5000 psi), given the in-place strengths presented in Table F.1.

**Table F.2: MA3 Results for Candidate  $f'c = 3000$  psi; Threshold Coefficient = 1.34.**

candidate $f'_c$ <b>3000</b>	$(x_i - f'_c - 1.34s)^2$ for adjusted core strengths, $x_i$										log-L (Eqn. 6.6)
	s	5100	4900	4700	4500	4500	4400	4200	4000	3800	
300	2883204	2244004	1684804	1205604	1205604	996004	636804	357604	158404	39204	-129.62
310	2837877	2204037	1650197	1176357	1176357	969437	615597	341757	147917	34077	-124.59
320	2792909	2164429	1615949	1147469	1147469	943229	594749	326269	137789	29309	-120.09
330	2748301	2125181	1582061	1118941	1118941	917381	574261	311141	128021	24901	-116.07
340	2704051	2086291	1548531	1090771	1090771	891891	554131	296371	118611	20851	-112.47
350	2660161	2047761	1515361	1062961	1062961	866761	534361	281961	109561	17161	-109.23
360	2616630	2009590	1482550	1035510	1035510	841990	514950	267910	100870	13830	-106.32
370	2573458	1971778	1450098	1008418	1008418	817578	495898	254218	92538	10858	-103.69
380	2530645	1934325	1418005	981685	981685	793525	477205	240885	84565	8245	-101.32
390	2488191	1897231	1386271	955311	955311	769831	458871	227911	76951	5991	-99.17
400	2446096	1860496	1354896	929296	929296	746496	440896	215296	69696	4096	-97.22
410	2404360	1824120	1323880	903640	903640	723520	423280	203040	62800	2560	-95.45
420	2362984	1788104	1293224	878344	878344	700904	406024	191144	56264	1384	-93.85
430	2321966	1752446	1262926	853406	853406	678646	389126	179606	50086	566	-92.39
440	2281308	1717148	1232988	828828	828828	656748	372588	168428	44268	108	-91.06
450	2241009	1682209	1203409	804609	804609	635209	356409	157609	38809	9	-89.85
460	2201069	1647629	1174189	780749	780749	614029	340589	147149	33709	269	-88.74
470	2161488	1613408	1145328	757248	757248	593208	325128	137048	28968	888	-87.74
480	2122266	1579546	1116826	734106	734106	572746	310026	127306	24586	1866	-86.82
490	2083404	1546044	1088684	711324	711324	552644	295284	117924	20564	3204	-85.98
500	2044900	1512900	1060900	688900	688900	532900	280900	108900	16900	4900	-85.22
510	2006756	1480116	1033476	666836	666836	513516	266876	100236	13596	6956	-84.52
520	1968970	1447690	1006410	645130	645130	494490	253210	91930	10650	9370	-83.88
530	1931544	1415624	979704	623784	623784	475824	239904	83984	8064	12144	-83.30
540	1894477	1383917	953357	602797	602797	457517	226957	76397	5837	15277	-82.77
550	1857769	1352569	927369	582169	582169	439569	214369	69169	3969	18769	-82.29
560	1821420	1321580	901740	561900	561900	421980	202140	62300	2460	22620	-81.84
570	1785430	1290950	876470	541990	541990	404750	190270	55790	1310	26830	-81.44
580	1749800	1260680	851560	522440	522440	387880	178760	49640	520	31400	-81.08
590	1714528	1230768	827008	503248	503248	371368	167608	43848	88	36328	-80.74
600	1679616	1201216	802816	484416	484416	355216	156816	38416	16	41616	-80.44
610	1645063	1172023	778983	465943	465943	339423	146383	33343	303	47263	-80.17
620	1610869	1143189	755509	447829	447829	323989	136309	28629	949	53269	-79.92
630	1577034	1114714	732394	430074	430074	308914	126594	24274	1954	59634	-79.70
640	1543558	1086598	709638	412678	412678	294198	117238	20278	3318	66358	-79.50
650	1510441	1058841	687241	395641	395641	279841	108241	16641	5041	73441	-79.32
660	1477683	1031443	665203	378963	378963	265843	99603	13363	7123	80883	-79.16
670	1445285	1004405	643525	362645	362645	252205	91325	10445	9565	88685	-79.02
680	1413245	977725	622205	346685	346685	238925	83405	7885	12365	96845	-78.89
690	1381565	951405	601245	331085	331085	226005	75845	5685	15525	105365	-78.78
700	1350244	925444	580644	315844	315844	213444	68644	3844	19044	114244	-78.69
710	1319282	899842	560402	300962	300962	201242	61802	2362	22922	123482	-78.60
720	1288679	874599	540519	286439	286439	189399	55319	1239	27159	133079	-78.53
730	1258435	849715	520995	272275	272275	177915	49195	475	31755	143035	-78.48
740	1228551	825191	501831	258471	258471	166791	43431	71	36711	153351	-78.43
750	1199025	801025	483025	245025	245025	156025	38025	25	42025	164025	-78.39
760	1169859	777219	464579	231939	231939	145619	32979	339	47699	175059	-78.36
770	1141051	753771	446491	219211	219211	135571	28291	1011	53731	186451	-78.34
780	1112603	730683	428763	206843	206843	125883	23963	2043	60123	198203	-78.33
790	1084514	707954	411394	194834	194834	116554	19994	3434	66874	210314	-78.32
800	1056784	685584	394384	183184	183184	107584	16384	5184	73984	222784	-78.32

**Table F.3:** MA3 Results for Candidate  $f'c = 4000$  psi; Threshold Coefficient = 1.34.

candidate $f'_c$ 4000	$(x_i - f'_c - 1.34s)^2$ for adjusted core strengths, $x_i$										
	s	5100	4900	4700	4500	4500	4400	4200	4000	3800	3600
300	487204	248004	88804	9604	9604	4	40804	161604	362404	643204	-77.62
310	468677	234837	80997	7157	7157	237	46397	172557	378717	664877	-77.28
320	450509	222029	73549	5069	5069	829	52349	183869	395389	686909	-77.01
330	432701	209581	66461	3341	3341	1781	58661	195541	412421	709301	-76.79
340	415251	197491	59731	1971	1971	3091	65331	207571	429811	732051	-76.62
350	398161	185761	53361	961	961	4761	72361	219961	447561	755161	-76.50
360	381430	174390	47350	310	310	6790	79750	232710	465670	778630	-76.41
370	365058	163378	41698	18	18	9178	87498	245818	484138	802458	-76.36
380	349045	152725	36405	85	85	11925	95605	259285	502965	826645	-76.33
390	333391	142431	31471	511	511	15031	104071	273111	522151	851191	-76.33
400	318096	132496	26896	1296	1296	18496	112896	287296	541696	876096	-76.34
410	303160	122920	22680	2440	2440	22320	122080	301840	561600	901360	-76.38
420	288584	113704	18824	3944	3944	26504	131624	316744	581864	926984	-76.43
430	274366	104846	15326	5806	5806	31046	141526	332006	602486	952966	-76.50
440	260508	96348	12188	8028	8028	35948	151788	347628	623468	979308	-76.57
450	247009	88209	9409	10609	10609	41209	162409	363609	644809	1006009	-76.66
460	233869	80429	6989	13549	13549	46829	173389	379949	666509	1033069	-76.76
470	221088	73008	4928	16848	16848	52808	184728	396648	688568	1060488	-76.86
480	208666	65946	3226	20506	20506	59146	196426	413706	710986	1088266	-76.98
490	196604	59244	1884	24524	24524	65844	208484	431124	733764	1116404	-77.09
500	184900	52900	900	28900	28900	72900	220900	448900	756900	1144900	-77.22
510	173556	46916	276	33636	33636	80316	233676	467036	780396	1173756	-77.35
520	162570	41290	10	38730	38730	88090	246810	485530	804250	1202970	-77.48
530	151944	36024	104	44184	44184	96224	260304	504384	828464	1232544	-77.61
540	141677	31117	557	49997	49997	104717	274157	523597	853037	1262477	-77.75
550	131769	26569	1369	56169	56169	113569	288369	543169	877969	1292769	-77.89
560	122220	22380	2540	62700	62700	122780	302940	563100	903260	1323420	-78.03
570	113030	18550	4070	69590	69590	132350	317870	583390	928910	1354430	-78.17
580	104200	15080	5960	76840	76840	142280	333160	604040	954920	1385800	-78.32
590	95728	11968	8208	84448	84448	152568	348808	625048	981288	1417528	-78.46
600	87616	9216	10816	92416	92416	163216	364816	646416	1008016	1449616	-78.61
610	79863	6823	13783	100743	100743	174223	381183	668143	1035103	1482063	-78.76
620	72469	4789	17109	109429	109429	185589	397909	690229	1062549	1514869	-78.90
630	65434	3114	20794	118474	118474	197314	414994	712674	1090354	1548034	-79.05
640	58758	1798	24838	127878	127878	209398	432438	735478	1118518	1581558	-79.20
650	52441	841	29241	137641	137641	221841	450241	758641	1147041	1615441	-79.34
660	46483	243	34003	147763	147763	234643	468403	782163	1175923	1649683	-79.49
670	40885	5	39125	158245	158245	247805	486925	806045	1205165	1684285	-79.64
680	35645	125	44605	169085	169085	261325	505805	830285	1234765	1719245	-79.78
690	30765	605	50445	180285	180285	275205	525045	854885	1264725	1754565	-79.93
700	26244	1444	56644	191844	191844	289444	544644	879844	1295044	1790244	-80.07
710	22082	2642	63202	203762	203762	304042	564602	905162	1325722	1826282	-80.22
720	18279	4199	70119	216039	216039	318999	584919	930839	1356759	1862679	-80.36
730	14835	6115	77395	228675	228675	334315	605595	956875	1388155	1899435	-80.51
740	11751	8391	85031	241671	241671	349991	626631	983271	1419911	1936551	-80.65
750	9025	11025	93025	255025	255025	366025	648025	1010025	1452025	1974025	-80.79
760	6659	14019	101379	268739	268739	382419	669779	1037139	1484499	2011859	-80.93
770	4651	17371	110091	282811	282811	399171	691891	1064611	1517331	2050051	-81.07
780	3003	21083	119163	297243	297243	416283	714363	1092443	1550523	2088603	-81.21
790	1714	25154	128594	312034	312034	433754	737194	1120634	1584074	2127514	-81.34
800	784	29584	138384	327184	327184	451584	760384	1149184	1617984	2166784	-81.48

Table F.4: MA3 Results for Candidate  $f'c = 5000$  psi; Threshold Coefficient = 1.34.

candidate $f'_c$	$(x_i - f'_c - 1.34s)^2$ for adjusted core strengths, $x_i$										
5000											
s	5100	4900	4700	4500	4500	4400	4200	4000	3800	3600	log -L (Eqn. 6.6)
300	91204	252004	492804	813604	813604	1004004	1444804	1965604	2566404	3247204	-136.73
310	99477	265637	511797	837957	837957	1031037	1477197	2003357	2609517	3295677	-134.03
320	108109	279629	531149	862669	862669	1058429	1509949	2041469	2652989	3344509	-131.58
330	117101	293981	550861	887741	887741	1086181	1543061	2079941	2696821	3393701	-129.33
340	126451	308691	570931	913171	913171	1114291	1576531	2118771	2741011	3443251	-127.28
350	136161	323761	591361	938961	938961	1142761	1610361	2157961	2785561	3493161	-125.40
360	146230	339190	612150	965110	965110	1171590	1644550	2197510	2830470	3543430	-123.67
370	156658	354978	633298	991618	991618	1200778	1679098	2237418	2875738	3594058	-122.07
380	167445	371125	654805	1018485	1018485	1230325	1714005	2277685	2921365	3645045	-120.60
390	178591	387631	676671	1045711	1045711	1260231	1749271	2318311	2967351	3696391	-119.23
400	190096	404496	698896	1073296	1073296	1290496	1784896	2359296	3013696	3748096	-117.97
410	201960	421720	721480	1101240	1101240	1321120	1820880	2400640	3060400	3800160	-116.80
420	214184	439304	744424	1129544	1129544	1352104	1857224	2442344	3107464	3852584	-115.71
430	226766	457246	767726	1158206	1158206	1383446	1893926	2484406	3154886	3905366	-114.69
440	239708	475548	791388	1187228	1187228	1415148	1930988	2526828	3202668	3958508	-113.74
450	253009	494209	815409	1216609	1216609	1447209	1968409	2569609	3250809	4012009	-112.86
460	266669	513229	839789	1246349	1246349	1479629	2006189	2612749	3299309	4065869	-112.03
470	280688	532608	864528	1276448	1276448	1512408	2044328	2656248	3348168	4120088	-111.26
480	295066	552346	889626	1306906	1306906	1545546	2082826	2700106	3397386	4174666	-110.54
490	309804	572444	915084	1337724	1337724	1579044	2121684	2744324	3446964	4229604	-109.86
500	324900	592900	940900	1368900	1368900	1612900	2160900	2788900	3496900	4284900	-109.22
510	340356	613716	967076	1400436	1400436	1647116	2200476	2833836	3547196	4340556	-108.62
520	356170	634890	993610	1432330	1432330	1681690	2240410	2879130	3597850	4396570	-108.05
530	372344	656424	1020504	1464584	1464584	1716624	2280704	2924784	3648864	4452944	-107.52
540	388877	678317	1047757	1497197	1497197	1751917	2321357	2970797	3700237	4509677	-107.02
550	405769	700569	1075369	1530169	1530169	1787569	2362369	3017169	3751969	4566769	-106.55
560	423020	723180	1103340	1563500	1563500	1823580	2403740	3063900	3804060	4624220	-106.10
570	440630	746150	1131670	1597190	1597190	1859950	2445470	3110990	3856510	4682030	-105.68
580	458600	769480	1160360	1631240	1631240	1896680	2487560	3158440	3909320	4740200	-105.29
590	476928	793168	1189408	1665648	1665648	1933768	2530008	3206248	3962488	4798728	-104.91
600	495616	817216	1218816	1700416	1700416	1971216	2572816	3254416	4016016	4857616	-104.55
610	514663	841623	1248583	1735543	1735543	2009023	2615983	3302943	4069903	4916863	-104.22
620	534069	866389	1278709	1771029	1771029	2047189	2659509	3351829	4124149	4976469	-103.90
630	553834	891514	1309194	1806874	1806874	2085714	2703394	3401074	4178754	5036434	-103.60
640	573958	916998	1340038	1843078	1843078	2124598	2747638	3450678	4233718	5096758	-103.31
650	594441	942841	1371241	1879641	1879641	2163841	2792241	3500641	4289041	5157441	-103.04
660	615283	969043	1402803	1916563	1916563	2203443	2837203	3550963	4344723	5218483	-102.78
670	636485	995605	1434725	1953845	1953845	2243405	2882525	3601645	4400765	5279885	-102.53
680	658045	1022525	1467005	1991485	1991485	2283725	2928205	3652685	4457165	5341645	-102.30
690	679965	1049805	1499645	2029485	2029485	2324405	2974245	3704085	4513925	5403765	-102.08
700	702244	1077444	1532644	2067844	2067844	2365444	3020644	3755844	4571044	5466244	-101.87
710	724882	1105442	1566002	2106562	2106562	2406842	3067402	3807962	4628522	5529082	-101.67
720	747879	1133799	1599719	2145639	2145639	2448599	3114519	3860439	4686359	5592279	-101.48
730	771235	1162515	1633795	2185075	2185075	2490715	3161995	3913275	4744555	5655835	-101.30
740	794951	1191591	1668231	2224871	2224871	2533191	3209831	3966471	4803111	5719751	-101.13
750	819025	1221025	1703025	2265025	2265025	2576025	3258025	4020025	4862025	5784025	-100.97
760	843459	1250819	1738179	2305539	2305539	2619219	3306579	4073939	4921299	5848659	-100.81
770	868251	1280971	1773691	2346411	2346411	2662771	3355491	4128211	4980931	5913651	-100.66
780	893403	1311483	1809563	2387643	2387643	2706683	3404763	4182843	5040923	5979003	-100.52
790	918914	1342354	1845794	2429234	2429234	2750954	3454394	4237834	5101274	6044714	-100.39
800	944784	1373584	1882384	2471184	2471184	2795584	3504384	4293184	5161984	6110784	-100.26

### **Conclusions and Recommendations**

The discrete MLE approach provides a powerful, statistically robust method to identify the specified design strength most closely associated with the distribution of equivalent in-place strengths obtained from cores. The methodology is recommended for further development with applied in-place strength data sets from existing field studies. Additionally, research to extend the MLE application to nondestructive evaluation techniques would be useful. The MLE model presented in this appendix is only useful for determining the most likely design compressive strength of concrete from a sufficient number of drilled cores. Therefore, a model which is adjusted for nondestructive evaluation results would enable practicing engineers to determine the most likely design compressive strength of an in-service superstructure without drilling cores, which compromise the structural integrity of the flexural element and are labor intensive to obtain.